Frictional and transport properties of simulated faults in CO_2 storage reservoirs and clay-rich caprocks

Elisenda Bakker

Utrecht Series in Earth Sciences
№. 124

Members of the dissertation committee

Prof. dr. J-P. Burg
Institute of Geology, ETH Zürich
Zürich, Switzerland

Prof. dr. D. Elsworth
Dept. of Energy and Mineral Engineering, Dept. of Geosciences,
Centre for Geomechanics, Geofluids, and Geohazards,
Pennsylvania State University, United States of America

Prof. dr. Y. Guglielmi
Earth and Environmental Sciences, Lawrence Berkeley National Laboratory, United States of America; Université d'Aix-Marseille, France

Prof. Dr. C. He
State Key Laboratory of Earthquake Dynamics,
Institute of Geology, China Earthquake Administration,
Beijing, People's Republic of China

Dr. N. de Paola
Department of Earth Sciences, University of Durham,
Durham, United Kingdom

This study was conducted at the High Pressure and Temperature Laboratory (Experimental Rock Deformation Group), Department of Earth Sciences, Faculty of Geosciences, Utrecht University, Utrecht, the Netherlands.

This study was funded by CATO-2 and ULTimateCO_2

Printed by: Gildeprint – Enschede

ISBN/EAN: 978-90-6266-4481

Cover image: Boundary shear of a 50:50 quartz-calcite sample (see Chapter 4)

Frictional and transport properties of simulated faults in CO_2 storage reservoirs and clay-rich caprocks

Frictie en vloeistof transport eigenschappen van gesimuleerde breuken in CO_2 opslag reservoirs en klei-rijke afdekgesteentes
(met een samenvatting in het Nederlands)

Proefschrift

ter verkrijging van de graad van doctor aan de Universiteit Utrecht op gezag van de rector magnificus prof. dr. G. J. van der Zwaan, ingevolge het besluit van het college voor promoties in het openbaar te verdedigen op

woensdag 22 februari 2017 des middags te 12.45 uur

door

Elisenda Bakker

geboren op 29 september 1987 te Zwijndrecht

Promotor:	**Prof. dr. C. J. Spiers**
Copromotoren:	**Dr. S.J.T. Hangx**
	Dr. A.R. Niemeijer

“Zonder wrijving geen glans”

Contents

Summary

In order to mitigate CO_2 and meet CO_2 emission regulations, storage of CO_2 in depleted hydrocarbon reservoirs is an attractive option, because of the well-known reservoir structure, proven sealing capability and pre-existing surface infrastructure. Potential storage complexes may consist of quartz-rich sandstones capped by clay-rich seals. To ensure safe anthropogenic CO_2 storage, it is important to maintain the sealing integrity of any (pre-)existing faults, which might start to leak due to fault re-activation upon any physical or chemical perturbation resulting from CO_2 injection or exposure. In addition, reactivation of faults might lead to induced seismicity. In order to improve seismic risk assessment as well as potential leakage due to geological CO_2 storage a quantitative understanding of the coupling between the chemical-mechanical effects of CO_2 injection and exposure on the frictional strength and stability as well as the transport properties of faults intersecting quartz-rich sandstones and/or clay-rich caprocks is needed.

In this thesis, I report the results of an experimental study of the coupled chemical-mechanical effects of long-term CO_2-fluid-rock interactions on the frictional and transport properties of fault materials composed of reservoir sandstones and carbonate-bearing clay-rich caprocks. Independently from the context of CO_2-storage, the reported results are also relevant for tectonically active faults in quartz-calcite and clay-rich formations or sequences in for example subduction zones and orogens at converging plate boundaries, where major and destructive natural earthquakes occur.

Chapter 1 outlines the motivation and scope of this thesis, including a brief overview of relevant previous research performed in the context of anthropogenic CO_2 storage in geological storage reservoirs. The chapter lists the overarching general aims of the research presented in this thesis.

Chapter 2 describes the chemically-induced effects of long-term CO_2 exposure on the frictional and transport properties of simulated quartz-rich fault gouges, by comparing naturally CO_2-exposed samples with their unexposed equivalents. In addition, the quartz-rich reservoir rock samples are compared to simulated

carbonate-rich fault gouges recovered from an ancient CO_2-leaking fault. Friction experiments consist of direct shear experiments, both lab-dry and wet, performed in a triaxial deformation apparatus at a temperature (T) of 23 and 100°C, effective normal stresses (σ_n^{eff}) of 5-50 MPa, and sliding velocities (V) of 0.22-11 µm/s, simulating in-situ storage conditions. Wet tests were conducted using a saturated-sample solution at a 25 MPa pore pressure (P_f). In addition to measuring the frictional properties of these fault gouges, permeability measurements were obtained for single experiments on each of the three simulated fault gouges (σ_n^{eff} = 50 MPa, $P_f \approx$ 2 MPa, $T \approx$ 23°C). Both lab-dry and wet simulated unexposed and CO_2-exposed quartz-rich samples exhibited mostly similar frictional behaviour (friction coefficient μ = shear stress / normal stress = 0.5-0.6) and consistently increasing friction coefficients with increasing sliding velocity (velocity-strengthening behaviour) for 23 and 100°C. The simulated CO_2-exposed carbonate-rich samples were only slightly stronger, showing a change from velocity-strengthening behaviour at 23°C to velocity-weakening behaviour at 100°C for both the lab-dry and wet samples. All three simulated fault gouge types showed argon gas permeability values in the order of 10^{-16} to 10^{-17} m^2, decreasing with increasing shear displacement. The obtained results imply that long-term CO_2 exposure will not affect the frictional behaviour and transport properties of a quartz-rich fault gouge significantly. On the contrary, a 40% increase in carbonate content, resulting from CO_2 leakage along a fault, will alter the sliding behaviour significantly, enhancing the potential for seismic slip.

In **Chapter 3**, I started by investigating the effects of shear displacement, dynamic shear and static holding, and effective normal stress on the potential anisotropy of permeability along and across a simulated clay-quartz-calcite fault gouge. Simulated fault gouge was prepared by crushing and sieving (<35 µm) Opalinus Claystone (OPA). This was followed by testing the effect of calcite content on the frictional strength and stability of the same simulated fault gouge material (OPA) by removing the naturally-present calcite from half of the tested material (calcite-free OPA, hence CFOPA) and comparing the observed behaviour of the calcite-bearing (OPA) samples to the calcite-free (CFOPA) samples. Room temperature direct shear experiments, in combination with permeametry, were performed in the same triaxial deformation apparatus as used in Chapter 2, employing effective normal stresses ranging between 5 and 50 MPa, a pore pressure of ~2 MPa, and sliding

velocities of 0.05-5.5 µm/s. The direct shear experiments, without permeametry, conducted to investigate the effect of calcite content were performed both vacuum-dry and wet (P_f = 25 MPa) at temperatures of up to ~150°C, an effective normal stress of 50 MPa, and sliding velocities of 0.22-11 µm/s. The permeability results show, irrespectively of the fluid flow orientation, a decrease in permeability with increasing shear displacement, dynamic shear and static holding, as well as with increasing effective normal stress. When comparing along- and across- fault permeability, a permeability anisotropy of up to 1 order of magnitude is observed pre-shear. With increasing shear displacement, the permeability anisotropy decreases to <0.5. The friction results show temperature insensitive friction coefficients for both calcite-bearing and calcite-free OPA gouges, with the calcite-free gouge ($\mu \approx 0.27$) being consistently 10-20% weaker than the calcite-bearing gouge ($\mu \approx 0.31$). Dry OPA gouge is almost double as strong as wet OPA ($\mu \approx 0.58$). For all experimental conditions tested, the calcite-bearing OPA and calcite-free OPA gouges exhibited velocity-strengthening behaviour. The results imply that a sheared gouge-filled fault is more likely to act as leakage pathway than the intact caprock, with a slight preference for along-fault leakage. Moreover, assuming wet in-situ conditions, slip reactivation in calcite-bearing and calcite-free OPA gouges is unlikely to lead to (induced) (micro)seismicity in the framework of rate-and-state friction.

In **Chapter 4**, I investigated the effect of calcite content on the frictional behaviour of clay-quartz-calcite fault gouge mixtures. For these experiments a new batch of CFOPA, similar to the one used in Chapter 3, had been prepared. Additionally, I explored the effects of added calcite on pure clay (kaolinite) and pure quartz independently, investigating 100% pure end-members plus 50:50 mixtures. Ring-shear experiments were performed at σ_n^{eff} = 50 MPa, P_f = 25 MPa, $T \approx$ 23-100-150°C and sliding velocities ranging between 0.22 and 100 µm/s. At a temperature of 23 and 100°C, the frictional strength and slip stability for CFOPA-calcite and kaolinite-calcite mixtures increase with increasing calcite content, while exhibiting stable, velocity-strengthening behaviour. A transition from velocity-strengthening to velocity-weakening behaviour is observed between 100 and 150°C for CFOPA-calcite mixtures containing >90% calcite, and for the kaolinite-calcite series the 100% calcite sample only. The frictional behaviour exhibited by the quartz-calcite mixtures is rather different, showing an increase in friction coefficient with

increasing calcite content at room temperature and no clear trend at 100 and 150°C. At 23 and 100°C, all quartz-calcite samples exhibited velocity-strengthening behaviour, whereas a transition from velocity-strengthening to velocity-weakening behaviour is observed between 100 and 150°C for the 50:50 quartz-calcite and the 100% calcite samples. Striking is the highly unstable, velocity-weakening behaviour exhibited by the 50:50 quartz-calcite mixtures, with velocity-dependence values more negative than obtained for either one of the end-members. Microstructural observations for the CFOPA-calcite mixtures suggest a change in controlling microscales processes with increasing calcite content, from shear being concentrated in phyllosilicate-rich shear bands (0-50% calcite samples) to more homogenously distributed cataclastic shear with grain size reduction of the calcite grains (70-100% calcite samples). Additionally, the transition from velocity-strengthening to velocity-weakening suggests the growing importance of time-dependent thermally-activated processes at calcite-calcite grain contacts such as diffusion, enhancing compaction. Microstructural observations for the quartz-calcite samples show a more reduced calcite grain size when mixed with quartz, potentially enhancing the effect of thermally-activated deformation mechanisms, e.g. diffusion, operating in the calcite component on the slip stability. Our results imply that significant changes in frictional strength or (micro)seismic potential of fault gouges with a clay-quartz-calcite composition are only expected following major carbonate precipitation (>90%) in the fault damage zone, potentially due to rapid CO_2 leakage and degassing. For quartz-calcite compositions, unstable behaviour is expected for near equal amounts of both phases.

Assessing the chemical effects of long-term CO_2-fluid-rock interactions on the frictional behaviour of a clay-quartz-calcite fault gouge in laboratory experiments is challenging due to the mineral reaction time-scales being much longer (>years) than the experimental time-scales of days to weeks to months. Therefore, I integrated predictive geochemical modelling and friction experiments in **Chapter 5** to investigate the effects of long-term CO_2-fluid-rock interaction on the frictional properties of clay-rich fault gouges. We started by investigating the effects of long-term CO_2-fluid-rock interaction on the chemical composition of two clay-quartz-calcite compositions for various pore fluid replacement times (i.e. the duration a fault gouge being exposed to a batch of pore water before being replaced with a new batch; 10 and 1000 years) and time frames (10 ka and 1 Ma) using

geochemical modelling. For the subsequent friction experiments, we focused on geochemical modelling results showing mineralogical changes that are expected to have a notable effect on the frictional behaviour. The selected geochemical modelling compositions were then prepared manually by mixing pure minerals according to the selected compositions. These mixtures were subsequently sheared, using the same experimental procedure and apparatus as used in Chapter 4, to determine the corresponding frictional properties. Our results show that integrated geochemical modelling and subsequent friction experiments may encounter some artificially-induced problems, such as the manual mixed illite and smectite to represent diagenetic illite-smectite. However, at the moment, it is the best practice available to assess the effect of long-term CO_2-fluid-rock interactions on the frictional behaviour of (simulated) fault gouges. Overall, our results show that the frictional strength increases due to the exposure-induced mineralogic changes. Furthermore, the frictional strength increases with increasing temperature, while showing a transition to velocity-weakening behaviour between 100 and 150°C. Mixtures consisting of extremely weak clay minerals (i.e. smectites) show a lower frictional strength, while exhibiting velocity-strengthening behaviour. Overall, our results show that the observed CO_2-induced mineralogic changes depend on the starting composition, residence time, and total reaction time. The observed correlation between the friction coefficient and quartz:calcite ratio, along with the dependence of the velocity-dependency of the same mixtures on the temperature, similar as reported in Chapter 4, suggest interaction between quartz and calcite, leading to the preferential crushing of the calcite component, causing enhanced time-dependent compaction, potentially explaining the observed velocity-weakening behaviour at 150°C.

This thesis is concluded with **Chapter 6**, listing a summary of all the main results and conclusions that can be drawn from the reported research along with the main implications for long-term CO_2-storage in sandstone reservoirs or capped by clay-quartz-calcite caprocks. Issues that remain unsolved are listed along with suggestions for future research.

Samenvatting

In een poging de CO_2 uitstoot te beperken en aan de CO_2 emissie regels te voldoen is de opslag van CO_2 in lege olie- en/of gas velden een aantrekkelijke oplossing. Onder andere vanwege de kennis over de reservoir structuur, de bewezen opslagcapaciteit en de aanwezige pijpleidingen aan het aardoppervlak. Potentiele opslag complexen kunnen bestaan uit quartz-rijke zandsteen formaties en klei-rijke afdekgesteentes ("caprocks"). Om veilige CO_2 opslag te kunnen garanderen is het van essentieel belang om de afdichtcapaciteit van aanwezige breuken intact te houden, aangezien deze kunnen gaan lekken door breuk reactivatie ten gevolgen van fysieke of chemische veranderingen die gepaard gaan met CO_2 injectie of blootstelling. Daarnaast kan reactivatie van deze breuken leiden tot seismiciteit. Om een beter idee te krijgen van de seismische risico's en de mogelijkheid tot lekkage ten gevolge van CO_2 opslag is het belangrijk om een kwantitatief begrip te krijgen van de koppeling tussen de chemisch-mechanisch effecten van CO_2 injectie en CO_2 blootstelling op de wrijvingssterkte en stabiliteit, alsmede de vloeistof doorstroom eigenschappen van breuken door quartz-rijke zandsteen formaties en/of klei-rijke afdekgesteentes.

In dit proefschrift rapporteer ik de resultaten van een experimenteel onderzoek dat zich richt op de gekoppelde chemisch-mechanische effecten van lange termijn CO_2-water-gesteente interactie op de wrijvings- ("frictie") en vloeistof doorstroom ("transport") eigenschappen van breuk materialen ("breukmeel") gemaakt van reservoir zandstenen en carbonaat-houdende, klei-rijke afdekgesteentes. Naast de toepassing voor CO_2-opslag zijn de resultaten ook relevant voor tectonisch actieve breuken in quartz-calciet en klei-rijke formaties in bijvoorbeeld subductie zones en gebergtes langs convergente plaatranden waar grote en destructieve, natuurlijke aardbevingen plaats vinden.

Hoofdstuk 1 beschrijft de motivatie en het toepassingsgebied van dit proefschrift, alsmede een kort overzicht van eerder, relevant onderzoek dat is gedaan in de context van CO_2 opslag in geologische opslag reservoirs. Hierbij wordt ook stilgestaan bij de tekortkomingen van de huidige kennis. Tenslotte worden in dit

hoofdstuk de hoofddoelen van het experimentele onderzoek dat in dit proefschrift wordt gepresenteerd gedefinieerd.

Hoofdstuk 2 beschrijft de chemische effecten van blootstelling aan CO_2 (op geologische tijdschaal, i.e. miljoenen jaren) op de frictie en vloeistof transport eigenschappen van gesimuleerde quartz-rijke breuk materialen. Hiervoor hebben we natuurlijk CO_2-blootgesteld materiaal vergeleken met niet aan CO_2-blootgesteld materiaal. Daarnaast zijn de hand-verpoederde ("gesimuleerde") quartz-rijke breuk materialen vergeleken met gesimuleerd carbonaat-rijk breuk materiaal dat verzameld is van een oude, CO_2-lekkende breuk. De experimenten, zowel droog (laboratorium-droog) als nat, omvatten testen in de zogenoemde directe-verschuivingsconstructie ("direct shear") en zijn uitgevoerd in een siliconen olie-gevuld triaxiaal deformatie apparaat op een temperatuur (T) van 23 en 100°C, een effectieve normaalspanning (σ_n^{eff}) van 5-50 MPa, en wrijvingssnelheden (V) van 0.22-100 µm/s, representatief voor reservoir condities. Tijdens de droge testen staan de breuk materialen in direct contact met de atmosfeer zoals aanwezig in het laboratorium, terwijl de natte experimenten zijn gedaan in de aanwezigheid van een gesatureerde materiaal-poeder oplossing met een poriëndruk (P_f) van 25 MPa. Naast het meten van de frictie eigenschappen van deze materialen, hebben we de vloeistof transport eigenschappen van deze drie materialen gemeten op een effective normaalspanning van 50 MPa ($P_f \approx 2$ MPa, $T \approx 23$°C). Zowel de laboratorium-droge als de natte, gesimuleerde niet CO_2-blootgestelde en CO_2-blootgestelde quartz-rijke breuk materialen laten vergelijkbaar frictie gedrag zien (wrijvingscoefficient ("frictie coefficient") μ = schuifspanning / normaal-spanning = 0.5-0.6) alsmede een consequente toename in wrijvingsweerstand met toenemende wrijvingssnelheid ("snelheidsversterkend" gedrag) op 23 en 100°C. Het gesimuleerde, CO_2-blootgestelde carbonaat-rijke breuk materiaal is slechts een klein beetje sterker dan beide quartz-rijke materialen, en laten een overgang van snelheidsversterkend gedrag op 23°C naar snelheids-verzwakkend gedrag op 100°C zien voor zowel de laboratorium-droge als de natte testen. Alle drie de gesimuleerde breuk materialen hebben argon gas transport ("doorstroming") waardes in de order van 10^{-16} tot 10^{-17} m^2 en laten een afname in waardes zien met toenemende wrijvingsverplaatsing. De resultaten suggereren dat blootstelling aan CO_2 op de lange termijn de frictie en vloeistof transport eigenschappen van quartz-rijke breuk materialen niet significant zullen veranderen. Daarentegen, een

toename van 40% in carbonaat concentratie, als gevolg van CO_2-lekkage langs een breuk, zou kunnen leiden tot een significante verandering van het wrijvingsgedrag van een breuk, waardoor een grotere kans op seismisch gedrag ontstaat.

In **Hoofdstuk 3** onderzoek ik eerst de effecten van wrijvingsverplaatsing, breukbeweging en onderbreking van breukbeweging, alsmede de normaalspanning op de potentiële anisotropie (= de eigenschap dat een parameter afhankelijk is van de orientatie waarin deze gemeten wordt) van vloeistof doorstroming langs en haaks op gesimuleerd klei-quartz-calciet breuk materiaal. Het gesimuleerde breuk materiaal is gemaakt door het verpoederen en zeven (<35 µm) van Opalinus Claystone (OPA). Daarna heb ik het effect van calciet concentratie op de wrijvingssterkte en stabiliteit van hetzelfde materiaal (OPA) getest door de natuurlijk aanwezige calciet op te lossen in de helft van de hoeveelheid verpoederd materiaal (calciet-vrije OPA) om vervolgens het geobserveerde frictie gedrag te vergelijken met het gedrag van calciet-houdend materiaal (OPA). Directe verschuivingstesten op kamer temperatuur in combinatie met vloeistof doorstroom metingen zijn gedaan in hetzelfde triaxiale deformatie apparaat als gebruikt in Hoofdstuk 2, voor effective normaalspanningen van 5 tot 50 MPa, een poriëndruk van ~2 MPa en wrijvingssnelheden variërend tussen 0.05 en 5.5 µm/s. De directeverschuivingstesten zonder vloeistof doorstroom metingen, gedaan om het effect van calciet concentratie te testen, zijn uitgevoerd zowel vacuüm-droog als nat (P_f = 25 MPa) op temperaturen tot ~150°C, een effective normaalspanning van 50 MPa, en wrijvingssnelheden van 0.22-11 µm/s. De doorstroom resultaten laten, ongeacht de vloeistof stroomrichting, een afname in waardes zien voor toenemende wrijvingsverplaatsingen, breukbeweging, onderbreking van breukbeweging, en toenemende effectieve normaalspanning. Vergelijking van de doorstroom waardes voor verplaatsing voor transport langs de breuk met die voor haaks op de breuk laten een anisotropie van maximaal 1 order van grootte zien. Met toenemende wrijvingsverplaatsing neemt de anisotropie in doorstroom waardes af tot <0.5. De resultaten voor zowel de calciethoudende als de calciet-vrije breuk materialen laten frictie coefficient waardes zien die niet afhankelijk zijn van temperatuur. Zo is het calciet-vrije breukmateriaal ($\mu \approx 0.27$) ongeveer 10-20% zwakker dan het calciet-houdende materiaal ($\mu \approx 0.31$). Het droge klei-quartz-calciet materiaal (calciethoudende) is zelfs bijna twee keer zo sterk ($\mu \approx 0.58$) als het natte klei-quartz-calciet materiaal ($\mu \approx 0.31$). Voor alle condities getest in deze

studie laten zowel de de calciethoudende als de calciet-vrije breuk materialen snelheidsversterkend gedrag zien. De resultaten in dit hoofdstuk suggereren dat een breuk gevuld met breukmeel, zelfs wanneer deze breukverplaatsing heeft geaccomodeerd, eerder als lekroute zal fungeren dan een intakt afdekgesteente. De resultaten laten verder zien dat lekkage langs de breuk makkelijker gaat dan haaks op de breuk. Daarnaast, aangenomen dat op diepte breuken nat zijn, is het niet aannemelijk dat wrijvingsreactivatie van calciethoudende en calciet-vrije breuk materialen zal leiden tot (micro)seismiciteit.

In **Hoofdstuk 4** onderzocht ik het effect van calciet concentratie op het frictie gedrag van klei-quartz-calciet breukmeel mengsels. Voor deze experimenten is een nieuwe hoeveelheid calciet-vrije Opalinus Claystone (CFOPA) poeder gemaakt, identiek met die gebruikt is in Hoofdstuk 3. Daarnaast heb ik gekeken naar wat het effect is van calciet op een pure klei (kaoliniet) en pure quartz door voor deze mineralen composities 100% pure eindmateriaal poeders en 50:50 mengsels te testen. Experimenten in een ringwrijvingsmachine ("ring-shear") zijn uitgevoerd op σ_n^{eff} = 50 MPa, P_f = 25 MPa, T = 23-100-150°C en wrijvingssnelheden variërend van 0.22 tot 100 µm/s. Op 23 en 100°C stijgen de wrijvingssterkte en wrijvingsstabiliteit van CFOPA-calciet en kaoliniet-calciet mengsels voor een toename in calciet terwijl ze snelheidsversterkend gedrag laten zien. Een overgang naar snelheidsverzwakkend gedrag is te zien tussen 100 en 150°C voor CFOPA-calciet composities met meer dan 90% calciet, en in de kaoliniet-calciet serie voor alleen de 100% calciet compositie. Het frictie gedrag van de quartz-calciet composities is anders en laat op 23°C een toename in frictie coefficient zien met toenemende calciet concentratie en geen trend op 100 en 150°C. Alle quartz-calciet composities laten op 23 en 100°C snelheidsversterkend gedrag zien, gevolgd door een verandering naar snelheidsverzwakkend gedrag op 150°C voor de 50:50 quartz-calciet en 100% calciet composities. Opmerkelijk is het onstabiele en snelheidsverzwakkend gedrag van de 50:50 quartz-calciet mengels aangezien dit negatiever is dan respectivelijk pure quartz en calciet. Microstructurele observaties voor de CFOPA-calciet mengels suggereert een geleidelijke verandering van controlerende deformatie proccesses op de micro-schaal met toenemende calciet concentratie. Deformatie lijkt te verschuiven van deformatie in voornamelijk de phyllosilicaat-rijke zones in de phyllosilicaat-rijke mengsels naar meer homogene cataclastische deformatie van de calciet korrels, resulterende in een sterke

korrelgrootte afname. Daarnaast suggereert de overgang van snelheidsversterkend gedrag naar snelheidsverzwakkend gedrag het toenemende belang van tijdsafhankelijke, temperatuur geïnitieerde processen op de calciet-calciet korrel contacten, zoals diffusie, die zorgen voor toenemende compactie. Microstructurele observaties voor de quartz-calciet mengels laten een grotere korrelgrootte afname zien in de calciet component wanneer deze is gemengd met quartz. Mogelijk versterkt die korrelgrootte afname het effect van temperatuur geïnitieerde deformatie processes, e.g. diffusie, wat zorgt voor toenemende compactie in de calciet-rijke delen en wat bijdraagt aan de afnemende slip stabiliteit. Onze resultaten impliceren dat significante veranderingen in de wrijvingssterkte of het (micro)seismische potentieel van breukmeel met een klei-quartz-calciet compositie alleen te verwachten is na carbonaat neerslag van >90%, wat mogelijk een gevolg zou kunnen zijn van snelle CO_2 lekkage langs een breuk. Quartz-calciet mengsels laten onstabiel gedrag zien wanneer er gelijke hoeveelheden quartz en calciet zijn.

Het beoordelen van de chemische effecten van lange termijn CO_2-water-gesteente interacties op het wrijvingsgedrag van klei-quartz-calciet breukmeel in laboratorium experimenten is lastig vanwege de langere tijdschalen waarop mineraal reacties plaats vinden (>jaren) dan de tijdschalen van laboratorium experimenten die variëren van dagen tot weken, tot maanden. Naar aanleiding daarvan heb ik in **Hoofdstuk 5** geochemisch modeleren gecombineerd met frictie experimenten, om het effect van lange termijn CO_2-water-gesteente interacties op de frictie eigenschappen van klei-rijk breukmeel te onderzoeken. Als eerste hebben we de effecten van lange termijn CO_2-water-gesteente interacties op de mineralogische compositie van twee verschillende klei-quartz-calciet start composities geochemisch gemodeleerd voor verschillende breukwater ververstijden (i.e. de hoeveelheid tijd die een hoeveelheid breukwater in contact is met breukmeel voordat deze vervangen (“ververst”) wordt met een nieuwe hoeveelheid breukwater; 10 en 1000 jaar) en de totale duur van de blootstelling van breukmeel met breukwater (10.000 en 1.000.000 jaar). Voor de frictie experimenten hebben we vervolgens de geochemisch gemodeleerde resultaten geselecteerd waarvan verwacht wordt het grootste effect te zullen zien op het wrijvingsgedrag. De composities zijn vervolgens gemengd van pure mineralen en getest, volgens dezelfde procedure en in hetzelfde apparaat als gebruikt in Hoofdstuk 4, om de frictie eigenschappen te bepalen. Onze

resultaten laten zien dat de combinatie van geochemisch modeleren en frictie testen gepaard kunnen gaan met enkele beperkingen, zoals het met de hand mengen van illiet en smectiet om diagenetisch afgezette illiet-smectiet na te bootsen. Maar voor nu is het de beste mogelijke manier om lange termijn CO_2-water-gesteente interacties en het effect daarvan op het frictie gedrag van breukmeel te kunnen simuleren. Onze resultaten laten verder zien dat de wrijvingssterkte toeneemt door de door blootstelling geïnitieerde mineralogische veranderingen. Daarnaast neemt de wrijvingssterkte toe met toenemende temperatuur terwijl het een overgang van snelheidsversterkend naar snelheidsverzwakkend gedrag laat zien tussen 100 en 150°C. Mengsels met extreem zwakke klei mineralen (i.e. smectieten) laten een lagere frictie zien alsmede snelheidsversterkend gedrag. Verder laten onze resultaten zien dat mineralogische veranderingen door CO_2 blootstelling afhankelijk zijn van de begin compositie, de breukwater ververstijden en de totale reactie tijd. De relatie tussen de frictie coefficient en de quartz:calciet ratio, alsmede de temperatuur-afhankelijkheid van het snelheidsafhankelijke gedrag van de mengsels, net als in Hoofdstuk 4, suggereert een interactie tussen quartz en calciet die leidt tot het preferentieel verpoederen van de calciet korrels tijdens wrijving, wat zorgt voor een toenemende tijdsafhankelijke compactie en wat mogelijk het snelheidsverzwakkende gedrag op 150°C kan verklaren.

Dit proefschrift wordt afgesloten in **Hoofdstuk 6** waarin de hoofdresultaten en conclusies van dit experimentele onderzoek worden samengevat alsmede de hoofdimplicaties voor lange termijn opslag van CO_2 in zandsteen reservoirs of onder klei-quartz-calciet houdende afdekgesteentes. Tenslotte worden openstaande problemen die niet worden besproken in dit proefschrift geïdentificeerd en worden suggesties gedaan voor verder onderzoek.

List of symbols used in this thesis

Symbol	Definition	Symbol	Definition
a	Magnitude of the instantaneous change in μ upon a change in sliding velocity from a reference value V_0 to a value $V = exp\ V_0$	$\overline{p}$	Mean pore pressure [MPa]
ac	Activity of species	P	Pressure [MPa]
A	Cross-sectional area [m^2]	P_f	Pore fluid pressure [MPa]
A_{rs}	Reactive surface area [cm^2/g]	q	Fitting parameter [-]
b	Klinkenberg slip factor [Pa]	Q	Reaction quotient [-]
b	Magnitude of the change in μ during evolution to a new steady-state value over a characteristic slip distance D_c	μ	Dynamic friction coefficient [-]
BS	Boundary shear	μ_i	Internal friction coefficient [-]
c	Mineral concentration [%]	μ_0	Steady-state friction coefficient at the reference velocity V_0 [-]
C_0	Cohesion [MPa]	μ_{final}	Friction coefficient at the end of an experiments or stage [-]
D_c	Characteristic slip distance for reaching a new steady-state friction [µm]	μ_m	Friction coefficient of a mixture
D_f	Final displacement [mm]	μ_{ss}	Steady-state friction coefficient [-]
δ	dynamic viscosity of argon gas at room temperature [Pa s]	σ	Normal stress [MPa]
E	Equilibrium constant	σ_n^{eff}	Effective normal stress [MPa]; $\sigma_n^{eff} = \sigma - P_f$
η	argon compressibility [Pa^{-1}]	r	Kinetic rate
θ	gouge state variable [-]	R_i	Volume reservoir [ml]
k	Kinetic rate constant [$mol/m^2/s$]	S	Shear stiffness of the fault zone

K_a	Apparent permeability [m^2]	τ	Shear stress [MPa]
K	Intrinsic permeability [m^2]	t	Time [s]
κ	Permeability [m^2]	t_r	Residence time of fluid in a fault zone [s]
κ_g	Gas permeability [m^2]	T	Temperature [°C]
K_{ic}	Critical stress intensity factor [$MN \cdot m^{-3/2}$]	V	Sliding velocity of fault; $V = exp\ V_0$ [μm/s]
κ_l	Liquid permeability [m^2]	V_0	Reference sliding velocity [μm/s]
$\kappa_\perp$	Across-fault permeability [m^2]	V_{lp}	Load point velocity [μm/s]
$\kappa_{//}$	Along-fault permeability [m^2]	x	Shear displacement [mm]
l	Length [mm]		

Chapter 1

General introduction and aims

1.1 Background and scope of the study

It has been recognized that global atmospheric CO_2 emissions need to be maintained at levels at or below 450 ppm (IPCC, 2007), in order to keep global temperature changes due to climate change below two degrees, i.e. ETP 2DS scenario (Elzinga et al., 2014). This means that CO_2 emissions needs to be cut by 60% by 2050, compared to 2012 levels, in order to meet this target (Elzinga et al., 2014). At global CO_2-emissions rates of about 36 Gt/year (IPCC, 2014), mitigation strategies include energy conservation and efficiency, and a transition to low carbon energy resources, such as geothermal energy, solar energy and wind power. However, fossil fuels are expected to continue to play an important role in the energy mix, in order to keep up with the increasing global energy demand. One important strategy for mitigation of CO_2 emissions generated from fossil fuel burning is the implementation of Carbon Capture and Storage (CCS) technology. CCS entails the capture of CO_2 at large point sources, such as power plants and steel or cement factories, and subsequent transport to and injection into geological formations at several kilometres depth (Benson and Cook, 2011; Haszeldine, 2009; Shukla et al., 2010). In addition to deep saline aquifers and unminable coal seems, depleted hydrocarbon reservoirs offer potential storage sites for geological storage of CO_2 (e.g. Alvarado and Manrique, 2010; Holloway, 2001). Such reservoirs are attractive, since the reservoir structure is generally well-known and has held fluids in place for time-scales of over 10^4 years (Haszeldine, 2005). Furthermore, the low pore pressure at the end of depletion offers a larger storage capacity, compared to (hydrostatically) pressurised aquifers. CO_2 injection into hydrocarbon field is not a new concept as it has been implemented for decades in Enhanced Gas Recovery (EGR; e.g. van der Meer et al., 2006), and Enhanced Oil Recovery (EOR; e.g. Gozalpour, et al., 2005). Both can be considered applications for Carbon Capture, Utilisation and Storage (CCUS), thereby making CO_2 storage more economically attractive (Guéllar-Franca and Azapagic, 2015). Though CO_2 storage, either via CCS or CCUS, is recognised to be an important technology needed to mitigate global CO_2 emissions – without CCS the cost of mitigation would more than double (IPCC, 2014) – it still meets with resistance from the public due to the perceived potential for leakage to the surface. To ensure safe, long-term storage of CO_2, maintaining caprock integrity, i.e. preventing the creation of new leakage pathways, is important and has been the focus of much research within the CCS community (e.g.

Andreani et al., 2008; Cappa and Rutqvist, 2011; Hangx et al., 2010a; Shukla et al., 2011). Creation of new leakage pathways can be mitigated by safe injection strategies, for example by keeping injection pressure below the fracture pressure when injecting into depleted reservoirs (Marston, 2013). However, injection may lead to reactivation and potentially induced (micro)seismicity (Zoback and Gorelick, 2012) of pre-existing faults, which in turn may lead to escape of CO_2 from the storage reservoir due to fault permeability changes upon slip.

1.2 Maintaining fault stability and fault sealing integrity

Many reservoir systems, including those that are used in CCS, generally contain pre-existing, penetrating and/or bounding faults, which are potential nucleation sites for aseismic creep events or seismic (low-magnitude) earthquakes in response to changes in reservoir pore pressure (Zoback and Gorelick, 2012). In depleted hydrocarbon reservoirs, these faults may become critically stressed as a result of a drop of the reservoir pressure below hydrostatic values upon hydrocarbon extraction (Suckale, 2010). While on the one hand CO_2 injection may stabilise such faults by restoring the reservoir pressure, injection of large volumes of fluid can also lead to induced (micro)seismicity (McGarr, 2014; Verdon, 2014). Since pre-existing faults also offer potential leakage pathways for CO_2 to leave the storage reservoir, the impact of pore pressure changes on fault stability as well as the direct impact of CO_2 on the frictional properties of the fault, need to be understood. Fault re-activation may lead to enhanced transport properties of the fault, hence it is key to understand the coupling between fault stability and fault permeability to ensure safe and efficient geological CO_2 storage in depleted hydrocarbon reservoirs (Hawkes et al., 2005).

Recent work has focused on understanding the reactivation potential and changes in frictional slip behaviour of typical fault materials in the presence of CO_2, whether through short-term lubrication effects or long-term CO_2-fluid-rock interactions (Hangx et al., 2015; Pluymakers et al., 2014b; Rohmer et al., 2016; Samuelson and Spiers, 2012). Though it is important to evaluate the direct effect of CO_2 on fault mechanical properties (e.g. Lamy-chappuis et al., 2016; Pluymakers et al., 2014; Samuelson and Spiers, 2012), the impact chemically-induced reactions and/or mechanically-induced fault reactivation has on fault transport properties and permeability evolution has to date received little attention (Armitage et al., 2011;

Cappa and Rutqvist, 2011; Lamy-chappuis et al., 2016; Lamy-Chappuis et al., 2014; Rutqvist et al., 2013).

In Europe, many current and potential CCS storage sites consist of sandstone reservoirs overlain by shaly caprocks (Chadwick et al., 2004; Hangx et al., 2013; Orlic, 2013; Samuelson and Spiers, 2012). Therefore, it is important to investigate the coupled chemical and mechanical effects of long-term CO_2-fluid-rock interactions on the frictional and transport properties of fault materials composed of reservoir sandstones and carbonate-bearing clay-rich caprocks. The work on simulated sandstone fault materials presented in this thesis was carried out within the Dutch national research program CATO-2 on CO_2 capture, transport and storage, within WorkPackage 3.3 on caprock and fault integrity, in close collaboration with Shell Global Solutions. The work done on carbonate-bearing clay-rich fault materials was performed within the European Union's Seventh Framework Programme (FP7 – WorkPackage 4.3) as part of the project on Understanding the Long-Term fate of geologically stored CO_2 (ULTimateCO_2).

In this thesis, I report the results of an experimental study of the coupled chemical-mechanical effects of long-term CO_2-fluid-rock interactions on the frictional and transport properties fault materials composed of reservoir sandstones and carbonate-bearing clay-rich caprocks. Shear experiments were conducted at pressure and temperature conditions relevant for potential CO_2 storage reservoirs located at ~2 to 4 km depth. Additional frictional sliding tests, at room temperature, were coupled with permeametry measurements, to assess the sealing integrity and anisotropy of a faulted caprock during fault (re-)activation and inter-seismic quietness. A fundamental understanding of the microscale mechanisms operating during frictional deformation was obtained via structural observations down to the nano-scale, made using state-of-the-art microscopy.

1.3 Fault zones; frictional and transport properties: knowledge gaps

Fault zones form weak surfaces within the upper crust along which slip and fluid leakage occur (Cappa and Rutqvist, 2011; Hooper, 1991; Sibson, 1992, 1990; Wiprut and Zoback, 2000; Zoback and Gorelick, 2012). They are typically characterised by a fault core and surrounding damage zone, bounded by wall rock (Caine et al., 1996).

Though the damage zone may be a zone of enhanced permeability, depending on its fracture density and connectivity (Chen et al., 2013; Mitchell and Faulkner, 2012), slip is mainly accommodated along the fault core, consisting of fractured rock wear products, so-called "fault-gouges" (Twiss and Moore, 2000). The resistance of fault gouge to sliding, i.e. the shear strength, is expressed in terms of the friction coefficient (μ): $\mu = \tau/\sigma_n$ where τ is the shear stress and σ_n is the applied normal stress. This expression follows from the empirical relation known as "Byerlee's Law": $\tau = C + \mu\sigma_n$ (Byerlee, 1978), assuming that cohesion C is zero in the case of fractured rock. Any fluids present with pore pressure P_f reduce the normal stress to the effective normal stress σ_n^{eff}, given as: $\sigma_n^{eff} = \sigma_n - P_f$, changing the definition of the friction coefficient to $\mu = \tau/\sigma_n^{eff}$. Determination of the (sliding) friction coefficient has been the topic of many experimental studies and has been shown to depend on the mineralogy, temperature, normal stress, sliding velocity and pore fluid pressure, as well as pore fluid composition (see Carpenter et al., 2016; Crawford et al., 2008; Den Hartog and Spiers, 2013; Giorgetti et al., 2015; Mair and Marone, 1999; Moore and Lockner, 2004; Morrow et al., 2000; Pluymakers et al., 2014; Shimamoto and Logan, 1981; Tembe et al., 2010; Verberne et al., 2014, and references therein).

Whether fault movement is stable or unstable, i.e. seismic or aseismic, is controlled by the velocity-dependent frictional behaviour of the fault gouge. The velocity-dependence of a fault rock is analysed in the frame-work of rate-and-state (RSF) friction (e.g Marone, 1998), and describes the evolution of the dynamic friction coefficient μ following a change in sliding velocity V with respect to a reference state V_0 (Dieterich, 1979, 1978; Ruina, 1983):

$$\mu = \mu_0 + a \ln\left(\frac{V}{V_0}\right) + b \ln\left(\frac{V_0\theta}{D_c}\right) \qquad (1.1)$$

where, θ is a gouge state variable, a reflects the magnitude of the instantaneous change in μ upon a change in sliding velocity from a reference value V_0 to a value V = *exp* V_0, b represents the magnitude of the change in μ during subsequent evolution to a new steady-state value over a characteristic slip distance D_c, and μ_0 is the steady-state friction coefficient determined at the reference velocity V_0 (Figure 1.1). One way to describe θ is via the "slowness" formulation inferred from earlier work of Dietrich (Dieterich, 1979, 1978; Ruina, 1983):

$$\frac{d\theta}{dt} = 1 - \frac{V\theta}{D_c} \quad (1.2)$$

A stepwise change in sliding velocity thus yields a change in steady-state friction coefficient μ_{ss}, quantified by the rate parameter (a-b):

$$(a\text{-}b) = \Delta\mu_{ss}/\Delta \ln V \quad (1.3)$$

Generally speaking, positive (a-b) values describe velocity-strengthening behaviour, whereas negative (a-b) values reflect a decrease in frictional strength with increasing sliding velocity, resulting in accelerated slip, which is a prerequisite for seismicity nucleation on a moving fault plane (e.g. Scholz, 1998). As such the friction coefficient (resistance to shear) and the velocity-dependence of shear (a-b), particularly in relation to gouge composition, are key parameters in assessing fault stability.

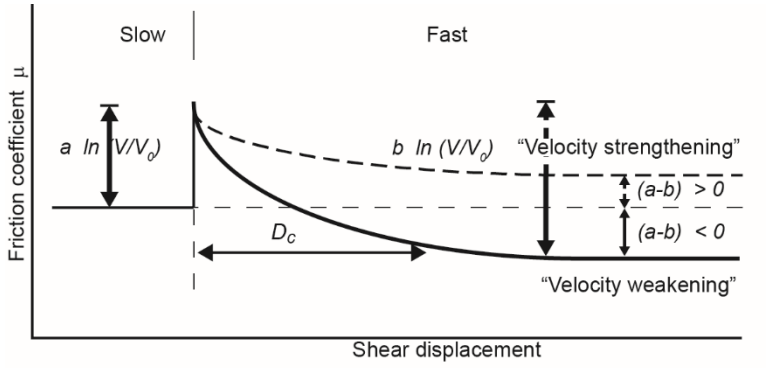

Figure 1.1. Schematic illustration of the velocity-dependence of steady-state fault friction in response to an instantaneously imposed velocity increase from V_0 to V. Upon the velocity increase friction increases by an amount "$a\ ln\ (V/V_0)$", which is known as the direct velocity effect, followed by an evolutionary decrease of magnitude "$b\ ln\ (V/V_0)$" to a new steady-state.

Intimately coupled to fault slip and stability are changes in the transport properties of the fault (porosity and permeability). While fault gouges may exhibit low permeability under static conditions (i.e. unmoving), especially for high normal stresses acting on the fault plane (e.g. Faulkner and Rutter, 1998), slip may lead to dilation (permeability enhancement) or compaction (permeability reduction), depending on the microphysical processes controlling deformation (e.g. Den Hartog and Spiers, 2014; Uehara and Shimamoto, 2004; Zhang and Tullis, 1998). Existing

faults present in CO_2 storage sites will be verified to be sealing prior to injection. Nonetheless, if slip will be induced, this may lead to enhanced permeability, and potential leakage of CO_2. However, few studies have attempted to quantify the direct impact of slip-induced dilation and compaction on permeability (Samuelson et al., 2009; Uehara and Shimamoto, 2004; Zhang and Cox, 2000; Zhang et al., 2007). Furthermore, studies reporting on fault gouge permeability measurements have focused predominantly on measuring (static) across fault permeability (e.g. Faulkner and Rutter, 2000, 1998; Ikari et al., 2009), while leakage may not only occur from the storage reservoir to adjacent reservoirs, but also along fault to underlying or overlying formations. It should be noted that for depleted hydrocarbon reservoirs, if safe injection practices are adhered to, fluid pressure gradients will be unfavourable for promoting along fault flow and more research for dynamic along-fault permeability is therefore needed (Zhang et al., 2001, 1999; Zhang and Tullis, 1998).

1.3.1 Mechanical-hydrological impact of CO_2 injection: coupling fault slip and fault permeability

In addition to a direct mechanical effect of pore fluid pressure, injection of CO_2 into depleted reservoirs will lead to an increase in pore pressure, causing a direct poro-elastic response of the storage complex (Wang, 2000). Furthermore, thermal effects resulting from injection of high-pressure CO_2 into a low-pressure, depleted reservoir may lead to local stress changes in the reservoir and caprock near the injection well (Preisig and Prévost, 2011; Vilarrasa et al., 2014). Such local stress changes could potentially lead to fault reactivation, which in turn could lead to fault dilatation (Brace, 1978; Hooper, 1991) and subsequently changes in fault core permeability. Once slip has ceased, the dilated fault rock relaxes and permeability may decrease due to fault gouge compaction (Hooper, 1991; Sibson, 1992, 1990; Wiprut and Zoback, 2000). As a result, the integrity of a previously sealing caprock-cutting fault may be altered during or following CO_2 injection and the storage system may become prone to CO_2 leakage.

Experimental studies, performing static permeametry measurements on fault gouges taken at various orientations from natural shear zones or dynamic permeametry measurements on actively shearing simulated fault gouges, have

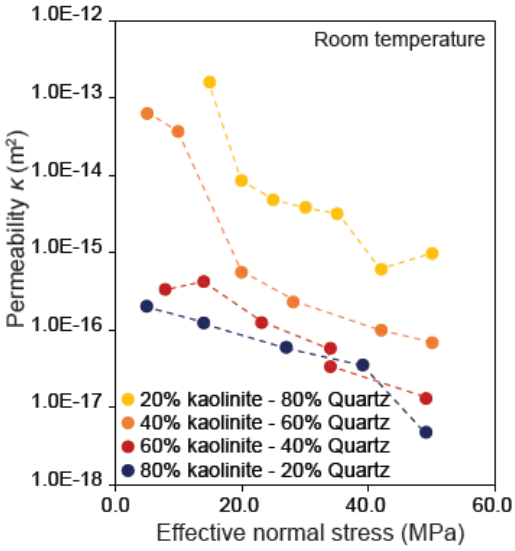

Figure 1.2. Argon gas permeability, *κ*, as a function of effective normal stress for an increasing clay content in kaolinite-quartz mixtures (Crawford et al., 2008).

shown that fault gouges typically have a strong permeability anisotropy (Dewhurst et al., 1996; Farrell et al., 2014; Faulkner and Rutter, 2000, 1998, Zhang et al., 2001, 1999; Zhang and Tullis, 1998). These studies show that the permeability along-fault may be up to several orders of magnitude higher than across-fault (Hooper, 1991; Sibson, 1992), both when the fault is static and during slip. This anisotropy is attributed to the development of a fault gouge foliation, which is easier achieved in materials rich in platy minerals, such as phyllosilicates, hence permeability anisotropy being higher in clay- or mica-rich fault gouges (Faulkner and Rutter, 1998; Zhang and Cox, 2000; Zhang and Tullis, 1998). Note, however, that permeability anisotropies obtained for natural gouges might differ from those obtained for simulated fault gouges due to the difference in scale and off-set, impacting the control slip may have on the foliation, hence anisotropy. Generally, studies reporting on static permeability measurements investigated the effect of normal stress on the permeability (e.g.Faulkner and Rutter, 1998), whereas dynamic measurements are often performed at single normal stress, at very high normal stress combined very long shear displacements, or for a normal stress decrease (e.g. Zhang et al., 2001, 1999; Zhang and Cox, 2000). However, in context of CO_2 storage, it is important to assess the impact of fault slip on the leakage potential of a fault, as well as understanding the control of changing normal stress

on the static and dynamic permeability. It should be noted that in addition to normal stress, fault mineralogy strongly influences permeability (Figure 1.2). For example, an increase in phyllosilicate concentration tends to decrease the permeability of a fault, as such enhancing the sealing integrity of a fault (Crawford et al., 2008; Takahashi, 2003). As such, CO_2-induced mineralogical changes may potentially lead to changes in the transport properties of the fault gouge. Therefore, the effect of CO_2 injection is a complex interplay of processes (Johnson et al., 2004), and chemical-mechanical-hydrological coupling is key in understanding long-term CO_2 storage integrity.

1.3.2 Chemical-mechanical impact of CO_2 injection: coupling reaction and fault friction

Previous research has shown that the frictional strength and stability of (simulated) fault gouge depends on the mineralogy (e.g. Giorgetti et al., 2015; Moore and Lockner, 2011; Tembe et al., 2010) (Figure 1.3). Therefore, if fluid penetration of the fault occurs, any alteration of the mineral composition of the gouge due to CO_2-fluid-rock interactions may change its frictional strength and stability behaviour (e.g. Hangx et al., 2015; Pluymakers et al., 2014b; Samuelson and Spiers, 2012). In turn, the chemical alteration may also result in a change in fault permeability, hence affecting the sealing capacity of the fault, especially if reactions result in large porosity increase or precipitation of phyllosilicates (e.g. Crawford et al., 2008; Gunter et al., 1993; Takahashi, 2003). After injection, CO_2 dissolves into the formation brine, forming carbonic acid (Bachu, 1994). Interaction between the rock and carbonic acid may induce mineral alterations (Busch et al., 2014; Hangx et al., 2015; Kampman et al., 2016; Kaszuba et al., 2005), though the extent of such reactions is strongly dependent on the fluid-rock ratio (see Hangx et al., 2015, 2013; Rohmer et al., 2016). Furthermore, it is known that most CO_2-fluid-rock interactions are very slow and strongly depend on the availability of reactive minerals (Bachu et al., 1994; Baines and Worden, 2004). In recent years a significant amount of geochemical modelling and experimental studies have investigated CO_2-fluid-rock interactions, predicting and showing CO_2 induced chemical alterations in both pore water and mineralogy (e.g. Alemu et al., 2011; André et al., 2007; Gaus et al., 2005; Kaszuba et al., 2013; Marcon and Kaszuba, 2015). Typical reactions in relatively clean, quartz-rich sandstone reservoir rocks include the dissolution of cementing phases such as anhydrite and carbonates, and

depending on the minerals phases present feldspar and mica, and the precipitation of clays (i.e. illite, kaolinite) (Hangx et al., 2015; Huq et al., 2015; Pearce et al., 2004; Watson et al., 2004). For clay-rich caprocks, containing clays, quartz, plagioclase and carbonates, typical reactions lead to the dissolution and re-precipitation of carbonates, the dissolution of plagioclase, illite and chlorite, and the precipitation of smectite (Alemu et al., 2011; Kampman et al., 2016).

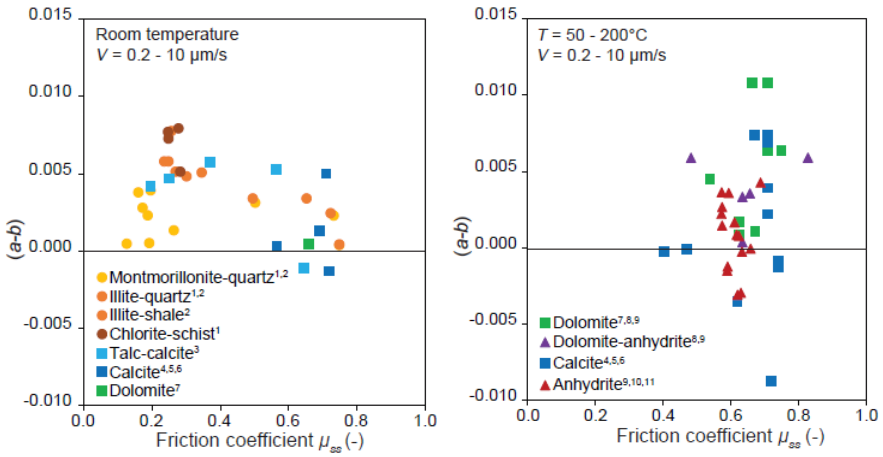

Figure 1.3. Velocity-dependence of steady-state friction, (*a-b*), as a function of steady-state friction coefficient μ_{ss} for wet gouges at room temperature (a) and elevated temperatures (b). Data plotted in the figures are derived from: [1] Ikari et al. (2011), [2] Tembe et al. (2010), [3] Giorgetti et al. (2015), [4] Verberne et al. (2010), [5] Verberne et al. (2013), [6] Verberne et al. (2015), [7] Samuelson et al., pers. com., [8] Pluymakers et al. (2016), [9] Scuderi et al. (2013), [10] Pluymakers et al. (2014), [11] Pluymakers et al. (2105).

However, due to the long time-scales and the complexity of brine-rock systems, it has been difficult to reproduce these CO_2-fluid-rock interactions in the laboratory, for experiments aimed at coupling geochemical changes to geomechanical and transport properties. Therefore, experimental research considering the coupled chemical-mechanical effects (Hangx et al., 2010a; Le Guen et al., 2007; Liteanu et al., 2013; Pluymakers et al., 2014b; Samuelson and Spiers, 2012; Vialle and Vanorio, 2011) and/or hydrological effects (Edlmann et al., 2013; Hangx et al., 2010b; Lamy-Chappuis et al., 2014; Luquot and Gouze, 2009; Vialle et al., 2014) of CO_2 exposure so far have focused on short-term effects of relatively rapid, short-term CO_2-brine-rock interactions on intact and faulted reservoir rocks and caprocks.

Despite all of these experimental studies, data on the long-term effects of CO_2-fluid-rock interactions on the mechanical strength and stability of (simulated) quartz-rich and carbonate-quartz-clay fault gouges is still needed. Potential approaches to determine the long-term effects of CO_2-fluid-rock interactions on the mechanical strength and stability of fault gouges include the use of natural analogues, comparing the behaviour of naturally CO_2-exposed samples to their unexposed equivalents, as well as use geochemical modelling predictions of CO_2-altered mineralogies as a basis for the preparation of simulated gouges.

1.4 Aims of this thesis

From the foregoing, it is evident that CO_2-fluid-rock interactions accompanying long-term CO_2 storage may have a coupled chemical-mechanical-hydrological effect, but that still little is known about the effects of long-term CO_2-fluid-rock interaction on the frictional and transport properties of fault gouges composed of reservoir sandstones and carbonate-bearing clay-rich caprock material. Clearly, experimental data on the effects of long-term CO_2 exposure on the frictional and transport properties of simulated fault gouges composed of aforementioned compositions is needed to assess the viability of long-term storage of CO_2 in depleted hydrocarbon, preferably gas, reservoirs. The current research addresses these points by providing new frictional, hydrological and microstructural data on simulated fault gouges composed of reservoir sandstone and carbonate-bearing clay-rich caprock material to predict and discuss fault frictional behaviour. Shearing experiments, partly in combination with permeability measurements, were conducted at (near) in-situ conditions, relevant for long-term CO_2 storage and analysed using state-of-the-art in electron microscopy. Accordingly, the aims for this thesis are defined as follows:

1) To determine the chemical effect of long-term CO_2 exposure on the frictional and transport properties of (simulated) reservoir sandstone fault gouges sheared at sliding velocities and at pressure-temperature conditions relevant for long-term CO_2 storage in reservoirs located at a depth of ~2 – 4 km depth. The primary focus here is to compare the frictional strength and stability, as well as the permeability of an unexposed (simulated) sandstone fault gouge with a gouge prepared from a long-term CO_2-exposed (simulated) sandstone. Additionally, these

gouges are compared to a (simulated) CO_2-exposed carbonate-rich fault gouge.

2) To determine the effect of fault reactivation, due to CO_2 injection, on the frictional and transport properties of a (simulated) clay-quartz-calcite fault gouge during shear deformation in both the along- and across-fault orientation. This aim targets the permeability anisotropy known to develop in phyllosilicate-rich fault gouges. And additionally, to investigate the effect of removing calcite, simulating long-term CO_2-exposure, on the shear resistance and slip stability of the (simulated) clay-quartz-calcite fault gouge. The combined aim is to determine the fault reactivation and leakage potential of a clay-quartz-calcite fault gouge.
3) To investigate the effect of systematically adding calcite to a (simulated) clay-quartz fault gouge, simulating calcite-precipitation due to long-term CO_2-exposure, on the frictional properties, i.e. strength and stability, of the gouges and to determine the deformation mechanisms involved, characterising how these control the shear resistance and slip stability of the gouge material. This aim particularly targets at investigating the physical conditions at which a fault gouge composition that is expected to be prone to earthquake nucleation will fail seismically.
4) To determine the shear resistance and slip stability of artificially-composed clay-quartz-calcite fault gouge compositions predicted by geochemically modelled long-term CO_2 exposure of a clay-quartz-calcite fault gouge.

The first aim is tackled in Chapter 2, whereas the second through fourth aims are tackled in Chapters 3 to 5. The work presented here will improve the general understanding of the chemical effects of long-term anthropogenic CO_2 storage on the strength and stability, as well as the reactivation and leakage potential of faults in sandstone reservoir and clay-quartz-calcite caprock complexes. It will also improve the general understanding of fault behaviour in mixed compositions, in which natural earthquake may nucleate. General conclusions, implications and suggestions for future research will be summarized in Chapter 6.

Chapter 2

Frictional behaviour and transport properties of simulated fault gouges derived from a natural CO_2 reservoir

Elisenda Bakker, Suzanne J.T. Hangx, André R. Niemeijer and Christopher J. Spiers

This chapter is based on:

Bakker, E., Hangx, S.J.T., Niemeijer, A.R., Spiers, C.J., 2016. Frictional behaviour and transport properties of simulated fault gouges derived from a natural CO_2 reservoir. Int. J. Greenh. Gas Control.

Abstract

We investigated the effects of long-term CO_2-brine-rock interactions on the frictional and transport properties of reservoir-derived fault gouges, prepared from both unexposed and CO_2-exposed sandstone, and from aragonite-cemented fault rock of an active CO_2-leaking conduit, obtained from a natural CO_2 field (Green River, Utah). Direct shear experiments (5-90 MPa effective normal stress; lab-dry or wet; 20-100°C) showed that the sandstone-derived gouges are characterised by virtually normal stress- and temperature-independent friction coefficients ($\mu \approx 0.5$-0.6). The data exhibited stable, velocity-strengthening behaviour moving towards near-neutral velocity-dependent behaviour with increasing effective normal stress. The carbonate-rich fault rock gouges exhibited higher friction coefficients ($\mu \approx 0.6$-0.7), with a transition from velocity-strengthening behaviour at room temperature (lab-dry) to velocity-weakening behaviour at 100˚C (lab-dry and wet), i.e. a transition from stable sliding to potentially unstable or seismogenic slip. Across-fault permeability decreased up to 1.5 orders with increasing displacement, showing slightly lower values for the carbonate-rich gouges. We infer that the mechanical behaviour of fault gouges derived from the sandstones studied will not be strongly influenced by long-term CO_2-exposure, due to the low content of reactive minerals in the protolith. Significant changes in frictional strength or (micro)seismic potential of faults present in a CO_2 storage system are only expected when there is major carbonate precipitation in the fault damage zone due to rapid CO_2 leakage and degassing.

2.1 Introduction

Carbon Capture and Storage (CCS) remains one of the few options for reducing CO_2 emissions while fossil fuels dominate the global energy mix. CCS entails carbon capture at point sources, followed by transport to and injection into geological formations (Benson et al., 2005; Haszeldine, 2009), such as saline aquifers (Bachu et al., 1994; Gunter et al., 1997; Hitchon, 1996) or depleted natural oil and gas reservoirs (Holloway, 2001). The latter are particularly attractive, as the reservoir structure is generally well-know and has proven capability of structurally trapping hydrocarbons for time-scales greater than ~100 years (Haszeldine et al., 2005). Oil and gas fields also possess the infrastructure needed to transport and inject large volumes of fluids. Moreover, CO_2 injection has been used for decades for enhanced oil and gas recovery (EOR: Gozalpour et al., 2005; EGR: Van der Meer et al., 2006), and is therefore not a radically new concept (Baines and Worden, 2004). Last but not least, long-term structural trapping of CO_2 in reservoir formations is not only an engineering concept, but also a natural phenomenon observed in numerous CO_2-charged reservoirs globally (Kampman et al., 2016; Pauwels et al., 2007; Pearce et al., 2004).

To ensure safe, long-term subsurface storage of anthropogenic CO_2, it is important to maintain sealing integrity of the reservoir-caprock system, and of faults therein, during and after CO_2 injection (e.g. Hawkes et al., 2005; Kampman et al., 2016). In addition to a direct poro-elastic response of the reservoir to the increase in pore pressure (Wang, 2000), it is well established that, unlike methane, reaction with injected CO_2 can result in a range of chemically-coupled mechanical (Hangx et al., 2013; Hangx et al., 2010a; Le Guen et al., 2007; Liteanu and Spiers, 2009; Liteanu et al., 2013; Major et al., 2014; Mikhaltsevitch et al., 2014) and/or hydrological effects (Huq et al., 2015; Lamy-Chappuis et al., 2014; Luquot and Gouze, 2009; Smith et al., 2013; Vialle et al., 2014; Vialle and Vanorio, 2011). In general, CO_2 will dissolve in the formation brine, forming carbonic acid thus releasing H^+ and inducing chemical interaction with the host rock (Bachu et al., 1994). However, CO_2-brine-rock interactions are very slow and strongly depend on the availability of reactive minerals (Bachu et al., 1994; Baines and Worden, 2004). The long time-scales and the complexity of brine-rock systems make it difficult to reproduce these processes in geomechanical experiments. For this reason, most experimental studies of chemical-mechanical interactions have focused on the effects of relatively rapid,

short-term CO_2-brine-rock interactions on the mechanical behaviour of intact reservoir rocks and caprocks (Hangx et al., 2013; Le Guen et al., 2007; Liteanu et al., 2013; Major et al., 2014; Mikhaltsevitch et al., 2014; Vialle and Vanorio, 2011), and of faults and fractures (Edlmann et al., 2013; Pluymakers et al., 2014; Samuelson and Spiers, 2012).

In order to investigate the effects of long-term CO_2-brine-rock interactions on reservoir and caprock properties, an alternative approach is to study samples recovered from natural CO_2 fields. Well-known examples of clastic CO_2 fields include the Werkendam field, near Rotterdam, the Netherlands (Hangx et al., 2015), the Brae and Miller fields, in the UK section of the North Sea (Haszeldine et al., 2005), the fields close to Green River in the Colorado Plateau, USA (Kampman et al., 2016; Pearce et al., 2004), and the Otway Basin fields of Australia (Watson et al., 2003). These fields are charged naturally with high concentrations of CO_2 and have experienced CO_2-brine-rock interactions over geological time-scales. Comparison of rocks exposed to CO_2 from such fields with laterally equivalent but unexposed material offers an opportunity to better understand the long-term effects of CO_2 on rock composition and properties, thus aiding the assessment of risks related to CO_2 storage. Such studies have focused on the mineralogical, geochemical and diagenetic effects of long-term CO_2-exposure (Kampman et al., 2016; Watson et al., 2003), with only a few studies investigating the coupled effect of CO_2-brine-rock interactions on the mechanical and/or transport properties of reservoir rocks and caprocks (Busch et al., 2014; Hangx et al., 2015). Even fewer studies have been published on the effects of long-term CO_2-brine-rock interaction on the properties of fault rocks (Hangx et al., 2015; Trippetta et al., 2013). Within a CO_2 storage system, faults that either cross-cut or bound the reservoir offer a variety of potential leakage risks (White and Foxall, 2016). For example, in response to stress changes resulting from CO_2 injection, faults may be reactivated, with internal damage enhancing leakage path potential. Moreover, long-term CO_2-induced changes in mineralogical composition and porosity may influence fault integrity directly or may promote fault slip by changing fault frictional behaviour, slip stability and hence transport properties (Hangx et al., 2015; Samuelson and Spiers, 2012; Trippetta et al., 2013). It is well established that mineral composition strongly influences fault frictional properties (e.g. Moore and Lockner, 2004; Tembe et al., 2010). However, effects of long-term CO_2-brine-rock interactions on

the mineralogical, frictional and transport properties of fault rock have not been specifically studied to date.

In an attempt to help fill this knowledge gap, we performed direct shear experiments aimed at assessing the long-term effect of CO_2-brine-rock interactions and resulting mineralogical changes on the frictional strength, slip stability (seismogenic potential), and permeability of simulated fault gouges prepared from samples of the Entrada Sandstone formation, taken from a natural CO_2 reservoir located in the Paradox Basin in the Green River region of the Colorado Plateau, SE Utah, USA (in this study referred to as the Green River reservoir). These simulated gouges consisted of finely powdered host rock material, as opposed to natural fault gouge. The gouges were prepared from intact unexposed (unreacted) and CO_2-exposed (reacted) quartz-rich, Entrada Sandstone reservoir rock, as well as from carbonate-cemented fault rock taken from the Salt Wash Fault (SWF) at a point where this fault, which is an active conduit for leaking CO_2, cuts the Entrada Sandstone. It should be noted that comparative studies have shown that the microstructures and frictional behaviour of natural gouges can be simulated realistically using this method (for example see Rutter et al. (1986), Haines et al. (2009) and Delle Piane et al. (in press)). The experiments were performed under in-situ reservoir conditions relevant for CCS projects, i.e. at temperatures of 20 and 100°C, effective normal stresses (σ_n^{eff}) in the range 5-90 MPa, both lab-dry and in the presence of an aqueous pore fluid (pore pressure P_f = 25 MPa). Direct shearing velocities of 0.22-10.86 µm/s were used. We discuss how differences in mineralogical composition due to CO_2-exposure, superimposed on primary lithological variation, affect fault rock properties and the implications that this has for long-term CO_2 storage.

2.2 Geological setting and starting material

2.2.1 Geological setting of the Entrada Sandstone

The Entrada Sandstone starting material was collected near Tenmile Butte, from surface exposures located close to and within, the Salt Wash Fault zone, in the northern part of the Paradox Basin, SE Utah, USA (see Figure 2.1). The material was provided courtesy of Dr. Niko Kampman (Shell Global Solutions).

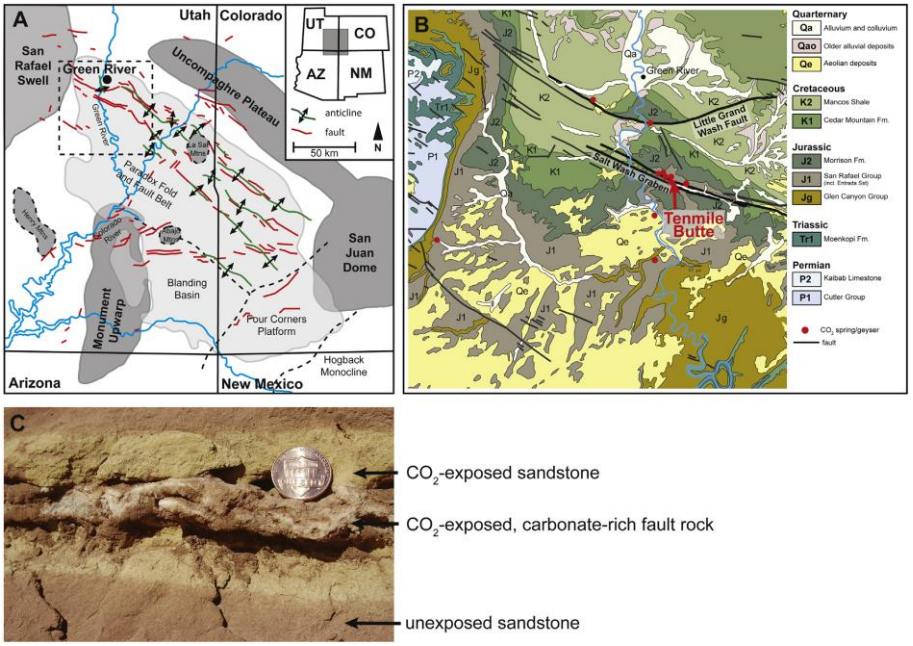

Figure 2.1. Sampling location in the Green River Field, Paradox basin, Utah, USA. a) Map illustrating the main anticlinal structures, faults and structural provinces of the Paradox Basin and adjacent areas. Dashed lines indicate transitional or indefinite boundaries between elements (after Condon, 1997). b) Geological map of area near the Salt Wash Graben and Little Grand Wash Fault (location inset Figure 2.1a) showing the position of the sampling location at Tenmile Butte (after Hintze et al., 2000). c) Photograph of the Entrada Sandstone showing a CO_2-exposed fault zone cutting the virgin (red, unexposed) sandstone (courtesy of Dr. N. Kampman). Note the bleached, CO_2-exposed sandstone at the margins of the fault zone.

The extent of the Paradox Basin is defined as the area of salt deposition in the Middle Pennsylvanian Paradox Formation. To the north-west and north, the basin is bounded by the San Rafael Swell and Uncompahgre Plateau, while the east and south-east ends of the basin are defined by the San Juan Dome and Hogback Monocline (see Figure 2.1a) (Nuccio and Condon, 1996). Sediment deposition occurred in a half-graben structure adjacent to the SW-bounding faults of the Pennsylvanian Uncompahgre uplift, which supplied arkosic debris to the northern margin of the basin (Baars and Stevenson, 1981). Basin filling consists of a sequence of Palaeozoic marine sediments overlain by Triassic and Jurassic mainly alluvial sediments, including alternating sequences of low conductivity silts and

mudstones (aquitards) and hydraulically conductive, predominantly aeolian sediments, such as the Jurassic Entrada Sandstone (Figure 2.1b).

During the Cretaceous, diapiric rise of thick Carboniferous evaporites and movement along pre-existing faults in the Precambrian basement resulted in the formation of NW-SE-trending faults, anticlines and synclines, the so-called Paradox Fold and Fault belt (Figure 2.1a), in the northern part of the basin (Baars and Stevenson, 1981; Nuccio and Condon, 1996). Though the timing is poorly constrained, it has been postulated that reactivation of these fold and fault structures occurred during the Laramide orogeny (Baars and Stevenson, 1981; Shipton et al., 2004).

The north-plunging Green River anticline is cut by two east-west trending steeply-dipping, normal faults: the Little Grand Wash Fault (LGWF) and the Salt Wash Fault (SWF). At the crest of the anticline, beneath the south-dipping faults, CO_2 has accumulated. The CO_2 was sourced by clay-carbonate reactions in underlying limestones of the Paradox Formation (Shipton et al., 2004), possibly supplemented by a magmatic source (Wilkinson et al., 2008). Leakage of subsurface CO_2 along the LGWF and SWF commenced approximately 100 to 400 ka ago (Burnside et al., 2013), leading to CO_2-induced reactions in the corresponding fault cores and adjacent damage zones, such as seen in the Entrada Sandstone (Kampman et al., 2014; Shipton et al., 2004).

The Entrada Sandstone unit is a ~150-450 m thick (Ogata et al., 2014), reddish sandstone, which crops out as shown in Figure 2.1B. It consists mainly of quartz and feldspar and is cemented predominantly by quartz, dolomite and calcite (Wigley et al., 2012). The Entrada sandstone is therefore lithologically similar, in broad terms, to many natural gas reservoirs around the world (Shipton et al., 2004). Locally, however, it contains bleached zones that consist of reduced amounts of quartz and feldspar with calcite and dolomite cement filling the pores (Wigley et al., 2012). In the case of the SWF, CO_2 leakage has led to extensive carbonate precipitation, where it traverses the Entrada Sandstones (Burnside et al., 2013).

2.2.2 Sample material

The Entrada Sandstone and fault rock material used in this study was taken from three nearby outcrops at Tenmile Butte (Figure 2.1b), in the Green River field,

Table 2.1. XRD data for the simulated gouges derived from the unexposed and CO_2-exposed reservoir rock, and the CO_2-exposed, carbonate-rich fault rock samples. Note: 'n.d.' indicates that the corresponding phase is below the detection limit.

mineral (mass-%)	unexposed sandstone	CO_2-exposed sandstone	CO_2-exposed fault rock
quartz	58.8-70.5	75.9-90.5	31.1-71.5
calcite	2.1-5.9	< 1.2	0.6-7.2
dolomite	1.1-4.7	1.0-2.2	< 3.7
aragonite	n.d.	n.d.	26.7-40.0
albite	< 6.6 (occasionally 19.7)	n.d.	n.d.
microcline	9.9-13.3	3.1-5.4 (occasionally 19.8)	n.d.
bytownite	n.d.	n.d.	< 5.0
dickite	< 2.1	n.d.	n.d.
phyllosilicate (muscovite)	4.2-8.9	1.9-3.4	4.8-18.0
hematite	0.4	< 0.5	< 1.5
magnetite	n.d.	< 1.0	n.d.

showing varying degrees of CO_2-exposure: 1) red-coloured, unreacted and mechanically intact reservoir material, referred to here as 'unexposed sandstone', 2) pale yellow-coloured, mechanically intact reservoir rock exposed to CO_2-rich fluid, i.e. 'CO_2-exposed sandstone', and 3) white-coloured fault rock obtained from the footwall of the actively CO_2-leaking SWF, referred to as 'CO_2-exposed, carbonate-rich fault rock' (Figure 2.1b).

Each of these materials was characterised using optical microscopy and X-ray diffraction (XRD) analysis (see Table 2.1). The red, unexposed sandstone samples consisted mainly of quartz (60-70%), feldspar (11-15%, occasionally up to ~20%) and minor amounts of phyllosilicates (muscovite; 6-9%). The grains are angular to rounded (grain size: ~100µm), locally indented by pressure solution, and cemented by predominantly dolomite and calcite (3-10%), resulting in ~10% porosity. Moreover, minor amounts of hematite (~0.40%) were detected, being optically visible as grain coatings and giving the rock its characteristic reddish colour. The bleached, CO_2-exposed sandstone samples consisted of increased amounts of quartz (75-90%) and mostly lower amounts of feldspar (3-5%, occasionally ~20%), phyllosilicate (muscovite; 2-3.5%), carbonates (calcite plus dolomite: 1.5-3.0%) and hematite (< 0.5%), in rough accordance with expectations for reaction of the red

protolith with CO_2 (Wigley et al., 2012). The grains in this material are a little more angular (grain size: ~125µm), with some grains showing irregular boundaries, suggesting corrosion due to dissolution. Cement is predominantly formed by large, irregularly shaped patches of quartz-cement (250-300µm), with clearly less carbonate. The porosity of the bleached samples is 5-10%. Cemented fault rock sampled from the SWF consisted of veins containing large (1 cm) spheroidal aggregates of radiating acicular aragonite (27-51%), plus minor amounts of calcite and dolomite (0.6-11%), embedded in a fine-grained sandstone matrix consisting of quartz (31-72%) with minor amounts of feldspar (5%) and phyllosilicates (muscovite; 5-19%). Locally, traces of hematite were detected. Simulated fault gouges were prepared from these three materials by crushing cm-sized samples using a mortar and pestle. The material was further crushed using a ball-mill until it attained a grain size that passed through a 35 µm sieve, representing the typical grain size range observed in simulated and natural fault gouges (Byerlee and Summers, 1976; Keulen et al., 2007).

2.3 Experimental aspects

A total of 23 direct shear experiments were conducted to investigate the effects of effective normal stress (σ_n^{eff}), temperature (T) and pore fluid (added at pressure P_f) on the frictional properties of the three types of simulated fault gouge samples described above. We performed four series of experiments on each of these three sample types:

1) Experiments at room temperature, under lab-dry conditions (room humidity) and at σ_n^{eff} of 5 to 90 MPa (Data-set 1),
2) Experiments at elevated temperature (T = 100˚C), under lab-dry conditions and at σ_n^{eff} = 50 MPa (Data-set 2),
3) Experiments at elevated temperature (T = 100˚C) employing an aqueous pore fluid at a pressure P_f = 25 MPa and at σ_n^{eff} = 50 MPa (Data-set 3),
4) Experiments performed on vacuum-dried samples at room temperature and at σ_n^{eff} = 50 MPa, using argon as the pore fluid (P_f = 2 MPa) and making argon permeability measurements before, during and after shear (Data-set 4).

Aqueous pore fluid solutions were prepared by adding excess amounts of fine-grained, crushed powder of the respective sample material to distilled water and stirring until used in the wet experiments (i.e. for at least 24 hours). These solutions were assumed to be saturated with soluble components before use, thereby preventing dissolution of these components during our wet experiments. All experiments performed are summarised in Table 2.2.

Table 2.2. Overview of the experiments performed in this study. Samples were tested lab-dry, wet with a sample saturated-solution or using dry argon gas.

Expt	*Material*	*σ_n^{eff} (MPa)*	*V (µm/s)*	*μ_{final} (-)*	*Motion*
Data-set 1: effect of effective normal stress, σ_n^{eff} (lab-dry (room humidity), room temperature)					
Un01	unexposed sandstone	5	5.43-0.22-1.086-10.86-1.086-0.22	0.71	VS
Un02	unexposed sandstone	25	5.43-0.22-1.086-10.86-1.086-0.22	0.56	VS
Un03	unexposed sandstone	50	5.43-0.22-1.086-10.86-1.086-0.22	0.57	VS
Un04	unexposed sandstone	50	5.43-0.22-1.086-10.86-1.086-0.22	0.61	VS
Un05	unexposed sandstone	75	5.43-0.22-1.086-10.86-1.086-0.22	0.58	VS
Un06	unexposed sandstone	75	5.43-0.22-1.086-10.86-1.086-0.22	0.56	VS
Un07	unexposed sandstone	90	5.43-0.22-1.086-10.86-1.086-0.22	0.60	VS
Ex01	CO_2-exposed sandstone	5	5.43-0.22-1.086-10.86-1.086-0.22	0.71	VS
Ex02	CO_2-exposed sandstone	25	5.43-0.22-1.086-10.86-1.086-0.22	0.59	VS
Ex03	CO_2-exposed sandstone	50	5.43-0.22-1.086-10.86-1.086-0.22	0.53	VS
Ex04	CO_2-exposed sandstone	50	5.43-0.22-1.086-10.86-1.086-0.22	0.53	VS
Ex05	CO_2-exposed sandstone	75	5.43-0.22-1.086-10.86-1.086-0.22	0.61	VS
Ex06	CO_2-exposed sandstone	75	5.43-0.22-1.086-10.86-1.086-0.22	0.59	VS
Ex07	CO_2-exposed sandstone	90	5.43-0.22-1.086-10.86-1.086-0.22	0.62	VS
FR01	CO_2-exposed fault rock	5	5.43-0.22-1.086-10.86-1.086-0.22	0.82	VS
FR02	CO_2-exposed fault rock	5	5.43-0.22-1.086-10.86-1.086-0.22	0.92	VS
FR03	CO_2-exposed fault rock	5	5.43-0.22-1.086-10.86-1.086-0.22	0.89	VS
FR04	CO_2-exposed fault rock	25	5.43-0.22-1.086-10.86-1.086-0.22	0.57	VS
FR05	CO_2-exposed fault rock	50	5.43-0.22-1.086-10.86-1.086-0.22	0.65	VS
FR06	CO_2-exposed fault rock	50	5.43-0.22-1.086-10.86-1.086-0.22	0.66	VS
FR07	CO_2-exposed fault rock	75	5.43-0.22-1.086-10.86-1.086-0.22	0.60	VS
FR08	CO_2-exposed fault rock	75	5.43-0.22-1.086-10.86-1.086-0.22	0.63	VS
FR09	CO_2-exposed fault rock	90	5.43-0.22-1.086-10.86-1.086-0.22	0.60	VS
Data-set 2: effect of temperature (σ_n^{eff} = 50 MPa, lab-dry (room humidity), T = 100°C)					

Table 2.2. *continued*

Un09	unexposed sandstone	50	5.43-0.22-1.086-10.86-1.086-0.22	0.66	VS-VW
Ex09	CO_2-exposed sandstone	50	5.43-0.22-1.086-10.86-1.086-0.22	0.65	VS-VW
FR11	CO_2-exposed fault rock	50	5.43-0.22-1.086-10.86-1.086-0.22	0.61	VW
Data-set 3: effect of saturated-solution (σ_n^{eff} = 50 MPa, P_f = 25 MPa, T = 100°C)					
Un10	unexposed sandstone	50	5.43-0.22-1.086-10.86-1.086-0.22	0.55	VS-VW
Ex10	CO_2-exposed sandstone	50	5.43-0.22-1.086-10.86-1.086-0.22	0.42	VS
FR12	CO_2-exposed fault rock	50	5.43-0.22-1.086-10.86-1.086-0.22	0.62	VW
Data-set 4: effect of shear on across-fault argon permeability (σ_n^{eff} = 50 MPa, P_f = 2 MPa, room temperature)					
Un08	unexposed sandstone	50	5.43-0.543 (3x)	0.47	-
Ex08	CO_2-exposed sandstone	50	5.43-0.543 (3x)	0.55	-
FR10	CO_2-exposed fault rock	50	5.43-0.543 (3x)	0.49	-

Symbols: σ_n^{eff} denotes effective normal stress, P_f denotes pore pressure, T denotes temperature, V denotes sliding velocity and μ_{final} denotes the friction coefficient measured at the end of each experiment (~ 5-7 mm displacement). Motion: 'VS' indicates that a sample exhibited velocity-strengthening slip behaviour, while 'VW' indicates velocity-weakening slip behaviour.

2.3.1 Experimental procedure: direct shear experiments

Direct shear experiments were performed on the simulated fault gouges using a conventional triaxial compression machine (see Supplementary Material, Figure S2.1), equipped with a specially-designed direct shear assembly (Figure S2.2 – see also Samuelson and Spiers (2012)). The apparatus consists of an externally-heated main pressure vessel, with silicone oil as the confining medium, linked to an auxiliary pressure-compensation vessel (Hangx et al., 2010b; Peach, 1991). Load is transmitted to the sample using a yoke/piston assembly, which is driven by a motor/gearbox/ball-screw system. Upon advancement of the piston, a shear stress is imposed on the gouge layer and sliding is initiated at a constant sliding velocity of ~5 µm/s. To investigate the velocity-dependence of friction of the three types of simulated fault gouges a five-step velocity-stepping sequence is employed. The displacement velocity is determined by the gears of the motor driving the loading piston, being equivalent to sliding velocities of 0.22-1.086-10.86-1.086-0.22 µm/s.

During each shear experiment, internal axial load, piston displacement, confining pressure and sample temperature were logged every 2 s. The shear stress is equal to the internal axial load divided by the contact area of the shear surface, which is assumed to remain equal to the initial contact area. From the shear stress and the

normal stress, the apparent coefficient of friction μ was calculated as $\mu = \tau/\sigma_n^{eff}$, in effect including any minor cohesion effects in μ (cf. den Hartog et al., 2013; Niemeijer and Vissers, 2014). For the sake of simplicity, we will refer to μ as the friction coefficient.

The slip rate-dependence of μ, obtained from the velocity-stepping shear experiments, was analysed using the rate-and-state friction (RSF) approach (Marone, 1998) and expressed in terms of (a-b) (see Supplementary Material Section S1.4). In short, a positive (a-b)-value means the material exhibits 'velocity-strengthening' behaviour, implying that the system is inherently stable and that the accelerating slip needed for seismogenesis cannot occur (Scholz, 1998), at least within the RSF approach to quantifying friction. On the other hand, 'velocity-weakening' behaviour occurs if (a-b) is negative. In this case, the system is potentially unstable (Scholz, 1998), i.e. able to produce repetitive stick-slip events or seismogenic slip provided that the elastic stiffness of the loading system falls in the right range (e.g. Scholz, 2002). It should be noted that velocity step-related changes in friction coefficient are often superimposed onto a gradual increase or decrease of μ with increasing slip distance, a so-called slip-hardening or slip-softening trend, respectively. Slip-hardening is often associated with ongoing grain size reduction through cataclasis, whereas slip-softening is associated with ongoing localization of shear deformation (Kanagawa et al., 2000; Niemeijer et al., 2008). However, in our experimental configuration, slip-softening might be an artefact from a decreasing load-bearing area of contact.

2.3.2 Experimental procedure: permeability measurements

A total of three direct shear experiments coupled to 'across-fault permeability' (κ) measurements were performed on dry samples, at room temperature, using argon gas permeametry. This method employed the decay of a 0.2 MPa argon gas pressure difference imposed suddenly across the sample (Sutherland and Cave, 1980) – see Supplementary Material Section S2.2 for more details. Permeametry was carried out before, during and after shear using the same direct shear and velocity-stepping procedure as described above. The argon pressure signals measured at each end of the sample were logged and used to calculate across-fault permeability by analysing the pressure decay using the method described by Sutherland and Cave (1980).

2.4 Results

In this chapter, we adopt the convention that compressive stresses are positive. In our friction experiments, we take the yield point in the run-in stage of individual experiments as the point of maximum curvature of the friction coefficient vs. displacement curves. We take the effective normal stress (σ_n^{eff}) as the applied confining pressure hence normal stress (σ_n) minus the applied pore pressure (P_f), thus defining it as:

$$\sigma_n^{eff} = \sigma_n - P_f \quad (2.1)$$

2.4.1 Mechanical data

2.4.1.1 Frictional behaviour of lab-dry gouges at room temperature (Data-set 1)

The evolution of the friction coefficient as a function of shear displacement is shown in Figures 2.2a and b for representative subsets of experiments performed under lab-dry conditions on all three sample types, at room temperature and at 5, 25, 50 and 90 MPa effective normal stress (Data-set 1). All μ vs. displacement curves obtained at room temperature in the present study are characterised by a near-linear increase in μ until yielding occurs. Yielding is observed at a shear displacement x of 0.4-0.6 mm and at a friction coefficient of ~0.55 to 0.75 at low σ_n^{eff} (5 MPa), versus 0.5-1.0 mm and $\mu \approx 0.55$ at intermediate to high σ_n^{eff} (25-90 MPa) (Figure 2.2a-b). Yielding is usually followed by minor slip-hardening, reaching near steady-state friction values at a shear displacement x of ~1.6 mm. At this displacement, the first velocity step was applied. In subsequent velocity-stepping stages, similar velocity-strengthening (stable slip) frictional behaviour is observed for all three materials when performed at the same applied normal stress. The frictional response to upward velocity steps frequently lacks a distinct peak due to the absence of subsequent weakening (cf. compare Figures 2.2a-b and S2.3).

Though steady-state is approached in most tests shortly beyond yield, tests performed on all three sample materials at low normal stress (σ_n^{eff} = 5 MPa) show slip-hardening superimposed on the majority of subsequent velocity- steps, resulting in relatively high friction coefficient values of ~0.70-0.90 in later stages of the experiments (Figures 2.2a and b). The friction coefficient curves obtained at

intermediate to high normal stress (σ_n^{eff} = 25-90 MPa) are characterised by zero to minor slip-hardening, and/or minor slip-softening towards higher displacements, superimposed onto a modest velocity-strengthening response to the applied velocity-steps. This results in final friction coefficient values ranging between ~0.60 and 0.63 (see Figures 2.2a and b). An exception is experiment EX03 (CO_2-exposed Entrada Sandstone, 50 MPa, Figure 2.2b), which shows yielding behaviour similar to unexposed Entrada Sandstone (UN03) and CO_2-exposed, carbonate-rich fault (FR05) gouges, but with the subsequent slip-softening upon velocity stepping, resulting in a final friction coefficient of only ~0.53.

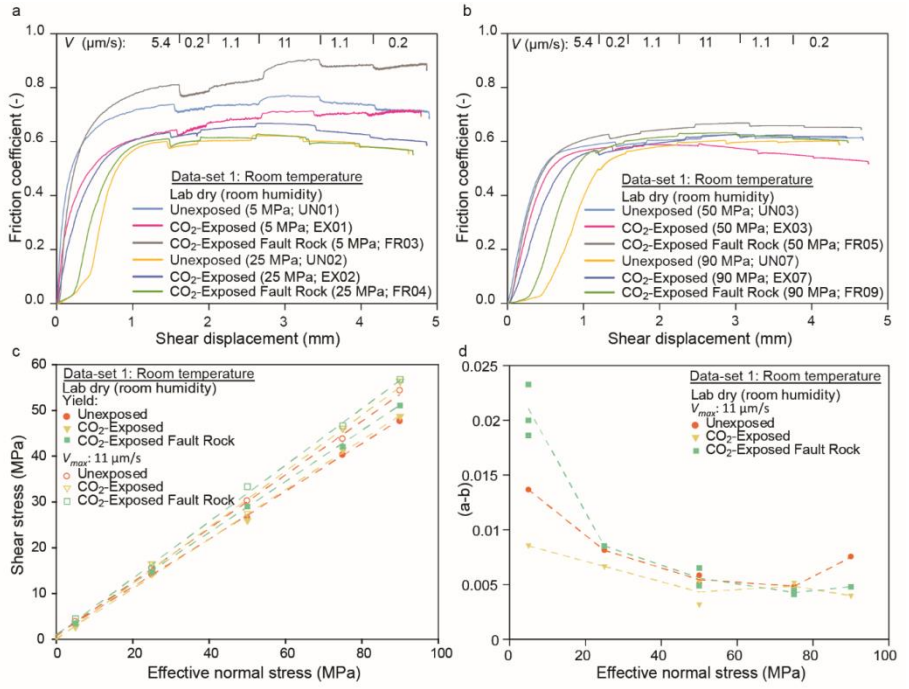

Figure 2.2. Representative mechanical data for all sample types sheared under lab-dry conditions at room temperature (Data-set 1). a) Friction coefficient vs. shear displacement curves for velocity-stepping experiments conducted at normal stresses of 5 and 25 MPa using the velocity-steps indicated at the top of the figure. b) Similar data for samples tested at normal stresses of 50–90 MPa. Note that samples tested at 25–90 MPa show similar behaviour. c) Shear stress at yield (solid symbols) and shear stress at maximum sliding velocity (open symbols) vs. the effective normal stress for experiments performed at room conditions. d) Velocity-dependence parameter (*a*–*b*) versus normal stress. All samples show a decrease in (*a*–*b*) with increasing effective normal stress, at least up to σ_n^{eff} = 75 MPa.

The dependence of shear stress, supported both at yield and at maximum sliding velocity, on σ_n^{eff} is shown for all three sample types deformed lab-dry at room temperature in Figure 2.2c. For all three materials, the data show a linear trend between shear and effective normal stress, which can be described by a Coulomb-type criterion given as:

$$\tau = \mu_i \sigma_n^{eff} + C_0 \quad (2.2)$$

where μ_i is the internal friction coefficient (i.e. the slope of the trend) and C_0 represents the cohesion of the simulated fault gouge (i.e. the intercept of the trend with the vertical axis). It should be noted that for granular materials, like fault gouge, cohesion is generally low, but not necessarily zero. Cohesion is in essence a measure for the extent to which grain-to-grain contacts present in the gouge material are actively experiencing frictional sliding or deformation during shear. In our experiments, the shear stress obtained at yield was used as a reference strength parameter, thus excluding any secondary effects of slip-hardening, when interpreting μ_i and C_0 values. At yield, linear least square fits to the data show that μ_i has values of 0.52±0.011, 0.54±0.017, 0.56±0.007 and C_0 is of the order of 0.71±0.64, 0.0 (zero)±1.0 and 0.73±0.36 MPa, for unexposed sandstone, CO_2-exposed sandstone, and carbonate-rich fault rock gouges respectively. The linear relations describing the steady-state shear stress supported at maximum sliding velocity (V_{max} = 11 µm/s), show higher internal friction coefficients, 0.58±0.017, 0.62±0.03, 0.61±0.014, and cohesion values, 0.89±1.0, 0.0 (zero)±1.3, and 1.39±0.76 MPa. Gouge cohesion is mainly a minor feature, as suggested by the cohesion values. In most cases, certainly in experiments performed at σ_n^{eff} ≥25 MPa, the relative contribution of cohesion to μ is negligible, justifying the use of $\mu = \tau / \sigma_n^{eff}$ as a measure of frictional strength in our RSF analysis. However, cohesion is significant in the tests performed at σ_n^{eff} = 5 MPa, as reflected in the higher μ-values for these samples seen in Figure 2.2a. Note, that the cohesion observed for the CO_2-exposed, carbonate-rich fault-derived gouge is consistently higher than observed for the unexposed as well as the CO_2-exposed reservoir rock gouges.

Focusing now on the friction coefficient values obtained at or near steady-state (μ_{ss}) in the dry experiments at room temperature, it is evident from Figures 2.2a and b that these values increase with sliding velocity, reaching maximum values at velocities of ~11 µm/s ranging from 0.63 to 0.67 at σ_n^{eff}-values of 25 to 90 MPa (for

$x \approx 3.3$ mm) and from 0.71 to 0.91 at σ_n^{eff} = 5 MPa (for $x \approx 3.5$ mm). This is followed by a decrease in frictional strength upon decreasing sliding velocity. In general, the unexposed and CO_2-exposed sandstone gouges show slightly lower μ-values than the carbonate-rich fault gouges.

The (a-b) values obtained for all three gouges under dry, room temperature conditions are all positive and overall very similar at σ_n^{eff} ≥25 MPa. Representative data are shown in Figure 2.2d. Although velocity down-steps were analysed and show similar (a-b) values to up-steps, we focus on (a-b) values obtained for the up-steps as it is these that are relevant for earthquake nucleation. For readability we present only data for up-steps from 1 to 11 µm/s. The (a-b) values obtained at σ_n^{eff} = 5 MPa are consistently higher (0.002-0.05) for all three sample types than those obtained at higher effective normal stresses (0.0007-0.01), especially for the fault rock-derived samples. CO_2-exposed Entrada Sandstone gouge generally shows slightly lower (a-b) values, for the intermediate effective normal stresses, compared to the unexposed quartz-rich and CO_2-exposed, carbonate-rich fault rock. Though part of the data-set is not shown here for readability reasons, we note that (a-b) for all three gouges shows a rough tendency to increase with increasing post-step velocity for up-steps (Figure 2.2d).

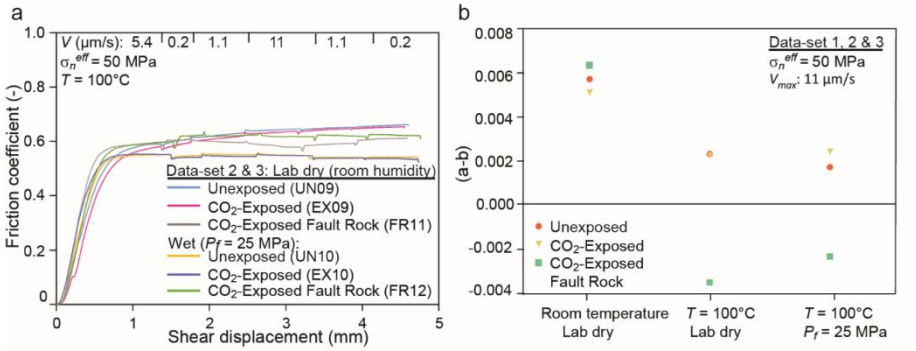

Figure 2.3. Representative mechanical data for all sample types sheared under lab-dry and wet conditions at room temperature and 100°C (Data-set 1–3). a) Friction coefficient vs. displacement curves obtained from experiments conducted at elevated temperature, both lab-dry and wet using the velocity steps indicated at the top. b) Velocity-dependence parameter (a–b) obtained for lab-dry and wet samples at 100°C, plus comparison with lab-dry, room temperature data. Velocity-dependence is shown for a velocity step from ~1 to 11 µm/s, but similar values were obtained for all steps conducted. Only the carbonate-rich fault gouges show a tendency towards velocity-weakening behaviour.

2.4.1.2 Frictional behaviour of lab-dry and wet samples at 100°C (Data-set 2 and 3)

Friction coefficient vs. displacement curves obtained at T = 100˚C and σ_n^{eff} = 50 MPa, for all three sample types under lab-dry (Data-set 2) and solution-flooded (Data-set 3: P_f = 25 MPa) conditions are shown in Figure 2.3a. As seen from this data, all three gouge types (unexposed sandstone (UN09), CO_2-exposed sandstone (EX09), and CO_2-exposed, carbonate-rich fault rock (FR11)) deformed lab-dry at 100˚C exhibited closely similar initial behaviour, characterised by a near-linear increase in μ until apparent yielding at a friction coefficient of ~0.56-0.57 (x ≈ 0.7-0.9 mm - Figure 2.3a), followed by minor slip-hardening. In the experiments on the lab-dry, quartz-rich sandstone-derived gouges (UN09 and EX09), the friction coefficient increased from ~0.58, just beyond yield and prior to the first velocity-step, to ~0.65 at the end of the experiment. By contrast, the lab-dry, carbonate-rich fault rock sample (FR11) displays slip-softening behaviour during the velocity up-steps, between a shear displacement of ~1.5 and 3.0 mm, followed by slip-hardening during the subsequent velocity down steps. Overall, the frictional strength of lab-dry samples, at 100°C and 50 MPa effective normal stress, is very similar to that seen in room temperature runs at the same conditions.

Compared with their lab-dry equivalents, the wet, unexposed (UN10) and CO_2-exposed (EX10) sandstone-derived samples are characterised by a more rapid increase in μ until yield at a slightly lower friction coefficient (μ ≈ 0.54 at x ≈ 0.66 mm). These samples exhibited steady-state sliding behaviour during the remainder of the experiments, characterised by a slightly lower frictional strength than lab-dry samples (~0.55 vs. ~0.65, respectively). The wet, CO_2-exposed, carbonate-rich fault-derived sample (FR12) exhibited near steady-state slip behaviour reaching a μ-value of ~0.62, comparable to the behaviour under lab-dry condition (μ ≈ 0.61).

Turning to the velocity-dependence of friction at 100˚C, our data for lab-dry samples derived from unexposed and CO_2-exposed sandstone (Data-set 2; UN09 and EX09) exhibit velocity-strengthening (stable slip) behaviour as illustrated by the positive (a-b) values shown in Figure 2.3b, with the values being very similar for both materials. By comparison, the (a-b) values obtained for the sample prepared from carbonate-rich fault rock (Data-set 2; FR11) are strongly negative, i.e. exhibiting markedly velocity-weakening (unstable slip) behaviour. All three

materials show much lower (*a*-*b*) values than obtained at room temperature (Figure 2.3b).

The presence of a pore fluid at 100˚C appears to have little to no effect on the velocity-dependence of friction for the unexposed and CO_2-exposed sandstone-derived gouges (UN10 and EX10), as the (*a*-*b*) values are closely similar at ~+0.002 for both materials under lab-dry and wet conditions (Figure 2.3b). The (*a*-*b*) values obtained for the samples derived from carbonate-rich fault rock (FR12) remain firmly negative in the wet condition, reflecting velocity-weakening behaviour (Figure 2.3b).

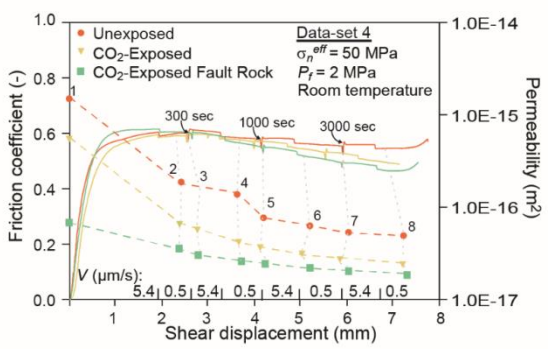

Figure 2.4. Friction coefficient (solid lines) and gouge permeability (symbols) vs. shear displacement data obtained in the permeability experiments. Dashed tie-lines connect permeability measurements performed on the same samples. The experiments consisted of velocity-stepping tests combined with slide-hold-slide testing. Velocity-steps are shown. Hold periods are indicated with arrows. Permeability data points 2, 4 and 6 were determined during shear. Points 3, 5, 7 and 8 were measured during the hold periods shown.

2.4.2 Permeability data

Values of κ obtained from our permeametry measurements performed on all three materials at room temperature, are plotted as a function of shear displacement in Figure 2.4, along with the friction coefficient measured during shearing (Data-set 4). Overall, the frictional behaviour observed during these experiments is very similar to that seen in all other lab-dry tests on the same materials (cf. Figures 2.2a and b). However, in contrast to the velocity-stepping tests on dry gouges, the present velocity-stepping plus slide-hold-slide experiments are dominated by slip-softening behaviour, reaching μ-values of ~0.50 to 0.55 for the samples prepared from unexposed and CO_2-exposed sandstone (UN08 and EX08), and 0.46 for the

sample derived from CO_2-exposed, carbonate-rich fault rock (FR10), at the maximum displacements attained of ~7 mm. All three experiments show relatively distinct peak stresses upon re-shearing after a period of hold. For all samples it is evident from Figure 2.4 that κ decreases with accumulated shear displacement. Initial values obtained prior to shearing (point 1 – Figure 2.4) vary between $1.5 \cdot 10^{-15}$ and $6.8 \cdot 10^{-17}$ m^2. These decrease by a factor of 10 for the sandstone-derived samples (unexposed and exposed) and a factor of around 2 for the carbonate-rich sample during the first stage of deformation at $V \approx 5.4$ µm/s. The permeability of all samples continues to decrease with on-going shear displacement by a factor of 2 or 3. At the same time, κ-values measured during both shear and hold periods appear to lie on more or less the same κ-x trend-lines, suggesting little reduction in permeability during the hold periods. The final across-fault argon permeability after ~7 mm of shear displacement (point 8), lies in the range of $5.0 \cdot 10^{-17}$ m^2 for unexposed sample material to $2.0 \cdot 10^{-17}$ m^2 for fault rock derived material.

2.5 Discussion

It has been widely suggested that geological storage of CO_2 can potentially lead to fault slip and induced seismicity via effects such as a reduction in effective normal stress and/or changes in the poro-elastic stress state of the storage reservoir, in response to an increase in pore pressure (e.g. Hawkes et al., 2005; Zoback and Gorelick, 2012). It has also been suggested that induced slip and seismicity can perhaps be promoted by a reduction in fault rock frictional strength and/or slip stability, i.e. a transition from positive to negative (a-b) values, caused by CO_2-brine-rock interactions (Samuelson and Spiers, 2012). Critically, from the point of view of system integrity, induced fault slip may cause dilatation, subsequently increasing fault permeability. To help evaluate the slip, seismogenic and leakage potential of faults cutting clastic CO_2 reservoirs, we have investigated the frictional behaviour, slip stability and transport properties of simulated fault gouges derived from Entrada Sandstone samples taken from unexposed and CO_2-exposed portions of the formation at the Green River CO_2 reservoir site, and from the carbonate cemented material of the Salt Wash Fault which is an active CO_2-leakage path.

In Europe, a significant number of recently investigated CCS pilot sites focus on sand and sandstone reservoir systems. Examples include the ROAD project (P-18

field, Triassic Bunter Sandstone; Dutch North Sea - Samuelson and Spiers (2012)), the (shelved) Peterhead CCS project (Goldeneye field, Lower Cretaceous Captain Sandstone; UK North Sea - Hangx et al. (2013)), and the Sleipner CO_2 Storage project (Sleipner field, Miocene-Pliocene Utsira Sandstone; Norwegian North Sea - Chadwick et al. (2004)). The Entrada Sandstone is considered a good analogue for many of these European sandstone reservoirs (Shipton et al., 2004), especially those that have a similar continental/aeolian origin, such as the Permian Rotliegend and Triassic Bunter gas reservoirs in the North Sea and onshore Netherlands regions. Accordingly, the long-term CO_2-charging of the Entrada Sandstone, and the effects of subsequent CO_2-induced mineral reactions superimposed on primary sediment and early diagenetic variability, offer a natural case-study for long-term CO_2 sequestration in sandstone reservoirs (Wigley et al., 2012).

Overall, our friction experiments on simulated fault gouges derived from naturally CO_2-exposed and unexposed Entrada Sandstone, are characterised by a friction coefficient ($\mu \approx 0.5$-0.6) that is virtually independent of normal stress- and temperature, within the range of reservoir-relevant conditions investigated, i.e. 20-100°C, $\sigma_n^{eff} \geq 25$ MPa (Figures 2.2a and b). This range of conditions corresponds well with the temperatures and effective stresses expected in reservoir systems at depths up to ~3-4 km. The sandstone-derived gouges studied exhibit velocity-strengthening slip behaviour under all conditions studied (i.e. $(a\text{-}b) > 0$), with no significant effect of temperature on (a-b). However, keeping in mind reproducibility in the (a-b) values (Niemeijer and Vissers, 2014), at room temperature they do show a slight decrease in (a-b) from velocity-strengthening at $\sigma_n^{eff} \leq 25$ MPa to near-neutral values at 75-90 MPa. Differences in mechanical behaviour between the CO_2-exposed and unexposed reservoir-derived gouges are clearly minor in our experiments (cf. Figures 2.2 and 2.3), which is perhaps not surprising in view of the fact that the compositional differences are relatively minor. By contrast, the simulated gouges derived from the carbonate-rich fault rock exhibited higher friction coefficient values ($\mu \approx 0.6$-0.7) than the sandstones, though again these values were temperature-independent at $\sigma_n^{eff} \geq 25$ MPa. Interestingly, the (a-b)-data obtained for the carbonate-rich fault gouge showed a transition from velocity-strengthening behaviour at room temperature (dry) to velocity-weakening behaviour at 100˚C (both dry and wet), i.e. from stable sliding to unstable and potentially seismogenic slip. Finally, while the sandstone materials tested showed a

decrease in across-fault permeability with accumulated shear displacement by up to 1.5 orders of magnitude, i.e. from ~10^{-15} m^2 in the undeformed state to ~$3.0 \cdot 10^{-17}$ m^2 at shear displacements of 6-7 mm, the carbonate-rich material showed a decrease only from ~$5.0 \cdot 10^{-17}$ m^2 to $2.0 \cdot 10^{-17}$ m^2 (cf. Figure 2.4).

In the following, we discuss the effects of fault rock composition, normal stress, temperature, pore fluid and time on fault cohesion, frictional strength, slip stability, deformation mechanism and permeability evolution. This is done in the context of evaluating the effects of long-term exposure to CO_2 on fault rock behaviour and fault integrity during geological storage of CO_2 in sandstone reservoir rocks.

2.5.1 Contribution of cohesion to fault strength under laboratory vs. in-situ conditions

The gouge cohesion values obtained at yield in the present experiments, for the unexposed and CO_2-exposed quartz-rich sandstone and for the carbonate-rich fault rock, are respectively 0.71±0.64, 0.0 (zero) ±1.0 and 0.73±0.36 MPa. This implies maximum cohesion values at yield of less than 1.5 MPa at our initial sliding velocity of ~5.4 µm/s. For steady-state shearing at maximum sliding velocity ($V \approx 11$ µm/s), the corresponding cohesion values are slightly higher, specifically 0.89±1.0, 0.0 (zero) ±1.3, and 1.39±0.76, implying maximum values around 2 MPa. Though gouge cohesion is minor, its relative contribution to the friction coefficient may be significant when the stresses acting on the fault plane are small, i.e. when C_0 is of the same order of magnitude as τ and σ_n^{eff} (cf. Equation (2.2)). Compared with the shear stresses of 30-55 MPa supported by our samples at $\sigma_n^{eff} > 50$ MPa, cohesion values of 1-2 MPa are negligible, so that fault rock shear strength can be represented simply taking the ratio of shear stress over effective normal stress as the friction coefficient. However, for the experiments performed at normal stresses between 5 and 25 MPa, a sample cohesion of ~1 MPa means that using $\mu = \tau/\sigma_n^{eff}$, leads to an underestimation of the shear strength that a fault can support by respectively 41 and 5%. In the case of real, reservoir-cutting faults that have been inactive over geological time, or have suffered only minor slip during hydrocarbons production, healing and cementation processes may lead to much higher cohesion (Tenthorey and Cox, 2006). The implication is that in establishing static failure criteria for faults in CO_2 storage systems where the effective pressure is expected to fall to say 25 MPa or less, cohesion cannot be neglected. Taking into account

cohesion means injection pressure, and hence storage capacity, can be estimated higher than expected from purely frictional behaviour.

2.5.2 Effects of compositional differences and deformation conditions on the frictional behaviour of sandstone-derived gouges

Entrada Sandstone that has not been exposed to CO_2 consists predominantly of quartz and feldspar, with smaller amounts of phyllosilicates, carbonate cement and hematite (see Table 2.1). The hematite, which is present as grain-coatings, imparts the characteristic reddish to the unaltered sandstone. As described by Ogata et al. (2014), CO_2-induced alterations of the Entrada sandstone result in 'bleaching' or discolouration of the rock from red to pale yellow, through the dissolution of hematite. This is visible in our CO_2-exposed samples from the absence of hematite in most XRD data (Table 2.1). These samples also contain larger amounts of quartz, either as grains or inter-granular cement, and smaller amounts of feldspar, phyllosilicates and carbonates (Table 2.1). So, overall, an increase in quartz and a change in feldspar, carbonate and hematite content has been observed. These mineralogical changes are in agreement with the following geochemical reactions expected for CO_2 reacting with this type of sandstone:

Albite:

$NaAlSi_3O_{8\ (s)} + H^+_{(aq)} + 4.5H_2O_{(l)} \leftrightharpoons Na^+_{(aq)} + 2H_4\ SiO_{4(aq)} + 0.5Al_2Si_2O_5\ (OH)_{4(s)}$

(Stumm and Morgan, 1981)

Calcite:

$CaCO_{3(s)} \leftrightharpoons Ca^{2+}_{(aq)} + CO_3^{2+}{}_{(aq)}$

(Stumm and Morgan, 1981)

Hematite:

$Fe_2O_{3(s)} + 2CO_{2(g)} + SO_{2(g)} + H_2O_{(l)} \leftrightharpoons 2FeCO_{3(s)} + H_2SO_{4(aq)}$

(Palandri and Kharaka, 2005)

Muscovite:

$KAl_2Si_3AlO_{10}{\cdot}(OH)_{2(s)} + 10H^+_{(aq)} \leftrightharpoons K^+_{(aq)} + 3Al^{3+}_{(aq)} + 3Si(OH)_{4(aq)}$

(Knauss and Wolery, 1989)

Weighed overall, our analyses of CO_2-exposed Entrada material, along with optical observations of grain surface corrosion and quartz cementation, suggest CO_2-related dissolution of feldspar, phyllosilicates and carbonate minerals plus precipitation of quartz (Table 2.1). Taking into account the composition of the unaltered samples, however, these inferred CO_2-related changes are most likely superimposed on local variations in mineralogy due to depositional fluctuations (Wigley et al., 2013) and early diagenetic variability.

In the present experiments, the unexposed and CO_2-exposed sandstone gouges exhibited closely similar frictional behaviour under dry conditions at room temperature (Figures 2.2a and b), and under dry and wet conditions at elevated temperature (Figure 2.3a). This behaviour is in good agreement with that observed in experiments on pure quartz and pure feldspar gouges (Mair and Marone, 1999; Morrow et al., 2000; Scruggs and Tullis, 1998; Shimamoto and Logan, 1981), as well as in experiments on simulated gouge prepared from gas reservoir sandstones (Hangx et al., 2015; Samuelson and Spiers, 2012), which generally show friction coefficients in the range 0.5 to 0.7, when tested dry and wet, at comparable conditions.

The slightly lower frictional strength exhibited by both our wet reservoir rock gouges (Figure 2.3a) compared to the dry gouges (Figures 2.2a and b) is also in agreement with the effect of water on pure quartz gouge prepared by Chester (1994). Furthermore, the observed slip-hardening behaviour seen under dry conditions is similar to that reported in other studies (Chester, 1994; Samuelson and Spiers, 2012; Tembe et al., 2010). This has previously been suggested to reflect cataclastic processes such as microcracking and comminution of the quartz grains, resulting in progressive compaction and thus strengthening of the gouge (Kanagawa et al., 2000; Niemeijer et al., 2008). Other clastic particles present in the gouge, such as feldspar and calcite, are expected to be affected by similar processes. Note that simulated gouges prepared from exposed and unexposed Entrada Sandstone samples show slip-neutral or truly steady-state sliding behaviour when sheared wet. This may be due to enhanced stress-corrosion cracking in the presence of water, allowing more rapid comminution and hence compaction in the initial stages of deformation, rendering a more mature and dense gouge, which is less prone to displacement-dependent evolution in the later stages of the deformation.

Focusing now on the velocity-dependence of friction, gouge samples prepared from both unexposed and CO_2-exposed reservoir rock consistently showed velocity-strengthening behaviour at all conditions investigated. This agrees well with results obtained previously for pure quartz, pure feldspar, and natural sandstone gouges tested under similar experimental conditions (Chester, 1994; Hangx et al., 2015; Morrow et al., 2000; Samuelson and Spiers, 2012; Scruggs and Tullis, 1998; Shimamoto and Logan, 1981). Although slightly more marked, the observed decrease in (*a*-*b*) with increasing normal stress seen in our room temperature experiments agrees well with that observed for pure quartz gouges (Mair and Marone, 1999). This decrease in (*a*-*b*) is attributed to the decreasing effect of cohesion with increasing normal stress. Additionally, our (*a*-*b*) values for lab-dry samples show a decrease with temperature, between room temperature and 100˚C (Figure 2.3b). Plotting our (*a*-*b*) data for lab dry and fluid-saturated samples together with data for pure quartz gouges (Chester, 1994) shows that all data sets show a roughly similar trend, i.e. a decrease in (*a*-*b*) with temperature, suggesting that temperature is important when evaluating the stability of a quartz-rich gouge (Figure 2.5a).

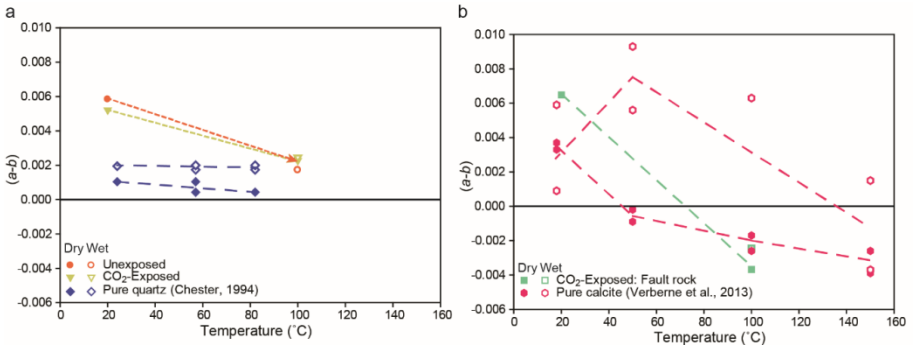

Figure 2.5. Comparison of the velocity-dependence parameter (*a*–*b*) vs. temperature data for present samples with literature data. a) (*a*–*b*) vs. temperature data for the unexposed and CO_2-exposed Entrada Sandstone gouges plus literature data on pure quartz (Chester, 1994). b) (*a*–*b*) vs. temperature data for CO_2-exposed fault rock plus previous data on pure calcite (Verberne et al., 2014b). Solid symbols represent room dry experiments, open symbols represent solution-flooded samples. Note that the method applied by Chester (1994) to determine (*a*–*b*)-values consisted of fitting a single (*a*–*b*)-value to two consecutive velocity-steps, plus a temperature-step.

Except for the tests performed at low effective normal stress (σ_n^{eff} = 5 MPa), where processes such as grain rolling/sliding may dominate deformation (Mair and

Marone, 2001), we assume cataclasis plus granular flow to be the main mechanisms controlling deformation at room temperature. At the same time, however, the transition from velocity-strengthening to near velocity-neutral behaviour seen between ~20 and 100°C (cf. Figures 2.3b and 2.5) suggests the activation of a temperature-dependent deformation process. Intracrystalline plasticity in quartz seems highly unlikely at such low temperatures, as it would occur at a vanishingly low rate (e.g. Hirth et al., 2001). However, in both wet and lab dry samples fluid-assisted processes such as pressure solution or subcritical crack growth are a possibility (Chester, 1994), recognizing that the lab dry (room humidity) samples must contain some water. In the case of a temperature-dependent, fluid-assisted process, such as pressure solution or subcritical crack growth, a clear effect of the addition of an aqueous pore fluid phase to dry samples might be expected to have a clear influence on strength and hence on (*a*-*b*). No such effects were seen in our experiments (see Figures 2.2a-b and 2.3). However, we cannot exclude an effect of water on the velocity-dependence of the lab dry Entrada Sandstone gouges, as at room humidity sufficient moisture might still be present to allow fluid-assisted processes.

In conclusion, the detailed mechanisms dominating the frictional behaviour of our sandstone-derived gouges remain unclear. However, our observations do demonstrate that the mechanical behaviour of fault gouges derived from quartz-rich reservoir sandstones, similar to the Entrada Sandstone, will not be strongly influenced by long-term CO_2-exposure. In the present samples, this is undoubtedly because of the minor mineralogical impact of exposure to CO_2, i.e. due to the lack of sufficiently reactive minerals present in the host rock. On this basis, we can say that CO_2-brine-rock interactions are not expected to lead to significant changes in frictional strength or in (micro)seismic potential of faults present in a CO_2 storage system, as long as the fault rock composition is dominated by minerals such as quartz, along with subordinate amounts of K-feldspar and albite.

2.5.3 Effects of carbonate precipitation on fault frictional behaviour

In the Green River area of the Colorado Plateau (UT, USA), CO_2-charged springs occur along the Little Grand Wash Fault and the Salt Wash Fault. Here, and at a number of poorly abandoned wellbores, CO_2-charged water, saturated with respect to calcite, aragonite, dolomite and hematite leached from formations below the

Entrada, leaks to the surface (e.g. see Kampman et al., 2016). As a result, multiple localised episodes of CO_2-degassing have led to extensive precipitation of aragonite, seen as cement within the leaking faults and surrounding damage zone, as well as in the form of travertine mounds at the surface, some of which date back 400 ka (Burnside et al., 2013). The SWF accordingly provides an interesting case-study for the loss of sealing integrity of a fault cross-cutting a CO_2-filled reservoir.

As shown in Table 2.1, material taken from a carbonate-filled section of the damage zone of the SWF consists of roughly equal amounts (~40 wt%) of quartz and aragonite, along with smaller amounts of calcite, dolomite, muscovite and hematite. It is not clear why aragonite preferentially precipitated over calcite, which is the more stable and less soluble polymorph of calcium carbonate (Langerak et al., 1999). Possible explanations lie in the faster precipitation kinetics of aragonite (e.g. Burton and Walter, 1987), together with the high supersaturation of the degassing fluid and high concentrations of Mg^{2+} and Fe^{2+} (Kampman et al., 2014), which inhibit calcite precipitation (e.g. Burton and Walter, 1987; Herzog et al., 1989).

As far as we are aware, no previous data exist on the frictional behaviour of aragonite-rich gouge materials, such as that investigated here. The present data therefore provide a new and useful contribution to understanding the frictional behaviour of faults in CO_2 storage systems that became cemented with aragonite due to leakage of CO_2-charged, Ca-saturated fluids (cf. the SWF). At room temperature conditions, the frictional strength of the fault samples that we have tested is similar to that of the quartz-dominated, sandstone-derived gouges (see Figures 2.2a and b). The friction coefficient of 0.57 to 0.66 displayed by the dry, carbonate-rich samples is intermediate between that of simulated quartz (μ = 0.5-0.7) and calcite gouges (μ = 0.6-0.8) (Carpenter et al., 2016; Morrow et al., 2000; Shimamoto and Logan, 1981; Verberne et al., 2014b), and very similar to the values obtained for our unexposed and CO_2-exposed quartz-dominated samples. At 100°C, both dry and wet samples of the carbonate-rich fault material showed frictional behaviour similar to that of pure calcite, as evidenced by a slight decrease in frictional strength, in agreement with experiments on calcite gouges (Verberne et al., 2014b).

In terms of (*a*-*b*) values, dry, aragonite-rich fault samples deformed at room temperature showed stable, velocity-strengthening behaviour, in agreement with results for quartz-rich gouges (Chester, 1994; Samuelson and Spiers, 2012), and for calcite gouges (Verberne et al., 2014b). This presumably reflects cataclastic deformation plus granular flow. The observed decrease in (*a*-*b*) with increasing normal stress, also seen in the quartz-dominated gouge, is again attributed to the decreasing contribution of cohesion with increasing normal stress. By contrast, at 100°C, both dry and wet carbonate-rich sample material consistently showed unstable, velocity-weakening behaviour (Figure 2.3b). This is comparable to results obtained for pure calcite gouges which exhibit a transition from velocity-strengthening to velocity-weakening behaviour at temperatures above about 80°C, as seen in Figure 2.5b (Verberne et al., 2014b). By analogy with observations on lab dry and wet calcite (Verberne et al., 2014a; Verberne et al., 2014b), the transition from velocity-strengthening behaviour at room temperature to velocity-weakening behaviour at 100°C seen in our carbonate-rich (aragonite) gouge samples is cautiously inferred to reflect an increase in the importance of time-dependent, thermally-activated plastic or else water-assisted diffusive deformation of aragonite grains. Some support for crystal plasticity can be found in previous experiments on aragonite crystals that have demonstrated the operation of such deformation mechanisms at room temperature (e.g. Kearney et al., 2006). Furthermore, pressure solution is another possible process, being enhanced relative to calcite by aragonite's higher solubility (Morse et al., 1980). Again by comparison with friction experiments on calcite (Verberne et al., 2014a; Verberne et al., 2014b) and with the model for velocity-weakening behaviour of NaCl aggregates put forward by Niemeijer and Spiers (2007), we speculate that both granular flow and crystal plastic deformation, or else diffusive mass transfer, are operative and compete in the temperature range investigated, producing velocity-weakening via the mechanisms described by Niemeijer and Spiers (2007) and by Verberne et al. (2014a).

In summary, our results for the fault-derived samples show that significant quantities (~40%) of aragonite precipitated within a fault can result on the one hand to fault re-strengthening or healing due to cementation, increasing cohesion and hence frictional strength relative to sandstone-derived gouge. At the same time, aragonite precipitation can result in velocity-weakening behaviour under in-

situ reservoir conditions (100°C) leading the potential for unstable, seismogenic slip. Of course, the occurrence of velocity-weakening behaviour might be linked to a minimum quantity of aragonite versus quartz, sufficient to form a load-bearing framework that dominates the frictional behaviour (Handy, 1990). Here, we can only infer that this threshold for velocity-weakening lies at aragonite contents below 40%.

2.5.4 Across-fault permeability of quartz-rich and carbonate-rich faults

Across-fault permeability measured at room temperature showed one to 1.5 orders of magnitude decrease during shearing, from ~10^{-15} m^2 to ~10^{-17} m^2, for both sandstone-derived gouges (Figure 2.4). The CO_2-exposed, carbonate-rich fault gouge, on the other hand, showed a smaller reduction in permeability, i.e. by a factor of 5 (cf. Figure 2.4). The sharp, initial decrease in permeability upon shearing of the sandstone-derived samples, followed by the levelling off to more or less constant permeability values, is in good agreement with the trend seen by Zhang and Tullis (1998) in their experiments on pure quartz gouges (σ_n^{eff} = 21 MPa, 10 mm displacement). This sharp decrease is inferred to be the result of shear-enhanced gouge compaction, as grain size reduction and rearrangement of grains allow for a denser grain packing (e.g. Marone and Scholz, 1989; Zhang and Tullis, 1998). The more or less constant permeability values obtained afterwards most likely reflect the transition from shear-enhanced compaction, by optimal packing of crushed grains in the body of the sample, to localisation of gouge shearing into very thin, layer-parallel shear bands (Carpenter et al., 2016; Chen et al., 2015; Verberne et al., 2014a; Zhang and Tullis, 1998). Note that shear-enhanced compaction is more effective than compressive loading (e.g. Mandl et al., 1977), explaining the slightly larger permeability reductions seen upon re-shearing than observed after periods of static holding.

From Figure 2.4, it is clear that the total reduction in cross-fault permeability for the two quartz-rich reservoir gouges is larger than for the carbonate-rich fault material. This difference is presumably related to differences in grain size reduction, compaction and localisation of shear between the quartz-rich vs. carbonate-rich gouges. However, due to the limited number of experiments conducted as well as poor preservation of the samples after removal from the

sample assembly, we do not have microstructural evidence to support any particular mechanism of permeability reduction.

Finally, comparing our across-fault permeability data for the two sandstone-derived gouges, our experiments suggest that minor mineralogical differences related to sediment variability or to long-term exposure of such materials to CO_2 will not have a major influence on the transport properties of gouge-filled faults or on how the permeability evolves with shear deformation after gouge formation associated with fault slip. Across-fault permeabilities of the order of 10^{-17}–10^{-16} m^2 can be expected in such gouges at effective normal stresses of ~50 MPa. Our results also show that reactivated aragonite-rich (cemented) fault rock can be expected to show similar permeability at comparable conditions. We also observed that across-fault permeability decreased in all sample materials predominantly because of accumulated shear, with little effect of time during periods of hold (Section 2.4.2, Figure 2.4). However, during long periods of static healing under geological conditions, time-dependent, thermally-activated compaction and sealing processes will likely lead to lower permeabilities developing after fault slip then seen in our gouge shearing tests at room temperature.

2.5.5 Implications for fault integrity in sandstone CO_2 storage systems

2.5.5.1 Effects of CO_2 exposure on fault strength and slip stability

Understanding the frictional behaviour and transport properties of faults, bounding or within a reservoir, plays an important role in assessing the integrity of potential CCS sites. Our results have demonstrated that faults formed in quartz-rich sandstones (58-90% quartz) and filled with gouges of sandstone composition can be expected to show stable, velocity- strengthening sliding behaviour with an apparent friction coefficient of 0.5-0.6 under in-situ conditions. Even after long-term CO_2-exposure and gouge bleaching, the frictional strength and velocity dependent behaviour of such faults is not affected significantly, as CO_2-induced mineralogical changes are minimal due to the limited reactive mineral content of quartz-rich sandstones. Indeed the effects of reaction with CO_2, and of the associated bleaching, on rock mineralogy will often be subordinate to variations in initial composition. However, if extensive calcite or aragonite precipitation has occurred, in a leaky, degassing fault for example, then potential exists for increased cohesive strength upon slip and for unstable sliding at in-situ temperatures of >80-

100°C, both dry and in the presence of fluids. Apparent friction coefficient values in such carbonate-rich fault rock lie in the range 0.6-0.7. Extensive precipitation of carbonate minerals, as observed along the SWF, is unlikely to occur by simple CO_2 leakage from a CCS site, as large volumes of Ca-rich fluids would have to pass along the fault. However, there may be implications for carbonate-rich faults that are present within the field prior to CO_2 injection. Assuming a geothermal gradient of 20-25°C/km, carbonate-rich fault gouges can be expected to become velocity-weakening at depths > 3-4 km, and in the framework of RSF modelling then have the potential to exhibit enhanced (micro)seismicity compared with purely clastically-derived gouges, when actively slipping.

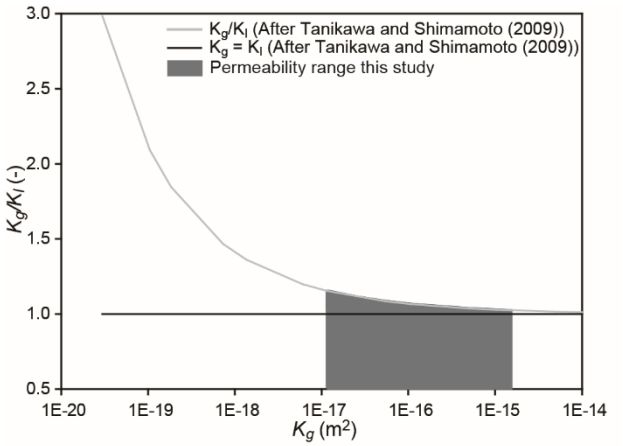

Figure 2.6. Argon gas/liquid permeability ratio to liquid permeability calculated for the conditions used in our permeability tests using the relation suggested by Tanikawa and Shimamoto (2009). The K_g/K_l line is plotted for the mean pore pressure of 1.9 MPa used in our experiments. Based on the relation derived by Tanikawa and Shimamoto (2009), liquid permeability values for our samples are expected to be a maximum of 1.2 times lower than obtained for our argon gas permeability values. Our gas permeability values can therefore be taken as a good approximation for true permeability.

2.5.5.2 Permeability evolution within an active fault

Although limited, our room temperature across-fault permeability data showed a roughly two order of magnitude decrease in permeability over only a few mm of shear displacement. These findings suggest that while fault slip may lead to initial dilational cataclasis and a significant increase in permeability, as new fault gouge is produced, this will be rapidly reduce with on-going displacement. Such faults may even become more of a barrier than a conduit with increasing shear displacement.

Similarly, mature faults are assumed to have a (well-developed) internal foliation, and as a result a relatively low starting permeability and more limited potential for compaction or dilation than observed in this study. Slip of such faults will likely cause little change in permeability. What is apparent from our data is that gouges derived from the rather different simulated gouges tested show evolution to a cross-fault permeability of between 10^{-17}–10^{-16} m^2 within 2-7 mm of shearing. This suggests a likely upper bound for the transverse permeability of reactivated faults in sandstone reservoir systems.

One last point that should be noted, is that there may be a discrepancy between our argon permeability values and the cross-fault permeability to other fluids. The permeability of a porous medium represents a property that depends on material properties such as porosity, pore shape and pore size distribution. Therefore, permeability is a property of the porous medium itself, independently of fluid properties (Klinkenberg, 1941; Tanikawa and Shimamoto, 2009). However, especially at low permeability ($\kappa < 10^{-18}$ m^2), gas permeability values are generally higher than liquid permeability values (Faulkner and Rutter, 2000; Klinkenberg, 1941; Tanikawa and Shimamoto, 2009). This phenomena is known as the Klinkenberg effect and reflects the difference in interaction between gasses and liquids with the pore-walls. In the case of liquids, a thin layer of molecules adsorbs to the pore-walls, having zero velocity, whereas as in the case of gases, molecules slip along the pore-walls with a non-zero velocity, yielding higher permeability values. The relationship between the gas and liquid permeability of a medium is given by Tanikawa and Shimamoto (2009):

$$\kappa_g = \kappa_l [1 + b/P_f] = \kappa_l [1 + (0.15\kappa_l - 0.37/P_f)] \quad (2.3)$$

where κ_g is the gas permeability (m^2), κ_l is the liquid permeability (m^2), b is the Klinkenberg slip factor (Pa) and P_f is the pore pressure, defined as $½(P_{upstream} + P_{downstream})$ (Pa). Tanikawa and Shimamoto (2009) assumed that the b-factor they obtained for their experiments on sandstone samples is applicable to all rocks. Using Equation (2.3) and putting $b = 0.15\kappa_l - 0.37$ (following Tanikawa and Shimamoto 2009), we derived the liquid permeability expected for our samples. The results are plotted in Figure 2.6 in terms of a graph of κ_g/κ_l vs. κ_g. As seen, Equation (2.3) predicts that gas permeability measurements made under the conditions of our tests are expected to be a maximum factor of 1.2 higher than

liquid permeability values over the range of conditions investigated. On this basis, we consider our gas permeability values for the simulated Entrada Sandstone and carbonate-rich fault gouges equally valid for CO_2-charged pore water, liquid CO_2 and supercritical CO_2, as for gaseous CO_2 or argon, assuming there are no chemical reaction effects during flow-through. It should be noted that this minor impact of the Klinkenberg effect on across-fault permeability may be overprinted by larger-scale variations along the fault plane, which should be kept in mind when using these values for upscaling to the reservoir scale.

Finally, we note that we did not determine the along-fault permeability. While the cross-fault permeability is important for controlling lateral leakage of CO_2 from a storage reservoir, the along-fault permeability will generally control any potential leakage to overlying formations. Though the cross-fault permeability is generally one to 1.5 orders of magnitude lower than the along-fault permeability (Zhang et al., 1999), it should be kept in mind that with the current injection regulations the pressure within the reservoir will be lower than the pressure in the directly overlying formation (e.g. Marston, 2013; Verdon et al., 2013). The pressure gradient will therefore inhibit leakage up the fault, and fault leakage will rather result in fluids being transferred from the overlying rock into the reservoir.

2.6 Conclusions

We have performed direct shear experiments on simulated gouges derived from 1) unexposed Entrada Sandstone, 2) CO_2-exposed Entrada Sandstone and 3) carbonate-rich fault rock (40% aragonite) obtained from a CO_2-leaking/degassing fault cutting the Entrada Sandstone. The Entrada Sandstone is considered to be a good analogue for many European sandstone reservoirs considered or used for CO_2 storage. Our findings can be summarised as follows:

1) Long-term CO_2-exposure and gouge bleaching does not affect the frictional behaviour of faults significantly, as CO_2-induced mineralogical changes are minimal due to the limited reactive mineral content of quartz-rich sandstones. Simulated gouges derived from both unexposed and CO_2-exposed, Entrada Sandstone showed apparent friction coefficients typical for quartz-bearing gouges (μ = 0.50-0.70). Furthermore, the Entrada Sandstone show stable (non-seismogenic) slip behaviour prior to exposure, and remains to exhibit stable, velocity-strengthening behaviour

after CO_2-exposure, under dry and wet conditions at room temperature and 100°C. At low effective normal stresses (<25 MPa), cohesion played a significant role in controlling the shear strength of the gouge, meaning that the estimated injection pressure, and hence storage capacity, can be somewhat higher than simply expected from frictional behaviour at low effective normal stresses acting on the fault plane.

2) Simulated gouges derived from the carbonate-rich fault rock exhibited apparent friction coefficient values similar to the quartz-rich gouges (μ = 0.56-0.9). Although unlikely to occur by slow CO_2 leakage from a CCS site, if extensive calcite or aragonite precipitation would occur in a leaky, degassing fault, then the potential exists for a transition from stable sliding behaviour (room temperature, dry conditions) to velocity weakening, and hence unstable or seismogenic slip, at in-situ temperatures of > 80-100°C, both dry and in the presence of fluids. Carbonate cementation will also likely increase cohesive strength upon fault slip, especially at low σ_n^{eff} (<25 MPa).
3) Argon gas permeability measurements on dry, unexposed and CO_2-exposed Entrada showed κ- values on the order of ~10^{-15}-10^{-16} m^2 prior to shear, decreasing to ~10^{-17} m^2 after 7 mm of displacement. The gas permeability values for the simulated Entrada Sandstone and carbonate-rich fault gouges are equally valid for CO_2-charged pore water, liquid CO_2 and supercritical CO_2, as for gaseous CO_2 or argon, assuming there are no chemical reaction effects during the flow through. However, larger-scale variations along the fault plane, which should be kept in mind when using these values for upscaling to the reservoir scale.

Acknowledgements

This research has been carried out in the context of the CATO-2-program. CATO-2 is the Dutch national research program on CO_2 Capture and Storage technology (CCS). The program is financially supported by the Dutch government (Ministry of Economic Affairs) and the CATO-2 consortium parties. We thank Dr. Niko Kampman (Shell Global Solutions) for providing the sample material and Shell Global Solutions (Rijswijk, the Netherlands) for the allowance to publish this study. EB thanks Shell Global Solutions for providing funding for the research. ARN was funded by

European Research Council starting grant SEISMIC (335915) and by the Netherlands Organisation for Scientific Research (NWO) through a VIDI grant (854.12.011). Eimert de Graaff, Gert Kastelein and Peter van Krieken are thanked for their technical support.

Supplementary Material

S2.1 Direct shear experiments

S2.1.1 Deformation apparatus

The deformation apparatus consists of an externally-heated main pressure vessel, with silicone oil as the confining medium, linked to an auxiliary pressure-compensation vessel (Hangx et al., 2010; Peach, 1991) – see

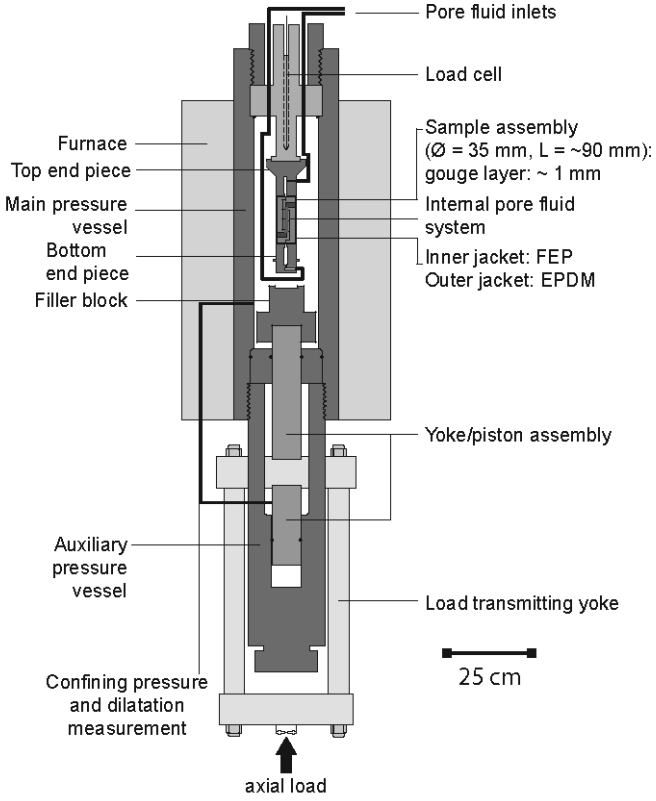

Figure S2.1. Load is transmitted to the sample using a yoke/piston assembly, which is driven by a motor/gearbox/ball-screw system. The main and the auxiliary vessels are directly connected, allowing confining fluid to be displaced from the main vessel into the auxiliary vessel, and vice versa, maintaining the total system volume

nominally constant when the yoke/piston assembly advances to load the sample. During deformation, confining pressure (P_c) is maintained at the desired value using a servo-controlled volumometer pump (resolution ± 20 µl) and is measured using a pressure transducer (100 MPa range, resolution ± 0.02 MPa; Jensen©). All dynamic and static seals consist of Viton O-rings.

Axial load is measured using a DVRT-based, semi-internal load cell, located at the top of the main vessel (DVRT = Differential Variable Reluctance Transformer; 400 kN range, resolution ± 0.035 kN). Displacement of the advancing piston is measured using a high precision LVDT (Linear Variable Differential Transformer; 100 mm range, resolution ± 0.8 µm), located externally at the yoke. Temperature is controlled using a process controller (400°C range, accuracy ± 0.1°C, precision ± 0.02°C) and sample temperature is measured at two locations, the outer surface of the jacketed sample and the sample loading frame, using K-type (chromel/alumel) thermocouples (Rössel©).

Pore fluid can be introduced into the sample via two ports in the load cell block using stainless steel tubes connected to inlets at the top and bottom of the sample

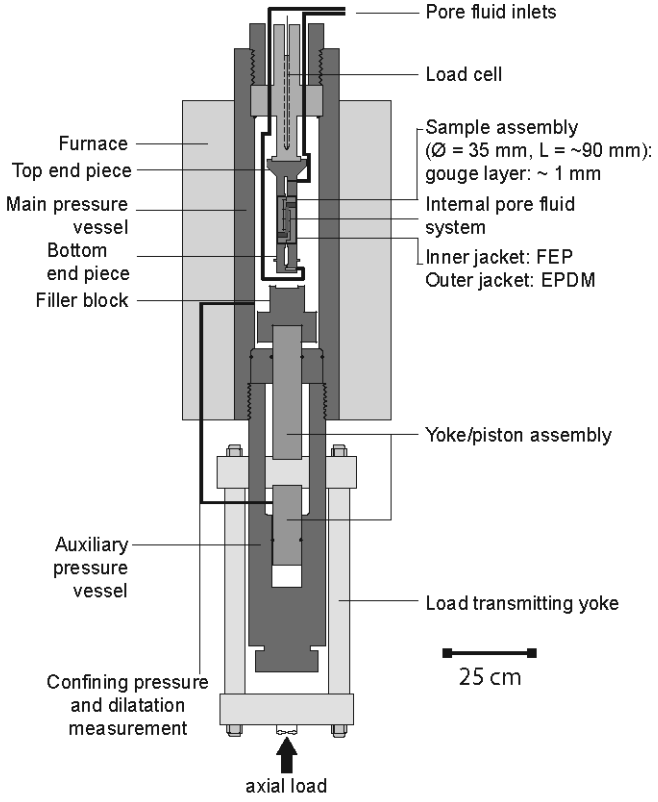

assembly (**Figure S2.1**). In the solution-flooded experiments, a constant pore fluid pressure was applied using a servo-controlled volumometer pump, equipped with a linear potentiometer to record pore volume changes. Pore fluid pressure was measured using a second pressure transducer (50 MPa range, resolution ± 0.02 MPa; Jensen©).

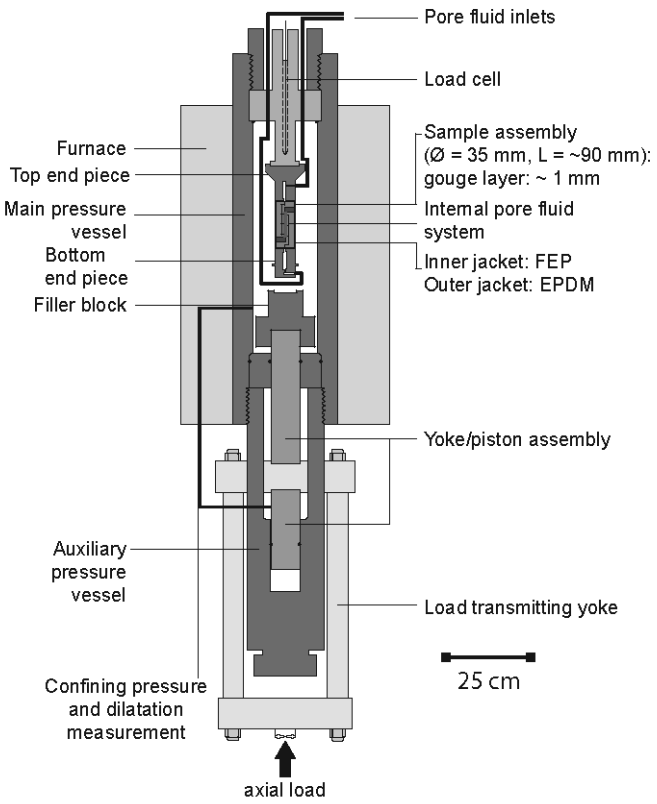

Figure S2.1. Schematic diagram of the triaxial deformation apparatus used in the present study (modified after Hangx et al. (2010)).

S2.1.2 Sample assembly

In preparing individual 'gouge' samples for testing, the powdered starting material was mixed with distilled water to create a paste (~3 g solid, 1 ml water), which was then evenly distributed to form a 1 mm thick layer on the sliding surface of one of the grooved shear blocks constituting the two halves of the direct shear assembly (grooves 60 µm deep, 120 µm wide and 200 µm apart – see Figure S2.2). Each of the two shear blocks is equipped with a porous stainless steel plate (permeability > ~10^{-14} m^2) to allow pore fluid access to the sample. To aid in confining the sample layer, thin bars of indium (1 mm by 1 mm by 35 mm) were placed at both ends of the sample layer, resulting in effective sample layer dimensions of 47 mm by 35 mm by ~1 mm. The contribution of the indium bars (melting point 153°C) to the mechanical strength of the sample material is negligible under the experimental

conditions used here (Samuelson and Spiers, 2012). For experiments conducted under lab- dry conditions, the gouge layer was then dried in a standard laboratory oven prior to assembly. The gouge layers prepared for fluid-flooded experiments were used as prepared, without any drying.

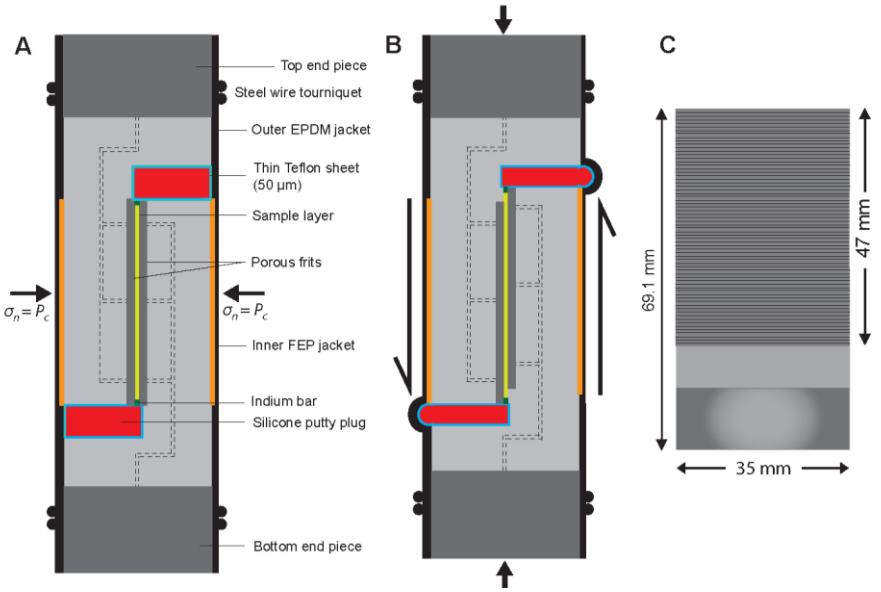

Figure S2.2. Schematic representation of the inverted shear assembly. a) Pre-shear schematic of inverted shear blocks (grey), fluid distribution frits (dark grey), internal pore fluid system (dashed lines), gouge layer (yellow), indium bars (green), FEP inner jacket (orange), EPDM outer jacket (black), and silicone putty plugs (red). The blocks are assembled with a relative offset, creating gaps filled with the silicone plugs, to provide space for the necessary displacement distance. Between the two pistons a ~ 1mm thick simulated gouge layer is sandwiched. b) Post-shear configuration of the inverted shear blocks. Note that during the experiment, the silicone putty (wrapped in teflon sheets - light blue) becomes compressed and extrudes. c) Schematic drawing of the active face a shear block, showing the toothed porous frit which grips the sample (modified after Samuelson and Spiers, 2012).

After preparation, the second shear block was placed in contact with the sample, sandwiching it as shown in Figure S2.2a and leaving a 10 mm gap at both ends of the gouge layer. These gaps are were lined with Teflon foil (50 µm) and filled with soft silicone polymer ('silly putty') plugs. Note that the indium bars prevent contamination of the gouge sample by polymer intrusion during the experiment. Once assembled, the shear blocks plus sample and polymer plugs form a 35-mm diameter cylinder, which is then sealed by heat-shrinking on a 0.45 mm thick

fluorinated ethylene propylene (FEP) sleeve. The whole is then covered by a 1.4 mm thick, EPDM outer jacket, which extends over the cylindrical end pieces of the shear blocks, and is sealed against the top and bottom end pieces using wire tourniquets. Following Samuelson and Spiers (2012), the load supported by the FEP and EPDM sleeves and the polymer during the axial loading of the sample assembly is assumed to be negligible.

S2.2 Experimental procedure

After sealing, and subsequent vacuum-saturation when using a pore fluid, the sample assembly was emplaced in the pressure vessel (

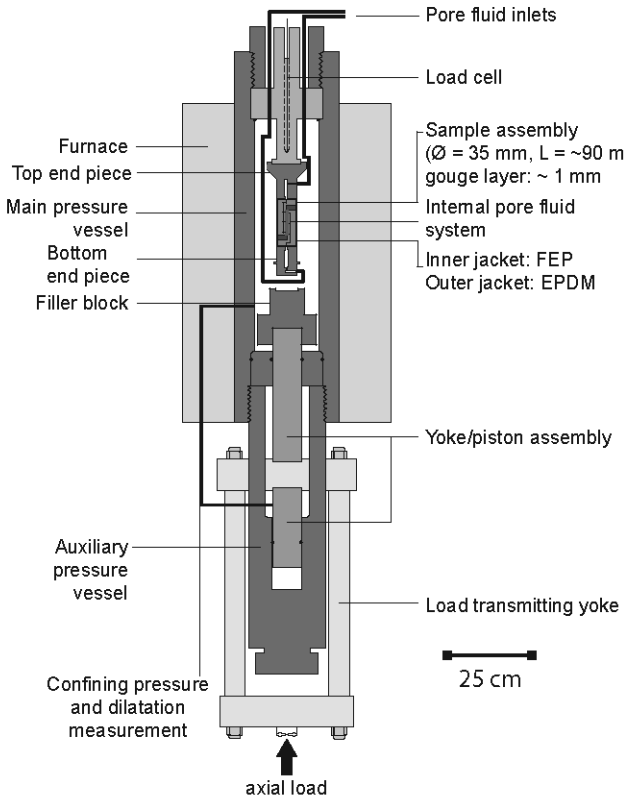

Figure S2.1) and a confining pressure was applied. Given the configuration of the direct shear assembly (Figure S2.2), the applied normal stress (σ_n) is always equal to the confining pressure on the sample. For tests at elevated temperature, the

apparatus was then brought to the desired temperature (taking ~4 hours to reach 100°C), maintaining the confining pressure below the target value. After heating, the confining pressure was adjusted to that value. In wet experiments, the pore pressure was applied before heating, ensuring that the effective pressure was never higher than the targeted values. After the desired confining and pore pressure conditions were achieved, the system was left to mechanically and thermally equilibrate for ~2 hours.

Following equilibration, the loading ram was advanced and brought into contact with the sample. Upon further advancement, a shear stress is imposed on the gouge layer and sliding is initiated. During each direct shear experiment a velocity-stepping sequence was adopted to investigate the velocity-dependence of friction of the three types of simulated fault gouges. Each velocity-stepping sequence consisted of five imposed velocity steps, following a run-in stage at a velocity of ~5.5 µm/s maintained over ~1.6 mm of displacement. This was followed by a velocity down-step, to 0.22 µm/s, after which the velocity was increased to 1.1 µm/s and 11 µm/s. Subsequently the sliding velocity was reduced back to 1.1 µm/s and 0.22 µm/s. Each shear velocity was maintained for a sliding distance of up to 0.7 mm.

Upon reaching steady-state during the last velocity step, each experiment was terminated by halting and reversing the loading ram at a velocity of 2.0 µm/s, until the sample was fully unloaded. Where used, the pore fluid pressure was then removed, followed by removal of the confining pressure. In tests at elevated temperature, the furnace was then switched off and the apparatus left to cool to ~50°C. Finally, the sample assembly was extracted from the apparatus and the sample removed and impregnated. Unfortunately, the samples were so fragile that they proved impossible to preserve for further analysis.

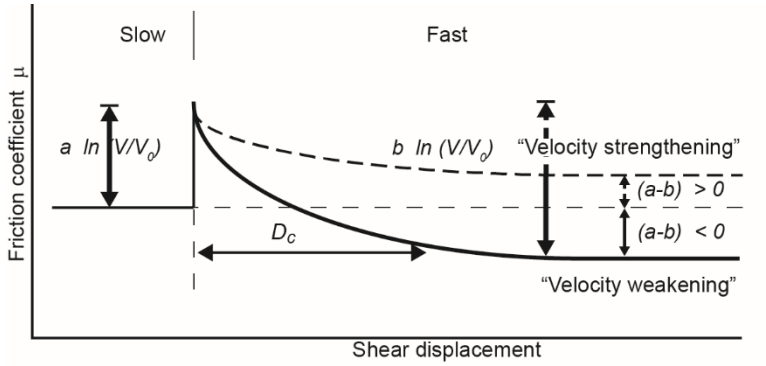

Figure S2.3 Frictional response to an instantaneous imposed velocity increase from V_0 to V. Friction typically increases by an amount "a ln (V/V_0)", upon a velocity increase, which is known as the direct velocity effect. This initial increase in friction is followed by an evolutionary decrease, of magnitude "b ln (V/V_0)".

S2.3 Data acquisition and processing

In all of our direct shear experiments, internal axial load, piston displacement, confining pressure and sample temperature were logged every 2 s using a 16-bit NI A/D converter and Labview VI Logger system. The raw data was processed to obtain the shear stress (τ) versus shear displacement (x), accurately correcting the displacement data for apparatus distortion using pre-determined, polynomial stiffness calibrations. Using the present direct shear assembly, the shear stress is equal to the internal axial load divided by the contact area of the shear surface, which is assumed to remain equal to the initial contact area. From the shear stress and the normal stress, the apparent coefficient of friction μ was calculated as $\mu = \tau/\sigma_n^{eff}$, in effect including any minor cohesion effects in μ (cf. den Hartog et al., 2013). For the sake of simplicity, we will refer to μ as the friction coefficient.

The slip rate-dependence of μ, obtained from the velocity-stepping shear experiments, was analysed using the rate-and-state friction (RSF) approach (Marone, 1998). Giving steady-state sliding at velocity V_0 and at a friction level μ_0,

then upon an instantaneous step in sliding velocity from velocity V_0 to $V = exp\ V_0$ (

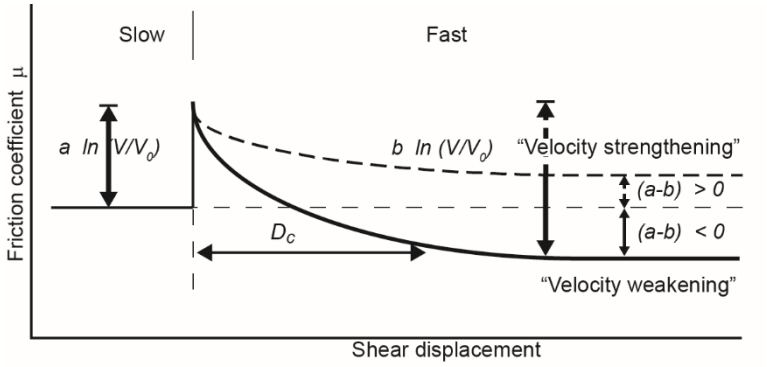

Figure S2.3), a direct change in friction generally occurs in the same direction as the velocity-step, which in the RSF approach is quantified using the parameter *a*, i.e. taking the direct effect as having magnitude $a\ ln\ (V/V_0)$. This direct effect is followed by an evolutionary drop in the friction coefficient to a new steady-state value, quantified through the parameter *b* and having magnitude $b\ ln\ (V/V_0)$. At steady-state, the friction coefficient is accordingly described by the following relation, adopting the Dieterich-type evolution formulation ('slowness law') (Dieterich, 1978; Dieterich, 1979):

$$\mu = \mu_0 + a \ln\left(\frac{V}{V_0}\right) + b \ln\left(\frac{V_0\theta}{D_c}\right), \text{ with} \qquad \frac{d\theta}{dt} = 1 - \frac{V\theta}{D_c} \qquad \text{(S2.1)}$$

Here, θ is a gouge state variable and D_c reflects the characteristical sliding distance required to reach the new steady-state value following a velocity-step. As a result, a finite change in steady-state friction ($\Delta\mu_{ss}$) for a change in velocity is defined by the parameter (*a*-*b*), given as (Marone, 1998; Scholz, 1998):

$$(a\text{-}b) = \frac{\partial\mu}{\partial \ln V} \approx \frac{\Delta\mu_{ss}}{\Delta \ln V} \qquad \text{(S2.2)}$$

If (*a*-*b*) is positive, the friction coefficient increases with increasing velocity, which is known as 'velocity-strengthening' behaviour. This implies that the system is inherently stable and that the accelerating slip needed for seismogenesis cannot occur (Scholz, 1998), at least within the RSF approach to quantifying friction. 'Velocity-weakening' behaviour occurs if (*a*-*b*) is negative, which means that friction decreases with increasing velocity. In this case, the system is potentially unstable (Scholz, 1998), i.e. able to produce repetitive stick-slip events or seismogenic slip

provided that the elastic stiffness of the loading system falls in the right range (e.g. Scholz, 2002). In this study, individual values for a, b and d_c values were obtained by fitting Equation (S2.1) to the μ vs. x data obtained in our velocity-stepping experiments using Xlook, which is a rate and state friction modelling program, kindly made available by C. Marone at Penn State University. As such, the RSF approach can only be applied to steady-state friction behaviour, therefore we applied the de-trending procedure for μ vs. x curves as described by Blanpied et al. (1998) when our data showed minor slip-strengthening or weakening.

S2.4 Permeametry experiments: apparatus and data acquisition

'Across-fault' permeability (κ) measurements were performed on dry samples, at room temperature, using argon gas permeametry (Figure S2.4) previously described by Hangx et al. (2010) and Peach (1991) and employing the transient-step method. This method is based on measuring the decay of a pore pressure difference imposed suddenly across the sample (Sutherland and Cave, 1980). The permeametry set-up consists of two symmetrical, low-volume tube/valve systems, located up- and downstream of the sample. These can be pressurised independently at pressures up to 2 MPa (Figure S2.4), thus allowing for the application of a pressure difference across the sample assembly and gouge layer, following pre-equilibration at a uniform pressure. In this set-up, the argon pressure was measured at each end of the sample, at the entrance of the pore pressure lines to the triaxial pressure vessel, using a high-precision pressure transducer (2 MPa range, ± 0.001 kPa resolution; Keller©). To avoid argon flow between the sample assembly and the jacket, the applied confining pressure was always maintained higher than the argon pressure.

Permeametry was carried out before, during and after shear using the same direct shear and velocity-stepping procedure as described above. However, in these experiments a slide-hold-slide approach was also used. The approach adopted involved sequential repetition of shear at a sliding velocity of ~5.4 µm/s, followed by shear at a sliding velocity of ~0.5 µm/s, followed by a 'hold' period in which the piston was halted. In order to systematically investigate the effect of sliding and re-sliding on permeability, permeability measurements were made prior to shear,

during active shear (at a sliding velocity of ~0.5 µm/s) and at the end of the hold periods. This alternation of shearing and holding was performed for hold periods of 300, 1000 and 3000 seconds. Experiments were terminated with a final permeability measurement made after a final hold.

In preparation of the permeametry experiments (T = 20˚C, σ_n^{eff} = 50 MPa), each dry sample was evacuated within the triaxial testing machine at approximately 1 MPa confining pressure, for up to 60 minutes. After evacuation, the confining pressure was increased to 52 MPa and the argon pore pressure to 2 MPa. The latter was then allowed to equilibrate throughout the sample and the up- and downstream portions of the argon system. Following equilibration, the downstream part of the permeability apparatus was isolated from the sample and from the upstream part, using valves A and B (see Figure S2.4). The pressure in the downstream system was then lowered by 0.2 MPa, and, after stabilisation, reconnected to the upstream part via the sample, by opening valve B. This results in a nearly instantaneous pressure difference across the sample, leading to argon gas flowing through the sample from the upstream to the downstream reservoir. The argon pressure signals measured at each end of the sample were logged using a NI 16-bit A/D converter and Labview VI Logger software. Across-fault permeability κ was calculated by analysing the decay of the pressure difference across the sample, using the method described by Sutherland and Cave (1980). Note that a very small background leakage of the argon permeameter prevented accurate measurements of sample permeabilities less than ~10^{-21} m^2 (Hangx et al., 2010).

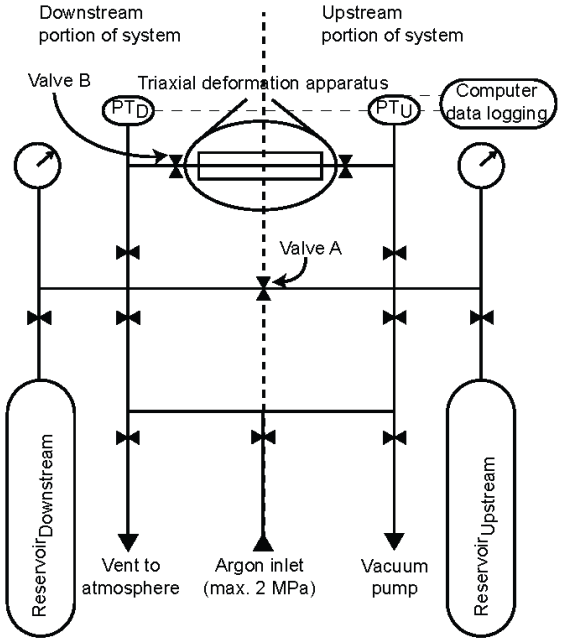

Figure S2.4. Schematic representation of the argon permeameter set-up used in this study in conjunction with the triaxial deformation apparatus.

Chapter 3

Anisotropic transport and mechanical properties of simulated clay-rich fault gouges

Elisenda Bakker and Johannes H.P. de Bresser

Abstract

We aimed to evaluate various factors that control the frictional and transport properties of gouge-filled faults cutting carbonate-bearing shale or claystone formations. The research experimentally determined i) the effect of shear displacement, dynamic shearing, static holding, and effective normal stress on fault gouge permeability, both parallel and perpendicular to the fault boundaries, and ii) the effect of calcite removal by dissolution on the frictional strength and stability of a simulated clay-rich gouge. The simulated gouge was prepared from crushed Opalinus Claystone (OPA). A second batch of simulated gouge was prepared from which the natural carbonate was dissolved (Calcite-Free or CFOPA). Two types of direct shear experiments were performed. The first set of direct-shear experiments (σ_n^{eff} = 5-50 MPa, P_f = 2 MPa, and $T \approx$ 20°C) showed ~1 order of magnitude decrease in permeability with shear displacement (up to ~6 mm), for both along- and across-fault fluid flow orientation. Moreover, our data showed an initial, pre-shear permeability anisotropy of up to ~1 order of magnitude, which decreased with increasing shear displacement (maturity) to <0.5, with the along-fault permeability being consistently higher. The second set of experiments (σ_n^{eff} = 50 MPa, P_f = 0 or 25 MPa, and $T \approx$ 20-60-100-120-150°C) showed stable, velocity-strengthening behaviour for the OPA gouge. The removal of calcite (CFOPA) resulted in a 10-20% reduction in friction coefficient, while remaining to exhibit velocity-strengthening behaviour. Overall, our results have important implications for calcite-rich claystones and shale formations, and in particular any pre-existing faults therein, that seal hydrocarbon reservoirs and potential CO_2 storage reservoirs, as the current results point to a higher leakage potential of pre-existing faults compared to the intact caprock. In addition, the frictional data shows that the frictional strength of a clay-quartz-calcite fault gouge is reduced following calcite dissolution, but is expected to exhibit velocity-strengthening behaviour.

3.1 Introduction

In ambition to lower anthropogenic CO_2 emissions, Carbon Capture and Storage (CCS), the capture of CO_2 at large point sources followed by injection into geological formations, e.g. hydrocarbon reservoirs or aquifers, is one of the remaining potential methods to mitigate anthropogenic CO_2 emissions on a relatively large scale. However, CCS is only a viable option when the long-term sealing integrity of the storage complex, i.e. the reservoir and overlying caprock, can be maintained. Many of the geological storage reservoirs considered for CO_2 storage are hydrocarbon reservoirs capped by clay-rich formations, such as the Kimmeridge Clay overlying the Brae Formation of the Miller and Brae fields (Scottish North Sea (Haszeldine et al., 2006)), the Röt or Solling Formations overlying the Triassic Hardegsen (Upper Bunter) Sandstone formations of the P-18 gas field (Dutch North Sea (Samuelson and Spiers, 2012)), and the Tournasian-Viséan mudstones overlying the Carboniferous Tournasian Sandstone unit of the Krechba gas field (Algeria (White et al., 2014)). These clay-rich formations are known to be low permeable rocks (e.g. Armitage et al., 2011; Ingram and Urai, 1999; Neuzil, 1994) and have proven capacity of structurally trapping hydrocarbons on geological time scales, hence for far longer than required for anthropogenic CO_2 storage. However, the potential storage complexes are usually intersected, compartmentalised or bounded by through-going brittle faults. Such faults may represent preferential, naturally occurring, leakage pathways for CO_2 during and after injection (e.g. Cappa and Rutqvist, 2011; Hawkes et al., 2005). The integrity of CO_2 storage complexes is therefore critically dependent on the sealing capacity and strength of caprock penetrating faults (Knipe et al., 1998).

Brittle fault zones, and specifically clay-rich ones, are structurally anisotropic and lithologically heterogeneous by nature (Caine et al., 1996; Faulkner et al., 2010; Faulkner and Rutter, 1998). These clay-rich fault zones are typically characterised by aligned clay minerals, which are known to weaken the frictional strength of the gouge material and more importantly, in relation to potential CO_2 storage, to significantly reduce the gouge permeability to as low as 10^{-22} m^2, making the fault zone relatively impermeable (Crawford et al., 2008; Takahashi et al., 2007). As such, many faults filled with clay-rich fault gouge have proven to be efficient seals, acting as structural barriers to across-fault fluid flow (Faulkner and Rutter, 1998; Takahashi, 2003). However, the internal architecture of these fault zones is usually

characterised by several distinct structural units, which actually dictate whether the fault zone will indeed act as a structural barrier, or that it behaves as a conduit or combined conduit-barrier system (Caine et al., 1996). The fault architecture usually comprises a fault core surrounded by a pervasively fractured damage zone. Most of the displacement along a fault is accommodated by the fault core, which is characteristically filled with very fine-grained wear-product, so-called fault gouge. Fault gouge is generally considered to have a low permeability, hence inhibit fluid flow (Takahashi, 2003). Contrary, the surrounding damage zone, may, due to its fractured character, enhance the fault zone permeability, depending on the fracture density and connectivity of the fractures in the damage zone (Mitchell and Faulkner, 2012). In case the fracture density and connectivity of a damage zone is such that a pre-existing fault is likely to form a leakage pathway for fluids, the sealing integrity of the caprock is considered insufficient and potential reservoirs capped by such seals should not be considered for CCS.

Over time, the sealing capacity of fault gouges from fault cores might be altered by various processes, closely related to the slip behaviour and the stability of a fault gouge. These processes may act on geological time-scales and/or human time-scales. Processes that can alter the fault permeability at geological time-scales include grain size reduction and gouge compaction, as well as dilation. Under static conditions (i.e. unmoving), a fault gouge may exhibit a low permeability, especially when high normal stresses act on the fault plane (Faulkner and Rutter, 1998). Upon slip, however, a fault gouge may dilate (permeability enhancement) or compact (permeability reduction), depending on the mechanisms controlling deformation of the gouge (Den Hartog and Spiers, 2014). Triggered by human intervention, such as CO_2 injection, the same processes that operate on geological time scales may also act on short, human time-scales. The injection of CO_2 could potentially lead to 1) a direct increase in pore pressure and associated reduction in effective normal stress acting on pre-existing fault planes, 2) a pore-elastic response of the storage system, via compaction or heave, or 3) thermal expansion or shrinkage near the well (Vilarrasa et al., 2014; Wang, 2000). As a result of the reduction of normal stress on the fault, the slip reactivation potential and the fault permeability (i.e. leakage potential), which are closely related, will reduce as well (Hooper, 1991; Wiprut and Zoback, 2000; Zoback and Byerlee, 1975). Consequently, the storage system might fail to retain the injected CO_2 in the subsurface. However, only few studies, some in

the context of CO_2 storage, have attempted to quantify the direct impact of slip-induced dilation and compaction on the permeability (Samuelson et al., 2009; Zhang et al., 2007). Furthermore, fault gouge permeability measurements have focused on measuring across-fault permeability, while leakage may not only occur from the storage reservoir to adjacent reservoirs, but also along-fault to underlying or overlying formations (Bense and Person, 2006). Such along-fault leakage may particularly play a role in CO_2 storage in aquifers where an outward pressure gradient may be established following CO_2 injection. It should be noted that for CO_2 storage, if safe injection practices are adhered to, such an outward fluid pressure gradient will be unfavourable for promoting along-fault flow.

Usually, the integrity of a gouge-filled fault is attributed to the frictional stability and sealing capacity of the fault gouge (Song and Zhang, 2013). Therefore, previous work has focused on understanding the effect of normal stress, shear displacement, sliding velocity and healing (reactivation potential) on the frictional slip behaviour as well as on understanding the effect of shear displacement on the permeability of a fault gouge (e.g. Chen et al., 2015; Ikari et al., 2009; Soltanzadeh and Hawkes, 2008). In the case of CO_2 injection, maintaining the fault integrity is even more complex due to the chemical nature of CO_2. CO_2-induced fluid-rock interactions are suggested to result in mineralogical changes that have the potential to reduce the frictional strength and stability of a fault gouge, promoting fault slip and/or induced seismicity (Samuelson and Spiers, 2012). Therefore, it is important to evaluate the impact of CO_2-induced mineralogy changes on the frictional stability of a fault gouge. Typical CO_2-induced alteration processes in clay-rich caprock compositions, following the dissolution of CO_2 into the formation brine forming acidic acid (Bachu, 1994), include the dissolution and re-precipitation of carbonates, if present, the dissolution of plagioclase, illite and chlorite, and the precipitation of smectite (Alemu et al., 2011). Generally, CO_2-induced mineralogy changes in clay-rich caprock compositions have relatively long reaction times (Hawkes et al., 2005). Consequently, on the relatively short time span relevant for CO_2 storage, only carbonate dissolution may be important. So, in a scenario in which the poro-elastic response of a CO_2 storage system results in slip reactivation and an associated increase in permeability of any gouge-filled fault cutting the clay-rich caprock, the leaked CO_2 may subsequently induce chemical processes such as the dissolution of carbonates in the fault gouge, further modifying the character of

the gouge and thereby affecting its frictional behaviour. This has been shown by extensive laboratory research (e.g. Byerlee, 1978; Lockner and Beeler, 2002; Moore and Lockner, 2004). And since the frictional behaviour and the permeability of a fault gouge are closely related, calcite dissolution may eventually affect the gouge permeability, hence enhance or reduce the sealing integrity of the fault.

In order to predict with some confidence what may happen in faults cutting the caprock of a storage system, it is thus of great importance to fully understand what factors control the frictional and transport properties of a fault gouge. In this paper, we focus on two aspects, namely i) the effect of shear displacement, dynamic shear, static holding and effective normal stress on fault gouge permeability, parallel and perpendicular to the gouge layer, and ii) the effect of calcite dissolution on the frictional strength and stability of a simulated clay-rich gouge. We report on two types of experiments, namely direct shear experiments in combination with permeability measurements, before, during and after shear, and direct shear experiments on two types of simulated clay-rich fault gouge of which one still consists of the naturally present calcite and the other is treated to dissolve the calcite, simulating the chemical effects of CO_2 exposure.

3.2 Experimental methods

We performed two types of direct shear experiments namely i) 10 direct shear experiments in combination with permeability measurements and ii) 10 direct shear experiments on two types of fault gouge composition. The first 10 experiments are conducted to investigate the effect of shear displacement (x) and fluid flow orientation on the transport (κ) and frictional properties (μ) of a simulated clay-quartz-calcite fault gouge. The additional 10 direct shear experiments are performed to investigate the effect of temperature (T) and pore fluid (P_f) on the frictional properties of a simulated clay-quartz-calcite fault gouge compared to a clay-quartz fault gouge (i.e. calcite free). To this end we performed four series of direct shear experiments on either a simulated clay-quartz-calcite fault gouge or a simulated clay-quartz fault gouge:

1) Room temperature experiments on vacuum-dried, simulated clay-quartz-calcite fault gouge material at an applied normal stress (σ_n) of 7 to 52 MPa, using argon gas as the pore fluid (P_f = 2 MPa) and making along-fault permeability measurements before, during and after shear (Data-set 1).
2) Room temperature experiments on vacuum-dried, simulated clay-quartz-calcite fault gouge material at σ_n of 7 to 52 MPa, using argon gas as the pore fluid (P_f = 2 MPa) and making across-fault permeability measurements before, during and after shear (Data-set 2).
3) Experiments on (vacuum-dried), simulated clay-quartz-calcite fault gouge material at $T \approx$ 20-150˚C and at an σ_n of 75 MPa, under different chemical environments (dry at 20°C and 120°C and wet (P_f = 25 MPa) at 20-150˚C – Data-set 3);
    a) Vacuum-dried gouge pre-dried at $T \approx$ 120°C and tested at room temperature,
    b) Vacuum-dried gouge tested at $T \approx$ 120˚C (dried in-situ)
    c) Water-saturated gouge tested at $T \approx$ 20-150°C and at an σ_n of 75 MPa, employing a pore fluid pressure of P_f = 25 MPa,
4) Experiments on simulated clay-quartz fault gouge material (i.e. calcite-free) at $T \approx$ 20-100°C and at an σ_n of 75 MPa, employing a pore pressure of P_f = 25 MPa (Data-set 4).

3.2.1 Sample material

The clay-rich material used in this study was collected from the "silty-shaly" sub-unit of the Opalinus Claystone formation, accessible via the Mont Terri Underground Rock Laboratory (URL) (Courtesy of Swisstopo, Dr. C. Nussbaum), and is described in more detail in Pearson et al. (2003). A permeability measurement conducted on an intact piece of OPA (σ_n^{eff} = 15 MPa) resulted in a permeability value in the order of 10^{-21} m^2. Simulated fault gouge was prepared by coarsely crushing small samples of Opalinus Claystone using a pestle and mortar, followed by finer grade crushing using a ball-mill. The powder was then sieved to obtain the grain size fraction <35 µm. X-Ray Diffraction analysis (XRD) performed on the powdered sample material showed that our material consists of quartz (23%), calcite (26%), pyrite (4%) and phyllosicilates (47%) (Table 3.1). We will refer to this gouge as OPA gouge hereafter. In order to test the effect of calcite content we prepared a second batch of powdered Opalinus Claystone, derived from the same block of Opalinus Claystone as used for the first batch, which we then exposed to

an excess amount of HCl (pH 0, $T \approx 20°C$) to remove any calcite present. The clay-acid mixture was subsequently heated to 80°C, while being stirred, to remove any remaining carbonates, exposing the material to the HCl for 24 hours in total. After the acid-treatment, the calcite-free Opalinus Claystone material (referred to as CFOPA) was retrieved by washing, with demineralized water, centrifuging and successively drying it in a 60°C oven for several days. After drying, the coarse CFOPA-powder was crushed and sieved to a grain size <35 µm. XRD analysis of the CFOPA material showed a composition of predominantly phyllosilicates and quartz (Table 3.1).

Table 3.1. Mineralogical composition of untreated, carbonate-bearing Opalinus, i.e. "OPA", and acid-treated, carbonate-free Opalinus, i.e. "CFOPA", simulated fault gouges given in percentages (%).[a] The uncertainty is given as the mean value of the difference in percentages of multiple batches analysed.

Mineral	Proportion in OPA (%)	Proportion in CFOPA (%)
Quartz	21	35 ± 6
Calcite	17 ± 3	-
Pyrite	2	2
Muscovite	33 ± 11	30 ± 6
Illite	23	-
Kaolinite	12 ± 1	15 ± 2
Chamosite/chlorite	7	18 ± 3

3.2.2 Deformation apparatus

The direct shear experiments described in this study were performed using a conventional triaxial deformation apparatus, comprising a pressure-compensated main vessel linked to an auxiliary vessel (Figure 3.1; Chapter 2). The externally heated, oil-filled main vessel is equipped with a specially-designed direct shear assembly, which can be loaded via a yoke/piston combination, driven by a motor/gearbox/screwball system, to apply an axial load to the sample assembly, while simultaneously keeping the system pressure nominally-constant during deformation (resolution ± 0.20 µl). During an experiment, the confining pressure, the axial load, the displacement of the advancing yoke/piston and sample temperature are measured using respectively a Jensen pressure transducer (100 MPa range, resolution ± 0.02 MPa), a DRVT-based, semi-internal load cell (DVRT =

Differential Variable Reluctance Transformer; 400 kN range, resolution ± 0.035 kN), a high precision LVDT (Linear Variable Differential Transformer; 100 mm, ± 0.8 µm) and two K-type (chromel/alumel) thermocouples (400°C, accuracy ± 0.1 °C, precision ± 0.02 °C). Sliding velocities can be changed near instantaneously, for velocities ranging between ~0.05 and 50 µm/s. The machine is described in detail in Chapter 2 and by Peach and Spiers (1996) and Hangx et al. (2010a, 2010b). Pore fluids can be introduced into the gouge layer via two stainless steel tubes, mounted in the load cell block, which are connected to inlets at the top and bottom end pistons inclosing the sample assembly (Figure 3.1). We used two different types of pore fluids, 1) argon gas (99.9% pure), and 2) distilled water. During the wet direct shear experiments a constant pore pressure was maintained using a servo-controlled volumometer pump and measured using a Jensen pressure transducer (50 MPa range, resolution ± 0.02 MPa).

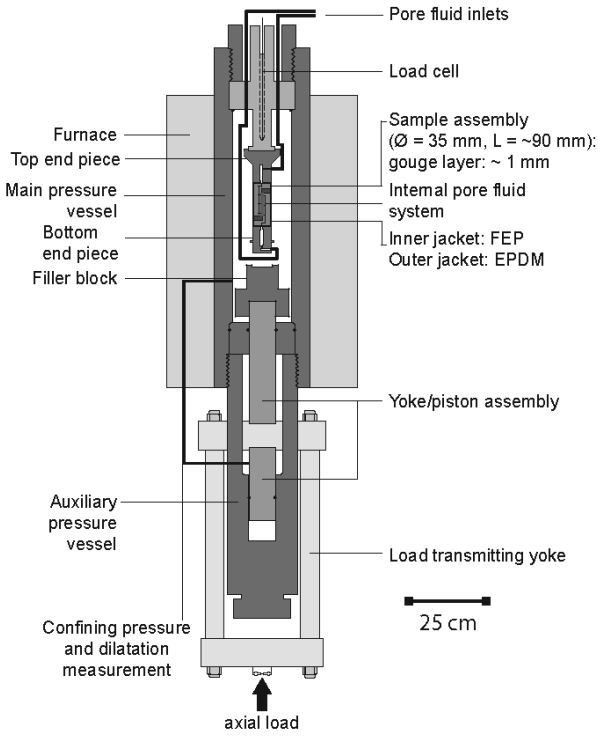

Figure 3.1. Schematic diagram of the triaxial deformation apparatus used in the present study (modified after Hangx et al., 2010).

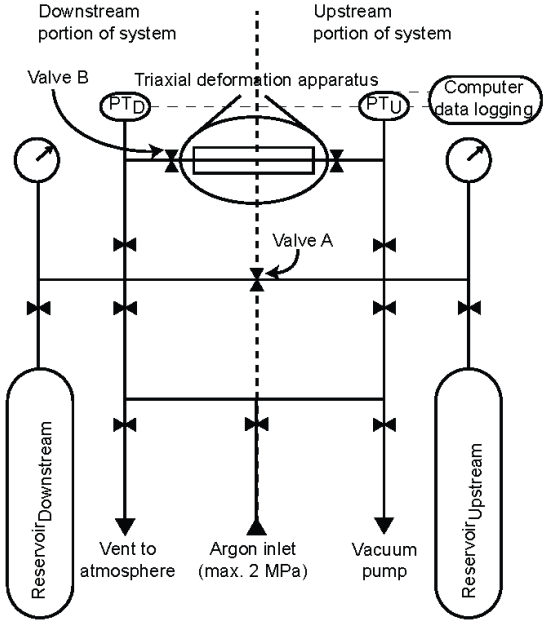

Figure 3.2. Schematic representation of the argon permeameter set-up used in this study in conjuction with the triaxial deformation apparatus.

The argon permeability (κ) of simulated fault gouge was measured using the permeameter previously described in Chapter 1 and Peach (1991) (Figure 3.2). The set-up consists of two symmetrical, low-volume tube/valve systems, located at both the up and downstream end of the sample assembly, which can be independently pressurized up to 2 MPa, as such allowing the application of a pressure difference across the gouge layer. The system may be evacuated via a vacuum pump connected to a vent valve, whereas argon, from a nearby bottle and regulator, is supplied via a second valve. To avoid argon flow between the sample assembly and the jacket, the applied confining pressure was always maintained higher than the argon pressure and the gouge layer-piston-jacket contact was taped with Teflon tape. To measure the argon permeability we logged the pressure decay across the sample following an imposed pressure difference, using two temperature-compensated pressure transducers, up- and downstream (2 MPa range, resolution ± 0.001 kPa) (Sutherland and Cave, 1980). Note, that a very small background leakage of the argon permeameter prevented accurate measurements of samples with permeabilities of less than 10^{-21} m^2 (Hangx et al., 2010a).

3.2.3 Sample assembly

For the various direct shear experiments described above we used two types of specially-designed direct shear assemblies. Both direct shear assemblies consist of two "L-shaped", direct shear blocks (Figure 3.3), constituting a 35 mm diameter cylinder when assembled. Note that given the configuration of the two inverted direct shear blocks, for both sets of direct shear blocks, the applied normal stress (σ_n) is equal to the confining pressure (P_c) and independent of the shear displacement, at all times during deformation. Each of the two direct shear blocks is equipped with a grooved (60 µm deep, 120 µm wide and 200 µm apart) shear surface (47 mm long and 35 mm wide – Figure 3.3). To allow for uniform pore fluid access to the gouge layer, via pore fluid channels connected to the tubes in the load cell block, strategically placed porous stainless steel plates (permeability >~10^{-14} m^2) were placed in the shear surface. The difference between the two sets of direct shear blocks is the location of the porous frits, and is described in more detail below.

In preparing each experiment, 3.7 g of loose simulated fault gouge was evenly distributed on the shear interface of the bottom direct shear block and pre-pressed, using a hydraulic press by loading the gouge layer two times for ~30 seconds (~60 seconds in total), at orientations 180° apart (rotation in the horizontal plane). The bottom block, with the gouge layer (dimensions: 49 mm x 35 mm x ~1 mm – cf. Figure 3.3) on top, was then covered with the upper shear block, leaving 10-mm gaps at both ends of the gouge layer. For the pre-dried experiment on OPA material (Data-set 3a), an excess amount of simulated OPA fault gouge was oven-dried overnight at 120°C prior to preparing. To avoid re-humidification of the gouge material during preparation, the gouge layer was prepared in a low-humidity room. For the experiments of Data-set 1 and 2, including the permeability measurements, the pre-pressing normal stress was chosen to be less than 6 MPa, to prevent for overcompaction. For the experiments of Data-set 3 and 4, without permeability measurements, the pre-pressing normal stress was chosen to be ~36 MPa. Both preparation methods resulted in coherent, reproducible gouge layers. The two shear blocks, forming a full cylinder and sandwiching the gouge layer, were then fixated using a heat-shrinking Fluorinated Ethylene Propylene (FEP) inner sleeve, while the 10-mm gaps were filled with 50 µm Teflon foil-wrapped Ecoflex (2-component epoxy) plugs. The whole was then placed in a 1.4 mm think Ethylene

Propylene Diene Monomer (EPDM) outer jacket, which is sealed against the upper and lower driver blocks using wire tourniquets. For the gouge layers prepared for Data-set 1 and 2, including permeability measurement, the FEP-gouge layer-pistons contact was taped off with gas tape to avoid argon flow between the sample assembly and the FEP jacket, rather than through the gouge layer. The soft Ecoflex plugs, and the FEP and EPDM sleeves are assumed to exert negligible resistance during deformation (Samuelson and Spiers, 2012). Upon jacketing, the sample assembly was attached to the loading frame, emplaced in the main pressure vessel and evacuated at a P_c of ~5 MPa, for up to ~60 minutes. After evacuation, the appropriate pore fluid was introduced.

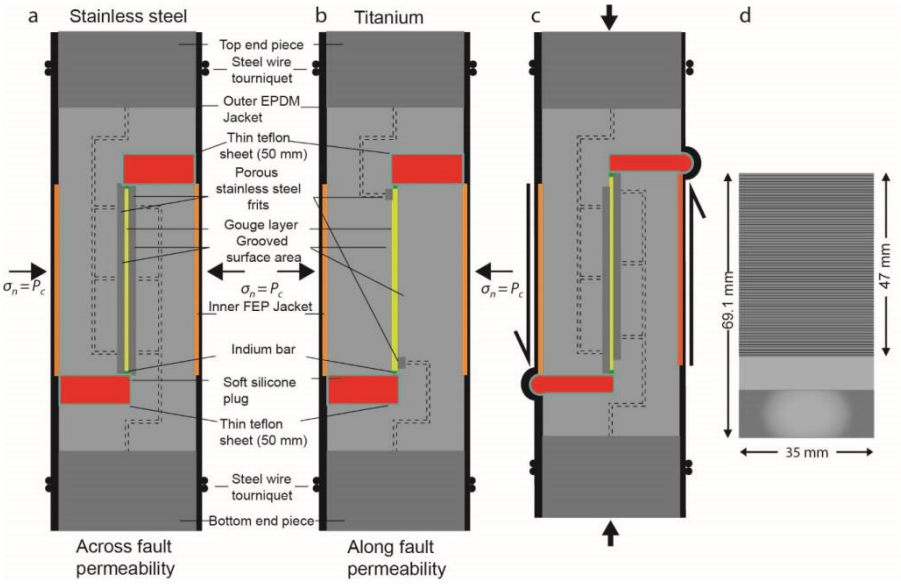

Figure 3.3. Schematic representation of the inverted shear assemblies DSB-1 (across-fault) and DSB-2 (along-fault). a) Pre-shear schematic of inverted shear blocks (grey), fluid distribution frits (dark grey), internal pore fluid system (dashed lines), gouge layer (yellow), indium bars (green), FEP inner jacket (orange), EPDM outer jacket (black), silicone putty plugs (red) and thin Teflon sheet (light blue). The blocks are assembled with a relative offset, creating gaps filled with the silicone plugs, to provide space for the necessary displacement distance. Between the two pistons a ~ 1mm thick simulated gouge layer is sandwiched. b) Post-shear configuration of the inverted DBS-1 shear blocks. Note that during the experiment, the silicone putty (wrapped in teflon sheets - light blue) becomes compressed and extrudes. c) Schematic drawing of the active face a shear block, showing the toothed porous frit which grips the sample (modified after Samuelson and Spiers, 2012).

Although the direct shear assemblies are similar for all three experiment types (Data-sets 1-4), the details of the pore fluid systems are slightly different. The direct shear assembly used to measure the across-fault permeability and the frictional strength of the OPA and CFOPA gouges (Data-set 2, 3 and 4), consist of two stainless steel direct shear blocks (Figure 3.3a – Chapter 2), each equipped with a grooved (60 µm deep, 120 µm wide and 200 µm apart) and porous stainless steel plate (frit) (effective shear surface: 47 mm long and 35 mm wide and permeability >~10^{-14} m^2 – Figure 3.3d). Uniform pore fluid access to the entire gouge layer is allowed via multiple internal pore fluid channels in the shear blocks (Figure 3.3a). We will refer to these direct shear blocks as the "across-fault permeability blocks". The along-fault permeability and frictional strength of the OPA gouge (Data-set 1) is measured with the "along-fault permeability blocks", which consists of two titanium shear blocks, each with a grooved (60 µm deep, 120 µm wide and 200 µm apart – Figure 3.3b) shearing interface. Only 2 mm of the shearing interface, at the base of each shearing interface, is porous and permeable (permeability ~10^{-14} m^2 – frit), allowing pore fluid access to the sample layer from the upper and lower extent of the gouge layer, when assembled. This configuration restricts fluid flow from one end of the gouge layer to the other end through the long axis of the sandwiched gouge layer.

3.2.4 Experimental procedure

3.2.4.1 Direct shear experiments with permeability measurements: Slide-Hold-Slide (Data-set 1 and 2)

For the direct shear experiments with permeability measurements, evacuation of the pore fluid system was followed by argon flushing before increasing the P_c to ~3-10 MPa. Then the pore fluid pressure P_f was increased to 2 MPa (using 99.9% pure argon), after which P_c was increased further to the targeted value. After applying the pre-determined P_c and P_f-conditions, the system was allowed to equilibrate for ~3 h. Subsequently, the downstream part of the permeametry set-up was isolated from the sample and the upstream part (using values "A" and "B" – see Figure 3.2), to lower the downstream reservoir by 0.2 MPa with respect to the upstream part. After stabilisation, the downstream part was reconnected to the upstream part via valve "B", to allow pore fluid flow from up to downstream, which was measured

and logged as described above. This procedure was repeated for each permeability measurement.

The permeability measurements performed in the experiments of Data-sets 1 and 2 were conducted prior to shear, during shear at a sliding velocity of 0.05 µm/s and after a period of hold (referred to as Slide-Hold-Slide (SHS) experiments). The SHS sequence was employed to investigate the effect of static holding versus dynamic shearing on the evolution of fluid flow in a clay-rich gouge layer. The amount of sliding during a permeability measurement depended on the time required to reach full argon decay. In case full decay was reached within <2 hours, (for relatively "high" permeability samples or short path lengths), sliding was continued until full decay was reached, however, if full decay was reached in >12 hours ("low" permeability samples or long path lengths), the permeability measurement and sliding were terminated after 4.5 hours of decay.

A "regular" experiment was typically initiated with measuring the initial permeability (κ_i), prior to sliding, followed by a run-in at ~5.4 µm/s. Upon reaching steady-state sliding (at ~2 mm), the velocity was reduced to 0.05 µm/s. Once stable sliding was established (after ~0.02 mm), a dynamic permeability measurement was initiated. Upon full argon decay, the piston was arrested for ~12 h, after which the static permeability was measured. Shear was re-induced (at ~5.4 µm/s), reaching steady-state shearing after ~ 0.7 mm, before reducing the sliding velocity to 0.05 µm/s. At steady-state (after ~0.02 mm), the dynamic permeability measurements was conducted. Subsequently, the piston was halted for ~1 hour before the static permeability was measured. The experiments were terminated by subsequently halting and reserving the loading ram at a velocity of 2.0 µm/s until the sample was fully unloaded. Next, the pore fluid was removed, followed by removal of the confining pressure, after which the sample assembly was extracted from the apparatus.

Following the regular experiments, as described above, the 5 and 25 MPa along-fault samples (Data-set 1) were sheared for an additional velocity-stepping sequence, sequential to the SHS sequence. Upon the last static permeability measurement, shear was again induced at ~5.4 µm/s (for ~0.7 mm), and reduced to 0.05 µm/s (for ~0.02 mm). This procedure was repeated for a reduced sliding

velocity of 0.1 µm/s, 0.5 µm/s and 1.0 µm/s after which the experiments were terminated and unloaded.

In addition to the regular SHS experiments, supplementary experiments were conducted to investigate the effect of hold time on the gouge permeability and frictional strength. These experiments were initiated with an initial permeability measurement, followed by a run-in at ~5.4 µm/s and a reduction in sliding velocity to 0.05 µm/s at ~2 mm. Once a new steady-state was established, a dynamic permeability measurement was initiated. Subsequently, the piston was halted for 300s and a static permeability measurement was conducted. This procedure of shearing, measuring and holding, while measuring the permeability was repeated for progressively increasing hold periods of 1000s, 3000s, and ~12 hours prior to terminating the experiment. In case >1 mm of shear displacement was left, a last cycle of shearing and holding, for a hold time of ~1 hour, was applied before termination.

3.2.4.2 Direct shear experiments without permeability measurements: velocity-stepping (Data-set 3, 4 and 5)

For the vacuum-dry direct shear experiment, i.e. Data-set 3a – pre-dried, evacuation was followed by increasing the P_c to 50 MPa, after which the system was allowed to equilibrate for ~2 h. For the vacuum-dry test performed at 120°C, i.e. 3b - dried in-situ, the apparatus was brought to the desired temperature (taking up to ~4-5 hours to reach 120°C), conjointly increasing P_c. During heating, P_c was maintained below the targeted value until thermal equilibrium was reached, after which the desired pressure was applied manually. For both vacuum-dry experiments (3a and 3b), the vacuum pump remained connected to the pore fluid system to evacuate the gouge layers for the total duration of the experiment.

Following initial evacuation of the sample assembly and the pore fluid system, the gouge layers tested in the wet direct shear experiments of Data-sets 4 and 5 were vacuum-saturated with destilled water, after which a low confining pressure ($\sigma_n > P_f$ ≈ 30 MPa) and the desired pore pressure (P_f = 25 MPa) were applied. Following the application of the pore pressure, the sample temperature was increased to the pre-determined experimental temperature (taking up to ~4-5 hours), simultaneously increasing P_c. Upon achieving the desired experimental conditions, the system was left for full *P-T* equilibration (~1-2 hours).

After equilibration, frictional sliding was initiated at a sliding velocity of ~5.4 µm/s, reaching steady-state sliding at ~2 mm shear displacement. During the experiments of Data-sets 3, 4, and 5, a velocity-stepping sequence was adopted to investigate the frictional strength and stability of the two types of simulated fault gouges at various sliding velocities. The velocity step sequence employed is 0.22-1.086-10.86-1.086-0.22 µm/s and followed the run-in stage. Each shear velocity was maintained for a sliding distance of up to 0.7 mm. Upon termination, the loading ram was arrested and reversed as described above, followed by the removal of the pore fluid pressure or vacuum, when applied, and confining pressure. The system was then left to cool down, when needed, after which the sample assembly was extracted from the apparatus.

3.2.5 Data acquisition and processing

During each experiment, the internal axial load, piston displacement, confining pressure, sample temperature and argon pore pressure decay were logged every 2 s using a 16-bit National Instrument A/D converter and Labview VI Logger system. To obtain the shear stress (τ) vs. and shear displacement (x), the raw data was processed. Elastic machine distortion effects were corrected for using pre-determined, polynomial stiffness calibrations performed at or near the pressure and temperature conditions applied in this study to obtain true axial displacement values. For the used assembly configuration, the shear stress is equal to the internal axial load divided by the contact area of the shear surface, which is assumed to remain equal to the initial contact area during the experiment.

3.2.5.1 Permeability calculations

The argon permeability κ was calculated using the transient-pressure decay method described by Sutherland and Cave (1980). To calculate κ, a pressure difference ΔP_0 [MPa] is applied between two gas reservoirs (R_1, R_2 [m^3]), located up- and downstream of the gouge layer, and allowed to equilibrate with time t [s] through the layer over length l [m] and across-sectional area A [m^2], following the exponential pressure decay equation (Sutherland and Cave, 1980):

$$\Delta P = (\Delta P_0) exp^{-\alpha t} \quad (3.1)$$

With

$$\propto = \kappa \left(\frac{A}{l}\right)\left(\frac{R_1+R_2}{R_1R_2}\right)\left(\frac{1}{\delta\eta}\right) \quad (3.2)$$

Yielding

$$\kappa = \frac{d}{dt}\left(\ln\left(\frac{\Delta P}{\Delta P_0}\right)\right)\frac{l}{A}\left(\frac{R_1R_2}{R_1+R_2}\right)\delta\eta \quad (3.3)$$

where δ represents the dynamic viscosity of argon gas at room temperature [Pa s] and η the argon compressibility [Pa^{-1}]. The permeability is then determined from the linear slope fitting $\ln\left(\frac{\Delta P}{\Delta P_0}\right)$ vs. t using an in house developed computer program, READ30 (Peach, 1991). The permeability is flow path length dependent. As such the path length for the "across-fault" permeability ($\kappa_\perp$) is equal to the thickness of the gouge layer, whereas for the "along-fault" ($\kappa_{//}$) permeability the path length is the long axis of the gouge layer. For the across-fault permeability calculations, we have to assume that the thickness of the gouge layer is equal to the final thickness at all stages in the experiment, as the current set-up does not allow us to measure the change in layer thickness during the experiment. For the along-fault permeability calculations, we assumed the changes in path length to be equal to the shear displacement at the various stages in the experiment.

The permeability is a measure of the mobility of a fluid within a medium, and as such is the property of the medium and not of the fluid (Klinkenberg, 1941). Under steady-state and laminar flow conditions ("Darcy flow"), the measured (apparent) permeability of a medium is therefore considered to be (close to) the true (intrinsic) permeability of a medium, for any kind of fluid (Klinkenberg, 1941). In Darcy flow, molecule-molecule collisions dominate fluid interactions, therefore molecule-wall collisions are neglected. However, when the pore radius of a medium decreases, approaching the mean free path of the fluid molecules, the frequency of molecule-wall collisions increases, resulting in gas slippage along the pore walls. This effect is known as the "slip effect" or "Klinkenberg effect". The true permeability can be derived from the apparent permeability when corrected for this slippage effect by using:

$$K_a = K\left(1 + \frac{\beta}{\bar{p}}\right) \quad (3.4)$$

where K_a [m^2] is the apparent permeability, K [m^2] the intrinsic permeability, β is the Klinkenberg constant and $\bar{p}$ the mean pressure. As a consequence,

extrapolation of the apparent permeability to infinite pressure ($\frac{1}{\bar{p}} = 0$) then gives the true permeability.

3.2.5.2 Rate-and-State Approach

From the shear stress and the normal stress, the apparent coefficient of friction μ was calculated as $\mu = \tau/\sigma_n$, in effect assuming the cohesion to be negligible (cf. Den Hartog et al., 2012). For the sake of simplicity, we will refer to μ as the friction coefficient.

The velocity-dependence of μ, obtained from the velocity-stepping experiments (Data-sets 3, 4 and 5), was interpreted in the framework of the rate-and-state dependent friction (RSF) approach (Dietrich, 1978,1979; Ruina,1983) and the empirical Dieterich type (''slowness'') formulation (Marone, 1998):

$$\mu = \mu_0 + a \ln\left(\frac{V}{V_0}\right) + b \ln\left(\frac{V_0\theta}{D_c}\right), \quad \text{with} \quad \frac{d\theta}{dt} = 1 - \frac{V\theta}{D_c} \tag{3.5}$$

Here, μ_0 is the friction coefficient measured at V_0 [µm/s], a represents the instantaneous increase in μ upon a velocity change from V_0 to $V = exp\ V_0$, or the "direct effect", b represents the evolution of μ towards a new steady-state value μ_{ss}, the "evolution effect", over the characteristic slip distance D_c and θ is a gouge state variable. As a result, a finite change in steady-state friction ($\Delta\mu_{ss}$) is defined by the parameter (a-b) (e.g. Marone, 1998; Scholz, 1998):

$$(a - b) = \frac{\partial \mu}{\partial \ln V} \approx \frac{\Delta \mu_{ss}}{\Delta \ln V} \tag{3.6}$$

A positive (a-b) value indicates an increase in friction coefficient with increasing sliding velocity, known as "velocity-strengthening" slip behaviour, signifying an inherently stable system in which seismogenesis due to accelerating slip is impossible (e.g. Scholz, 1998). A negative (a-b) value indicates a decrease in friction with increasing velocity, known as "velocity-weakening" slip behaviour, signifying a potentially unstable system, which a requirement for seismogenic slip (e.g. Scholz, 1998).

To obtain (a-b) values, the RSF approach requires steady-state friction behaviour, and as our data showed only very minor slip-strengthening or weakening, we applied the standard detrending procedure described by Den Hartog et al. (2012b)

where needed to determine (a-b) values. Taking into account errors in the internal force measurement (±0.223 kN), and preforming conventional Taylor error propagation analysis, the standard errors in a) the absolute friction coefficient (μ) and b) the frictional rate parameter (a-b) determined in our experiments were ±0.002 and ±40%, respectively.

3.3 Results

All direct shear experiments, experimental conditions and key data, including μ_{ss} at ~2.0 mm shear displacement, are listed in Table 3.2. We adopt the convention that compressive stresses are positive and take the effective normal stress σ_n^{eff} as the applied confining pressure, hence normal stress σ_n, minus the applied pore pressure P_f, yielding:

$$\sigma_n^{eff} = \sigma_n - P_f \quad (3.7)$$

3.3.1 Slide-Hold-Slide experiments: Permeametry

3.3.1.1 Permeability measurements

The evolution of the along- and across-fault permeability is plotted, together with the friction coefficient, as function of shear displacement in Figures 3.4a-h. The initial, pre-shear permeability, measured at effective normal stresses σ_n^{eff} of 5 to 50 MPa and $T \approx 20$°C, ranges between $1.2*10^{-15}$ (at 5 MPa) and $1.6*10^{-17}$ m^2 (at 50 MPa) for the along-fault orientation and $2.3*10^{-16}$ (at 5 MPa) and $1.8*10^{-18}$ m^2 (at 50 MPa) for the across-fault orientation. Note that the initial permeability measured along-fault is 2 to 7 times higher than measured for the across-fault orientation (Table 3.2). All experiments show a rapid change (i.e. decrease) in permeability in the first ~2 mm of shear displacement, down to $2.8*10^{-16}$ (5 MPa – 77% decrease) and $8.4*10^{-19}$ m^2 (50 MPa – 95% decrease) for the along-fault orientation and $1.5*10^{-16}$ (5 MPa – 33% decrease) and $3.4*10^{-19}$ m^2 (50 MPa – 85% decrease) for the across-fault orientation. With increasing shear displacement, i.e. shear strain, all experiments show a continuous, though less substantial change in permeability, compared to that observed in the first 2 mm of shear displacement, reaching near-constant values towards the end of the experiments (Figure 3.4). In this range, the along-fault permeability is only 1 to 3 times higher than the across-fault permeability (Table 3.2). Overall, the permeability values obtained for the

along-fault orientation are consistently higher than obtained for the across-fault orientation, though the difference seems to diminish with increasing shear displacement (see permeability ratios in Table 3.2).

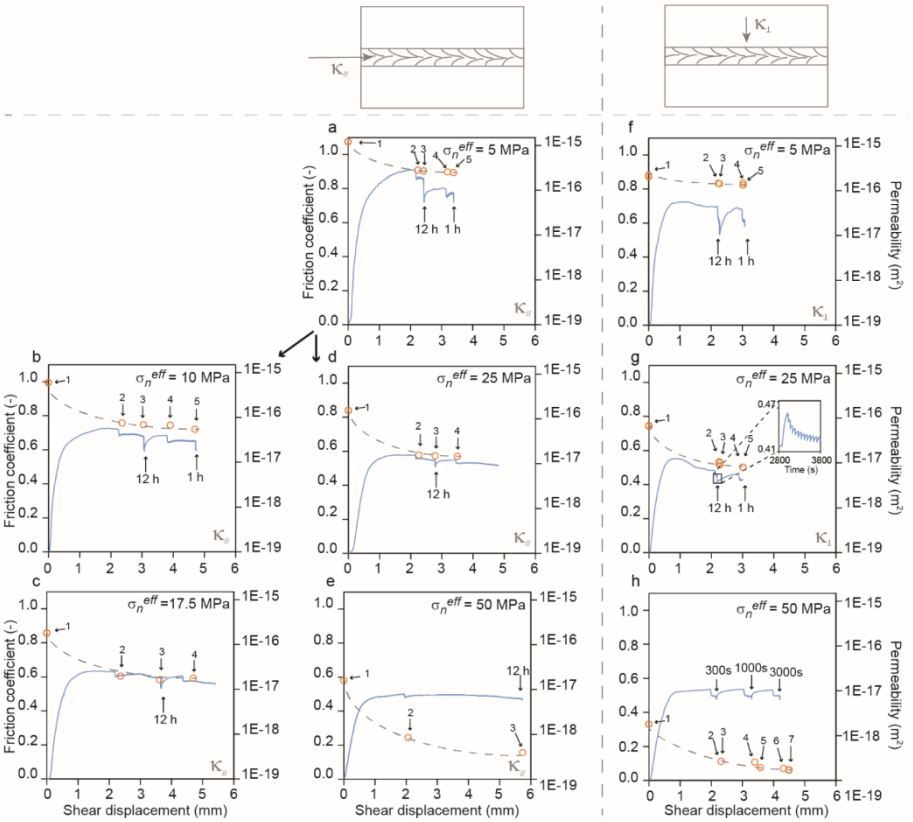

Figure 3.4. Frictional strength (solid blue line) and permeability evolution (orange dots connected by grey, hand-drawn tie-line) as a function of shear displacement observed for the slide-hold-slide direct shear experiments (Data-set 1 & 2) conducted at room temperature, σ_n^{eff} = 5-50 MPa and P_f = 2 MPa. a-e) Frictional strength and permeability evolution as a function of shear displacement for the along-fault experiments. f-h) Frictional strength and permeability evolution as a function of shear displacement for the across-fault experiments. Note the stick-slip in 3.4h.

Detailed analysis of the obtained permeability measurements shows, superimposed on the downward change in permeability with shear displacement, a reduction in permeability for each subsequent period of hold or sliding (Figure 3.4). Our data furthermore shows that the difference in permeability is <20% with respect to the preceding measurement, irrespectively if that it is a measurement

after hold or during shear. One exception to this trend is observed in the 17.5 MPa-across-fault experiment, where the third permeability measurement, during shear (Figure 3.4d), showed a relative increase in permeability with respect to the preceding value obtained during hold.

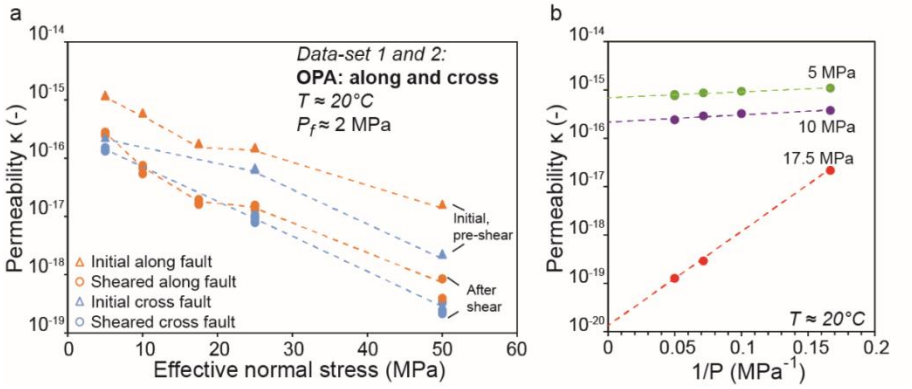

Figure 3.5. a) Permeability as a function of effective normal stress for the initial, pre-shear permeability, and during and after shear permeability. b) Evolution of permeability as a function of the inverse mean pore pressure at 5, 10 and 17.5 MPa effective normal stress.

Besides a decrease in permeability with shear displacement, our results show a decrease in permeability with increasing effective normal stress, irrespectively of orientation. This is explicitly shown in Figure 3.5a, where the permeability κ is plotted as a function of effective normal stress. Moreover, Figure 3.5a shows that the decrease in permeability is larger for an increase in effective normal stress from 5 to 50 MPa than for ~2-6 mm of shear displacement.

The initial, pre-shear permeability is plotted as a function of the inverse mean pore pressure in Figure 3.5b, for measurements obtained at a σ_n^{eff} of 5, 10 and 17.5 MPa in order to assess the Klinkenberg effect. At effective normal stresses of 5 and 10 MPa, the difference between the apparent (gas) obtained permeability for a mean pore fluid pressure of 2 MPa (cf. $1/P_m$ = 0.05 MPa^{-1}) and the true (intrinsic) permeability is <20%. At an effective normal stress of 17.5 MPa, the apparent (gas) permeability, for a mean pore fluid pressure of 2 MPa, deviates ~90% from the true permeability (Figure 3.5b).

Measurements of the initial, pre-shear permeability of the same sample always show a reproducibility within 4%, in most cases even to within 1%. The

reproducibility of the evolution of permeability with shear displacement between different experiments performed under the same conditions (σ_n^{eff} = 5 or 50 MPa, P_f = 2 MPa and T ≈ 20°C) is less good, as illustrated in Figure 3.6.

3.3.1.2 Frictional behaviour

The friction coefficient (μ) versus displacement curves obtained for the simulated, argon-saturated OPA gouges (Data-sets 1 and 2) are shown in Figures 3.4a-h. All experiments show a rapid increase in μ until apparent yielding (~0.43-0.73), occurring at a displacement of ~0.3-1.2 mm and occasionally followed by limited slip-hardening reaching a peak strength and a drop in μ, before reaching (near) steady-state friction coefficients of 0.54 to 0.91 at ~2 mm of shear displacement (Table 3.2). Moreover, they show a modest decrease in friction coefficient following the imposed reduction in sliding velocity.

Table 3.2. List of experiments performed and experimental conditions. Symbols: T = temperature, σ_n^{eff} = effective normal stress, P_f = pore fluid pressure, V = sliding velocity, T_h = holding time, μ_{ss} = steady-state friction coefficient at ~2.0 mm, $\mu_{\sim 3.4}$ = friction coefficient at ~3.4 mm, $\mu_{\sim 4.5}$ = friction coefficient at ~4.5 mm, (a-b) = velocity-dependence parameter.

Experiment	*T (°C)*	*σ_n^{eff} (MPa)*	*V (µm/s)*	*T_h (s/h)*	*μ_{ss} (~2.0 mm)*	*$\mu_{\sim 3.4}$*	*$\mu_{\sim 4.5}$*	*(a-b)*	*Permeability ratio (along vs. across)*
Data-set 1: carbonate-bearing at T_a ≈20°C (pre-dried at 120°C) or T_b = 120°C (dried in-situ), σ_n^{eff} = 50 MPa and under vacuum									
08OPDR	23	50	5.43 – 0.22 – 1.086 – 10.86 – 1.086 – 0.22	-	0.61	0.59	0.57	0.0037-0.0098	
10OP120D	120	50	5.43 – 0.22 – 1.086 – 10.86 – 1.086 – 0.22	-	0.63	0.62	0.59	0.0014-0.0034	
Data-set 2: carbonate-bearing at σ_n^{eff} = 50 MPa and P_f = 25 MPa									
05OP20	21	50	5.43 – 0.22 – 1.086 – 10.86 – 1.086 – 0.22	-	0.33	0.33	0.30	0.0050-0.0097	
12OP60	62	50	5.43 – 0.22 – 1.086 – 10.86 – 1.086 – 0.22	-	0.31	0.33	0.30	0.0043-0.0050	
14OP100	100	50	5.43 – 0.22 – 1.086 – 10.86 – 1.086 – 0.22	-	0.33	0.33	0.31	0.0031-0.0058	
13OP120	120	50	5.43 – 0.22 – 1.086 – 10.86 – 1.086 – 0.22	-	0.31	0.32	0.29	0.0044-0.0067	
24OP150	149	50	5.43 – 0.22 – 1.086 – 10.86 – 1.086 – 0.22	-	0.33	0.33	0.31	0.0049-0.0091	

Table 3.2. *Continued*

Data-set 3: carbonate-bearing - permeability measurements at T = room temperature and P_f = 2 MPa									
15OPAPC50	22	50	5.43 – 0.543 – 0.0543 (3 x)	300s, 1000s, 3000s, ~12 h, ~1 h	0.54	0.52	-	-	7.1-2.5-1.2
22OPAPA5	23	5	5.43 – 0.543 – 0.0543 (3 x)	300s, 1000s, 3000s, ~12 h, ~1 h	0.77	0.77	-	-	
23OPAPA5t	22	50	5.43 – 0.543 – 0.0543 (3 x)	300s, 1000s, 3000s, ~12 h, ~1 h	0.80	0.86	-	-	
25OPAPA25t	27	25	5.43 – 0.543 – 0.0543 (3 x)	~12 h, ~1 h	0.58	0.55	0.52	-	
26OPAPA10t	22	10	5.43 – 0.543 – 0.0543 (3 x)	~12 h, ~1 h	0.72	0.68	0.65	-	
27OPAPA5t	23	5	5.43 – 0.543 – 0.0543 (3 x)	~12 h, ~1 h	0.91	0.77	0.88	-	5.2-1.8-1.8-1.9
28OPAPA17.5t	23	17.5	5.43 – 0.543 – 0.0543 (3 x)	~12 h, ~1 h	0.63	0.60	0.58	-	
29POPAPA50t	23	50	5.43 – 0.543 – 0.0543 (3 x)	~12 h, ~1 h	0.50	0.50	0.49	-	
30OPAPA25t	22	25	5.43 – 0.543 – 0.0543 (3 x)	~12 h, ~1 h	0.48	0.46	0.47	-	2.2-1.5-1.6-1.6
31OPAPC5t	22	5	5.43 – 0.543 – 0.0543 (3 x)	~12 h, ~1 h	0.70	0.68	0.69	-	
Data-set 4: carbonate-free at σ_n^{eff} = 50 MPa and P_f = 25 MPa									
16TrOpclay20	24	50	5.43 – 0.22 – 1.086 – 10.86 – 1.086 – 0.22	-	0.29	0.30	0.28	0.0051-0.0088	
18TrOpclay60	62	50	5.43 – 0.22 – 1.086 – 10.86 – 1.086 – 0.22	-	0.27	0.27	0.25	0.0034-0.0065	
17TrOpclay100	100	50	5.43 – 0.22 – 1.086 – 10.86 – 1.086 – 0.22	-	0.27	0.26	0.25	0.0027-0.0065	

The steady-state friction coefficient obtained after re-shear is generally lower than the pre-hold steady-state value. Furthermore, the majority of the friction curves is characterised by (near) strain-neutral behaviour following the run-in stage, with the exception of the 25 and 50 MPa across-fault curves, which show minor strain-hardening (Figure 3.4).

The frictional strength decreases, independently of orientation, with increasing effective normal stress, from max. ~0.9 to as low as 0.5. However, this decrease is non-linear, which is explicitly shown in Figure 3.7a for the steady-state frictional strength at ~2 mm as a function of effective normal stress. Generally, stable sliding was observed for all sliding velocities, however during the 0.05 µm/s

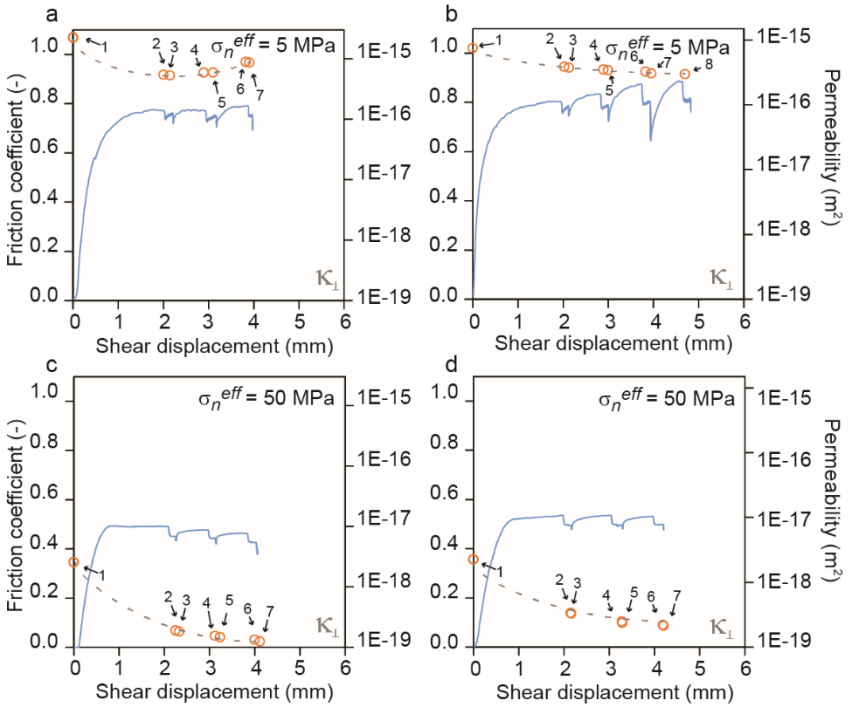

Figure 3.6. Additional direct shear experiments with across-fault permeability measurements and a slide-hold-slide sequence with increasing hold periods of 300, 1000, 3000 seconds (a, c,d) and additionally 12 h (b) to investigate the effect of hold duration on the decrease in permeability, tested at room temperature. a and b) Frictional strength and permeability evolution as a function of shear displacement for tested at σ_n^{eff} = 5 MPa, P_f = 2 MPa. c and d) Frictional strength and permeability evolution as a function of shear displacement for tested at σ_n^{eff} = 50 MPa, P_f = 2 MPa.

sliding intervals of the 5 MPa and 25 MPa across-fault experiments, plus the 5 MPa along-fault experiment (i.e. 27OPAPA5t, 30OPAPC25t and 31OPAPC5t), stick-slips were observed (see in-set in Figure 3.4g). Similarly, the additional velocity-steps following the regular slide-hold-slide sequence of 5 and 25 MPa across-fault experiments (i.e. 30OPAPC25t and 31OPAPC5t) showed stick-stick behaviour for the 0.05 to 0.5 µm/s interval. By plotting the steady-state frictional strength obtained at ~5.4 µm/s and 0.05 µm/s, complemented by the friction coefficient values obtained for the additional sliding velocities, the frictional strength is plotted as function of sliding velocity in Figure 3.7b for the 5 and 25 MPa across-fault samples (i.e. 27OPAPA5t, 30OPAPC25t). Although stick-slip behaviour was

observed in the friction curves, an increase in frictional strength with increasing sliding velocity is observed in Figure 3.7b.

The shear stress (τ) supported at steady-state at ~2.0 and at 3.4 and 4.5 mm shear displacement, is plotted as a function of the σ_n^{eff} in Figure 3.7 for all argon-saturated experiments performed. The data show a linear relation passing through or close to the origin, suggesting nearly cohesionless fault gouges (Figures 3.7c-d). Fitting the Mohr-Coulomb criterion, i.e. $\tau = \mu\sigma_n^{eff} + C_0$, to the linear τ vs. σ_n^{eff} data yields very similar cohesions (C_0) of roughly 2 MPa for both along- and across-fault orientation (Table 3.3), when considering the error bars. The cohesion furthermore appears to be independent of shear displacement, as the cohesion remains to be ~2 MPa (Figure 3.7c-d – Table 3.3).

The effect of the different hold time sequences employed in this study on the frictional and transport properties of OPA gouge used in the slide-hold-slide experiments is illustrated in Figure 3.6 for two sets of duplicate experiments employing increasing hold time (across-fault – at σ_n^{eff} = 5 or 50 MPa), and one experiment employing a 12h hold followed by a 1h hold (across-fault – at σ_n^{eff} = 5 MPa – Figure 3.6). Comparing Figures 3.6a with 3.6b, and 3.6c with 3.6d, no systematic effect emerges of increasing the hold time from 300 to 3000 seconds on the friction coefficient and permeability. The results in case of a different hold time history, from 12 to 1 hour hold (Figure 3.4g versus Figures 3.6a and 3.6b), neither show reason to infer such an effect.

Table 3.3. List of internal friction coefficient and cohesion values obtained for the argon-saturated experiments.

	Internal friction coefficient (-)	**Cohesion (MPa)**
Along fault at ~2.0 mm	0.47 ± 0.011	2.1 ± 0.31
Along fault at ~3.4 mm	0.48 ± 0.011	1.7 ± 0.30
Along fault at ~4.5 mm	0.47 ± 0.017	1.8 ± 0.55
Cross fault at ~2.0 mm	0.48 ± 0.042	0.76 ± 1.7
Cross fault at ~3.4 mm	0.47 ± 0.033	0.63 ± 1.34

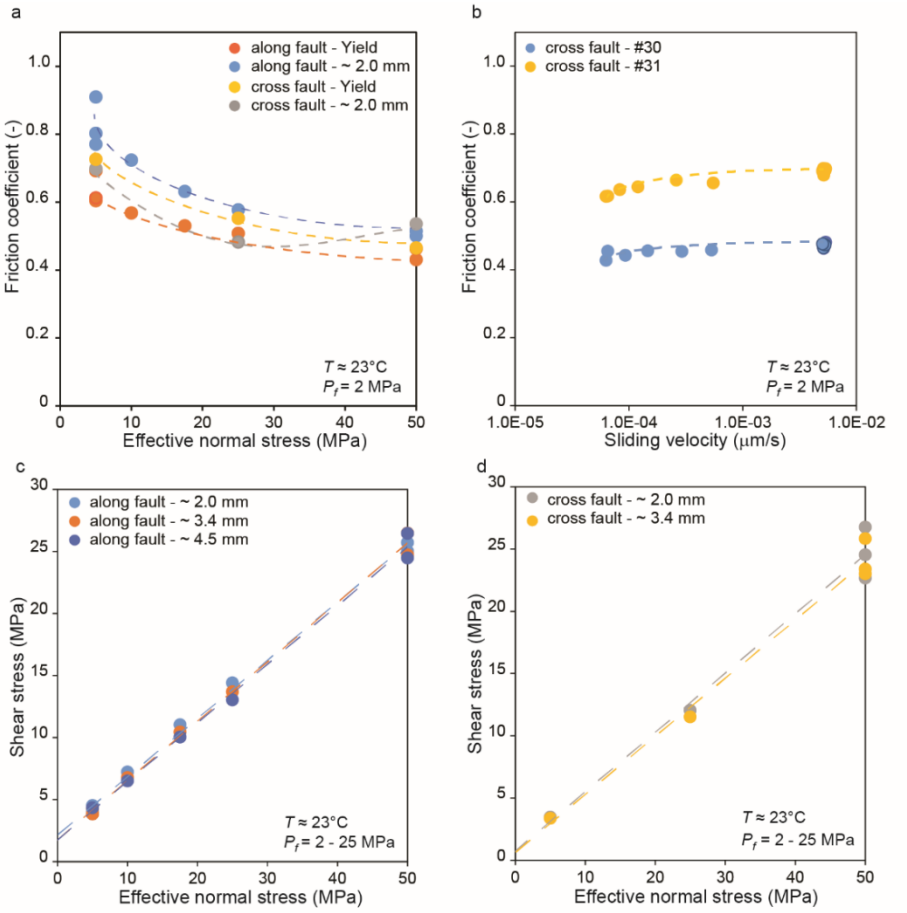

Figure 3.7. Shear stress at steady-state, i.e. at ~2 mm, 3.4 and 4.5 mm shear displacement, as a function of effective normal stress. The dashed linear trend lines and corresponding data points are colour-coded. a) For experiments in which the along-fault permeability is measured (Data-set 1). b) For experiments in which the across-fault permeability is measured (Data-set 2). c) Friction coefficient at yield and at steady-state (~2 mm) as a function of effective normal stress (Data-set 1 and 2). d) Friction coefficient at steady-state for the various sliding velocities used for the along- and across-fault orientation.

3.3.2 Velocity-stepping experiments: Frictional behaviour

A representative selection of friction coefficient (μ) versus displacement curves obtained in the velocity-stepping experiments on simulated OPA and calcite-free OPA (CFOPA – Data-sets 3 and 4) is shown in Figures 3.8a and b. All experiments show a rapid increase in μ until apparent yielding (0.28-0.54), occurring at a displacement of ~0.4-0.9 mm. For the wet OPA and CFOPA samples, this was followed by limited slip-hardening, reaching a peak strength and a small drop in μ before reaching (near) steady-state friction coefficients of 0.28 to 0.33 at ~1.8-2 mm shear (Figure 3.8a). In all these experiments, subsequent velocity steps are characterised by (near) strain-neutral behaviour, i.e. no change in strength with continued shearing, and show a modest, but positive effect of sliding velocity on the friction coefficient. For the two dry OPA samples, apparent yielding was followed by strain-hardening in the first ~2 mm ($\mu_{ss} \approx 0.54$) of shear and strain-weakening between ~2 to 6 mm shear, i.e. respectively a gradual increase or decrease in frictional strength with increasing shear displacement, also showing a modest, but positive effect of sliding velocity on the friction coefficient (Figure 3.8b). Occasionally, small, abrupt drops in friction coefficient have been observed around ~0.2-0.4 mm, attributed to the alignment of the sample assembly with the loading ram (Figures 3.8a and b).

The frictional strength obtained for the wet OPA samples ranges between 0.29 and 0.33, and demonstrates little or no effect of temperature, for the tested temperature range of ~23-150°C (Figure 3.8a). This is explicitly shown in Figure 3.8c where the steady-state frictional strength at ~2 mm is plotted as a function of temperature. A similar trend is observed for the wet carbonate-free OPA fault gouges (CFOPA – Data-set 4; Figures 3.8a and c), tested for a temperature range of ~23-100°C. Overall, the frictional strength (μ) of the carbonate-free OPA gouges (CFOPA – Data-set 4) is 10 to 20% lower than observed for their carbonate-bearing equivalents (OPA – Data-set 3). The friction coefficient obtained for the dry OPA samples ranges between 0.57 and 0.63, with the in-situ dried 120°C – OPA gouge being consistently ~10% stronger than the pre-dried 20°C – OPA gouge (Data-sets 3a,b; Figures 3.8b and c).

Returning to the velocity dependence seen in Figures 3.8a and b, both the OPA (wet and dry) and CFOPA (wet) samples exhibited velocity-strengthening behaviour at the conditions tested. This is reflected by positive (a-b) values, which are plotted

as a function of temperature in Figure 3.8d for 2 post step velocities, i.e. 1.1 and 11 µm/s. Furthermore, for both the OPA and CFOPA the velocity-dependence shows a weak decreases with increasing temperature, for both velocity up and down steps, reaching the lowest values between 60 and 120°C (Figure 3.8d). No systematic trend in (*a*-*b*) with composition, i.e. OPA vs. CFOPA, is observed. For the investigated conditions, the (*a*-*b*) values obtained for the down steps are consistently higher than the up steps. Additionally, at 120°C, the (*a*-*b*) values obtained for the wet OPA samples are consistently higher than for the dry OPA samples (Figure 3.8d).

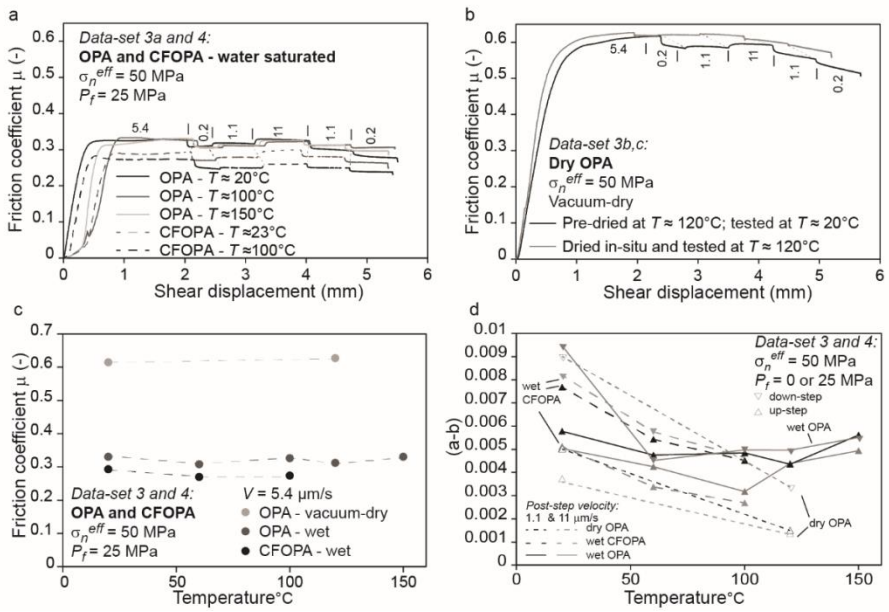

Figure 3.8. Frictional characteristics of simulated OPA and CFOPA fault gouges. The velocity-steps are indicated in µm/s, with the location of the instantaneous velocity-steps marked using vertical "ticks", and connected with dashed lines to the same velocity step in different experiments (*a*-*b*) a) Representative curves showing the evolution of friction coefficient with shear displacement for the velocity-stepping experiments on simulated wet OPA and CFOPA gouges. b) Evolution of friction coefficient with shear displacement for the velocity-stepping experiments on simulated, vacuum-dry OPA gouges. c) Friction coefficient supported at ~2.0 mm shear displacement versus temperature for all OPA and CFOPA samples. d) Values of (*a*-*b*) versus temperature for up and down steps with velocities of 1.1 and 11 µm/s.

3.4 Discussion

One of the major concerns of CO_2 injection in geological formations is the potential risk of inducing fault slip and (micro)seismicity along previously sealing (i.e. impermeable) gouge-filled faults (Hawkes et al., 2005; Zoback and Gorelick, 2012). Fault slip and induced seismicity are most likely the result of a change in the stress conditions on pre-existing faults. This can occur via 1) (local) compaction or heave of the reservoir (poro-elastic effect), 2) thermal expansion or shrinkage near the well, or 3) an increased pore pressure in a pre-existing fault, effectively reducing the normal stress on the fault (Hawkes et al., 2005; Wang, 2000). Besides these geomechanical effects, in the case of CO_2-injection, one also needs to consider the potential impact of chemical interaction with reactive, CO_2-rich fluids. CO_2-induced reaction may lead to mineralogical changes in the fault gouge, which could reduce its frictional strength and stability, i.e. lead to a transition from positive to negative (a–b)-values (Chapter 2; Samuelson and Spiers, 2012; Song and Zhang, 2013). Once fault slip is induced, this may cause dilatation, potentially increasing fault permeability. Upon slipping, leakage of CO_2 could then either occur across the fault, i.e. between two adjacent reservoir compartments, or along the fault, e.g. into an over- or underlying formation, in case an outward pressure gradient is in place (Bense and Person, 2006).

To help evaluate the potential for leakage and/or seismogenic slip along gouge-filled faults cutting clay-quartz-calcite caprock, we have investigated (Aim 1) the effect of shear displacement, dynamic shear, static holding, and normal stress on the transport properties (both along- and across-fault) of a simulated clay-quartz-calcite fault gouge. In addition, to evaluate the potential effects of chemical reactions (Aim 2), we have investigated the effects of compositional differences and deformation conditions on the frictional strength (μ) and slip stability (expressed in terms of (a-b)) of a simulated clay-quartz-calcite gouge. To simulate the effect of chemical reactions, an additional fault gouge was prepared by removing the naturally occurring calcite from the initial simulated clay-quartz-calcite fault gouge, hence clay-quartz gouge. The frictional behaviour of this artificially reacted gouge (CFOPA) was subsequently compared with that of the initial composition (OPA), simulating a scenario of total calcite dissolution following CO_2 injection.

In the following, we will first discuss our findings regarding the effects of shear displacement, dynamic shear, static holding, and effective normal stress on the permeability evolution of a simulated clay-quartz-calcite fault gouge (OPA – Aim 1). We will then continue with discussing the observed effects of mineralogy, temperature and pore fluid on the frictional strength and slip stability of the same clay-quartz-calcite fault gouge (OPA vs. CFOPA – Aim 2). Finally, we will consider our data in the context of evaluating the effects of long-term CO_2 exposure and discuss then implications for sealing integrity and frictional behaviour of a gouge-filled fault cutting a potential clay-quartz-calcite caprock in CO_2 storage systems.

3.4.1 The effect of shear displacement, dynamic shear, static hold, and normal stress on fault gouge permeability: parallel and perpendicular to the fault

In discussing our experimental data on gouge permeability, we note that, as shown in the results section (see section 3.3.1.1), hold periods of different time spans and different sequences, do not show a systematic effect on the permeability or friction coefficient. This justifies the grouping, for analysis reasons, experiments with different hold histories, including both along- and across-fault permeability measurements, in one figure as done in Figure 3.4.

Overall, our data show a decrease in permeability with shear displacement (i.e. fault maturity) and with effective normal stress (Figure 3.5a) for both along- and across-fault orientation. The most significant reduction in permeability is observed in the first few millimetres of shear displacement, reaching (near) constant values during further shear displacement. Over a shear displacement of up to ~6 mm, the permeability changed by up to an order of magnitude compared with the pre-shear permeability. Comparing the along- and across-fault permeability measurements demonstrates an initial anisotropy of up to 1 order of magnitude. Furthermore, our permeability results, both along- and across-fault, show that the decrease in permeability with increasing displacement coincides with a decrease in frictional strength (Figure 3.4). Note also that the friction coefficient decreases with increasing effective normal stress.

The observed sharp decrease in permeability, characteristic for the initial stage of shear, followed by a more gradual decrease towards more or less constant values with continuous shear is reported for a broad range of clastically-derived

compositions (e.g. Chapter 2; Morrow et al., 1984; Zhang and Tullis, 1998). Furthermore, the total decrease of about one order of magnitude upon shear, both along- and across-fault, is in agreement with permeability measurements on mixtures rich in phyllosilicates, including chlorite, illite, kaolinite, montmorillonite and muscovite (Figure 3.4 – e.g. Crawford et al., 2008; Morrow et al., 1984; Zhang et al., 1999). Besides the reduction in permeability with shear displacement, we observe a reduction in permeability with increasing effective normal stress, again in agreement with many previous studies (e.g. Behnsen and Faulkner, 2012; Crawford et al., 2008; Morrow et al., 1981b; Zhang et al., 1999).

During initial loading, prior to shear, mineral alignment of the clay-quartz-calcite mixtures is assumed to be dominated by rotation of phyllosilicates towards an orientation perpendicular to the highest principal stress orientation, i.e. the applied normal stress, hence parallel to the boundaries of the gouge layer (Zhang et al., 2001). As a consequence, fluid flow across the fault is more tortuous than along the fault, which is supported by the permeability anisotropy observed for the pre-shear permeability values (Figure 3.5). The sharp, initial decrease in permeability during the run-in stage of the experiments is inferred to reflect shear-enhanced compaction of the bulk gouge layer, as rearrangement of grains and grain size reduction allow for a denser grain packing (e.g. Marone and Scholz, 1989; Zhang et al., 2001). Upon reaching steady-state shearing, shear bands are expected to have developed accommodating localised shear on very thin and dense shear bands (Haines et al., 2009), which will not affect the bulk permeability of the gouge layer any further during subsequent shear displacement, dynamic shear and/or periods of holding. This is supported by the transition to more or less constant permeability values for the bulk of the gouge layer obtained during this stage of the experiment. Moreover, the permeability anisotropy shows a decrease with respect to the initial permeability anisotropy. This suggests a shear-induced reduction in tortuosity contrast between along- and across-fault fluid flow, in agreement with observation for mica-gouges by Zhang et al. (1999), who inferred the reduction to result from an anisotropic enhancement of fluid flow by P-shear and Y-shears. Permeability measurements obtained during dynamic shear and static holding show little difference, suggesting a limited effect of holding versus shearing on the permeability, especially when a well-defined foliation is established (Figure 3.4).

The difference in permeability and permeability evolution observed for the various effective normal stresses (Figure 3.5a), i.e. high permeability values at low effective normal stress and lower values at higher normal stresses (Figure 3.4), suggests various degrees of compaction via grain rearrangement and grain crushing (Zhang and Tullis, 1998). At the same time, the observed decrease in frictional strength with increasing effective normal stress suggests an indirect correlation between the friction coefficient and permeability. A similar relation has been observed between the mineral composition and permeability by Crawford et al. (2008). However, we have too little experimental data to confirm such correlation with friction coefficient. What also plays a role is the fact that at high effective normal stress (>17.5 MPa), the Klinkenberg effect cannot be ignored. Given the specific experimental procedure employed in this study, a systematic Klinkenberg correction (Equation (3.4)) could not be applied, as during shear the maturity of the fault, and therefore the experimental situation, continuously changed. As a consequences, observed trends of increasing or decreasing permeability are meaningful, but not too much importance can be attributed to absolute values, at least not at effective normal stress above 17.5 MPa. More work is needed on these aspects.

3.4.2 The effects of compositional differences and deformation conditions on the frictional behaviour of simulated clay-quartz-calcite fault gouges

In discussing our friction results, obtained for the argon-saturated OPA samples (see sections 3.3.1.2), we begin by noting that the effect of calculated cohesion of ≤2 MPa (Table 3.2) is relatively high at low effective normal stresses (<25 MPa), and relatively small at higher effective normal stress (>25 MPa). Therefore, we infer that the shear strength of our samples, expressed as friction coefficient, can be represented by the ratio of the shear stress over the effective normal stress at effective normal stresses ≥25 MPa, and justifying use of the RSF framework to describe our mechanical results, especially at σ_n^{eff} = 50 MPa. This inference is further supported by the fairly good agreement between the experimentally-derived friction coefficients at 25 and 50 MPa and the internal friction coefficient at yield or peak, derived via Equation (3.3) (Table 3.3). However, the cases that the agreement is less good convey the samples performed at effective normal stresses <25 MPa. These should therefore be assessed carefully.

In general, our data show that the calcite-bearing OPA is consistently stronger, by 10-20%, than the calcite-free OPA (CFOPA), i.e. $\mu_{ss} \approx 0.30$ vs. $\mu_{ss} \approx 0.27$ for the tested temperature ranges of ~20 to 150°C vs. ~20 to 100°C, respectively. Our results for the OPA gouge are in agreement with μ-values obtained for calcite-bearing fault gouges (Chen et al., 2015a), whereas the results for the CFOPA are in rough agreement with calcite-free gouges dominated by phyllosilicates (e.g. Ikari et al., 2009; Tembe et al., 2006). The observed trend with composition for these natural rock-derived gouges is in agreement with many studies documenting artificially composed mixtures of pure end-members (e.g. Crawford et al., 2008; Takahashi et al., 2007; Tembe et al., 2010). Drying of the OPA gouge strengthens the gouge material by ~100%, from ~0.30 to ~0.60 (Figure 5.8), which is in agreement with the known (intergranular) lubricating effect of water (e.g. Den Hartog et al., 2014; Moore and Lockner, 2004; Verberne et al., 2014). This allows us to compare the frictional strength obtained for the argon-saturated OPA gouge (0.50-0.54; σ_n^{eff} = 50 MPa, P_f = 2 MPa, $T \approx 20$°C – Figure 3.4) with that obtained for the water-saturated (σ_n^{eff} = 50 MPa, P_f = 25 MPa, $T \approx 20$°C – Figure 3.8a) and the vacuum-dry (σ_n^{eff} = 50 MPa, $T \approx 20$°C, pre-dried at 120°C – Figure 3.8b) OPA gouges, being respectively up to 60% stronger and up to 20% weaker, suggesting a minor weakening effect of water. This limited weakening effect might be the result of partial lubrication of the gouge layer by residual water in the pore fluid system that was not removed during the initial evacuation of the system prior to the experiment.

Our argon-saturated friction data furthermore showed higher friction coefficient values at lower effective normal stresses than at 50 MPa (Figure 3.7a). A similar gradually decreasing friction coefficient to more constant values at higher effective normal stresses has been observed for various phyllosilicate-bearing mixtures (Behnsen and Faulkner, 2012; Ikari et al., 2007; Saffer and Marone, 2003), and is assumed to reflect the influence of gouge cohesion at low effective normal stresses as mentioned above.

In addition to evaluating the change in absolute frictional strength, it is also important to evaluate the change in velocity-dependence of the fault friction with mineralogy and deformation conditions. Our results indicate velocity-strengthening behaviour for all mineral compositions and deformation conditions tested (Figures 3.4 and 3.8). Furthermore, our results demonstrate no significant difference in

velocity-dependence between wet OPA and wet CFOPA samples (Figure 3.8d). This suggests that while calcite-dissolution may result in the frictional weakening of a gouge-filled fault, aseismic slip (i.e. velocity-strengthening) behaviour is still expected in gouges having a CFOPA composition. Comparing the slightly decreasing (*a*-*b*) values with temperature for the dry and wet OPA samples shows similar values at ~20°C, but consistently lower values for dry material at ~120°C (Figure 3.8d). This suggests an increasing effect of water at higher temperature, superimposed on the decrease in velocity-strengthening behaviour of OPA in the temperature range investigated. Similar effects of temperature and water have been observed for pure calcite (Verberne et al., 2014) and illite-quartz mixtures (Den Hartog et al., 2014) at comparable experimental conditions. Assuming that the velocity-dependence of steady-state friction reflects competition between dilation and compaction, as put forward in the model presented by Den Hartog and Spiers (2014), we infer that a combination of thermally-activated and/or water-assisted compaction processes increasingly controls slip stability at elevated temperature. Potential controlling processes include intergranular lubrication by water complemented by thermally-activated creep of quartz and/or calcite by water-assisted diffusion processes (Den Hartog et al., 2014; Den Hartog and Spiers, 2014; Verberne et al., 2014). Other possibilities might be stress corrosion cracking (Den Hartog and Spiers, 2014) or dislocation glide (Verberne et al., 2014).

Despite the positive (*a*-*b*) values obtained for both dry and wet OPA samples (Data-set 3), and the similarly positive dependence of friction coefficient on velocity seen in the experiments involving argon-permeametry (Figure 3.7d), it is striking that low amplitude, stick-slip behaviour was observed in several of the argon-saturated OPA samples. Specifically, stick-slip was observed in argon-saturated samples 27OPAPA5t, 31OPAPC5t and 30OPAPC25t, which were sheared at room temperature, at sliding velocities of 0.05-0.50 µm/s and effective normal stresses of respectively 5, 5, and 25 MPa. Based on the velocity-strengthening behaviour stick-slip is not expected. It is unlikely that this behaviour is a chemical effect of the argon gas, given its inert nature. There is also no systematic correlation between the observed stick-slip behaviour and across- versus along-fault argon flow. Possible explanations that we can propose for the “anomalous” stick-slip include the following:

1) Local, stepwise penetration of argon into previously unpenetrated shear bands, due to shear band dilatation at the low effective normal stresses used in the experiments showing stick-slip. This could be possible without affecting sample scale permeability if it is transport through the body of the sample that determines its permeability.
2) Overpressurization of argon trapped in small pores not penetrated by water in the wet experiments due to the higher viscosity of water (0.89 mPa; Kestin et al., 1978) compared to that of argon (0.23 mPa; Kestin and Wakeham, 1972).
3) We cannot exclude the possibility mentioned earlier that small amounts of water may be introduced into the sample during argon injection, from traces left in the pore fluid system after earlier wet experiments, which could not be removed during argon flushing prior to applying the argon pore pressure. Gradual penetration of water introduced into the gouge in this way, could conceivably lead to slip-weakening and associated stick-slip. Some support for this is offered by the correlation between slip-weakening and stick-slip seen in the relevant argon-saturated experiments.
4) A further possibility is that the samples showing stick-slip at σ_n^{eff} = 5 MPa became over-consolidated, with respect to shear-testing, due to pre-pressing during preparation. This would produce a peak strength during shear followed by slip-weakening (Ide and Takeo, 1997) and hence potential for unstable slip events.

3.4.3 Implications

In order to predict with some confidence what may happen in faults cutting the caprock of a potential CO_2 storage system, it is of importance to understand what factors control the frictional and transport properties of a gouge-filled fault. The goal of this research was therefore to evaluate i) the effect of shear displacement, dynamic shear, static holding and effective normal stress on fault gouge permeability, both parallel and perpendicular to the fault boundaries, and ii) the effect of calcite dissolution on the frictional strength and stability of a simulated clay-rich gouge. Both aims are particularly relevant for, but not limited to, CO_2 injection and storage in potential storage reservoirs in the subsurface as for both aims different aspects of fault integrity are evaluated. The implications of our results are listed below:

1) Faults intersecting a clay-quartz-calcite-bearing formation, such as a calcite-rich claystone or shale, may be (re-)activated upon hydrocarbons production or CO_2-storage, potentially leading to induced (micro-)seismicity, fault zone dilation, permeability enhancement and as a consequence a reduction of sealing capacity. It is therefore critical to know how shear displacement, dynamic shear, static holding and effective normal stress affect the along- and across-fault permeability. Assuming a clay-quartz-calcite caprock composition resembling the Opalinus Claystone (40-50% phyllosilicates, 20-25% quartz, and 20-30% of calcite) the present results imply that with increasing shear displacement the permeability will reduce up to an order of magnitude, with the most significant reduction occurring in the first millimetres of shear displacement. Upon reaching steady-state frictional behaviour, the internal foliation has been developed. With increasing maturity, faults acquire a well-developed internal foliation, which has only limited potential for compaction or dilation. As a consequence, re-shear or static holding will only slightly decrease the permeability further, before levelling off to near constant permeability.
2) Potential CO_2 storage reservoirs are located at 1-4 km depth (cf. 25-100 MPa). The present results (Figure 3.4) show that pre-existing gouge-filled faults at these depths are expected to have permeabilities ranging between 10^{-16} and 10^{-19} m^2 (Klinkenberg uncorrected). Comparing these values with the permeability of an intact slice of Opalinus Claystone ($7.7 \cdot 10^{-20}$ m^2 (Klinkenberg uncorrected) at 15 MPa effective normal stress or ~0.7 km depth) shows that, even at normal stresses corresponding to 2 km, the gouge permeability of 10^{-19} m^2 is still 1-2 orders of magnitude higher than the intact rock, and therefore more likely to act as a leakage pathway.
3) If the pore fluid pressure in a fault zone increases due to migration of supercritical CO_2 from a storage reservoir, the effective normal stress can decrease. Our results show that with increasing pore pressure, and decreasing effective normal stress, the permeability of simulated clay-quartz-calcite fault gouge will increase, irrespectively of fluid flow orientation, reducing sealing capacity. Moreover, our results show that leakage along a fault into an over- or underlying formation is easier than leakage across the fault into neighbouring reservoir compartments, with

our simulated fault gouges showing ~1 order of magnitude anisotropy in permeability.

4) The coupled chemical-mechanical effect of CO_2-exposure is another factor that should be considered when assessing the integrity of a potential CO_2 storage complex. Our results have demonstrated that faults formed in clay-quartz-calcite claystone or shale can be expected to exhibit stable, velocity-strengthening behaviour with a relatively weak resistance to shear ($\mu_{ss} \approx 0.30$) at in-situ conditions. In case of calcite dissolution associated with CO_2-charged fluid migration, the frictional strength will be slightly reduced (~10-20%), though stable, velocity-strengthening behaviour will remain little affected at the conditions investigated.
5) On-going flow-through of dry CO_2 has been suggested to have the potential to cause desiccation of fault gouge (Duan and Sun, 2003; Pluymakers et al., 2014b), as well as possible clay mineral shrinkage effects (Busch et al., 2016). The present results suggest that drying of fault gouges, with the clay-quartz-calcite composition investigated here and at conditions relevant for CO_2 injection, will strengthen such fault gouges by ~100%, while it becomes slightly less velocity-strengthening. Note that such desiccation effects will only be maintained during flow of dry CO_2. Moreover, fault gouge shrinkage caused by desiccation may both reduce effective normal stress and so increase permeability.

3.5 Conclusions

In this study, we aimed to evaluate various factors that control the frictional and transport properties of gouge-filled faults cutting carbonate-bearing shale or claystone formations. The research experimentally determined i) the effect of shear displacement, dynamic shearing, static holding, and effective normal stress on fault gouge permeability, both parallel and perpendicular to the fault boundaries, and ii) the effect of calcite removal by dissolution on the frictional strength and stability of a simulated clay-rich gouge. To achieve this, two types of direct shear experiments were performed. The first set consisted of direct shear experiments on simulated fault gouges prepared from Opalinus Claystone (OPA) performed at effective normal stresses of 5 to 50 MPa, in combination with along-fault and across-fault permeability measurements. The second set consisted of direct shear experiments conducted under upper crustal reservoir conditions on

the same simulated fault gouges, with the naturally occurring calcite content (~26%) both present and removed by pre-leaching. Our key findings are given below:

1) The Klinkenberg uncorrected, initial fault permeabilities for the (unleached) Opalinus Clay gouges, measured at room temperature, fell in the range of 10^{-15} (5 MPa) to 10^{-17} m^2 (50 MPa) along the fault, versus 10^{-16} (5 MPa) to 10^{-18} m^2 (50 MPa) across the fault. Both along- and across-fault permeabilities (Klinkenberg uncorrected) decreased with shear displacement, showing the largest drop in permeability in the first ~2 mm of shear displacement. At this stage, a well-developed internal foliation has developed, with the permeability decreasing to near constant values. Permeability decreased further with shear, and during static hold periods, via compaction of the fault gouge material. Up to an order of magnitude decrease in permeability is observed for up to 6 mm shear displacement, in both fluid flow orientations. Pre-shear permeability values show up to an order of magnitude difference (anisotropy) between along- and across-fault, with shear displacement this difference decreases.
2) Pre-existing gouge-filled faults with a clay-quartz-calcite composition located at a depth range of 1-4 km are expected to have permeabilities ranging between 10^{-16} and 10^{-19} m^2 (Klinkenberg uncorrected). The Klinkenberg uncorrected permeability of the intact rock ($7.7 \cdot 10^{-20}$ m^2 at 15 MPa effective normal stress or ~0.7 km depth) is, even at normal stresses corresponding to 2 km, 1-2 orders of magnitude lower than the fault gouge. Gouge-filled faults are therefore more likely to act as a leakage pathway.
3) The permeability of simulated clay-quartz-calcite fault gouge will increase, thereby reducing the sealing capacity, irrespectively of fluid flow orientation, if the pore fluid pressure in a fault zone increases due to migration of supercritical CO_2 from a storage reservoir. Moreover, leakage along a fault into an over- or underlying formation is easier than leakage across the fault into neighbouring reservoir compartments (~1 order of magnitude anisotropy in permeability).

4) Frictional strength decreases with increasing effective stress, illustrating an effect of cohesion on the resistance to shear observed at low effective normal stress (<25 MPa).
5) At ~20, 60 and 100°C, the steady-state frictional strength of the OPA-derived fault gouge was found to be consistently 10-20% stronger than calcite-free OPA gouge, i.e. ~0.30 versus. 0.27, which was temperature insensitive (up to 150°C in case of the OPA gouge). Both fault gouges exhibited velocity-strengthening behaviour at the temperatures studied (20-150°C OPA, 20-100°C CFOPA).
6) Drying of clay-quartz-calcite fault gouge, via desiccation induced by dry CO_2 through flow can roughly double the frictional strength of a fault gouge, while maintaining stable, velocity-strengthening slip behaviour. Overall, the rate-and-state friction parameter (*a*-*b*) for dry material is slightly lower than for the wet OPA samples.

Acknowledgements

This research has been carried out in the context of the ULTImateCO_2-program. ULTImateCO_2 is a research program on Understanding the Long-Term fate of geologically stored CO_2 and is financially supported by the European Union (FP7). We thank Dr. Christophe Nussbaum (The Mont Terri rock laboratory) for providing the sample material. EB thanks ULTImateCO_2 for providing funding for the research. Eimert de Graaff, Gert Kastelein, Peter van Krieken and Thony van der Gon Netscher are thanked for their technical support.

Chapter 4

Effects of carbonate content on the frictional properties of clastically-derived fault gouges

Elisenda Bakker, André R. Niemeijer and Christopher J. Spiers

Abstract

We investigated the effect of calcite content on the frictional behaviour of simulated clay-quartz-calcite fault gouge mixtures. The primary samples used were prepared from crushed Opalinus Claystone (OPA), from which the natural carbonate was dissolved (Calcite-Free or CFOPA) and replaced with systematically varied amounts of added calcite powder. We also performed tests on kaolinite-calcite and quartz-calcite mixtures, investigating 100% pure end-members plus 50:50 combinations. Ring-shear experiments (σ_n^{eff} = 50 MPa, P_f = 25 MPa, and $T \approx$ 23-100-150°C) showed that at 23 and 100°C, the steady- state frictional strength (μ_{ss}) and the velocity-dependence parameter (a-b), for CFOPA-calcite and kaolinite-calcite mixtures, increase with increasing calcite content. At these temperatures, all gouges exhibited stable, velocity-strengthening behaviour. A transition to velocity-weakening behaviour was observed between 100 and 150°C for CFOPA-calcite mixtures containing >90% calcite. Kaolinite-bearing samples showed velocity-strengthening behaviour only. The 100% quartz, 50:50 quartz-calcite and 100% calcite samples showed an increase in μ_{ss} with increasing calcite content at 23°C, but no clear trend at 100 and 150°C. At 23 and 100°C, all quartz-calcite samples exhibited velocity-strengthening behaviour, whereas a transition to velocity-weakening occurred between 100 and 150°C for the 50:50 quartz-calcite and the 100% calcite samples. Highly unstable, velocity-weakening behaviour was exhibited in the 50:50 quartz-calcite mixtures, with (a-b) values being lower than obtained for either end-member. Microstructural observations on the CFOPA-calcite mixtures suggest a change in controlling microscale processes with increasing calcite content, from shear within phyllosilicate-rich boundary and R_1-shear bands, in clay-rich samples, to more homogenously distributed cataclastic grain size reduction in calcite-rich samples. The transition from velocity-strengthening to velocity-weakening, at T >100°C calcite contents >90% in the CFOPA samples, suggests the growing importance of thermally-activated compaction processes at calcite-calcite grain contacts, such as diffusion. Our results have important implications for faults cutting calcite-rich claystones and shale formations that seal hydrocarbon reservoirs and potential CO_2 storage reservoirs, pointing to high seismogenic potential at calcite contents >90% or even >50% in quartz-calcite gouges at temperatures of 150°C.

4.1 Introduction

Carbonate-rich claystones and shales, containing biogenic calcite, primary calcite and/or calcite cement, form a major proportion of numerous sedimentary sequences around the world. Having generally low permeability, such rocks commonly form top-seals overlying hydrocarbon reservoirs. They may themselves constitute tight (shale) gas reservoirs or geothermal reservoirs. Understanding the properties of faults and fractures in these lithologies is accordingly of considerable importance in relation to i) hydrocarbons trapping (Aydin, 2000; R. J. Knipe et al., 1998), ii) the sealing of potential CO_2 storage systems (Aydin, 2000; R. J. Knipe et al., 1998), iii) shale gas and geothermal energy recovery, and iv) induced seismicity. Such lithologies are also frequent components of active fault systems present in subduction zones (Faulkner et al., 2011) and orogens at converging plate boundaries (Boulton et al., 2012), where major natural earthquakes occur. However, the frictional strength and slip stability of faults in carbonate-bearing claystone lithologies have received little attention, as have the transport properties of faults in such rocks.

Faults cutting carbonate-bearing claystones and shales generally contain fault gouge, with the proportion of gouge to clasts increasing rapidly with fault maturity (Vrolijk and Van Der Pluijm, 1999). Such fault gouges are polymineralic in nature, with varying amounts of clay, quartz and calcite (or dolomite) being present. Previous experimental research has demonstrated that the frictional strength and frictional slip stability of mixed gouges is determined by the mineral proportions present in the fault gouge (e.g. Byerlee, 1978; Moore and Lockner, 2004; Tembe et al., 2010; Verberne et al., 2010). Specifically, experiments investigating the frictional behaviour of binary and ternary clay-bearing gouge mixtures (Logan and Rauenzahn, 1987; Lupini et al., 1981; Tembe et al., 2010) have shown that gouge friction coefficient decreases with increasing phyllosilicate content and falls between the strengths of the pure end-member mineral components. However, most studies of mixed gouges to date have focused on quartz plus phyllosilicates (Crawford et al., 2008; Logan and Rauenzahn, 1987; Takahashi et al., 2007; Tembe et al., 2010), and, aside from a few recent studies (Chapter 2; Chen et al., 2015a; Giorgetti et al., 2015; Ikari et al., 2013; Tesei et al., 2012), the effect of calcite or other carbonate mineral content, on clastically-derived, clay- and/or quartz-rich gouge properties has remained relatively unexplored.

By contrast, the frictional behaviour of pure carbonate and carbonate-dominated gouges has been investigated extensively (Carpenter et al., 2016; Chen et al., 2015a; Collettini et al., 2011; Scuderi et al., 2013; Verberne et al., 2010). These studies have demonstrated an important role of calcite in causing frictional-weakening with increasing shearing velocity, hence potentially runaway seismogenic behaviour, notably at temperatures above about 80°C. For this reason, the effect of calcite on the frictional strength and stability of polymineralic gouge mixtures is gradually receiving more attention (Giorgetti et al., 2015). Nonetheless, numerous questions remain unanswered regarding both mechanical and transport properties. In particular, very little is known regarding how the proportion of calcite vs. clastically-derived minerals affects 1) the frictional strength and slip stability or seismogenic potential of gouge-filled faults, 2) the sealing capacity of calcite-bearing gouge mixtures during shear and static holding, and 3) the gouge microstructure and operative deformation mechanisms. Moreover, if calcite content does have a marked effect on mixed gouge behaviour, under what conditions and in what compositional ranges do these effects occur?

In an attempt to help answer these questions, this study experimentally investigates the effect of varying calcite content on the frictional behaviour of simulated clay-quartz-calcite fault gouge. The samples used were prepared from crushed blocks of Opalinus Claystone reference material (58-76% phylosilicates, 6-24% quartz, 6-34% carbonates and <2% pyrite) (Pearson et al., 2003), from which the natural carbonate was removed by dissolving it with a weak acid, then replacing it with systematically varied amounts of added calcite powder. In addition, the effects of added quartz and kaolinite content on the frictional behaviour of calcite powder were independently examined, using binary mixtures of these minerals with calcite powder. The experiments consisted of ring-shear tests performed under upper crustal conditions, i.e. at an effective normal stress (σ_n^{eff}) of 50 MPa, a pore pressure (P_f) of 25 MPa, and temperatures (T) of ~23, 100 and 150°C.

The primary motivation for the study lay in elucidating the frictional strength and seismogenic potential of faults in carbonate-bearing, clay-rich caprocks forming the top-seals to CO_2 storage reservoirs at depths of 2-4 km. To evaluate how faults in such caprocks behave in general, data on the behaviour of gouges with naturally varying compositions are essential. Moreover, penetration of CO_2 into the faults in

a clay-rich clastic capock might produce variations in calcite content through carbonate precipitation or leaching, so that properties determined for the initial composition might be modified. In addition, this study and the results presented are relevant for any type of natural, clay-bearing fault gouge containing significant amounts of calcite, and as such have important implications for the behaviour of tectonically active faults incorporating such gouges.

4.2 Methods

A total of 13 compositional mixtures were prepared and tested to investigate the effects of composition and temperature on the frictional properties of simulated clay-(phyllosilicate)-quartz-calcite fault gouges. We performed ring-shear experiments on the following three sample types:

1) Leached, calcite-free Opalinus Claystone material to which pre-determined amounts of pure calcite were added (Data-set 1),
2) Binary mixtures of pure kaolinite plus pure calcite (Data-set 2),
3) Binary mixtures of pure quartz plus pure calcite (Data-set 3).

4.2.1 Natural starting material: Opalinus Claystone

The Opalinus Claystone used in this study was collected from the Mont Terri Underground Rock Laboratory, Canton of Jura, Switzerland (Courtesy of Swisstopo, Dr. C. Nussbaum). The Middle Jurassic Opalinus Claystone is a relatively homogeneous, argillaceous sedimentary formation which was uniformly deposited in a shallow marine environment and can be found in large parts of Northern Switzerland (Pearson et al., 2003). The formation consists of three lithological sub-units, with the basal part of the formation being rich in clay minerals ("silty-shaly" facies), and the two other units being richer in either sand ("sandy" facies) or carbonate ("carbonate-rich-sandy" facies) (Pearson et al., 2003). The mineral assembly of the Opalinus Claystone Formation suggests a maximal burial temperature of about 80°C (Pearson et al., 2003).

The Opalinus Claystone (OPA) used in this study was taken from the "silty-shaly" facies. Conventional X-ray diffraction (XRD) analysis of five crushed samples of the OPA starting material indicated that the material consists of phyllosilicates (36-

Table 4.1. XRD data for the simulated gouges derived from the untreated OPAlinus and the Calcite-Free OPAlinus claystone simulated fault rock samples. Note: "n" denotes the number of each sample type analysed; "n.d." indicates that the corresponding phase is below the detection limit. Minerals left of the dotted line are considered frictionally strong, and minerals listed on the right side are frictionally weaker (e.g. Byerlee, 1978; Moore and Lockner, 2004).*Detailed XRD, including Rietveld refinement. **The mineral proportions for the CFOPA gouge were calculated using the mineral composition obtained for OPA (including the Rietveld refinement), assuming all calcite was removed by the leaching treatment applied to the crushed OPA material.

	"Strong" minerals					"Weak" minerals						
	Albite (mass-%)	Calcite (mass-%)	Dolomite (mass-%)	Pyrite (mass-%)	Quartz (mass-%)	Chamosite (chlorite) (mass-%)	Chlorite (mass-%)	Illite (mass-%)	Illite-smectite (mass-%)	Kaolinite (mass-%)	Muscovite (mass-%)	Phengite muscovite) (mass-%)
OPA Conv. XRD (*n* = 5)	6.6	12.23	1.17	n.d.	23.64	n.d.	n.d.	n.d.	n.d.	27.72	28.63	n.d.
	n.d.	40.13	n.d.	n.d.	28.31	19.82	n.d.	n.d.	n.d.	n.d.	n.d.	26.79
	n.d.	24.65	n.d.	1.76	27.81	19.47	n.d.	n.d.	n.d.	n.d.	n.d.	26.31
	n.d.	15.13	n.d.	n.d.	20.68	8.49	n.d.	n.d.	n.d.	n.d.	42.20	13.50
	n.d.	22.05	n.d.	n.d.	41.50	12.73	n.d.	n.d.	n.d.	n.d.	23.73	n.d.
OPA* (*n* = 1)	n.d.	26	n.d.	4	23	n.d.	4.23	5.17	24.4	13.16	n.d.	n.d.
CFOPA Conv. XRD (*n* = 3)	n.d.	n.d.	n.d.	1.65	29.53	n.d.	15.24	n.d.	n.d.	17.15	36.42	n.d.
	n.d.	n.d.	n.d.	2.16	40.70	12.56	20.72	n.d.	n.d.	n.d.	n.d.	23.86
	n.d.	n.d.	n.d.	3.45	38.85	16.65	n.d.	n.d.	n.d.	n.d.	41.04	n.d.
CFOPA**	n.d.	-	n.d.	5.41	31.08	n.d.	5.72	6.99	33.03	17.78	n.d.	n.d.

64%), quartz (20-42%), calcite (13-40%), feldspar (~7%) and pyrite (4%) (Table 4.1). Detailed XRD analysis of one further sample, including a full Rietveld refinement, showed an OPA composition consisting of phyllosilicates (47%), quartz (23%), calcite (26%) and pyrite (4%) (Table 4.1), which is closely in line with published data (Pearson et al., 2003).

4.2.2 Sample preparation

In order to test the effect of increasing calcite content on the frictional properties of clay-quartz-calcite fault gouge (Data-set 1), we first removed the calcite present in the OPA starting material by crushing cm-sized samples using a pestle and mortar. The resulting powder was then treated with acetic-acid ($C_2H_4O_2$; pH 3) at ~20°C. The clay-acid mixture was subsequently heated, while being stirred, at 80°C in a water-bath for 24 hours, to remove any remaining calcite. After the acid-treatment, the calcite-free Opalinus (CFOPA) material was retrieved by washing, with demineralized water, centrifuging and drying it in a laboratory oven at 60°C for several days. Following drying, the dense, cohesive product was crushed again and sieved to a grain size <35 μm. Conventional XRD analysis of this CFOPA fraction showed a composition of around 55-70% phyllosilicates and 30-45% quartz (Table 4.1). The composition calculated based on the full, Rietveld-refined XRD analysis of OPA includes phyllosilicates (54%), quartz (31%), and pyrite (5.4%) (Table 4.1). All calcite and other carbonates were removed to sub-detection levels. Both techniques showed that the pure smectite content of the material was below measurement resolution, hence less than 1-2%, and up to 5% for measurements below 5%, for the refined analysis and <5% in the conventional analysis.

The calcite-free OPA-samples with subsequently added calcite (Data-set 1), and the binary mixtures of calcite plus kaolinite (Data-set 2) and calcite plus quartz (Data-set 3), were prepared by mixing the various components by weight. Aside from the sieved CFOPA material (<35 μm), we used natural quartz powder (99.9% pure; Beaujean quartz sand), kaolinite powder (100% pure; Merkx) and crushed calcite (Iceland spar; (Verberne et al., 2014; Verberne et al., 2013)). All mineral powders were sieved to obtain a grain size <35 μm before mixing. The binary mixtures of kaolinite plus calcite and quartz plus calcite, as well as the CFOPA plus calcite mixtures, were prepared in the proportions listed in Table 4.2.

4.2.3 Experimental apparatus and procedure

The friction experiments reported in this study were conducted using the hydrothermal rotary shear apparatus at Utrecht University (Figure 4.1 – Niemeijer et al. (2008); den Hartog et al. (2012)). The apparatus consist of a water-cooled, 300 MPa pressure vessel, in which the sample-piston assembly is located. This

Table 4.2. Overview of the experiments performed in this study, including key data on friction coefficient (μ) and velocity dependence (a-b). Samples were tested at a constant effective normal stress (σ_n^{eff} = 50 MPa) and pore pressure (P_f = 25 MPa), at temperatures (T) of 23°C, 100°C and 150°C using sliding velocities (V) between 0.22 and 100 µm/s.

Sample	*Composition*	μ_{peak} (V = 5.43 µm/s) *Stage*			μ_{ss} (at displacement mm) *Stage*			μ_{final} (at displacement mm) *Stage*			D_f (mm)	μ_i (-)	C_0 (MPa)	*Stick-slip; Stage#; Velocity* (µm/s)	*Microstructure*
		1	2	3	1	2	3	1	2	3					
					4	*14.7*	*25.4*	*10.7*	*21.4*	*32.1*					
Data-set 1 –CFOPA plus added calcite at σ_n^{eff} = 50 MPa, P_f = 25 MPa, and T=23, 100 and 150°C, V = 0.22-100 µm/s															
	CFOPA–Calcite														
RS001	50% - 50%	0.39	0.39	0.40	0.37	0.39	0.41	0.45	0.42	0.45	32.9	-	-	N	BS, Phase segregation
RS002	100% - 0%	-	0.27	0.30	0.28	0.28	0.30	0.33	0.32	0.31	32.9	-	-	N	Not preserved
RS003	0% -100%	0.73	0.72	0.69	0.71	0.65	0.60	0.73	0.69	0.58	32.9	-	-	Y;	BS and comminution
RS004	30% -70%	0.43	0.40	-	0.38	0.45	0.48	0.45	0.47	0.49	32.9	-	-	N	Phase segregation
RS005	10% -90%	0.56	0.54	0.58	0.48	0.57	0.56	0.56	0.58	0.58	40.7	-	-	N	Phase segregation
RS006	95% -5%	0.61	0.55	0.57	0.54	0.56	0.47	0.60	0.58	0.48	40.7	0.41	1.06	Y; #3; 0.22-3.0	BS, Phase segregation
RS010	95% -5%	0.58	0.54	0.58	0.51	0.54	0.51	0.56	0.58	0.53	32.9	0.50	0.49	Y; #3; 0.22-3.0	Phase segregation
Data-set 2 –Kaolinite plus added calcite at σ_n^{eff} = 50 MPa, P_f = 25 MPa, and T=23, 100 and 150°C, V = 0.22-100 µm/s															
	Kaolinite – Calcite														
RS012	100% - 0%	0.24	0.27	0.30	0.26	0.28	0.29	0.29	0.31	0.28	40.7	0.26	-0.37	N	Not investigated
RS009	50% - 50%	0.34	0.27	0.33	0.31	0.28	0.34	0.31	0.31	0.38	40.7	0.36	-0.53	N	Not investigated
RS003	0% - 100%	0.73	0.72	0.69	0.71	0.65	0.60	0.73	0.69	0.58	32.9	-	-	Y; #3; 0.22-3.0	BS and comminution
Data-set 3 –Quartz plus added calcite at σ_n^{eff} = 50 MPa, P_f = 25 MPa, and T=23, 100 and 150°C, V = 0.22-100 µm/s															
	Quartz – Calcite														Zonation, comminution
RS008	100% - 0%	0.61	0.69	0.72	0.63	0.63	0.66	0.62	0.66	0.58	40.7	0.54	1.64	N	
RS007	50% - 50%	-	0.68	0.69	0.68	0.59	0.66	0.63	0.63	0.59	40.7	0.57	1.40	Y; #3; 0.22 -10.86	Not investigated
RS014	50% - 50%	-	0.75	0.77	0.68	0.68	0.62	0.67	0.62	0.59	40.7	0.59	0.93	Y; #3; 1.086-10.0	BS, Phase segregation
RS003	0% -100%	0.73	0.72	0.69	0.71	0.65	0.60	0.73	0.69	0.58	32.9	-	-	Y; #3; 0.22-3.0	BS and comminution

Symbols: μ_{peak} = peak frictional strength at V = 5.43 µm/s, μ_{ss} = frictional strength at steady state at V = 5.43 µm/s and μ_{final} = frictional strength at the end of Stage 1, 2, 3 at V = 100 µm/s, D_f = final shear displacement, μ_i = internal friction, C_o = cohesions, and BS = boundary shear.

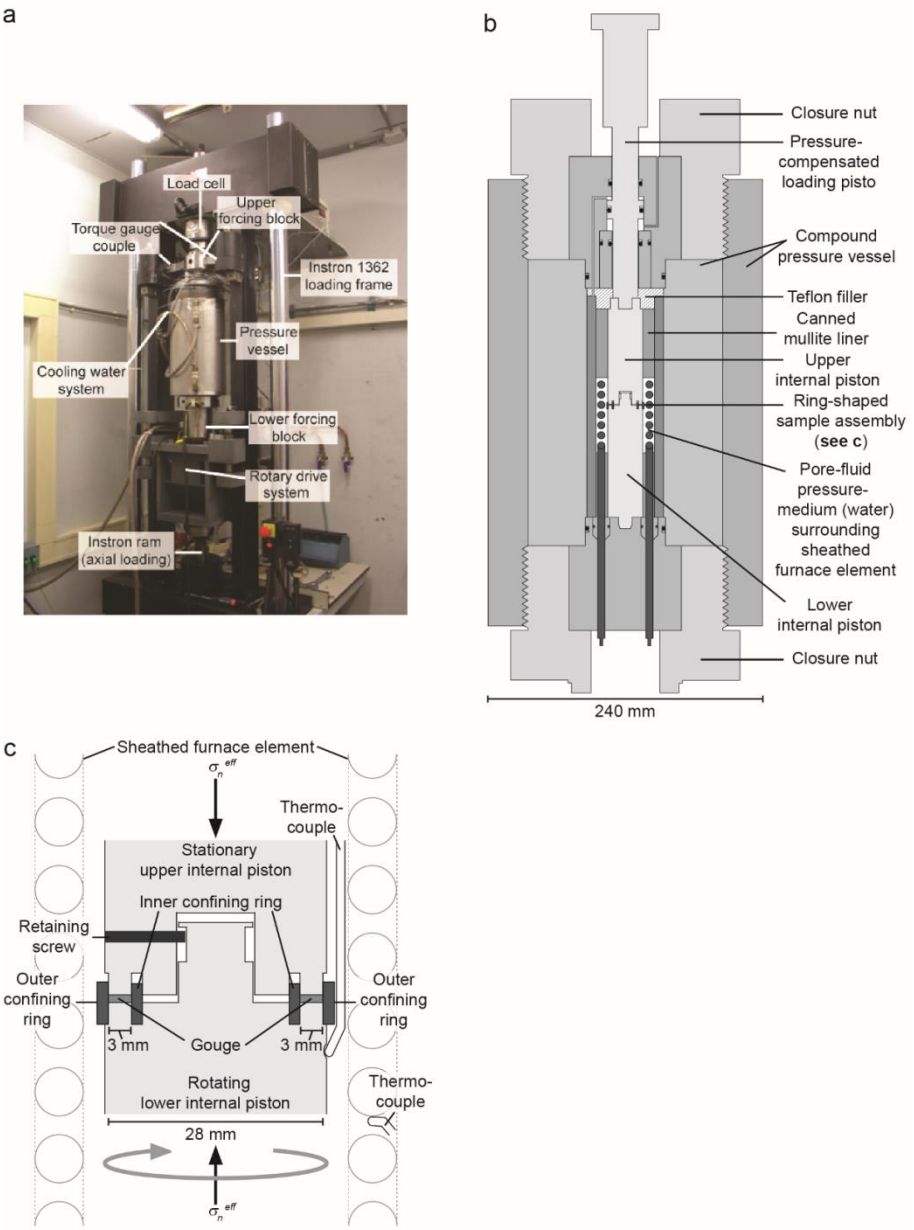

Figure 4.1. Experimental apparatus. a) Photograph of the ring-shear apparatus used in this study (after Niemeijer et al. 2008). The motor plus gearbox system constituting the rotational drive is installed behind the pressure vessel. b) Schematic representations of the pressure vessel. c) Schematic representation of the sample assembly (after Niemeijer et al., 2008, den Hartog et al, 2012).

vessel is positioned in an Instron 1362 servo-controlled loading frame, which is used to axially load the sample assembly via a pressure-compensated piston (Figure 4.1a and b). The resulting (effective) normal stress is externally measured using a 100 kN axial load cell. This is held constant via the load control function of the Instron machine, to within ~0.05 MPa. Demineralised water is used as the pore fluid phase and has direct access to the sample, providing a pore fluid pressure up to 300 MPa (resolution: ~0.015 MPa). The sample and surrounding pore fluid can be heated internally using a 3 kW, Inconel-sheathed furnace-element and external Eurotherm controller to temperatures up to 700°C. Temperature is regulated using a K-type thermocouple (accuracy: ~0.1°C), located on the furnace element close to the sample, and measured using a second thermocouple located just below the sample (~2 mm; Figure 4.1c). Displacement of the axial loading piston relative to the pressure vessel is measured externally using a linear variable differential transformer (LVDT; resolution: 0.005 mm). Shear is imposed on the sample by rotating the vessel plus lower piston, using a servo-controlled motor and gearbox system located on the Instron loading ram, while the upper pressure-compensated piston is held fixed by a torque bar. Sliding velocities range between ~0.010 and 300 µm/s, for displacements up to ~120 mm. The torque and hence shear stress supported by the torque bar and sample are measured using two external load cells (resolution: 0.006 MPa) located at the extremities of the torque bar. Shear displacement is measured, in terms of vessel rotation relative to the Instron frame, using a geared potentiometer (resolution: 0.001 mm).

Note that the normal stress (σ_n) applied to the pressure compensated piston is measured in excess of the pore fluid pressure (P_f). Assuming that the sample is fully saturated by the fluid at pore fluid pressure P_f (Den Hartog et al., 2012a), then the effective normal stress (σ_n^{eff}) experienced by the sample is equal to the axially applied stress σ_n (minus a small stress supported by seal friction in the internal system; Figure 4.1b). As a result, the total normal stress acting on the sample is (σ_n^{eff}+ P_f) and the effective normal stress is not significantly affected by changes in pore fluid pressure.

The experiments were performed on ring-shaped layers of simulated fault gouge with an inner diameter of 22 mm, an outer diameter of 28 mm (i.e. a width of 3 mm), and a thickness of ~1 mm. The sample assembly is shown in Figure 4.1c. Note the confining rings preventing sample extrusion. The gouge layer was prepared by

depositing the simulated gouge powder on the lower piston with the inner and outer confining rings in place, distributing it evenly with a specially-designed PVC spreading tool and then placing the upper piston on top. The gouge layer is then sandwiched between the grooved surfaces of the upper and lower pistons and kept in place by confining rings. Note that the upper and lower pistons and confining rings are composed of René-41 super-alloy.

Rotary shear experiments were performed by first applying an effective normal stress of 50 MPa, followed by the pore fluid pressure of 25 MPa and subsequently allowing the system to thermally and mechanically equilibrate at room temperature for ~30 minutes. After equilibration, the experiments were performed in three stages. During Stages 1, 2 and 3, respectively performed at ~23, 100 and 150°C, the gouge layers were sheared to a total displacement of 10.9 mm, first at a sliding velocity of 5.43 µm/s for 4.2 mm, and then employing a velocity-stepping sequence. The velocity stepping sequence employed was 0.22-1.086-10.86-1.086-3-10-30-100 µm/s. After shearing at the final velocity step imposed in Stage 1, the furnace was switched on to heat the sample to 100°C in about 10-15 minutes while maintaining a constant effective normal stress and an approximately constant pore pressure. After re-establishing thermal and mechanical equilibrium, the sliding velocity was again stepped following the same sequence as in Stage 1. This procedure was repeated for a third temperature of 150°C. As the samples were sheared for 10.9 mm during Stages 1-3, this resulted in a combined (uncorrected) displacement of 32.7 mm. In most but not all experiments, Stage 3 was followed by Stage 4, which consisted of a series of normal stress steps, from 50 to 60, 80 and 100 MPa, performed at 150°C over a displacement of 2 mm per step, at a constant sliding velocity of 10 µm/s. These experiments reached a maximum total (uncorrected) displacement of 40.7 mm. All experiments were terminated by removing the torque and axial load, turning off the furnace, allowing the sample to cool to ~50°C (~30 minutes) and finally removing the pore pressure and normal stress.

4.2.4 Data acquisition and processing

The shear displacement, and axial displacement, normal force, torque, pore fluid pressure and sample temperature signals were acquired at a 900 Hz sampling frequency using a 16 bit A/D converter. The data were logged at frequencies of 10-

100 Hz, depending on the sliding velocity. Torque and normal force data were corrected for pre-determined seal friction to obtain the average shear stress (τ) at a radius of 12.5 mm and the effective normal stress (σ_n^{eff}) acting on the sample layer. Shear displacement (x) was corrected for pre-calibrated machine stiffness (distortion). The apparent friction coefficient μ was calculated as the ratio of shear stress to effective normal stress, $\mu = \tau/\sigma_n^{eff}$, ignoring cohesion. Henceforth, the apparent friction coefficient is referred to as the friction coefficient.

The velocity-dependence of μ was interpreted in the framework of the rate-and-state dependent friction (RSF) theory (Dieterich, 1979, 1978; Ruina, 1983), in combination with the "slowness" formulation of Dietrich, i.e. using:

$$\mu = \mu_0 + a \ln\left(\frac{V}{V_0}\right) + b \ln\left(\frac{V_0\theta}{D_c}\right) \qquad \text{with} \qquad \frac{d\theta}{dt} = 1 - \frac{V\theta}{D_c} \tag{4.1}$$

[e.g *Marone*, 1998]. Here, θ is a gouge state variable, a reflects the magnitude of the instantaneous change in μ upon an instantaneous change in sliding velocity from a reference velocity V_0 to a velocity $V = exp\ V_0$, b represents the magnitude of the change in μ during subsequent evolution to a new steady-state value over a characteristic slip distance D_c, and μ_0 is the steady-state friction coefficient determined at the reference velocity V_0. A stepwise change in sliding velocity, represented as $\Delta\ ln\ V = ln\ (V/V_0)$, yields a change in steady-state friction coefficient $\Delta\mu_{ss}$. From (4.1), it follows that the velocity-dependence of steady-state frictional strength can be quantified via the parameter (a-b), given:

$$(a\text{-}b) = \frac{\Delta\mu_{ss}}{\Delta lnV} \tag{4.2}$$

If the steady-state friction coefficient increases with increasing sliding velocity, (a-b) is positive. This is known as "velocity-strengthening" behaviour and implies that the system is inherently stable. Seismogenesis due to accelerating frictional slip is therefore impossible (e.g. Scholz, 1998). Negative (a-b) values on the other hand, indicate potentially unstable, "velocity-weakening" behaviour, meaning that the friction coefficient decreases with increasing velocity, which is one of the requirements for regular stick-slip, i.e. for seismogenic slip. In the experiments exhibiting stable sliding, values for a, b, (a-b) and D_c for individual velocity-steps were obtained using the rate-and-state friction tool within the XLook program, which was kindly made available by C. Marone (PSU) (Blanpied et al., 1998;

Marone, 1998), to fit Equation (4.1) to our friction data. In the case that our data showed minor slip-strengthening or weakening we applied the detrending procedure for μ versus shear displacement curves described by Blanpied et al. (1998). Within XLook, the interaction between the gouge material and the elastic surroundings is described via the relation:

$$\frac{d\mu}{dt} = S\left(V_{lp} - V\right) \tag{4.3}$$

Here *S* is the shear stiffness of the fault zone plus surroundings (or in experiments, the gouge layer plus the shear apparatus) corrected for normal stress effects, V_{lp} is the load point velocity and *V* is the fault shearing velocity. With Equation (4.3) as a constraint, Xlook combines and solves Equation (4.1), using a fifth-order Runge-Kutta method. The constitutive parameters are then obtained as solutions to the nonlinear inverse problem using an iterative least squares method (Blanpied et al., 1998; Reinen and Weeks, 1993; Saffer and Marone, 2003). For the velocity-steps in which we observed stick-slip events, the maximum (peak) friction coefficient was taken as the steady-state friction coefficient and graphically used to estimate $\Delta\mu_{ss}$ and hence obtain apparent (*a*-*b*) values at consecutive velocities. Note that using average rather than peak friction values here made virtually no difference to the (*a*-*b*) values obtained.

As indicated already, for all experiments, the coefficient of friction was calculated as the ratio of the shear stress to the effective normal stress. Following Den Hartog et al. (2012), the cumulative relative error in μ in these experiments, including the effects of uncertainties in seal friction correction and sensor accuracy/linearity, is estimated to be ±3.8%. Absolute errors in (*a*-*b*) are at most ± 0.00078, with a single extreme value of ± 0.0025.

4.2.5 Sample recovery and microstructural analysis

After completing each experiment, the entire sample assembly (i.e. the sample plus upper-lower internal piston assembly) was extracted from the ring-shear machine and dried at 50°C in a laboratory oven for 12-24 hours. Upon subsequent disassembly, the gouge layers generally split into small, shear-band controlled fragments or flakes. Most recovered sample flakes were of sufficient quality for microstructural analysis. These were impregnated with Araldite 2020 epoxy resin and left for several days for the resin to harden. The completeness of the gouge

layers upon extraction from the sample assembly strongly depended on the density, configuration and cohesion of the shear bands present. Selected impregnated samples were wafer-sawn tangential to the shear direction and normal to the shear plane, and used to prepare thick sections, which were then analysed using optical and electron microscopy.

Incident light analysis of the selected thick sections was conducted using a Leica DMR polarizing light microscope. Carefully chosen areas were then analysed in more detail using a FEI XL-30S FEG scanning electron microscope (SEM), using a FEI Nova Nanolab 600 Focused Ion Beam (FIB)–SEM and using a FEI Helios 650UC FIB-SEM, equipped with a retractable, concentric backscatter detector (CBS). Qualitative chemical analyses of specific areas of selected samples were carried out using the electron dispersive X-ray (EDX) detector installed in the FEI Helios 650UC FIB-SEM. In all SEM work, the samples were imaged in backscatter electron (BSE) mode, using an acceleration voltage of 10-15 kV. Note that the samples selected for microstructural study corresponded to Data-set 1 (CFOPA-calcite) and Data-set 3 (quartz-calcite).

4.3 Results

A list of all experiments performed, the corresponding experimental conditions and key data obtained in Stages 1-3 is given in Table 4.2. The data presented include the friction coefficient measured at steady-state (μ_{ss}) for the three temperatures investigated at shear displacements of ~4.0, ~10.7 and ~25.4 mm, distinguishing Data-set 1 (CFOPA-calcite samples), Data-set 2 (kaolinite-calcite samples) and Data-set 3 (quartz-calcite samples). We will first describe the frictional behaviour seen in Stages 1-3 of our experiments. Results on frictional strength and its velocity dependence (a-b) are depicted in Figures 4.2-4.4.

To avoid cluttering Table 4.1 and Figure 4.2, the response of shear stress to the step-wise increases in effective normal stress, applied in experiments featuring Stage 4, is not shown in Figure 4.2 but in Figure 4.5. This displays yield or peak strength as a function of effective normal stress. Values at yield or peak are chosen to exclude any effects of strain-hardening. Here, yield is taken as the point of

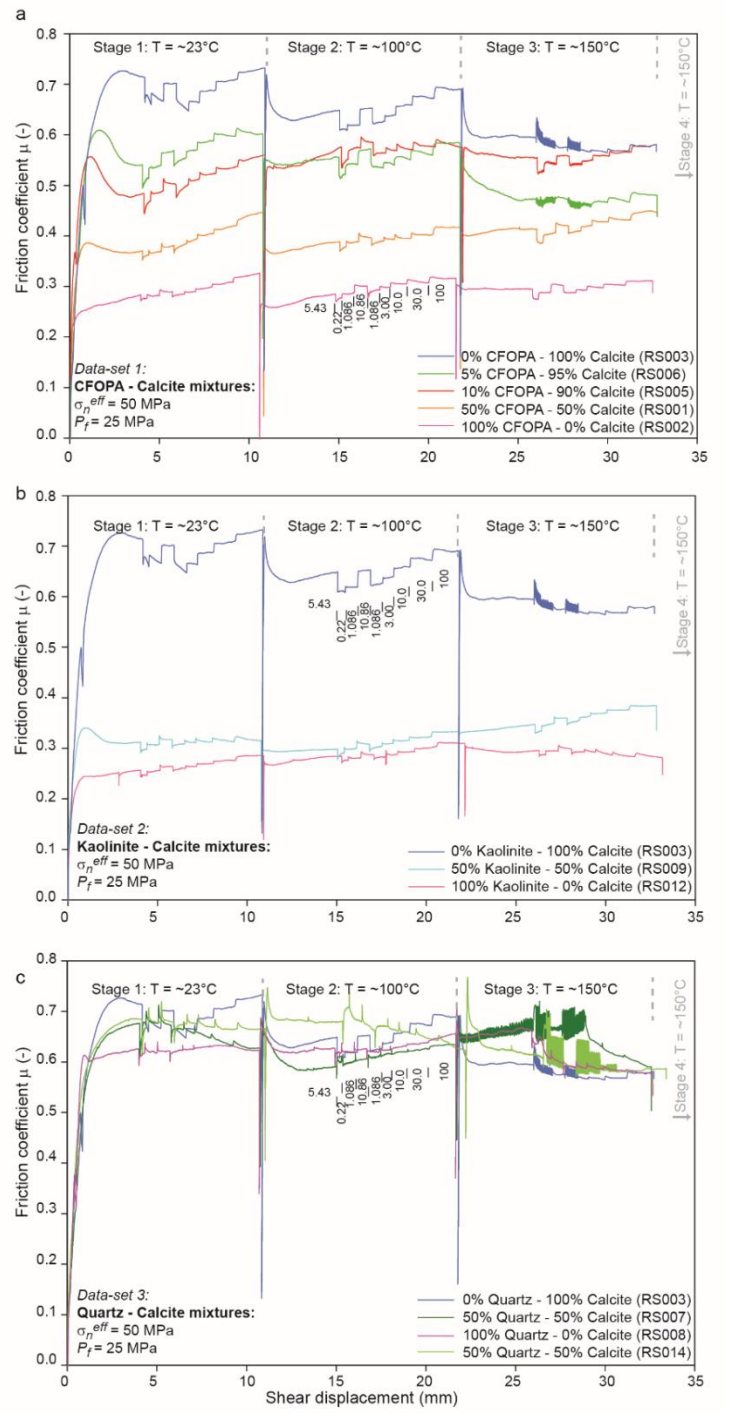
a
Stage 1: T = ~23°C
Stage 2: T = ~100°C
Stage 3: T = ~150°C
Stage 4: T = ~150°C
Friction coefficient μ (-)
5.43
0.227
1.086
10.86
1.086
3.00
10.0
30.0
100
Data-set 1:
CFOPA - Calcite mixtures:
σn eff = 50 MPa
Pf = 25 MPa
0% CFOPA - 100% Calcite (RS003)
5% CFOPA - 95% Calcite (RS006)
10% CFOPA - 90% Calcite (RS005)
50% CFOPA - 50% Calcite (RS001)
100% CFOPA - 0% Calcite (RS002)
b
Stage 1: T = ~23°C
Stage 2: T = ~100°C
Stage 3: T = ~150°C
Stage 4: T = ~150°C
Friction coefficient μ (-)
Data-set 2:
Kaolinite - Calcite mixtures:
σn eff = 50 MPa
Pf = 25 MPa
0% Kaolinite - 100% Calcite (RS003)
50% Kaolinite - 50% Calcite (RS009)
100% Kaolinite - 0% Calcite (RS012)
c
Stage 1: T = ~23°C
Stage 2: T = ~100°C
Stage 3: T = ~150°C
Stage 4: T = ~150°C
Friction coefficient μ (-)
Data-set 3:
Quartz - Calcite mixtures:
σn eff = 50 MPa
Pf = 25 MPa
0% Quartz - 100% Calcite (RS003)
50% Quartz - 50% Calcite (RS007)
100% Quartz - 0% Calcite (RS008)
50% Quartz - 50% Calcite (RS014)
Shear displacement (mm)

←**Figure 4.2. (see previous page)** Typical evolution of friction coefficient with shear displacement obtained in the present experiments tested at σ_n^{eff} = 50 MPa, P_f =100 MPa and T =~23, 100 and 150 °C. Velocity steps are indicated in μm/s, with the location of a change in velocity indicated using vertical "ticks". a) Effect of calcite fraction on the frictional strength of calcite-free OPA (CFOPA) plus added calcite mixtures (RS001-RS006, and RS010 - Dataset 1). b) Effect of calcite fraction on the frictional strength of kaolinite plus added calcite mixtures (RS003, RS009, and RS012 - Data-set 2). c) Effect of calcite fraction on quartz plus added calcite mixtures (RS003, RS007, RS008, and RS014 - Data-set 3). Note that to avoid cluttering of the plots, peak or yield values, obtained during the normal stress stepping sequence of Stage 4, are plotted as a function of effective normal stress in Figure 4.5 for all three data-sets. Peak or yield values, in absence of a clear peak, are taken to exclude strain-hardening effects.

maximum curvature of the friction coefficient vs. shear displacement curve in the run-in portion of Stage 4 in individual experiments. The relation between shear stress and effective normal stress provide a basis for assessment of the assumption of zero cohesion in taking $\mu = \tau/\sigma_n^{eff}$ (e.g. as depicted in Figure 4.2).

Our microstructural observations are illustrated in Figures 4.6-4.9. Because of the complex, multi-stage nature of the experiments (Figure 4.2 – Table 4.2), the observed microstructural features represent the net microstructural character of the samples. History effects might therefore be present, making interpretation in terms of temperature, velocity, normal stress or strain effects difficult. We therefore focus on relating microstructural differences between samples to differences in composition.

4.3.1 Frictional behaviour

Data on the frictional behaviour obtained for the three types of mixtures tested (i.e. Data-sets 1, 2 and 3) will be presented in the following three sub-sections. Note, from Table 4.2, that the 100% calcite sample forms part of all three data-sets. To avoid repetition, a detailed description of the data obtained from this experiment will be presented under Data-set 1 only.

4.3.1.1 CFOPA-calcite mixtures (Data-set 1)

Representative curves showing the evolution of friction coefficient (μ) as a function of shear displacement (x) in Stages 1-3 of the experiments on the CFOPA-calcite mixtures are shown in Figure 4.2a. Note the general increase in frictional strength level with increasing calcite content from ~0.3 for CFOPA (0% calcite) to ~0.7 for

the 100% calcite sample. Stage 1 (~23°C) of the 100% CFOPA (RS002) curve is characterised by a near-linear increase in μ, followed by apparent yielding and subsequent slip-hardening at a steady rate in the first and most subsequent velocity-intervals. All experiments with added calcite showed a similarly rapid increase in μ in Stage 1, followed by apparent yielding and slip-hardening towards a peak frictional strength at a displacement x of 0.6-2.9 mm. This is followed by slip-weakening towards (near) steady-state, reached at ~4 mm shear displacement at the initial sliding velocity of 5.43 µm/s. In all experiments, the subsequent velocity up-steps to the final sliding velocity of 100 µm/s, showed a clear and positive effect on the friction coefficient, i.e. an increase in the (near) steady-state frictional strength with increasing sliding velocity.

After increasing the temperature to 100°C and subsequently 150°C, in Stages 2 and 3 respectively, the frictional strength of the samples containing zero to 90% calcite remained roughly constant at each velocity investigated, or showed a slight increase with respect to the room temperature values (Figure 4.2a). By contrast, the samples containing ≥95% calcite showed a decrease in frictional strength in Stage 2 (100°C) and subsequently Stage 3 (150°C).

Overall, the steady-state frictional strength of the samples increased with increasing calcite content, with the strength of each mixture falling between the strengths of the two end-members, i.e. between the CFOPA (weakest - $\mu_{ss} \approx 0.27$) and the pure calcite (strongest - $\mu_{ss} \approx 0.71$; Figure 4.2a – Table 4.2). Only the 95% calcite sample deviated from the overall trend, becoming weaker than the 90% calcite sample in Stages 2 and 3. The dependence of yield or peak and steady-state strength on composition at the initial sliding velocity of 5.43 µm/s in Stage 1 is depicted explicitly in Figures 4.3a and b, where these quantities are plotted as a function of calcite content. Note the modest increase in frictional strength between 0-70% calcite, followed by a steeper increase between 70 and 100% calcite. The increase in strength is particularly steep between 95 and 100%, being almost one-third of the difference in strength between the two end-members. Similar trends apply in Stage 2 (100°C) and Stage 3 (150°C), again with the exception of the 95% calcite sample which becomes anomalously weak at elevated temperature.

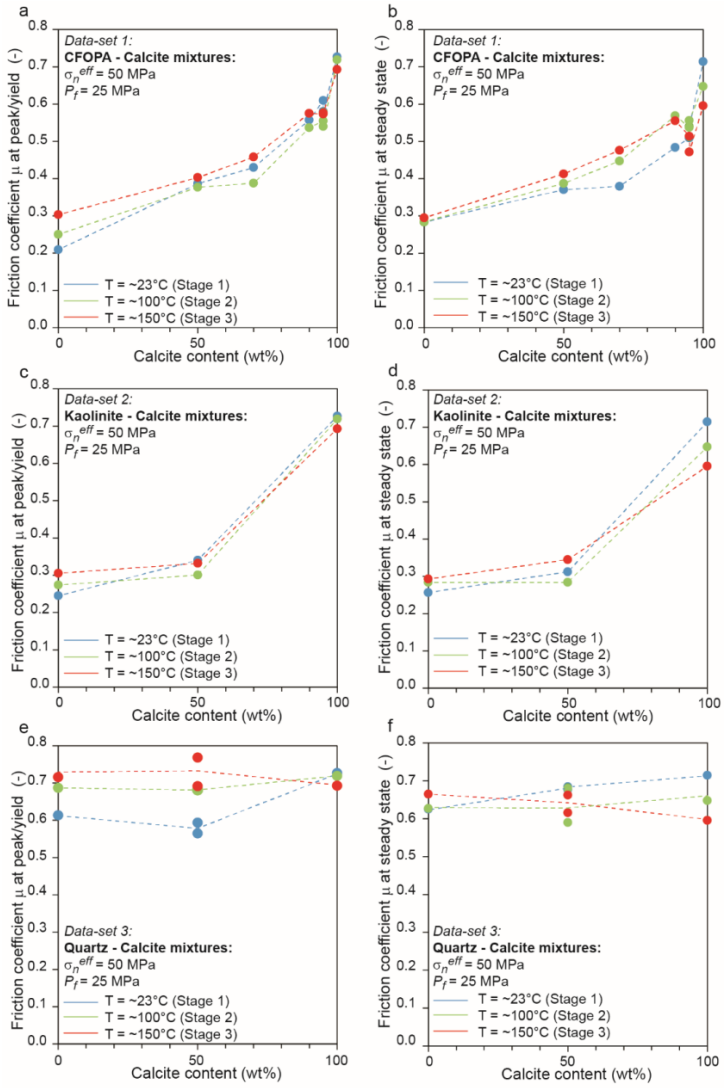

Figure 4.3. Friction coefficient at yield and at steady-state (at 5.43 mm/s) as a function of calcite content tested at σ_n^{eff} = 50 MPa, P_f =100 MPa and T =~23, 100 and 150 °C a) Effect of calcite fraction on the frictional strength at yield for calcite-free OPA (CFOPA) plus added calcite mixtures (Data-set 1). b) Effect of calcite fraction on the frictional strength at steady- state for calcite-free OPA (CFOPA) plus added calcite mixtures (Data-set 1). c) Effect of calcite fraction on the frictional strength at yield for kaolinite plus added calcite mixtures (Data-set 2). d) Effect of calcite fraction on the frictional strength at steady-state for kaolinite plus added calcite mixtures (Data-set 2). e) Effect of calcite fraction on the frictional strength at yield for quartz plus added calcite mixtures (Data-set 3). f) Effect of calcite fraction on the frictional strength at steady-state for quartz plus added calcite mixtures (Data-set 3).

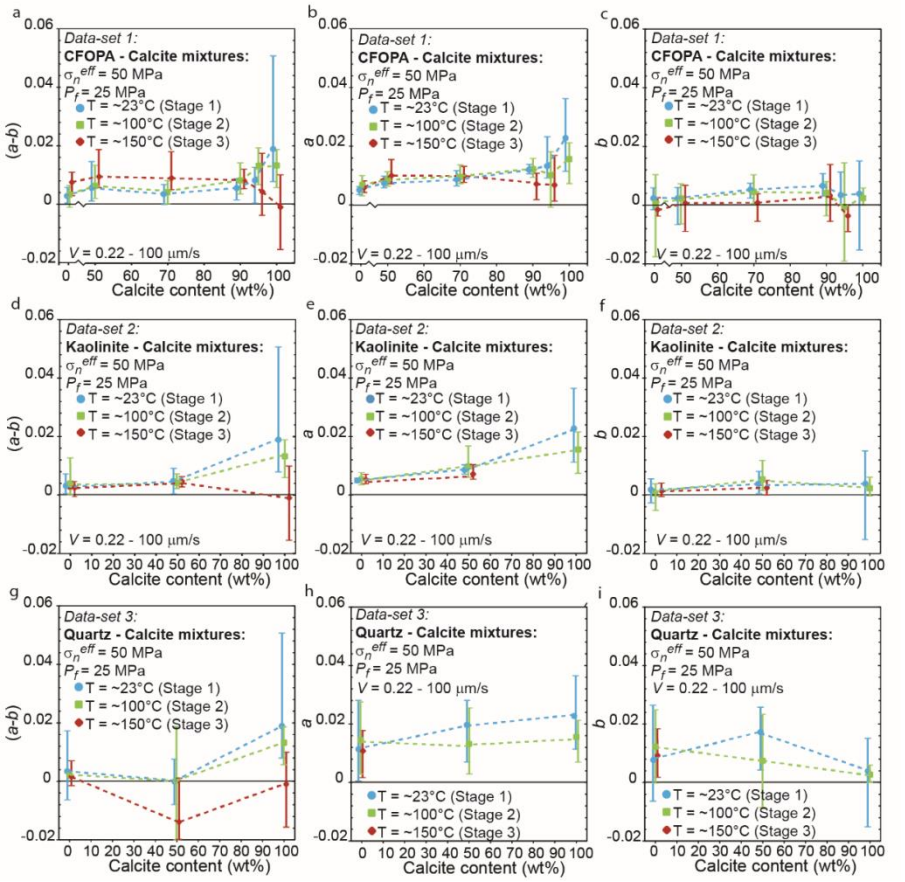

Figure 4.4. Friction parameters for velocity up-steps plotted as a function of calcite content for ~23°C (Stage 1), 100°C (Stage 2) and 150°C (Stage 3). Note that the symbols represent the average value of (*a*-*b*), *a* or *b*, respectively, whereas the vertical bars represent the range of the parameters and not the error to the respective values. Each average and range is based on 6 (*a*-*b*), *a* or *b* values determined in 6 velocity up-steps. Data available from author. a) (*a*-*b*) values for the CFOPA-calcite mixtures, showing an increase with calcite content, and a transition to negative values at 150°C, for >90%. b) The "direct effect" *a* increases with increasing calcite content at room temperature, and *a* decrease at 150°C for >90% calcite. c) The "evolution effect" *b* is positive at room temperature remaining constant with calcite content, whereas at 150°C *b* is weakly negative. d) Values (*a*-*b*) for the kaolinite-calcite mixtures increases with calcite content, transitioning to negative values at 150°C, for 100%. e) Values for *a* increase with increasing calcite content at 23°C and 100°C. f) Values for *b* are positive and negative at 23°C and 100°C remaining more or less constant with calcite content. g) (*a*-*b*) values for the quartz-calcite mixtures show an U-shaped trend with increasing calcite content, and a transition to negative values at 150°C, for

>50% calcite. h) Values for *a* increase with increasing calcite content at room temperature and are constant at 100°C. i) Values for *b* are positive at room temperature, showing an increase at 50% calcite content and a decrease at 100°C. In Figure 5b-c, e-f, h-I, the negative values for *a* and *b* separately are missing for >90% calcite, as these could not be determined.

At room temperature and 100°C (Stages 1 and 2), stable, velocity-strengthening behaviour is observed for all mixtures at all sliding velocities. However, a transition from stable to unstable, stick-slip behaviour is observed for the mixtures consisting of >90% calcite at a temperature of 150°C (Figure 4.2a). The velocity dependence of μ_{ss}, expressed in terms of (*a*-*b*), is plotted as a function of calcite content for velocity up-steps in Figure 4.4a. All experiments performed at 23°C and 100°C exhibit stable, velocity-strengthening behaviour (i.e. (*a*-*b*) > 0), except for the 100% CFOPA (0% calcite) gouge at 100°C (1.1 µm/s), which is just negative. In this temperature range of 23-100°C, (*a*-*b*) shows a weak increase with increasing calcite content up to ~70%, after which the increase steepens. At 150°C (Stage 3; Figure 4.4a), the majority of the CFOPA-calcite mixtures continues to show stable, velocity-strengthening behaviour, reflected by increasing (*a*-*b*) values up to ~50% of calcite. Above 90% calcite, the 150°C data are characterised by both velocity-strengthening and velocity-weakening behaviour, and by a decrease in mean (*a*-*b*) value, with velocity-weakening occurring at 0.2-1.1 µm/s (Figure 4.4a), where stick-slip is also observed. Note, however, that stick-slip behaviour was obtained in the 90% calcite experiments at 150°C (Figure 4.2a), though the corresponding (*a*-*b*) values remained positive for the unstable velocity steps, suggesting velocity-strengthening behaviour.

Plotting *a* and *b* separately (Figures 4.4b and c), for temperatures of 23°C and 100°C, shows that both parameters increase with increasing calcite content. This increase is more pronounced in *a* than in *b*, with the latter remaining close to zero (taking positive and negative values). Most of the negative values for *b* are obtained for the velocity-steps of 3-10, 10-30 and 30-100 µm/s. Additionally, with increasing calcite content, the values obtained for *a* and *b* show a wider spread. At 150°C, *a* continues to show an increase with increasing calcite content between 0 and 70%, steadying between 70 and 100%, whereas *b* shows a transition from predominantly positive to predominantly negative values for calcite contents above 90%. Although not explicitly shown in Figure 4.4, the velocity-dependence (*a*-*b*), obtained for individual samples at 150°C, depends on the sliding velocity, with

negative values of (*a*-*b*) being obtained mostly at low velocities and positive values at high velocities (*V* >3.0 µm/s).

4.3.1.2 Kaolinite-calcite mixtures (Data-set 2)

The μ vs. shear displacement curves for the kaolinite-calcite samples are shown in Figure 4.2b. In Stage 1 (~23°C), both the 100% kaolinite and the 50:50 kaolinite-calcite sample showed a rapid, near-linear increase in μ in the first 0.3-0.4 mm of displacement at *V* = 5.43 µm/s. This was followed by apparent yielding and subsequent slip-hardening towards a peak frictional strength of 0.23-0.33 at a displacement *x* of 1.0-1.1 mm, followed by minor slip-weakening before reaching near steady-state at ~2-3 mm, and then gentle slip-hardening (100% kaolinite) or else gentle slip-weakening (50:50 mixture). A modest effect of the successive velocity-steps on the friction coefficient of ~0.3 was observed. Overall, the frictional strength increased slightly with increasing sliding velocity, demonstrating velocity-strengthening behaviour. The effects on the 100% kaolinite and 50:50 kaolinite-calcite samples of an increase in temperature, to 100°C (Stage 2) and then 150°C (Stage 3), are relatively minor. The effects of shear displacement and sliding velocity are also relatively minor in Stages 2 and 3. Throughout Stages 1-3, the frictional strength for the 50:50 kaolinite-calcite mixture (μ_{ss} = 0.28-0.34) falls between the strength of the pure kaolinite (weakest - μ_{ss} = 0.26-0.29) and pure calcite (strongest - μ_{ss} =0.60-0.71) end-members, with the sharpest increase in μ_{ss} occurring between 50 and 100% calcite (Figures 4.3c and d).

The velocity-dependence, for velocity up-steps, for calcite contents of 0 and 50% are characterized by positive (*a*-*b*) values for all three temperatures (Stages 1-3) (Figure 4.4d), with the (*a*-*b*) values for the 50:50 kaolinite-calcite sample being slightly higher than for the pure kaolinite sample. The pure calcite sample, as already discussed, exhibited velocity-strengthening at ~23 and 100°C (Stages 1 and 2), but velocity-weakening at 150°C (Stage 3; Figure 4.4d). The parameters *a* and *b* increase slightly with increasing calcite content between 23°C and 100°C (Figures 4.4e and f), with *a* showing a more pronounced increase than *b*, which remains close to zero (positive and negative). Most of the negative values for *b* are obtained in the 3-10, 10-30 and 30-100 µm/s velocity-steps. Moreover, the values obtained for *a* and *b* show a wider spread with increasing calcite content. Progressing from 100°C to 150°C, values of *a* continue to increase with increasing calcite content,

whereas *b* shows a transition from predominantly positive to predominantly negative values for a calcite content of 100%.

4.3.1.3 Quartz-calcite mixtures (Data-set 3)

The μ vs. shear displacement curves for the quartz-calcite samples are shown in Figure 4.2c. All curves exhibit steady friction levels in the range of 0.6-0.7. In Stage 1 (~23°C), the pure quartz sample showed a very rapid, near-linear increase in μ towards a peak frictional strength of ~0.6 and minor load drop at $x \approx 1.0$ mm. This was followed by gradual slip-hardening, reaching (near) steady-state at ~4.0 mm displacement. The 50:50 quartz-calcite curves are characterised by a near-linear increase in μ in the first 1.0 mm displacement, followed by apparent yielding and subsequent slip-hardening towards a (near) steady-state value of 0.68, again at ~4 mm displacement. The sequential velocity-steps imposed in Stage 1, from the initial sliding velocity of 5.43 µm/s to the final sliding velocity of 100 µm/s, were characterised by a sharp direct effect, which become less distinct with decreasing sliding velocity. In general, the frictional strength in Stage 1 showed a slight decrease with sliding velocity, and as a result increasing shear displacement. After increasing the temperature to 100°C (Stage 2) and subsequently 150°C (Stage 3), again the sharp direct effect becomes less distinct with sliding velocity and the frictional strength decreases with sliding velocity and displacement. Moreover, between 100 and 150°C, the frictional behaviour exhibited by the 50-50 quartz-calcite and the 100% calcite samples, transitioned from stable sliding to highly unstable stick-slip behaviour. In Stage 1, the steady-state friction coefficient observed for the 50:50 quartz-calcite samples fluctuated around 0.68, falling in the range observed for pure quartz and pure calcite (respectively 0.63 and 0.71 – Figures 4.2c and 4.3f). In Stages 2 and 3, the observed steady-state and stick-slip friction coefficient values for the 50:50 quartz-calcite samples varied from 0.59 to 0.73, extending beyond the range of friction coefficient values obtained for pure calcite and pure quartz (respectively 0.63-0.66 and 0.60-0.65 – Figures 4.2c and 4.3f). Note the convergence in strength observed for the two 50:50 quartz-calcite compositions in Stage 3, resulting in final μ_{ss}-values of ~0.59, so more or less equal to that obtained for 100% quartz throughout Stages 1-3 (see Figure 4.2c).

The pure quartz and 50:50 quartz-calcite mixtures both exhibited stable, velocity-strengthening slip at room temperature (Figures 4.2c and 4.4g). With increasing temperature, this behaviour becomes velocity-weakening for the majority of the

velocity-steps in the 50:50 quartz-calcite composition at 150°C (Figure 4.4g), showing a U-shaped trend (cf. stick-slips events in Figure 4.2c). Although not explicitly shown in Figure 4.4g, the velocity-dependence obtained for the 50:50 quartz-calcite samples weakly depends on the sliding velocity, with most positive values of (*a*-*b*) being obtained at low velocities (V <3.0 µm/s) and negative values at high velocities (V >3.0 µm/s).

Values for *a* and *b* are plotted separately in Figures 4.4h and i. For temperatures of 23 and 100°C, parameter *a* shows an increase with increasing calcite content (Figure 4.4h). Contrary, parameter *b* shows a maximum at 50% calcite and positive and negative values for pure quartz and pure calcite (Figure 4.4i). At 150°C, stick-slip behaviour is exhibited by the 50:50 quartz-calcite and pure calcite samples, therefore values for *a* and *b* separately are only obtained for pure quartz.

4.3.1.4 Normal-stress stepping results

The velocity-stepping procedure employed in Stages 1-3 of selected experiments was followed in Stage 4 by four normal stress steps conducted at a temperature of 150°C. These were conducted to determine whether the description of the strength of our samples in terms of a coefficient of friction with zero cohesion is justified. The resulting shear stress (τ) at yield or peak vs. σ_n^{eff} data are plotted in Figure 4.5 for Data-sets 1- 3 in panel a-c, respectively. All our data show a systematic increase in τ with increasing effective normal stress, which can be described by a linear trend-line that passes through, or close to, the origin. The data can be described by a Mohr-Coulomb type of relationship given as (Jaeger et al., 2007):

$$\tau = \mu_i \cdot \sigma_n^{eff} + C_0 \qquad (4.4)$$

where μ_i is the internal friction coefficient of the fault gouge and C_0 represents the cohesion of the simulated gouge. The shear stress obtained at yield or peak was used as a reference strength parameter to exclude any secondary effects of slip-hardening when interpreting the μ_i and C_0 values. Values for μ_i and C_0 are listed in Table 4.2. Due to the absence of Stage 4 in the majority of the CFOPA-calcite experiments, no values for μ_i and C_0 were obtained for these samples, including the 100% calcite sample (RS003). Therefore, no systematic trends, correlating the parameters to mineral composition, hence calcite content, have been observed.

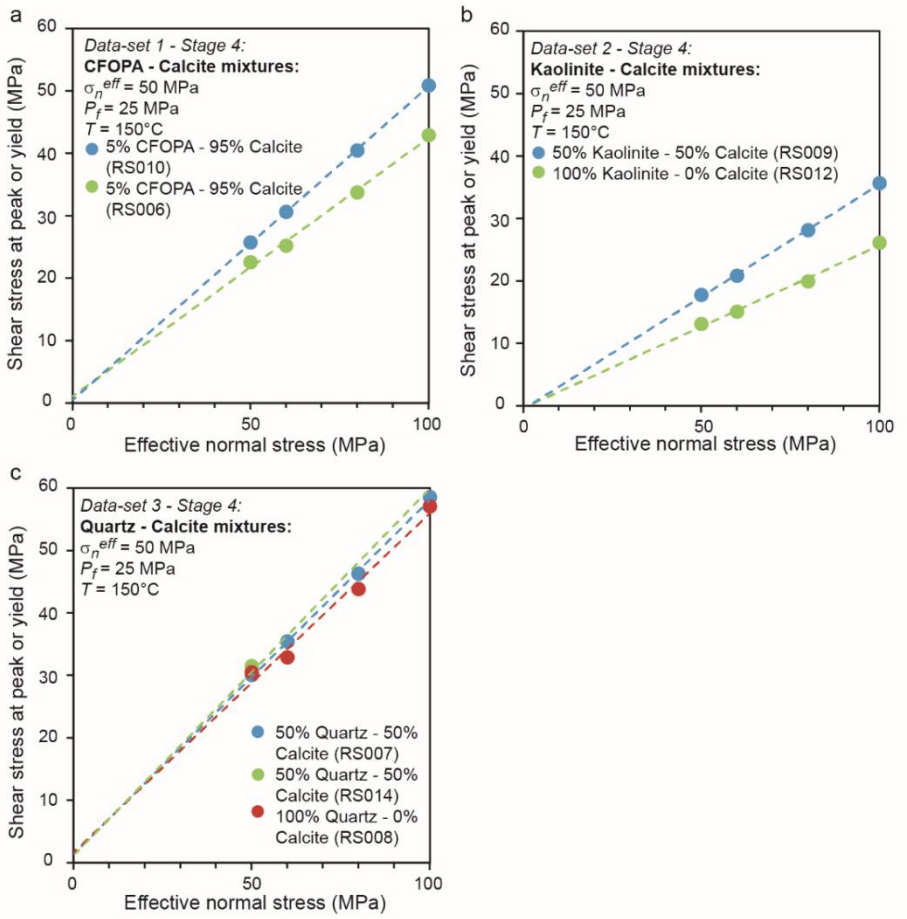

Figure 4.5. Shear stress supported at peak, or at yield in the absence of a clear peak, versus effective normal stress obtained during Stage 4 at T = 150°C. a) Two 5:95 CFOPA plus added calcite mixtures (Data-set 1). b) Kaolinite plus added calcite mixtures (Data-set 2). c) Quartz plus added calcite mixtures (Data-set 3). Linear trend lines and corresponding data points are colour-coded for the different compositions.

For the majority of the experiments, the cohesion C_0 is positive and <2.0 MPa (Table 4.2). Exceptions include the 50:50 kaolinite-calcite and 100% kaolinite samples (Figure 4.5b), for which we obtained a small negative cohesion, likely related to errors in our measurements, e.g. related to the seal friction correction. This means that, overall, friction coefficient values obtained at low effective normal stresses should be interpreted with caution for mixtures exhibiting a small

cohesion. However, at σ_n^{eff} > 50 MPa, the effect of cohesion becomes negligible, justifying the use of $\mu = \tau/\sigma_n^{eff}$ at such values of σ_n^{eff}.

4.3.2 Microstructural observations

When extracting our samples from the ring-shear piston assembly, most broke into small fragments, which made it difficult to prepare fully representative sections comprising the entire width of the gouge layer. Nonetheless, fragments of most deformed gouge samples could be preserved for microstructural analysis. We were not able to preserve a representative microstructure of the deformed 100% CFOPA sample (RS002).

Our microstructural investigations focused on the two sample-sets that showed the most notable change in friction with calcite proportion, namely Data-set 1 (CFOPA-calcite) samples and Data-set 3 (quartz-calcite) samples. A detailed description of the microstructures observed in the sheared 100% calcite sample (RS003) will be presented as part of the CFOPA-calcite data-set (Data-set 1) only. Overall, optical and SEM analysis of these samples showed all to contain horizontal and inclined shear bands, comprising mainly boundary and R_1-shears, and occasionally P- and Y-shears (using the terminology of Logan et al., 1979). However, major differences in microstructure were observed between the sheared CFOPA-calcite mixtures (Data-set 1) versus the pure calcite, as well as between the sheared pure calcite, the pure quartz and the 50:50 quartz-calcite mixtures (Data-set 3). In comparing the microstructures characterizing these different data-sets, note that the CFOPA-calcite samples examined (R001-R006) were sheared for 32.7 mm (Stages 1-3), whereas the kaolinite-calcite and quartz-calcite samples were sheared for 40.7 mm (Stages 1-4). Recall also that all samples examined underwent a complex shearing history, with the final stage of deformation (Stage 3 or 4) being conducted at 150°C in all cases. Accordingly, changes in microstructure are related to composition rather than to temperature.

4.3.2.1 Sheared CFOPA-calcite mixtures (Data-set 1)

Optical analysis and SEM (BSE) investigation of our sheared CFOPA-calcite mixtures showed that the shear-induced deformation microstructures as well as the distribution of mineral phases throughout the gouge layer changes as a

→ **Figure 4.6. (see next page)** Optical and backscatter electron (BSE) micrographs of representative CFOPA-calcite mixtures, showing a change in developed microstructure with increasing calcite content. Figure 4.6a-d shows microstructures developed in 50:50 CFOPA-calcite (RS001). a) Optical overview micrograph of the 50:50 CFOPA-calcite sample showing the formation of a boundary shear zone (BS zone - top), causing the gouge layer to separate in multiple zones. b) SEM close-up (BSE) of the upper margin boundary shear zone and the body of the gouge layer, showing alignment of elongated domains parallel to the R_1-orientation. The calcite grains in the calcite enriched domains show evidence of internal grain fracturing (igf) when sharing grain contacts. c) Higher magnification image of the upper margin boundary shear zone. Boundary shear is characterised by strongly comminuted calcite grains (scg) and surviving calcite grains (sg), floating in a submicron phyllosilicate matrix. d) The fine-grained phyllosilicates and strongly reduced calcite grains wrap (w) around internally fractured calcite grains.

function of the calcite proportion. We will first describe the microstructures observed in the relatively high CFOPA-content mixtures (30-50% CFOPA – RS001 and RS004) followed by the microstructures observed in the samples containing relatively low amounts of CFOPA (5-10% CFOPA – RS005 and RS006). We will conclude with the pure calcite sample (0% CFOPA – RS003).

4.3.2.1.1 Samples containing 30-50% CFOPA

The optical and SEM (BSE) microstructures of the sheared CFOPA-rich gouge samples (i.e. samples RS001 and RS004 – Figure 4.6a) show remnants of boundary shear zones at one or both of the gouge layer margins (top of Figure 4.6b). These remnants are visible as sharply-defined boundary shears (~70-90 µm wide), cutting the relatively coarse-grained matrix that forms the body of the gouge layer (bottom of Figure 4.6b). The boundary shears consist of fine-grained material with strongly comminuted (2-20 µm), and occasionally surviving (25-60 µm), calcite grains randomly distributed throughout the submicron-sized phyllosilicate-calcite matrix (Figure 4.6c). At the interface of the body of the gouge and the boundary shears, the grain size shows a decrease towards the boundary shear. The body of the gouge layer is characterised by an alternation of elongate domains, 10-70 µm thickness, which are aligned parallel to the R_1-orientation (Figures 4.6a and b). These domains contain either coarse-grained calcite (20-50 um – areas with a lighter contrast), which show evidence of internal fracturing when sharing grain contacts, or contain mainly fine-grained material consisting of phyllosilicates and crushed calcite (<15 µm –areas with a darker contrast; Figure 4.6b). The domains

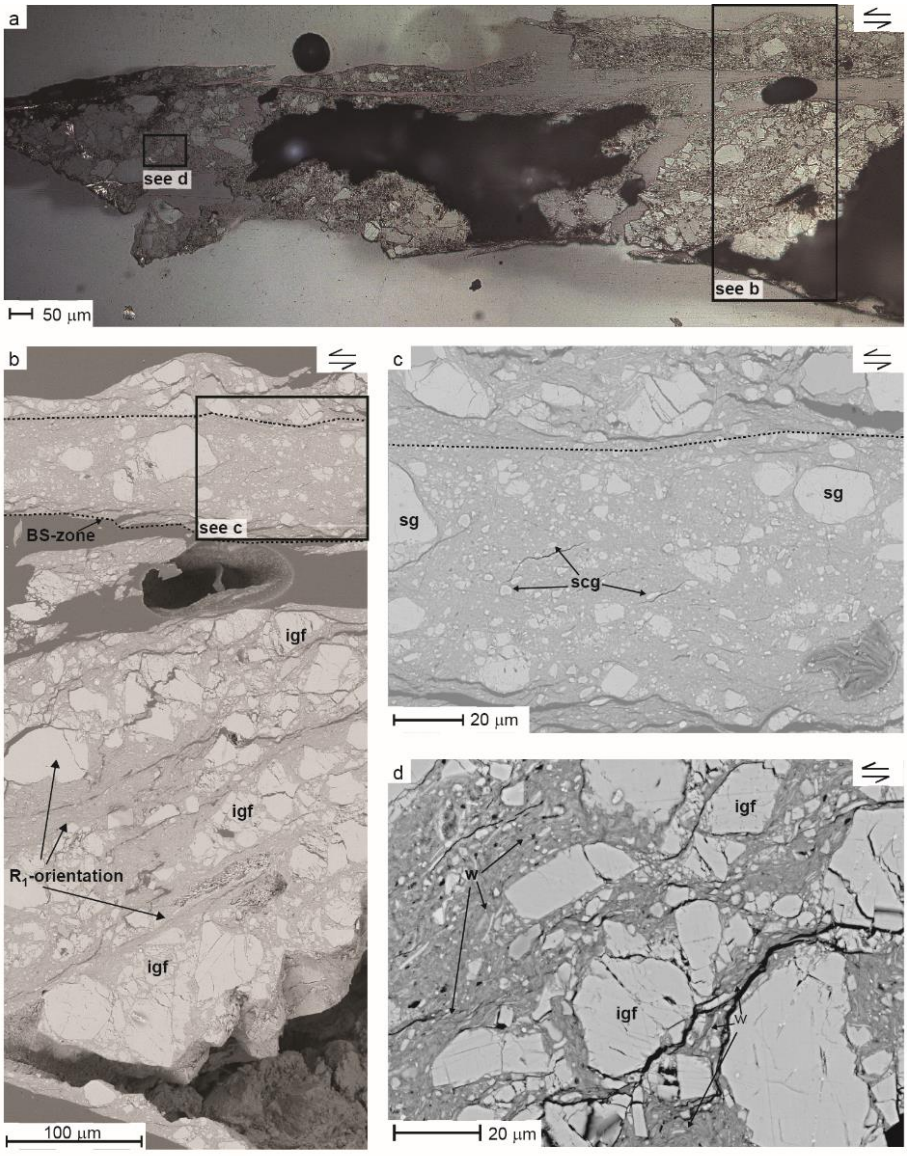
a
see d
see b
50 µm
b
see c
BS-zone
igf
igf
igf
R1-orientation
100 µm
c
sg
sg
scg
20 µm
d
igf
w
igf
w
20 µm

→ **Figure 4.7. (see next page)** Optical and SEM (BSE) micrographs of 5:95 CFOPA-calcite mixture (RS006). a) SEM micrograph of the starting microstructure (pre-shear) obtained after initial loading at 50 MPa confining pressure, 25 MPa pore pressure and room temperature for ~60 min, showing clusters of CFOPA embedded in calcite. Note that the boundary parallel openings are due to epoxy. b) Optical overview of 5:95 CFOPA-calcite, showing solely the body of the gouge layer with R_1, P and Y-shears. c) SEM overview of part of one of the boundary shears of the 5:95 CFOPA-calcite sample, including a shear surface emanating from the piston groove apice (a). d) SEM close-up of the body of the gouge layer with distributed internally fractured calcite grains (igf). e) Zoom of the body of the gouge layer, showing discontinuous CFOPA-enriched foliation aligned parallel to R_1 (*en echelon*). f) SEM close-up of boundary zone with both strongly comminuted calcite grains (scg) as well as surviving calcite grains (sg). g) High magnification zoom of boundary shear zone. h) EDX characterisation of the same area of the boundary shear, showing the preferential presence of phyllosilicates (aluminium) along the shear surfaces.

with fine-grained material wrap around the internally fractured calcite grains (Figure 4.6d). The R_1-oriented domains appear to be connected to the boundary shear, forming an interconnected network of oblique and boundary-parallel shear zones (Figure 4.6b). Note that deformation twins were not observed in the calcite clasts as these are not visible in BSE contrast mode, so they may have been present in all samples containing calcite.

4.3.2.1.2 Samples containing 5-10% CFOPA

The starting microstructure (SEM-BSE) developed in the pre-shear compacted 95% calcite sample (i.e. 5% CFOPA) is presented in Figure 4.7a. The starting microstructure shows clusters of CFOPA distributed throughout the calcite. The microstructures of the sheared 5-10% CFOPA-samples (i.e. samples RS005, RS006 and RS010 – Figure 4.7) are characterised by more sharply-defined boundary shears (~90-110 µm thickness – Figure 4.7c) and to fewer extent R_1-, P- and Y-shears, cutting the coarser-grained body of the gouge layer (~5-35 µm – grain-supported – Figure 4.7b). The boundary shears consist of a matrix with a strongly reduced grain size and occasional some coarser grains (respectively, <3 µm and 10-25 µm – matrix-supported – Figures 4.7f and g). The grain size of the intervening body of the gouge layers show an abrupt decrease towards the boundary and R_1-shear zones (Figure 4.7e). The body of the 5-10% CFOPA-samples is characterised by internally fractured calcite grains distributed throughout a matrix of mixed calcite and phyllosilicates with a grain size of <~15 µm (Figure 4.7e). Aligned, *en echelon* concentrations of phyllosilicate minerals, parallel to the R_1-orientation, are found throughout the gouge layers (Figure 4.7e).

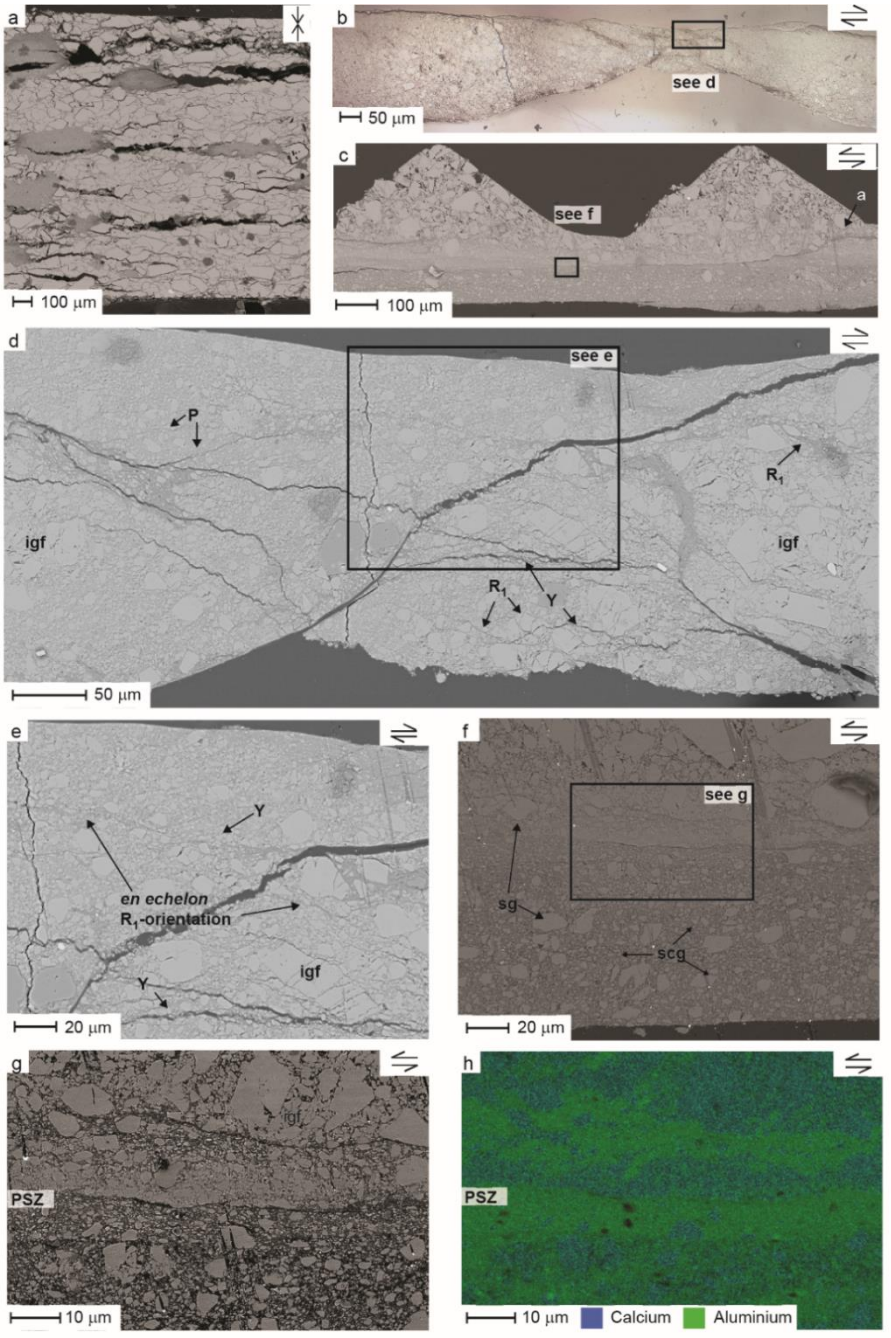
a
100 µm
b
see d
50 µm
c
see f
a
100 µm
d
see e
P
R1
igf
igf
R1
Y
50 µm
e
Y
en echelon
R1-orientation
igf
Y
20 µm
f
see g
sg
scg
20 µm
g
igf
PSZ
10 µm
h
PSZ
10 µm
Calcium
Aluminium

Detailed SEM (BSE) investigation of the boundary shear zones shows that their core generally consists of multiple shear surfaces, which sometimes emanate from the piston groove apices before merging within the boundary shear zone (Figure 4.7c). The core of the boundary shears is not only distinct because of its highly reduced grain size, but also because of the noticeable variation in grey contrast, hence mineral phase, compared to the body of the gouge layer (Figures 4.7c and f-h). The lower part of the boundary zone is characterized by relatively coarse calcite grains (3-6 µm – light grey) "floating" in a fine-grained matrix (dark-shaded – matrix-supported; Figures 4.7f and g). The upper part of the boundary zone is characterized by two denser zones with calcite grains sharing contacts (light-grey – grain-supported; Figures 4.7f and g). Towards the top, the calcite grain size appears to increase (from ~1 to 15 µm; Figure 4.7g). EDX analysis (Figure 4.7h), focusing on calcium, hence calcite, and aluminium, hence phyllosilicates, of the same area confirms the dominant presence of calcite in the lighter contrast zones and phyllosilicates in the darker contrast zones of the core of the shear zone.

4.3.2.1.3 Sample containing 0% CFOPA (100% calcite)

Optical analysis and SEM (BSE) investigation of this sample revealed preserved remnants of well-defined, fine-grained, boundary shear bands present along both margins of the gouge layer (Figure 4.8a). Open, sample-sized cracks, aligned parallel to the R_1-orientation were also locally visible, cutting the coarser-grained matrix of the gouge layer (Figure 4.8b). The preserved segments of the lower boundary shear suggest a minimum width of ~20-30 µm with ~2-15 µm sized calcite grains "floating" in a very fine-grained calcite matrix (hence <1 µm) (Figure 4.8c). The upper boundary shear is wider, with a minimum width of ~60-80 µm and ~1-27 µm sized calcite grains "floating" in a fine-grained matrix of calcite grains (Figure 4.8a). The zones bordering the inclined cracks, as well as adjacent to the boundary shear zone, show an abrupt fining of the grain size towards the shear zones (Figure 4.8b). The body of the gouge layer is characterised by larger calcite grains (~20-30 µm) fairly homogeneously distributed in a fine-grained matrix (Figure 4.8d). A high proportion of the large calcite grains are internally fractured, where sharing a grain contact (Figure 4.8a). However, other areas are dominated by fine-grained calcite only. The fractured pieces often cluster, reflecting the shape of the parent grain (Figure 4.8a). Throughout the matrix, *en echelon* fractures (~1 µm thickness), supposedly aligned to the R_1-orientation, are observed (Figure 4.8d).

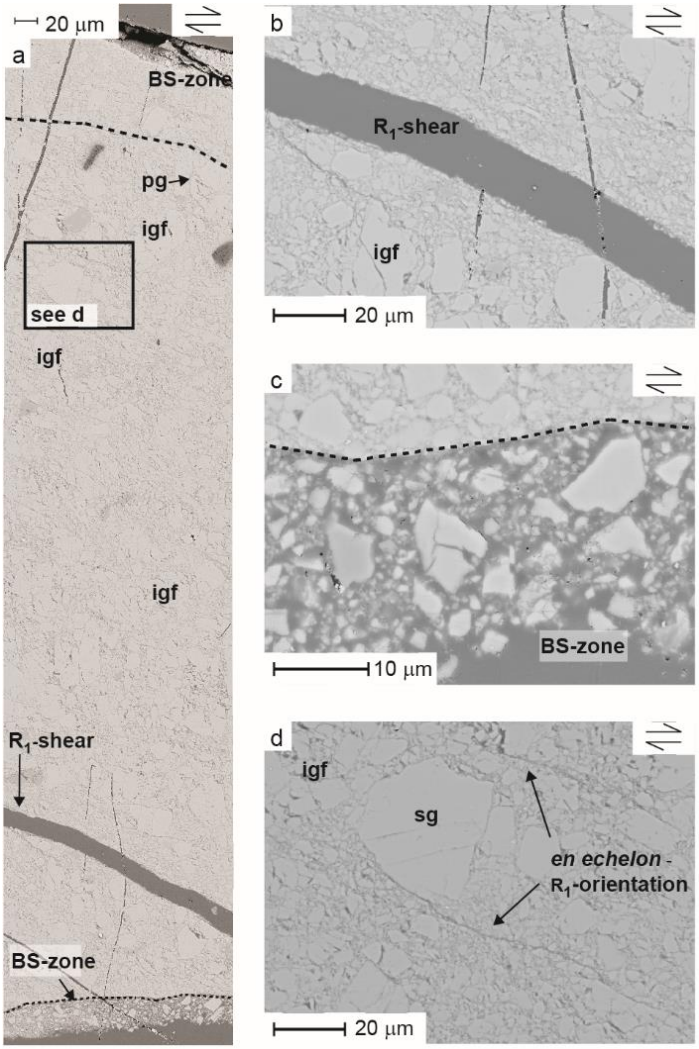

Figure 4.8. SEM (BSE) micrographs of 0:100 CFOPA-calcite mixture (100% calcite - RS003). a) SEM micrograph of the gouge layer, comprising both boundary shear zones and the body of the gouge layer. Internally fractured grains (ifg) are distributed throughout the gouge layer, whereas locally parent grains (pg) are observed. b) Close-up of the gouge body, showing a dilated crack aligned parallel to R_1, as well as the grain size reduction towards the shear zone. c) High magnification zoom of boundary shear zone, showing strongly comminuted calcite grains in a fine-grained calcite matrix. d) Close-up of a surviving calcite grain (sg) embedded in a fine-grained calcite matrix, bounded by *en echelon* R_1-oriented fractures.

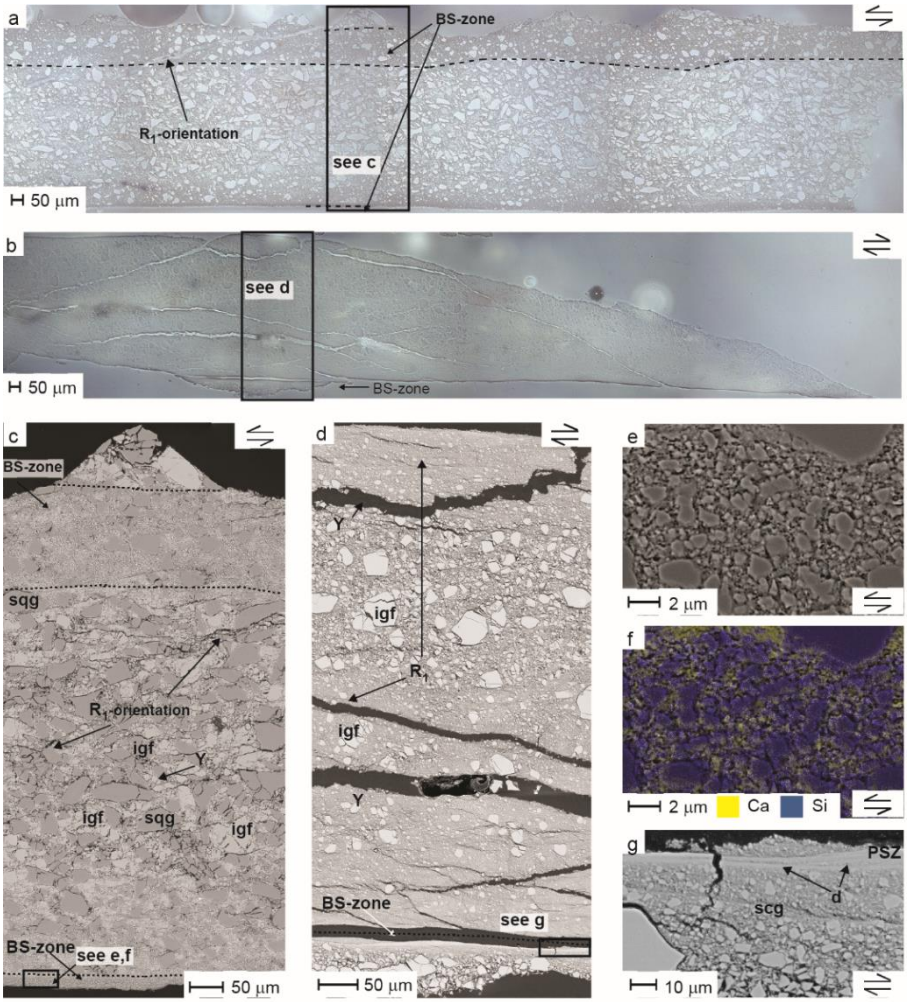

Figure 4.9. Optical and SEM (BSE) micrographs of 50:50 quartz-calcite (RS014) and 0:100 (100%) quartz (RS008) gouges, showing a change in developed microstructure with increasing calcite content. a) Optical overview micrograph of the 50:50 quartz-calcite sample showing (remnants of) the upper and lower boundary shear zone (BS zone), bounding the body of the gouge layer. b) Optical overview micrograph of the 100% quartz sample showing the formation of boundary, R_1- and Y-shear zones, causing the gouge layer to separate in multiple zones. c) SEM close-up of the 50:50 quartz-calcite sample. The calcite grains in the body of the sample show evidence of significant internal grain fracturing (igf), forming the intervening matrix in which surviving quartz grains (sqg) are distributed. d) SEM close-up of the body of the gouge layer bounded by the lower boundary shear zone of the 100% quartz sample. Some surviving grains (sqg) as well as internally fractured grains (ifg) are embedded in the fine-grained body of the sample. e) Close-up of the boundary shear zone of the 50:50 quartz-calcite sample, which is characterized by a very fine-

grained, intervening calcite matrix and strongly comminuted quartz grains. f) EDX characterisation of the same area of the boundary shear, showing the predominant presence of calcium (calcite) in the intervening matrix and silicon (quartz) in the relatively coarse grains. g) Higher magnification image of the lower margin boundary shear zone of the 100% quartz sample (RS008). Boundary shear is characterised by strongly comminuted quartz grains (sqg) with occasionally sub-micron duplexes (d) floating in the submicron quartz matrix of the principle shear zone (PSZ).

4.3.2.1.4 Overall trends in the CFOPA-calcite samples

In summary of the above, microstructural analysis of the CFOPA-calcite mixtures shows a change in observed microstructural features with increasing calcite proportion. Samples containing relatively low proportions of calcite and high concentrations of CFOPA show evidence of shear being primarily accommodated by sliding along fine-grained, optically phyllosilicate-rich, boundary shears, complemented by intergranular fracturing of large calcite grains in the calcite-rich domains in the gouge body (50% CFOPA - RS001; Figure 4.6). With increasing amounts of calcite and decreasing amounts of CFOPA, shear becomes increasingly accommodated by homogenously distributed cataclastic flow with grain size reduction of the calcite grains in the body of the gouge layer. This is accompanied by especially marked grain size reduction in the boundary shears. Locally, phyllosilicate-enriched shear surfaces developed in the core of the boundary shear (5% CFOPA-RS006; Figure 4.7). Shear in the 100% calcite sample (cf. 0% CFOPA – RS003; Figure 4.8) is more distributed, showing an overall grain size reduction, but still a sharp boundary shear.

4.3.2.2 Sheared quartz-calcite mixtures (Data-set 3)

4.3.2.2.1 Sample containing 50:50 quartz-calcite

Optical analysis and SEM (BSE) investigation of the 50:50 calcite-quartz sample show boundary-parallel shear zones developed at both margins of the gouge layers, as well as inclined shear bands cross-cutting the gouge layer, i.e. boundary, R_1- and Y-shears (Figures 4.9a and c). The ~20-135 µm wide upper boundary shear (dark-contrast), locally showing remnants of the original pistons' groove pattern, is characterised by 6 µm to sporadically ~40 µm-sized quartz grains distributed in a strongly reduced calcite grain matrix (<3 µm; Figure 4.9c). The lower boundary shear is a more sharply-defined and thinner shear zone (~10-30 µm) than the upper boundary zone, with maximum ~2-4 µm-sized quartz grains distributed in a submicron-sized calcite-matrix, lacking any trace of the original groove pattern

(Figure 4.9c). Towards the shear zones, an abrupt decrease in grain size is observed. The larger and angular grey-contrast grains (50-80 µm) distributed throughout the body of the gouge layer are mainly quartz grains, which show less evidence of internal deformation, i.e. less comminution, than the crushed and lighter-coloured calcite forming the intervening matrix (<35 µm; Figure 4.9c).

Throughout the gouge layer, *en echelon* fractures (~1 µm) are observed, aligned parallel to the R_1-orientation (Figure 4.9c). As observed for the CFOPA-calcite mixtures, the upper and lower boundary shear zones of the quartz-calcite mixture shows darker, more uniform BSE contrast than the body of the gouge layer, suggesting intense, pervasive grain size reduction, and possible quartz enrichment. Detailed SEM (BSE) analysis of the shear zone (Figure 4.9e) shows a fairly homogeneous distribution of darker, fine-grained quartz grains (3-4 µm) in a lighter interconnected, submicron calcite matrix. This is confirmed by EDX imaging (Figure 4.9f).

4.3.2.2.2 Sample containing 100% quartz

Optical and SEM (BSE) investigation showed a clear separation of the gouge layer into multiple domains, with boundaries aligned along R_1-, P- and Y-shears, as well as, local remnants of sharply-defined, fine-grained boundary shears (Figures 4.9b and d). Note that the dilation seen in some R_1-, P-, Y- and boundary shears (Figures 4.9b and d) is most likely the result of sample preservation (i.e. epoxy resin), causing the layer to dilate along less-cohesive bands. Towards the various shear bands, the grain size abruptly decreases. The intervening material forming the body of the gouge layer is characterised by a major reduction in grain size towards the lower part of the gouge layer and is bounded by a well-developed, very narrow boundary shear (Figure 4.9d). Coarser grains are found in the middle of the gouge body. These are similar to the starting grain size, being up to ~30-40 µm, and often show internal fracturing, while still reflecting the original shape of the parent grain, when sharing a grain contact. Remnants of boundary shears are found at the upper and lower margins of the gouge layer (Figure 4.9d). However, the lower margin shear band is better preserved and is characterised by a sub-micron-sized matrix forming the very thin shear zone core. SEM imaging of the ~1-5 µm wide boundary shear core revealed the presence of an internal structure of submicron-sized grain duplexes embedded in an even finer-grained matrix that falls below the SEM detection limits, hence with grains <1 µm (Figure 4.9g).

4.3.2.2.3 Overall trends in the quartz-calcite samples

The above microstructural analysis of the quartz-calcite mixtures has shown clear microstructural trends with composition. The sample containing 100% quartz showed significant, heterogeneous grain size reduction of the quartz throughout the gouge layer and the development of boundary, R_1-, P- and Y-shears. Shear in one of the boundary shears was localized on a very narrow shear surface, reflecting extreme grain size reduction (Figure 4.9g). By contrast, the sample containing both quartz and calcite, shows evidence of shear being primarily accommodated by the preferential crushing of calcite, resulting in a relatively homogenous calcite-dominated matrix in which the surviving and comminuted quartz is distributed (Figure 4.9). Moving to the 100% calcite sample, shear seems to be progressively accommodated by more homogenously distributed grain size reduction in the body of the gouge layer with few clasts surviving. This evolution is accompanied by significant grain size reduction in the boundary shears (Figure 4.8).

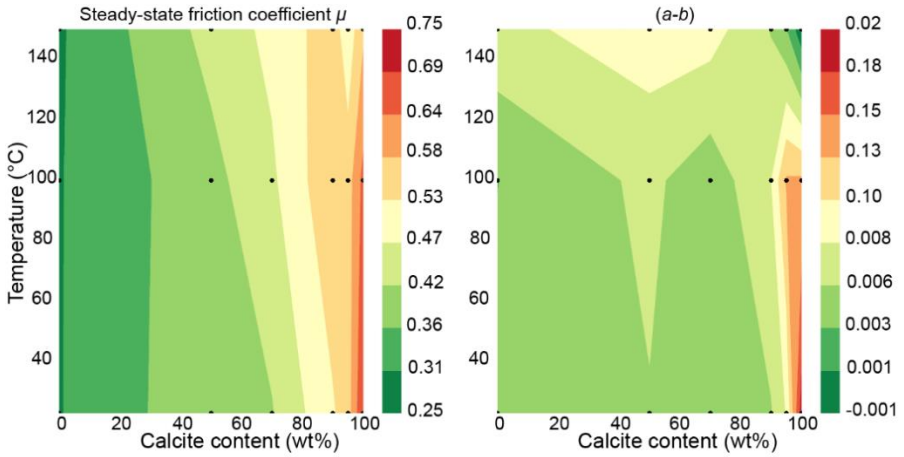

Figure 4.10. Contour map of friction parameters, steady-state μ and (a-b), as a function of calcite content. Points represent average values of steady-state friction coefficient or (a-b), from which contour maps are rendered.

4.4 Discussion

We begin here by noting that the calculated cohesion of <2 MPa (Table 4.2) compared with the shear stress of >30 MPa supported by our samples is relatively small (<7%). Therefore, we infer that the shear strength of our samples can be

represented by the ratio of the shear stress over the effective normal stress as a friction coefficient, justifying use of the RSF framework to describe our mechanical results, especially at the relatively high normal stress of σ_n^{eff} = 50 MPa. This is further supported by the fairly good agreement obtained between the experimentally-derived friction coefficient and the internal friction coefficient at yield or peak, derived via Equation (4.4) (Table 4.2). Note that the values that deviate, have cohesion values >1 MPa.

The present results on how the frictional behaviour of wet-tested clay-quartz gouge material (CFOPA) is affected by systematic variations in the calcite content show notable trends with increasing calcite content, temperature and sliding velocity (Figures 4.2-4.4, 4.10). For all temperatures, the (apparent) frictional strength data obtained showed a modest increase between 0-70% calcite (from μ_{ss} ≈ 0.28 to ~0.48), followed by a steeper increase between 70-100% calcite (from μ_{ss} ≈ 0.48 to ~0.71). The end-member μ-values obtained are similar to those recorded in previous studies on simulated gouges prepared from natural clay-rich rocks (e.g. calcite-free OPA; μ_{ss} ≈ 0.25 to 0.30 – Chapter 2, and chlorite schist and illite shale; 0.27-0.32 – Ikari et al., 2009) and simulated calcite gouges (~0.66 to 0.71 – Carpenter et al., 2016; Chen et al., 2015b; Giorgetti et al., 2015b; Tesei et al., 2014; Verberne et al., 2010). In addition, μ-values obtained for intermediate CFOPA-calcite mixtures are similar to those reported for simulated clay-quartz-calcite or clay-amphibole-calcite gouges reported in literature (Chen et al., 2015a; Tesei et al., 2012). Our CFOPA-calcite data also show a weak positive trend in (*a*-*b*) values with increasing calcite content up to ~100°C, followed by a transition from velocity-strengthening to velocity-weakening behaviour for calcite contents >90% at higher temperature (150°C). Individually, *a* appears to increase, whereas *b* remained more or less constant for increasing calcite content. Additionally, (*a*-*b*) tends to increase with sliding velocity. The observed velocity-strengthening behaviour for the 100% CFOPA sample (RS002) is in agreement with data from studies on calcite-free clay-rich gouge compositions (Chapter 2 – calcite-free OPA; Den Hartog et al., 2012 – Rochester shale; Ikari et al., 2009 - chlorite schist and illite shale), whereas the observed transition from positive to negative (*a*-*b*) for >95% calcite is in agreement with studies on calcite-rich compositions by Chen et al. (2015 – for clay-quartz-calcite gouges) and Verberne et al. (2010, 2013, 2014 – for pure calcite). Moreover, our sheared CFOPA plus calcite samples showed microstructural evidence for

mineral phase segregation. Specifically, microstructural analysis of the CFOPA plus calcite samples revealed a change in the distribution of shear deformation throughout the gouge layer with increasing calcite proportion, pointing to a transition from a) frictional sliding in relatively wide phyllosilicate-rich R_1- and boundary shear bands, in the phyllosilicate-rich samples, to b) more homogenous cataclastic grain size reduction in the pure calcite sample, with more closely spaced, but very narrow R_1- and boundary shears (Figures 4.6-4.8).

The trends observed for the wet kaolinite-calcite mixtures, though less extensively investigated, are similar to those found for CFOPA-calcite mixtures. At all temperatures investigated (~23, 100 and 150°C), the frictional strength data showed a modest increase from $\mu_{ss} \approx 0.26$ to 0.34 at calcite contents between 0-50%, followed by a steeper increase from $\mu_{ss} \approx 0.34$ to ~0.71 in the range 50-100% calcite. The values obtained for pure wet kaolinite agree well with those of 0.26-0.36 reported by Crawford et al. (2008), but are higher than the value of ~0.2 recorded by Bos and Spiers (2000), using a NaCl-saturated pore fluid and at low normal stress (5 MPa).

The trend in the frictional data obtained for the present quartz-calcite mixtures is different than for the CFOPA-calcite and kaolinite-calcite mixtures, as at room temperature the frictional strength tends to increase with increasing calcite content, whereas no clear trend was observed at 100°C and 150°C. The friction coefficient values obtained for pure, wet quartz at 23-150°C (μ_{ss} = 0.58 to 0.66) are similar to values obtained in previous studies on simulated quartz gouges at similar experimental conditions (μ = 0.66 to 0.75 - Tembe et al., 2010; Den Hartog et al., 2013). Additionally, the velocity-dependence of friction in pure, wet quartz is predominantly characterised by velocity-strengthening behaviour between 23 and 150°C, which is in agreement with the results of Tembe et al. (2010) and Den Hartog et al. (2013). However, striking is the highly unstable, velocity-weakening behaviour exhibited by the 50:50 quartz-calcite mixtures, with (a-b) values lower than obtained for either one of the end-members (Figure 4.4g). Analysis of the microstructure of the quartz-calcite samples revealed brittle grain failure and cataclastic granular flow dominated deformation of the end-members and the 50:50 quartz-calcite compositions (Figures 4.8 and 4.9). The 50:50 mixture showed evidence, both in the body of the gouge layer and in the extremely fine-grained

boundary shears, for preferential and more marked grain size reduction of the calcite grains compared to the quartz.

In the following, we will first evaluate whether the observed effects of composition on μ and (a-b) can be explained using a simple mixing model. We then focus on the microscale processes controlling the frictional strength and velocity-dependence obtained for the CFOPA-calcite mixtures. We go on to discuss the differences in behaviour between, and processes operating in, the CFOPA-calcite and kaolinite-calcite samples. For the quartz-calcite samples we will consider what controls the frictional strength and stability, and specifically the highly unstable, stick-slip (velocity-weakening) behaviour of the 50:50 quartz-calcite mixture at 150°C compared with the end-members which show similar frictional strength but predominantly velocity-strengthening for the pure quartz and velocity-weakening for the pure calcite (Figure 4.4). We conclude with a discussion of the implications of our findings for the integrity and stability of faults in clay-quartz-calcite-rich sequences, particularly in the context of subsurface CO_2 storage sites.

4.4.1 Effects of composition and mixing model

Previous studies of the frictional behaviour of simulated binary gouge mixtures have focused on the effects of adding a phyllosilicate powder to a granular powder, such as calcite, feldspar, quartz or serpentine (e.g. Crawford et al., 2008; Giorgetti et al., 2015b; Moore and Lockner, 2011; Tembe et al., 2010). Most such studies have investigated phyllosilicate-quartz mixtures at room temperature and showed either a near linear or sigmoidally-shaped decrease in frictional strength with increasing phyllosilicate content (e.g. Crawford et al., 2008; Tembe et al., 2010), between the end-members strengths. More complex mixtures, such as mixtures systematically combining two phyllosilicate phases with a strong, granular phase (such as calcite, feldspar, or quartz) or natural compositions, show similar strength trends when μ is plotted as a function of the total phyllosilicate or "strong mineral" content (Samuelson and Spiers, 2012; Tembe et al., 2010). In the following we compare our experimentally obtained data with mixing models such as proposed in these previous mixing studies (e.g. *Lupini et al.*, 1981; *Tembe et al.*, 2010). However, since the kaolinite-calcite and quartz-calcite data-sets presented here consisted of only 3 compositions, comparison with a mixing model is poorly constrained. Therefore we will focus on the CFOPA-calcite mixtures only.

In Figure 4.11 we plotted our CFOPA-calcite compositions together with the data for binary kaolinite-quartz and illite-quartz compositions reported in literature (Crawford et al., 2008; Tembe et al., 2010). As opposed to the pure phyllosilicate phases in these binary-mixtures, our CFOPA-calcite compositions consist of multiple phyllosilicates and naturally occurring quartz and pyrite in addition to the pure added calcite. As a consequence, the total granular or "strong mineral" content of the CFOPA-calcite mixtures represents the sum of the quartz, pyrite and calcite content, and not only added calcite, resulting in 36% granular mineral content shown for the 100% CFOPA sample in Figure 4.11.

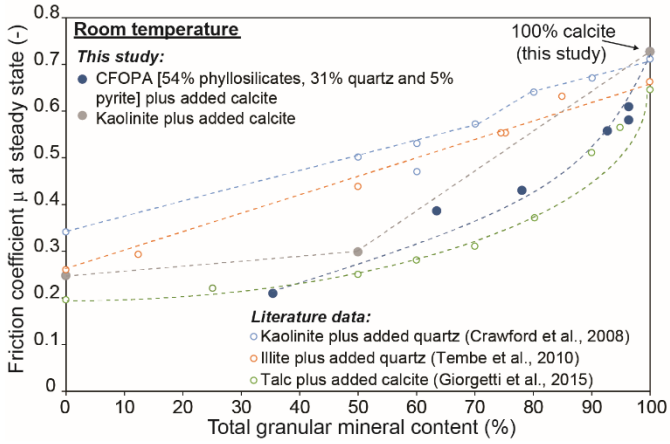

Figure 4.11. Friction coefficient at steady-state as a function of total granular or "strong" mineral content, respectively quartz, calcite or quartz, calcite and pyrite (CFOPA). Alongside our data for the CFOPA (containing quartz and pyrite) plus calcite and kaolinite plus calcite mixtures, obtained at ~23°C, literature data, obtained at room temperature, is shown for illite plus quartz (σ_n^{eff} = 40 MPa, P_f = 1 MPa and V =1.0 µm/s - Tembe et al., 2010), kaolinite plus quartz (σ_n^{eff} = 50 MPa, P_f = 5 MPa and V = 0.3 µm/s - Crawford et al., 2008) and talc plus calcite mixtures (σ_n^{eff} = 5 MPa and V= 10 µm/s - Giorgetti et al., 2015). Solid data-points represent data obtained in the current study, whereas open data-points represent data obtained from literature. Dashed lines represent hand-drawn trends, added for clarity.

Contrary to the linear trends reported in literature for illite-quartz and kaolinite-quartz compositions (Crawford et al., 2008b; Tembe et al., 2010 – Figure 4.11), the trend exhibited by our CFOPA-calcite compositions is characterised by a gradual initial increase in frictional strength, between 36 and 78% total granular content, followed by a more rapid increase from 78% to 100% total granular content. This trend roughly resembles that observed for talc-serpentine by Moore and Lockner

(2011). It also resembles that for talc and calcite reported by Giorgetti et al. (2015), which is plotted in Figure 4.11 for comparison. The rapid decrease in friction coefficient with the addition of a small amount of phyllosilicates seen in our experiments, in the range of 90-100% calcite, presumably reflects the formation of a through-going foliation composed of weak phyllosilicate phases. The difference between our observations and the linear trend reported by Tembe et al. (2010) and Crawford et al. (2008) may be related to the fact that the powders used in making the mixtures investigated here and by Giorgetti et al. (2015) were of similar grain size, while those reported previously were significantly different in grain size (with a grain size of <175 µm for quartz vs. ~2-3 µm for the clays). An alternative explanation may lie in the calcite clasts being more prone to grain size reduction than quartz clasts in mixtures with phyllosilicates.

In an attempt to model friction coefficient and (*a*-*b*) values, and their trends with increasing calcite concentration, for our CFOPA-calcite compositions, we tested the applicability of mixing equations reported in literature. As mentioned above, the trend observed in the frictional strength data for the talc-serpentine mixtures of Moore and Lockner (2011) resembles the trend observed in our CFOPA-calcite compositions best. Therefore, we will focus on the approach followed by Moore and Lockner (2011) in fitting the Reuss mixing equation to both the friction coefficient and the velocity-dependence data that we obtained at room temperature. The fitted correlation represents a weighted harmonic, which corresponds to the classical way of estimating the lower bound (mechanical) properties of a mixture, rather than the weighted arithmetic mean (or phase average), which is classically taken as the upper bound estimate of a property of a mixture. This approach lacks any further physical basis for the mixing model and, as a consequence, the fitted correlations merely give empirical fits to the friction vs. composition data presented. However, this approach does give a first-order impression of the dependence of mechanical properties of a mixture on its composition.

Following Moore and Lockner (2011), we first assume a simple two-component mixture in which all components are subjected to identical stress, ignoring the fact that CFOPA itself is a mixture. This allows us to write:

$$\frac{1}{\mu_m} = \frac{c_1}{\mu_1} + \frac{c_2}{\mu_2} = \frac{(1-c_2)}{\mu_1} + \frac{c_2}{\mu_2} \qquad (4.5)$$

where μ_m is the friction coefficient of the CFOPA-calcite mixture, μ_1 and c_1 the friction coefficient and concentration, respectively, of the CFOPA material, and μ_2 and c_2 the friction coefficient and concentration of the calcite. Even though the Reuss equation models a steepening of the frictional strength with increasing calcite content, it does not predict the steep increase in strength observed between 90 and 100% of calcite (Figure 4.12a). A similar overestimation of the frictional strength at high quartz concentrations was observed for talc-serpentine by Moore and Lockner (2011). To correct for the enhanced weakening effect of small concentrations of talc they introduced a fitting parameter q, which represents the dominance in frictional behaviour of each of the two constituting components, respectively CFOPA or calcite in our case. Thus we write:

$$\frac{1}{\mu_m} = \frac{(1-{c_2}^q)}{\mu_1} + \frac{{c_2}^q}{\mu_2} \tag{4.6}$$

Here, q <1 enhances the influence of the weaker "phase" on the mixture, i.e. CFOPA, whereas a q >1 enhances the effect of the stronger component, i.e. calcite. Our data suggests an enhanced weakening effect of the CFOPA. Consequently, taking a q of 0.6 results in a good fit to our experimental data (Figure 4.12a). The Reuss equation (i.e. Equation (4.5)) can also be applied to the velocity-dependence (Figure 4.12b). The trend observed for the calculated (a-b) data resembles the trend obtained for experimental data, again overestimating (a-b) at high calcite concentrations. A better, but a little less accurate fit than obtained for the friction coefficient, is obtained when fitting the Reuss equation with a q of 0.6 (Figure 4.12b).

Table 4.3. Overview of the friction coefficient μ and (a-b) values available in literature and as used for the present compositional modelling.

Mineral	*μ* *(-)*	*(a-b)* *(-)*	*Comments*	*Reference*
Calcite	0.71	0.0188		This study
Dolomite	0.63	0.0033	Room temperature, room humidity	(Scuderi et al., 2013)
Quartz	0.63	0.00344		This study
Pyrite	-	-	No data	-
Chlorite	0.37	0.005	Wet, room temperature - not pure	(Ikari et al., 2009; Moore and Lockner, 2004)
Illite	0.28	0.005	Wet, room temperature	(Tembe et al., 2010)
Kaolinite	0.26	0.00312		This study
Saponite	0.09		Brine, room temperature	(Carpenter et al., 2012; Sone et al., 2012)

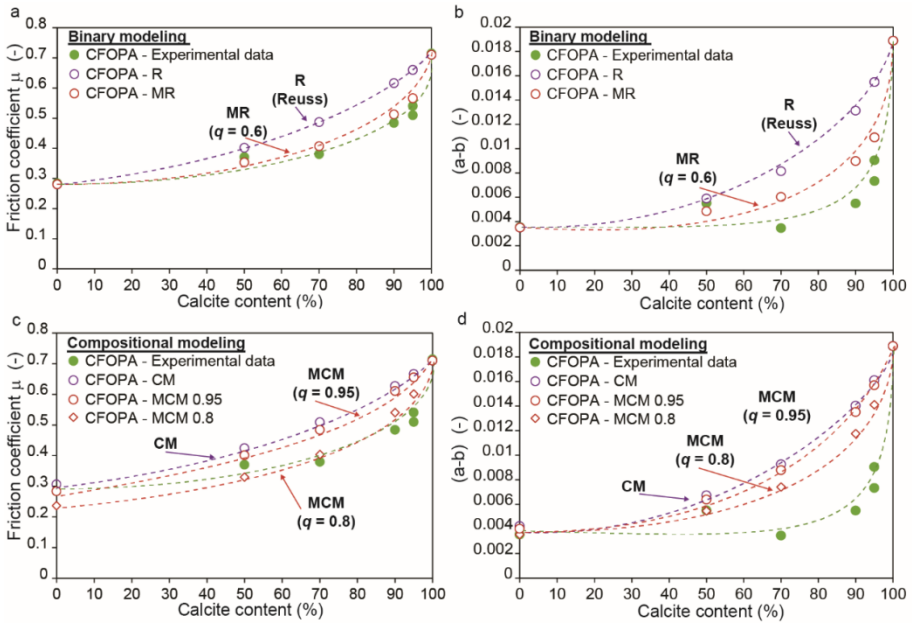

Figure 4.12. Steady-state friction coefficient data for CFOPA-calcite mixtures at $T \approx 23$°C. a and b) Comparison of experimentally-derived friction coefficient data and modelled friction coefficient data, following Moore and Lockner (2011) for a binary-system. c and d) Comparison of experimentally-derived friction coefficient data and modelled friction coefficient data, taking each mineral fraction into account. Solid symbols represent the experimental data derived in this study, open symbols represent modelled approximations labelled R for Reuss (Equation (4.5)), MR for Modified Reuss (Equation (4.6)), CM for Compositional Modelling (Equation (4.7)) and MCM (Equation (4.8)) for Modified Compositional Modelling.

Despite the fairly good fit, the model was originally developed to model the frictional strength of mixtures composed of two pure end-members, one weak and one strong phase. However, due to the nature of CFOPA, which includes quartz, pyrite, chlorite, illite, illite-smectite, and kaolinite, this clear separation of weak and strong phases does not strictly hold and the contribution of strong vs. weak phases is not fully accounted for. Another approach would therefore be to consider the different mineral phases separately and to calculate the frictional strength or (a-b) of a mixture using the friction coefficient and (a-b) values for the pure minerals, as presented here or as documented in literature (Table 4.3). To account for each mineral present in the CFOPA, we therefore extended the Reuss equation to cover

each main mineral phase, for a total of i = 6 phases, corresponding to calcite, quartz, chlorite, illite, smectite and kaolinite. The Reuss equation thus becomes:

$$\frac{1}{\mu_m} = \frac{c_1}{\mu_1} + .. + \frac{c_i}{\mu_i} \quad (4.7)$$

The results for the extended compositional modelling are shown in Figures 4.12c and d. The calculated values for both μ and (a-b) show a gradual increase with increasing calcite content. Again the calculations overestimate μ and (a-b) consistently, especially for the higher calcite concentrations. To correct for this, by enhancing the weakening effect of each of the four phyllosilicates, the fitting parameter q is incorporated into Equation (4.7) per phyllosilicate mineral present in the CFOPA as follows, taking illite and smectite as two separate mineral phases:

$$\frac{1}{\mu_m} = \frac{(1-c_2-c_3{}^q-c_4{}^q-c_5{}^q-c_6{}^q)}{\mu_1} + \frac{c_2}{\mu_2} + \frac{c_3{}^q}{\mu_3} + \frac{c_4{}^q}{\mu_4} + \frac{c_5{}^q}{\mu_5} + \frac{c_6{}^q}{\mu_6} \quad (4.8)$$

where mineral 1 is calcite, mineral 2 is quartz and minerals 3-6 are the four phyllosilicates. Results obtained for q = 0.8 and q = 0.95 are plotted in Figure 4.12c and d. Note, that since the enhanced weakening effect of each of the individual phyllosilicate minerals in unknown, a single value for q has been used for all four phyllosilicates when calculating the frictional strength and stability per composition. As the corrected trends show, the ideal q-value for the friction coefficient changes from 0.95 to 0.8 around 50% calcite, suggesting an increasing importance of the weakening effect of weak phyllosilicate phases at higher calcite concentrations. However, even though the fit of the calculated data to the experimentally obtained (a-b) data is improved by correcting for the weakening effect of the phyllosilicate phases, the fit remains poor.

Overall, the modelled friction coefficient and (a-b) data show that when the frictional strength and stability of the end-members are known, both parameters can be approximated adequately for an intermediate composition, especially when data for intermediate compositions are available to constrain fitting of the parameter q. Our results furthermore show that, at least for the present CFOPA-calcite mixtures, predicting the frictional strength or stability for changes in relative concentrations between two endmembers, even when one of the endmembers is a mixture itself, is likely to be slightly more accurate than predicting the frictional strength or stability of a composition based on data of the pure mineral phases.

However, the calculated data obtained via both approaches emphasise that in order to approximate the frictional strength and stability of a gouge more accurately, the weakening effect of phyllosilicate minerals at high calcite concentrations on both parameters has to be incorporated using the fitting parameter *q* to describe the non-linear effect of composition on μ and (*a*-*b*).

4.4.2 Microphysical mechanisms in (simulated) clay-quartz-calcite gouges

As illustrated in Figures 4.2a and 4.3a,b, the frictional strength of the CFOPA-calcite mixtures increases monotonically with increasing calcite content, or, conversely stated, decreases with increasing CFOPA content, falling between the two end-members at all temperatures investigated. As already stated, this is in broad agreement with previous findings for phyllosilicate plus quartz or calcite mixtures at room temperature (e.g. Crawford et al., 2008; Giorgetti et al., 2015b; Moore and Lockner, 2011; Tembe et al., 2010). The present data also show a parallel trend in the velocity-dependence (*a*-*b*) with calcite content (Figure 4.4a), showing temperature dependent behaviour for a temperature >100°C. Both the μ and (*a*-*b*) versus composition data show a high sensitivity to calcite content for calcite content ≥ 70%.

Based on these mechanical results and supported by our microstructural observations, which showed increased strain localization in clay-rich samples transitioning to distributed brittle grain failure and granular cataclastic flow in calcite-rich samples, we discern two deformation regimes for the conditions investigated (23-150°). These are: 1) localised shear and grain size reduction primarily in the sample boundary zone at calcite contents of 0 to 70%, and 2) more homogeneously distributed, cataclastic grain size reduction along with the development of very narrow shear bands at higher calcite contents.

In Regime 1, shear is primarily accommodated in the boundary shear, which consists of fine to very fine-grained calcite grains embedded in a predominantly submicron-sized phyllosilicate-rich matrix. Even though concentrations of relatively weak phyllosilicates, aligned parallel to the R_1-orientation, have been observed, these shear bands show limited signs of intense deformation, i.e. limited calcite grain size reduction or crushing (Figure 4.6), as opposed to the boundary shear, where predominantly very fine-grained calcite is observed (<20 µm), suggesting limited accommodation of shear along R_1. This is presumably because of their

oblique orientation to the macroscopic shear sense. With increasing calcite content in Regime 1 (0-70% calcite), the calcite grains present in the observed calcite-enriched domains start to form a locally connected network of load-bearing grains, showing evidence of brittle fracturing suggesting the onset of cataclastic comminution. Overall, the microstructures developed in Regime 1 are indicative of localised frictional sliding along through-going, phyllosilicate-enriched boundary shear zones, typically observed in phyllosilicate-rich gouges (e.g. Crawford et al., 2008), thus explaining the relatively low frictional strength, despite calcite contents up to 70%. On the basis of the microstructures of Regime 1 samples (Figure 4.6), we propose that increasing amounts of calcite in the range of 0-70% progressively increases resistance to the development of an interconnected network of frictionally weak, through-going, clay-rich shear zones, distributing shear strain and initiating cataclastic deformation in the gouge bulk, which gradually starts to increase the macroscopic friction coefficient. At intermediate calcite content (50-70%), this mechanisms does not yet dominate strength, as evidenced by the limited and localised grain fracturing of calcite. However, as the calcite content increases further, the grains start to form a well-connected network of load-bearing calcite grains and high-friction calcite-calcite grain contacts (>70% - Regime 2), increasing resistance further. At 90-95% of calcite, there is still interconnectivity of the phyllosilicate foliation, producing phyllosilicate-rich shear bands. However, shear deformation is also wide-spread in the body of the gouge layer, leading to overall cataclastic grain size reduction of the calcite matrix (Figure 4.7). While phyllosilicate concentrations are still elevated in the boundary shears, they are less continuously distributed in the bulk of the gouge layer, so that strength is high, but reduced compared with pure calcite. This is in agreement with observations for talc-calcite mixtures (Giorgetti et al., 2015).

At high to intermediate CFOPA contents (0-70% calcite), our CFOPA-calcite mixtures show (*a*-*b*) values close to zero at all temperatures investigated (Figure 4.4a). These near-neutral (*a*-*b*) values are similar to those observed for our pure kaolinite sample (Figure 4.4d) and values reported in literature for phyllosilicates (e.g. Ikari et al., 2009; Tembe et al., 2010 - see also Table 4.3), from which we infer that the phyllosilicates not only control the frictional strength but also the frictional stability of our mixtures at low to intermediate calcite content. At 23-150°C, increasing the calcite content shifts (*a*-*b*) gradually towards more positive values,

characteristic for pure calcite at these temperatures. The observed increase in (*a*-*b*) tracks the gradual increase in frictional strength with calcite content observed for the frictional strength. This implies an overall increase in dominance of the calcite phase, hence calcite-calcite grain boundary frequency, in controlling the frictional strength and stability of our CFOPA-calcite samples, progressively stabilizing the gouge at 23 and 100°C. Between 100°C and 150°C, the compositions with >90% calcite showed a transition from velocity-strengthening to velocity-weakening behaviour, suggesting growing importance of a thermally-activated process at calcite-calcite grain contacts. Similar behaviour was observed by Verberne et al. (2014a) for pure calcite at T > 80°C, who inferred cataclastic granular flow and thermally-activated dislocation glide and/or diffusion creep to be the operating deformation mechanisms, at all temperatures. With increasing temperature and at lower sliding velocity, dislocation glide and/or diffusion allows for compaction creep at grain contacts, causing the samples to exhibit velocity-weakening behaviour in line with the model proposed by Niemeijer and Spiers (2007).

The striking combination of velocity-strengthening behavior accompanied by stick-slip, observed for the 90% calcite samples, suggests that for this specific composition other processes might be active besides those described by the rate-and-state friction theory. Possibilities here include mechanical or thermal fluid pressurization effects (e.g. Chen et al., 2013), or flash heating (Niemeijer et al., 2012). In regions of the gouge where shear localizes intensely (increasing the shear strain rate), these phenomena can potentially reduce frictional strength, and hence produce an unstable (runaway) velocity or displacement weakening effect, despite displaying velocity-strengthening behaviour across the narrower range of sliding velocities explored via velocity-stepping.

4.4.3 Microphysical mechanisms in (simulated) kaolinite-calcite gouges

A similar change in frictional strength and (*a*-*b*) with increasing calcite content to that observed for the CFOPA-calcite samples was also observed for the kaolinite-calcite samples, at all temperatures investigated (Figures 4.2b, 4.3c,d and 4.4d). Due to the limited data (0, 50 and 100% calcite, respectively RS012, RS009 and RS003), precise specification of the compositional range in which (*a*-*b*) changes (i.e. transitions from velocity-strengthening to velocity-weakening, as observed for the 100% calcite sample (RS003) at 150°C) is not possible. Surprisingly, by comparison

with the 100% CFOPA sample (RS002), which contains mainly phyllosilicates and ~30% quartz, the 100% kaolinite sample shows slightly higher frictional strength (RS012 – Figures 4.2 and 4.3; Table 4.2). This is attributed to the presence of relatively weak illite-smectite minerals in the CFOPA (e.g. Carpenter et al., 2012; Tembe et al., 2010) and to the formation of a weak, fully interconnected network or matrix of phyllosilicate minerals, in which the 30% quartz grains moved passively during shear. However, the 50:50 kaolinite-calcite mixture is weaker than the 50:50 CFOPA-calcite mixture (Figures 4.2a,b and 4.3a,b – Table 4.2). This may be due to the increased granular mineral content carried in the CFOPA-calcite mixture, which presumably promotes the formation of a clast-supported network, increasing the bulk frictional strength of the gouge layer.

In general, the increase in frictional strength of the kaolinite-calcite samples with increasing calcite content is in agreement with previous binary mixture experiments addressing either kaolinite plus quartz or calcite plus talc, performed at room temperature (Crawford et al., 2008; Giorgetti et al., 2015). Based on the trends seen in our mechanical data, and the fact that kaolinite is one of the phyllosilicate minerals present in the CFOPA gouge (13%), we infer that the same two deformation regimes apply to shear of the kaolinite-calcite mixtures as for the CFOPA-calcite mixtures, namely: 1) localised shear in primarily a phyllosilicate-enriched boundary zone (~0-70% calcite), and 2) more homogeneously distributed, cataclastic deformation (~70-100% calcite). However, to gain better insight into the compositional range in which the velocity-dependence of friction shifts from velocity-strengthening (seen here at 0-50% of calcite at temperatures of 23 to 150°C – Figures 4.2b and 4.4d) to velocity-weakening behaviour (seen here at 100% of calcite at a temperature of 150°C – Figures 4.2b and 4.4d) more data are needed.

4.4.4 Microphysical mechanisms in (simulated) quartz-calcite gouges

At room temperature, the quartz-calcite compositions studied show intermediate frictional strength, with the strength (μ_{ss} ≈ 0.68) falling between the weakest (quartz with μ_{ss} ≈ 0.63) and strongest (calcite with μ_{ss} ≈ 0.71) end-members (Figure 4.3e,f), broadly in line with previous room temperature studies of the frictional behaviour of strong-weak binary mineral mixtures (e.g. Tembe et al., 2010; Giorgetti et al., 2015). The associated (a-b) values are slightly lower than obtained for 100% quartz (Figure 4.4g). However, at T ≥100°C, the present data showed that

for quartz-calcite mixtures the frictional strength (μ) and stability, expressed via (a-b), are not simply intermediate. At 100-150°C, pure quartz and pure calcite showed similar behaviour, specifically an increase in μ with increasing velocity and with shear displacement at 100°C, and a decrease in μ with increasing velocity and shear displacement at 150°C. However, the 50:50 quartz-calcite mixtures showed remarkably different behaviour, exhibiting stronger (μ_{ss} = 0.62-0.68) and weaker (μ_{ss} = 0.59-0.66) behaviour than the quartz (μ_{ss} = 0.63-0.66) and calcite (μ_{ss} = 0.60-0.65) end-members respectively (Figures 4.2c and 4.3e,f). This suggests some kind of direct interaction between the two phases during shear, or else rapid localisation of shear due to grain size reduction preferentially in the calcite compared with the more fracture-resistant quartz (Atkinson and Avdis, 1980).

Our microstructural observations of the pure quartz sample (0% calcite, RS008 – Figure 4.9) revealed that shear was heterogeneously distributed over the bulk of the gouge layer, along the boundary, R_1- and P-shear bands. Major grain size reduction was observed throughout the entire gouge layer, with an increasing intensity of grain size reduction towards the margins of the gouge layer and predominantly in the lower boundary shear, which suggests the lower boundary shear zone to be the principal slip zone. Based on these microstructural observations, which are in agreement with the microstructures observed by Tembe et al. (2010), we suggest brittle micro-cracking and comminution to be the controlling deformation mechanisms in the 100% quartz sample, complemented by granular flow.

However, totally different deformation features are observed in the pure calcite sample, even though cataclastic fracturing operated as the main deformation mechanism in both samples. Cataclasis in the 100% calcite sample is more evenly distributed and characterised by a less significant and intense grain size reduction than in the 100% quartz one (Figures 4.8 and 4.9). One possible explanation for this difference lies in the fact that the quartz sample was sheared to larger displacement (40.8 mm) compared with the pure calcite sample (32.7 mm). However, a difference in extent of cataclastic grain fracturing between the two mineral types is also observed when mixed, in the 50:50 quartz-calcite samples (40.8 mm). SEM analysis of the 50:50 quartz-calcite sample (Figure 4.9 – RS014), revealed that the relatively large quartz grains showed only minimal evidence for intergranular cracking, while “floating” in an interconnected matrix of very finely

comminuted calcite (Figure 4.9). This implies that the fine calcite matrix controls the overall frictional behaviour, with quartz grains being passively carried in the matrix. This is supported by the violent stick-slip behaviour observed for both 50:50 quartz-calcite samples at T = 150°C, typically reported for pure calcite, suggesting that a thermally-activated mechanism such as dislocation glide and/or diffusion enabled compaction creep to compete with granular flow-induced dilation (cf. Figure 4.2c and Verberne et al. (2014)).

Combining the observed difference in intensity of cataclastic grain size reduction between quartz and calcite, the interconnected calcite matrix in both the boundary shears and in the bulk of the quartz-calcite gouge layer (Figure 4.9), and the frictional strength data obtained for both end-members (Figures 4.2c and 4.3c,f), therefore suggests that the bulk frictional strength of a 50:50 quartz-calcite mixture is not simply a function of the frictional strength of the two end-members, as quartz is the frictionally weaker component of the two. Rather, we propose that the bulk frictional strength of quartz-calcite mixture is a function of the strength/energy of these phases. This is supported by multiple studies to the critical stress intensity factor K_{ic} of quartz and calcite (Atkinson and Avdis, 1980; Atkinson, 1984), which showed that the fracture mechanics parameters for quartz are higher than for calcite, promoting the preferential cracking of calcite. It is furthermore shown that the critical stress intensity factor for both quartz and calcite increases with increasing temperature (Atkinson and Avdis, 1980). Most likely the observed difference in fracture toughness between quartz and calcite is related to the perfect rhombohedral cleavage of calcite, lowering its fracture toughness with respect to the quartz (Schultz et al., 1994). Moreover, we propose that, at a temperature of 150°C, the very intense calcite crushing, probably due to grain neighbour swapping of the more fracture-resistant quartz, tends to promote thermally-activated compaction via diffusion, balancing granular flow induced dilation, producing velocity-weakening behaviour. This is supported by the more negative (a-b) values and the highly unstable, velocity-weakening behaviour obtained for the 50:50 quartz-calcite mixtures compared to the pure calcite (Figures 4.2c and 4.4g).

4.4.5 Implications

The experimental results presented here have several important implications for understanding the frictional behaviour of clay-quartz-calcite fault gouges, such as found in faults cutting carbonate-bearing claystone and shale sequences, or in faults cutting claystone and shale formations overlying limestone sequences located in marine and continental basins worldwide (Smith-Rouch et al., 2006). Our results are particularly relevant for, but not limited to, faults in calcite-rich claystones and shale formations that seal hydrocarbon reservoirs and potential CO_2 storage reservoirs. The implications of our results are listed below:

1) Faults intersecting clay-quartz-calcite-bearing formations such as calcite-rich claystones and shales may be (re-)activated upon hydrocarbons production or CO_2-storage, potentially leading to induced (micro-)seismicity, fault zone dilation and reduction of sealing capacity. It is therefore critical to know how calcite content will affect the frictional strength and slip stability of these fault gouge mixtures. When assuming a clay-rich caprock composition consisting of ~20 to 65% phyllosilicates, 30 to 9% quartz, and 70 to 0% of calcite, the present results imply that an increase or decrease in calcite content due to processes such as CO_2 leakage (causing calcite precipitation/dissolution) or clay smearing, will result in only minor changes in frictional strength (cf. Figure 4.3a and b). The same applies to (a-b) values, which will only slightly increase or decrease as an effect of varying calcite content in the range 0-70%, while remaining velocity-strengthening (Figure 4.4). There will therefore be no significant effect of CO_2-fault-rock interactions on seismogenic potential (see also Samuelson and Spiers (2012)). Moreover, a change in calcite content might slightly affect the permeability of natural OPA fault gouge (cf. Chapter 3) (Crawford et al., 2008). Where an increase in calcite content might potentially lead to a decrease in the influence of the interconnected network of (aligned) phyllosilicates on the anisotropy and flow paths in the gouge material, resulting in an increase in permeability, hence reducing the sealing integrity of the caprock, a decrease in calcite content, in favour of phyllosilicates, could potentially lead to a decrease in permeability, improving the sealing integrity (Crawford et al., 2008).
2) By contrast, in clay-quartz-calcite gouges with a relatively high calcite content (>70% calcite), variations in calcite content will affect the frictional

strength of a fault gouge significantly. Not only will the strength increase strongly with calcite content, from 0.38 to 0.71, but at T ≥100°C (a-b) becomes negative for a calcite content >90%, potentially decreasing frictional stability. When assuming a crustal geotherm of ~20-30°C/km, and a surface temperature of 20°C, faults cutting claystone and shale formations consisting of this compositional range may show unstable, velocity-weakening behaviour, hence seismogenic behaviour, at depths of ~4-6 km (140-175°C) and beyond. An increase in calcite content under these conditions, due to for example calcite precipitation resulting from CO_2 leakage, could consequently cause an initially seismically stable clay-bearing fault gouge to become prone to seismicity, similar as observed for a carbonate-rich sandstone fault gouge (Chapter 2). Fortunately, this transition from stable to unstable sliding is coupled to a significant increase in frictional strength, requiring a significant increase in shear stress on the fault to initiate shear. At the same time, the strengthening is likely to be accompanied by an increase in fault permeability, as such reducing the sealing integrity of the caprock. Similarly, a decrease in calcite content will weaken, but stabilize a fault, while reducing the permeability, thus increase the sealing integrity (Crawford et al., 2008).

3) Conversely, in a scenario in which a small amount of phyllosilicates (<10%) is introduced in to a pure calcite gouge, e.g. by clay-smearing, the phyllosilicates will cause a significant drop in frictional strength (from 0.71 to 0.54), making a fault more prone to shear failure. If a fault with such a composition is reactivated, at T ≥ 100°C (depth > 3-4 km in above scenario), unstable stick-slip behaviour will produce a stress drop, due to the velocity-weakening behaviour of calcite, while being in the velocity-strengthening regime for the clay components. Furthermore, the clay will reduce the permeability, enhancing the formations sealing potential (Crawford et al., 2008).
4) Our quartz-calcite results imply that for an increase in calcite content in a quartz-dominated fault gouge to nearly equal proportions of quartz and calcite, e.g. due to calcite precipitation associated with CO_2-leakage in sandstone reservoir rocks, the frictional strength of the gouge will remain more or less unchanged. However, the frictional stability of the gouge will shift from initially velocity-strengthening to strongly velocity-weakening and thus potentially seismogenic. Such a shift in frictional stability, at more

or less constant frictional strength, is consistent with behaviour observed in laboratory experiments on simulated, aragonite-rich sandstone gouges derived from a naturally leaking CO_2 reservoir (SE Utah, USA – Chapter 2). These results demonstrate that while cementation by calcite precipitation might reduce the fault permeability, large amounts of calcite precipitation might affect the seismogenic potential upon fault reactivation. Further work on a wider range of quartz-calcite compositions would therefore be useful.

4.5 Conclusions

In this study, we aimed to experimentally determine how the frictional strength and velocity-dependence (*a*-*b*) of a simulated clay-quartz fault gouge changes with calcite content under in-situ CCS (Carbon Capture and Storage) conditions. The compositions addressed were representative of clay-quartz-calcite gouges that are expected to form in faults in claystone or shaly caprocks, for example. The material was prepared by removing calcite from crushed Opalinus Claystone (Calcite-Free OPAlinus claystone or CFOPA), then adding controlled amounts of calcite. To explore the effects of added calcite on pure clay and pure quartz independently, we also performed limited tests on these materials, investigating 100% pure end-members plus 50:50 mixtures with kaolinite or quartz. The experiments consisted of rotary shear friction experiments on simulated fault gouges, with varied amounts of added calcite, performed at an effective normal stress of 50 MPa, a pore fluid pressure of 25 MPa, temperatures of ~23, 100 and 150°C, and sliding velocities of 0.22-100 µm/s. Our main conclusions are as follows:

1) At room temperature and 100°C, the steady-state frictional strength of the CFOPA fault gouge was found to increase systematically with increasing added calcite content with μ_{ss} varying from 0.28 (0% calcite) to 0.71 (100% calcite). Similarly, (*a*-*b*) increases with increasing calcite content, consistently exhibiting velocity-strengthening behaviour at these temperatures. A transition from velocity-strengthening to velocity-weakening behaviour was observed between 100 and 150°C for a calcite content >90%.
2) A similar dependence of the steady-state frictional strength and (*a*-*b*) on calcite content was obtained for the simulated pure clay (kaolinite) plus

calcite fault gouge, with μ_{ss} ranging from 0.26 (0% calcite) to 0.71 (100% calcite), with no systematic dependence on temperature. A similar transition to the above was observed from velocity-strengthening in the pure kaolinite and 50:50 mixture, at 23-100°C, to velocity-weakening behaviour, at 150°C, in the 100% calcite experiment only.

3) At room temperature and 100°C, the quartz-calcite mixtures showed steady-state frictional strength values of 0.58 to 0.73, however, this was not intermediate to the weaker quartz and stronger calcite. At these temperatures, the samples exhibit velocity-strengthening behaviour. Unlike the clay-quartz-calcite (CFOPA plus calcite) and the clay-calcite (kaolinite plus calcite) mixtures, which showed velocity-weakening only above 90% calcite content, highly unstable, velocity-weakening behaviour was observed for the 50:50 calcite-quartz samples at 150°C, with (*a*-*b*) being significantly lower than in either end-member (~zero for pure calcite and pure quartz).
4) The dependence of μ and (*a*-*b*) on the composition observed for the CFOPA-calcite samples cannot be explained by a classical Reuss mixing model. A better fit was obtained when using a non-linearity expression involving a) a power law dependence on the proportions of the CFOPA vs. calcite and b) a power law dependence on the composition of the individual phyllosilicate phases vs. the linear dependence on quartz and calcite content.
5) The above trends in friction coefficient and velocity-dependence (*a*-*b*) can be explained qualitatively in terms of a change in controlling microscales processes, evidenced by changes in microstructure. At low calcite concentrations, shear in phyllosilicate dominated samples is concentrated in shear bands rich in the frictionally weak phyllosilicate phases. With increasing calcite concentrations, hence total strong or granular gouge fraction (calcite, quartz and pyrite), deformation starts to become more and more accommodated by cataclastic comminution of the calcite grains. The transition from velocity-strengthening to velocity-weakening behaviour seen between 100°C and 150°C in calcite-rich (≥95%) clay-quartz-calcite samples and in 50:50 quartz-calcite mixtures, is inferred to reflect a thermally-activated compaction mechanism, operating in the calcite component, such as thermally-activated diffusion, competing with dilation.

6) For in-situ CCS conditions, our results imply that clay-quartz-calcite gouges will transition from velocity-strengthening to velocity-weakening behaviour between temperatures of 100°C to 150°C for calcite concentrations higher than 90%. Fortunately, for compositions consisting of phyllosilicates, this transition from stable to potentially unstable sliding is coupled to an increase in frictional strength, requiring a significant increase in shear stress on the fault to initiate shear. Additionally, our quartz-calcite results imply that fault gouges with nearly equal proportions of quartz and calcite will exhibit strongly velocity-weakening behaviour at 150°C, but with relatively unchanged frictional strength.
7) The main implication of this research for CCS and natural faults in seismically active terrains with clay-quartz-calcite claystones and shale formations is that, within the framework of the rate-and-state friction model, aseismic fault behaviour is expected for calcite contents <~90%. Seismogenic behaviour is possible for a calcite content >90% at a temperature >100°C and depth range >3 km. In the absence of clay, i.e. for quartz-calcite mixtures, seismogenic behaviour is possible at calcite contents >~50%, at a temperature of >100°C and at depths of 3 km and beyond.

Acknowledgements

This research has been carried out in the context of the ULTImateCO_2-program. ULTImateCO_2 is a research program on Understanding the Long-Term fate of geologically stored CO_2 and is financially supported by the European Union (FP7). We thank Dr. Christophe Nussbaum (The Mont Terri rock laboratory) for providing the sample material. EB thanks ULTImateCO_2 for providing funding for the research. ARN was funded by European Research Council starting grant SEISMIC (335915) and by the Netherlands Organisation for Scientific Research (NWO) through a VIDI grant (854.12.011). Eimert de Graaff, Floris van Oort, Gert Kastelein, Peter van Krieken and Thony van der Gon Netscher are thanked for their technical support. Leonard Bik is thanked for making the thick sections and Tilly Bouten is thanked for coating these sections. Bart Verberne and Serguei Matveev are thanked for their help using the SEM equipment.

Chapter 5

The effect of long-term CO_2-fluid-rock interaction on the frictional properties of clay-rich fault gouges; integrated geochemical modelling and friction experiments

Elisenda Bakker, John P. Kaszuba, Sabine A.M. den Hartog and Suzanne J.T. Hangx

Abstract

In this study we investigated the effects of long-term (10,000 years) CO_2-fluid-rock interactions on the frictional behaviour of simulated clay-quartz-calcite fault gouges, analogues to clay-rich caprocks capping CO_2 storage reservoirs. To this end, we integrated geochemical modelling and laboratory friction experiments. A carbonate-bearing claystone (Opalinus Claystone – OPA) was used as the starting material. To evaluate CO_2-induced mineralogical changes in such fault gouges, the CO_2-exposed mineral composition was modelled for various scenarios, including two reaction durations (10,000 vs. 1 000 000 years), two different residence times of the fluid in the fault (10 vs. 1000 years) and two starting mineral assemblies (illite- vs. muscovite-dominated). Fault gouges were prepared according to the modelled gouge compositions and tested in friction experiments. Ring-shear experiments (σ_n^{eff} = 50 MPa, P_f = 25 MPa, and $T \approx$ 23-100-150°C) showed that at 23 and 100°C, the frictional resistance of the fault gouges increases with respect to the unexposed clay-quartz-calcite composition, while the gouges exhibited stable (aseismic), velocity-strengthening behaviour. At 150°C, the gouges showed a further increase in the frictional resistance as well as the potential that upon slip the fault may become prone to unstable (seismogenic), velocity-weakening slip behaviour, as the velocity-dependence of shear tends to become neutral to slightly negative. Significant changes in frictional resistance or (micro)seismic potential of clay-quartz-calcite fault gouges are only expected when there is a major smectite precipitation or when there is a major carbonate precipitation in the fault damage zone, leading to respectively a reduction in the frictional resistance to shear or the possibility of unstable (seismogenic) slip behaviour at 150°C.

5.1 Introduction

In recent years a significant amount of research has been conducted to understand CO_2-fluid-rock interactions that will follow not only long-term CO_2 storage in depleted oil and gas reservoirs, but also Enhanced Oil Recovery and Enhanced Gas Recovery, respectively EOR and EGR (Gaus et al., 2005; Shukla et al., 2011). The first technique is solely focused on mitigating anthropogenic CO_2 emissions, whereas EOR and EGR are implemented to enhance oil and gas production to keep up with the current demand for energy, while controlling anthropogenic CO_2 emissions in the process. In order for long-term Carbon Capture and Storage (CCS), as well as EGR and EOR, to be safe it is crucial that the sealing integrity of the caprock overlying the targeted storage reservoir is maintained during and after CO_2 injection, for at least 10,000 years (Haszeldine et al., 2005). Sustaining the sealing integrity of such caprocks therefore critically depends on the presence of production/injection wells, as well as natural faults penetrating the caprock (Haszeldine et al., 2005).

To date, only a limited amount of experimental research has been conducted investigating the effects of CO_2-fluid-rock interactions on the mechanical and transport properties of both faulted reservoir rocks and caprocks (see Chapters 2, 3 and 4 of this thesis, as well as Edlmann et al., 2013; Hangx et al., 2015; Pluymakers et al., 2014b; Samuelson and Spiers, 2012; Trippetta et al., 2013). Short-term experiments (hours-days) aimed at studying the potential for CO_2 to lubricate or dry out the fault plane, potentially impacting the frictional behaviour of the fault gouge, i.e. the wear product created by fracturing of the intact host rock (Pluymakers et al., 2014b; Samuelson and Spiers, 2012), or to impact fault sealing (Edlmann et al., 2013). However, little research has been done investigating the effect of long-term CO_2-exposure on the mechanical and transport properties of faults (Chapter 2; Hangx et al., 2015; Trippetta et al., 2013).

Concerning caprock integrity, pre-existing faults in caprocks are natural, weak features that may be reactivated upon injection, via a reduction in the normal and/or shear stresses acting on the fault plane caused by pore pressure changes in the fault, thermally-induced local stress changes and the poro-elastic response of the surroundings (i.e. reservoir and caprock) to pressure changes (Cheng, 2016; Preisig and Prévost, 2011; Vilarrasa et al., 2014; Wang, 2000). Fault reactivation can

potentially lead to induced seismicity and associated CO_2 leakage (Rutqvist et al., 2013; Zoback and Gorelick, 2012). Numerous experimental studies to the frictional behaviour and transport properties of (simulated) fault gouges have demonstrated the importance of mineralogy (e.g. Tembe et al., 2010; Moore and Lockner, 2004). Strong minerals (e.g. quartz, feldspar, Ca-carbonate, anhydrite) are known to exhibit a high frictional strength (μ = 0.6-0.85), whereas platy minerals (e.g. clays, micas) are significantly weaker (μ =0.2-0.5 – Byerlee, 1978; Moore and Lockner, 2004). Natural faults are generally polymineralic mixtures consisting of these weak and strong minerals and exhibit therefore a rather complex frictional behaviour, typically controlled by the strength of the dominant mineral(s) (Rauenzahn and Logan, 1987).

CO_2-induced fluid-rock interactions in clay-rich caprocks, lithologies that commonly cap potential CO_2 reservoirs (Allen and Allen, 2005), can result in dissolution and re-precipitation of carbonates, dissolution of plagioclase, feldspar, clay minerals (illite, chlorite, and kaolinite) and, provided there is a source of magnesium, the precipitation of smectite (Alemu et al., 2011; Credoz et al., 2009). Mineralogical changes such as these might alter the frictional behaviour of a gouge material. However, because of the associated slow reaction rates, particularly of clays and micas (Cama et al., 2002, 2000; Kalinowski and Schweda, 1996; Knauss and Thomas J, 1989; Zysset and Schindler, 1996), it is challenging to reproduce such chemical mineral reactions on laboratory time-scales (week-months), hindering the study of coupled chemical-mechanical processes.

In order to assess the coupled chemical-mechanical effects of long-term CO_2 exposure on fault gouges, we combine predictive geochemical modelling with laboratory friction experiments. The effect of chemically-induced changes in mineralogy on frictional behaviour can be investigated by preparing "CO_2-exposed" fault gouges, which are subsequently tested in the laboratory to determine the corresponding frictional properties. This is done as follows: i) determining the change in mineralogy of a well-characterised starting material after 10 ka or 1 Ma of CO_2 exposure via geochemical modelling, ii) selecting the geochemical modelling results which are characterised by mineralogical changes that are expected to show a notable effect on the frictional behaviour, iii) preparing the simulated fault gouges (or as equivalent as possible) by mixing pure minerals, and iv) conducting friction experiments on the manually-mixed compositions, as means of evaluating

the effects of long-term CO_2-fluid-rock interaction on the frictional behaviour of clay-rich fault gouges.

As starting material we use the Opalinus Claystone (OPA), a carbonate-bearing claystone, as an analogue for clayey caprocks found overlying hydrocarbon reservoirs in sedimentary basins in Western-Europe. This material has a well-known mineralogical and geochemical character, including the pore water composition, needed for well-defined geochemical modelling. To evaluate how CO_2-fluid-rock interactions might alter the frictional behaviour of OPA fault gouges, we modelled various scenarios with reaction durations of 10,000 and 1 000 000 years, for two different fluid residence/refreshment times of 10 vs. 1000 years. In this way we simulate penetration of the fault by fluid in 10 and 1000 year pulses ("fault-valve" behaviour - Sibson, 1992). From a frictional perspective, we are interested in the impact of gouge composition on the frictional resistance of shear and on the potential transition from stable to unstable (potentially seismogenic) slip behaviour. Our results also have implications outside of the CCS community as major seismically active faults in clay-rich formations worldwide contain significant amounts of calcite (i.e. as veins and/or as cements – e.g. The Alpine Fault (Boulton et al., 2012)).

5.2 Methods

5.2.1 Natural starting material: Opalinus Claystone

The Opalinus Claystone (OPA – Middle Jurassic) sample material used in this study was collected from the Mont Terri Underground Rock Laboratory, Switzerland (courtesy of Swisstopo, Dr. C. Nussbaum). Conventional, quantitative X-ray diffraction (XRD) analyses of the OPA starting material, taken from the "silty-shaly" facies, showed that the material consists of quartz (~20-42%), carbonate (~12-40%), phyllosilicates (~36-64%), and pyrite (~2%) (see Appendix 5.A, Table 5.A1). Greater precision Rietveld refinement showed the Opalinus Claystone to consist of quartz (23%), calcite (26%), and minor pyrite (4%), with the clay fraction consisting of chlorite (4%), illite (5%), illite-smectite (24%), kaolinite (13%), (Table 5.A1). Our measured average composition is in accordance with previously reported compositions (Pearson et al., 2003).

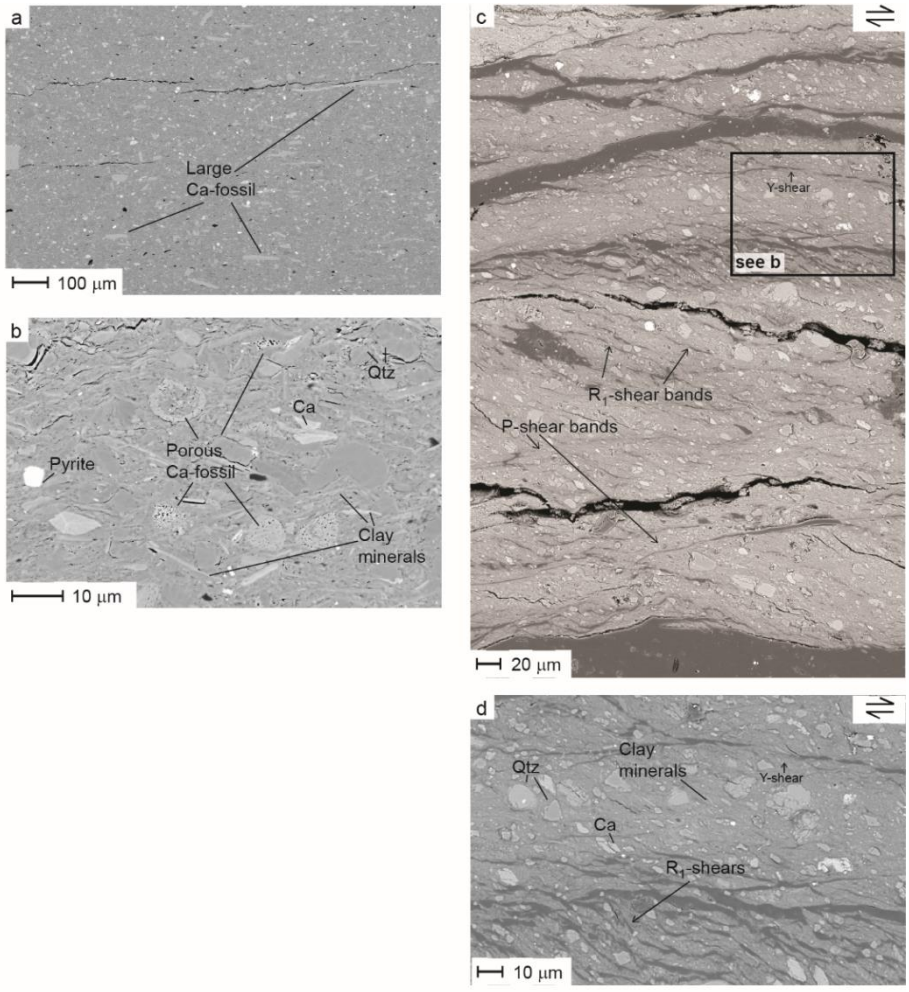

Figure 5.1. Backscatter Electron (BSE) micrographs of intact and sheared Opalinus Claystone (OPA). a) SEM (BSE) micrograph of the intact, uncrushed starting material microstructure, showing larger (up to 100-200 microns) calcite (Ca) fossils embedded in a fine-grained clay-matrix. b) Zoom of the intact microstructure showing the fine-grained matrix material, consisting of smaller porous calcite fossils (10-20 microns), quartz (Qtz), pyrite and clay minerals. c) Overview of the sheared OPA sample, showing R_1-, P- and Y-shear bands in the body of the gouge layer. Note that the boundary shears were not (fully) preserved in this section. d) In-set of (c), showing the main body of the gouge layer with distributed internally fractured quartz (Qtz) and calcite (Ca) grains. Locally the clay minerals are too small to be distinguished.

Backscatter Electron Microscopy of a Broad-Ion-Beam (BIB) polished intact OPA rock sample shows that the OPA is a very fine-grained, low porosity claystone consisting of homogenously distributed fossil shells and framboidal pyrite embedded in a phyllosilicate-dominated matrix (Figure 5.1). Detailed SEM (BSE) analysis of the intact OPA shows that each of the mineral phases present is characterized by their own shape and internal porosity. Generally, quartz is present as solid, rounded grains (up to 30 µm), whereas calcite is present as both solid, rounded grains (up to 20 µm in diameter) as well as porous, fossil shells (varying from rounded fossils up to several tens of microns in diameter, to elongated fossils up to 200 µm in length; Figure 5.1).

5.2.2 Geochemical simulations of CO_2-water-rock interactions in OPA

Three distinct conceptual scenarios have been developed to understand how fluids rising from an underlying sandstone storage reservoir may impact coupled chemical-mechanical processes within a faulted carbonate-bearing claystone caprock. The first scenario consists of the baseline scenario ("baseline") in which no CO_2 is injected into the underlying storage reservoir. Reservoir water that invades the fault within the overlying claystone caprock is therefore not saturated with CO_2. In the second scenario, CO_2 is injected into the reservoir, and the reservoir water is saturated with CO_2. Once CO_2-saturated water invades the faulted caprock, the fault is assumed to form a closed system, i.e. the fault is isolated from the underlying reservoir. The third scenario is in essence the same as the second, but the fault behaves as an open system with respect to the CO_2 (but not water) residing in the underlying reservoir. Dissolved CO_2 is consumed by water-rock interaction in the closed system, whereas in the open system it is buffered and CO_2 saturation remains constant.

Simulations for these three scenarios are constructed using Geochemist's Workbench 11.0 (GWB), the b-dot ion association model, and the resident thermo.tdat database (Bethke and Yeakel, 2014) according to previously described methods (Chopping and Kaszuba, 2012; Marcon and Kaszuba, 2015). We use thermo.tdat because it is internally consistent and addresses aluminium speciation more adeptly than other available databases (Kaszuba et al., 2011). This database is modified to simulate the salting-out behaviour of CO_2 by assigning the ion size parameter of CO_2 (aq) a value of -0.5 (Allen et al., 2005).

Simulations for each of the three scenarios require models of two separate fluid-rock systems, one equilibrating pore water from the claystone (Table 5.A2) with fine-grained OPA gouge material (Table 5.A3) at a temperature of 100°C and a second equilibrating reservoir water with a sandstone reservoir at 100°C, representative of a depth of about 3 km. Two different reservoir waters were developed (Table 5.A4), one equilibrated with sandstone prior to injection of CO_2 (baseline scenario) and a second equilibrated with sandstone after injection of CO_2 (both closed and open system scenarios). In subsequent kinetic models, water from the sandstone reservoir instantaneously displaced OPA pore water in the fault and reacted with OPA gouge material (Table 5.A1). To emulate the effect of periodical fault re-activation, leading to fault dilation and increased fault permeability (i.e. fault-valve behaviour – see Hooper, 1991; Sibson, 1992; Wiprut and Zoback, 2000), reacted fluid in the fault was periodically displaced by fresh reservoir water. We modelled two time intervals, residence/refreshment time t_r, of fluid displacement, 10 and 1000 years, to represent rapid and more gradual over-pressurization of the reservoir, respectively. CO_2 storage reservoirs are typically evaluated for time frames of 10,000 years; however, we simulated CO_2-fluid-rock interactions with fault gouge for as long as 1 Ma to better understand reaction processes and trends.

Kinetic modelling in this paper is based on transition state theory (Lasaga, 1984; Steefel and Lasaga, 1994) and uses the rate expression:

$$r = kA\left[1 - \left(\frac{Q}{E}\right)\right] \tag{5.1}$$

where r is the rate, k is the kinetic rate constant, A is the reactive surface area, Q is the reaction quotient, and E is the equilibrium constant. The kinetic rate constant k is summed from three mechanisms (Lasaga et al., 1994; Palandri and Kharaka, 2004):

$$k = k_{neutral} + k_{acid} ac_{H^+}^{n_{H^+}} + k_{base} ac_{OH^-}^{n_{OH^-}} \tag{5.2}$$

where subscripts for k indicate neutral, acid, and base mechanisms for the rate constant, ac is the activity of the species H^+ and OH^-, and n is a power term (a constant) for the indicated species. Kinetic parameters used in this study are tabulated in Table 5.A5.

The primary focus of the long-term CO_2-fluid-rock interaction investigation is on chemical alterations in illite-bearing OPA gouge. Commonly phyllosilicate-rich materials consist of mixed illite-smectite interlayered clays and/or illite, though on occasion they may contain smaller amounts of smectite, muscovite or illite-muscovite interlayered clays (e.g. Boulton et al., 2012), depending on the maturity of the material. Therefore an additional set of 3 closed-system scenarios was produced, considering muscovite to be the main phyllosilicate phase ("muscovite-bearing OPA" gouges – see Table 5.A4). Time-evolutions of the gouge compositions for the modelled reservoir water and CO_2-saturated water scenarios are shown in Appendix 5.B. The modelling and frictional testing results are then compared to the illite-bearing OPA results to evaluate if similar mineralogical alterations would occur and how they would affect the frictional behaviour. Note that for this comparison, we grouped the various minerals in the gouge according to four main mineral groups, depending on hardness and crystal morphology: quartz, carbonates (calcite, dolomite, and siderite), micas (paragonite) and clays (chlorite (daphnite), illite, kaolinite, smectite (nontronite, saponite)).

5.2.3 Sample preparation

The unreacted OPA fault gouge material (Data-set 1) was prepared by crushing pieces of OPA using a pestle and mortar, and sieving the powder to a grain size <35 µm. Calcite-free OPA (CFOPA) was prepared by exposing crushed OPA to an excess of acetic-acid ($C_2H_4O_2$; pH 3, at ~20-80°C), effectively removing any naturally-present calcite, after which the material was washed, dried and sieved again (<35 µm). The modelled fault gouge compositions of Data-sets 3-5 were prepared by mixing, by weight, finely powdered quartz (99.9% pure; Beaujean quartz sand), kaolinite (100% pure; Merkx®), muscovite (90% muscovite plus ~10% quartz impurities which has not been corrected for; commercially obtained), calcite (Iceland spar; Verberne et al. (2011)), dolomite (97% dolomite plus ~3% labradorite; Forno – Apuan Alps), and illite-shale (65% illite plus 35% quartz impurities, which has been corrected for; Den Hartog et al., 2011) according to the compositions listed in Table 5.1. Prior to mixing, the quartz, calcite, dolomite and illite-shale were crushed using a pestle and mortar. The mineral powders were sieved to a grain size of <35 µm, which is a typical size range observed in simulated and natural fault gouges (Byerlee and Summers, 1976; Keulen et al., 2007). Pure siderite, Ca-nontronite, paragonite and pyrite were difficult to obtain and therefore

Table 5.1. Geochemical modelling outcome. Listed is the illite-bearing OPA starting composition used for the geochemical modelling, followed by the outcomes for the reservoir water exposed, closed system CO_2-exposed and open system CO_2-exposed scenarios. The muscovite-bearing OPA starting composition used for modelling is listed next to the modelling outcomes for the closed system, CO_2-exposed scenarios.

	Illite-bearing starting composition													Muscovite-bearing starting composition			
	Reservoir water					*CO_2-saturated reservoir water*								*CO_2-saturated reservoir water*			
	Model composition	**RW-t,10-10ka**	RW-t,10-1Ma	RW-t,1000-10ka	RW-t,1000-1Ma	**IC-t,10-10ka**	**IC-t,10-1Ma**	**IC-t,1000-10ka**	**IC-t,1000-1Ma**	IO-t,10-10ka	IO-t,10-1Ma	IO-t,1000-10ka and	IO-t,1000-1Ma	***Model composition***	**MC-t,10-10KaS**	**MC-t,10-10Ka**	**MC-t,1000-10Ka**
Residence time t_r (yr)	0	10	10	1000	1000	10	10	1000	1000	10	10	1000	1000	0	10	10	1000
Reaction time t (yr)	0	10ka	10Ma	10ka	1Ma	10ka	10Ma	10ka	1Ma	10ka	10Ma	10ka	1Ma	0	10ka	10Ma	10ka
Pyrite	*4*	*4*	*4*	*5*	*4*	*4*	*4*	*5*	*4*	*4*	*4*	*5*	*4*	*0.04*	*0.04*	*0.04*	*5*
(Total) Quartz	**23/26**	**22**	**23**	**18**	**24**	**31**	**26**	**45**	**34**	**31**	**27**	**45**	**35**	**29**	**0.2**	**0.2**	**34**
Calcite	25	22	25	0	22	7	20	0	9	7	19	0	6	13	15	15	4
Dolomite	1	3	1	0	3	10	9	0	12	10	9	0	13	1	36	36	16
Siderite	0	0	0	0	0	4	3	0	4	4	3	0	4	0	0	0	0
Total carbonate	**26**	**25**	**26**	**0**	**25**	**21**	**32**	**0**	**25**	**21**	**31**	**0**	**23**	**14**	**51**	**51**	**20**
Paragonite (Total mica)	**0**	**11**	**1**	**0**	**18**	**0**	**0**	**0**	**0**	**0**	**0**	**0**	**0**	**20**	**0**	**0**	**20**
Illite	25/24	23	25	0	13	23	21	0	0	23	19	0	0	2	0	0	0
Kaolinite	14/13	5	13	38	6	21	17	50	38	21	19	50	39	17	0	0	22
Daphnite (chlorite)	4	0	3	0	0	0	0	0	0	0	0	0	0	6	5	0	0
Saponite (smectite)	5/0	5	5	32	0	0	0	0	0	0	0	0	0	11	44	49	0
Nontronite (smectite)	0	6	1	7	6	0	0	0	0	0	0	0	0	0	0	0	4
Pyrophyllite	0/1	0	0	0	0	0	0	0	0	0	0	0	0	0	0	0	0
Total clay	**48/42**	**39**	**47**	**77**	**25**	**44**	**38**	**50**	**38**	**44**	**38**	**50**	**39**	**36**	**49**	**49**	**26**
Weak:strong (excluding pyrite)	49:48 52:42	50:47	48:49	77:18	43:49	44:52	38:58	50:45	38:59	44:52	38:58	50:45	39:58	56:43	49:51	49:51	46:54

RW = reservoir water exposure, I = illite-bearing OPA starting composition, M = muscovite-bearing OPA starting composition. S denotes smectite referring to the "10 years residence time – 10,000 years reaction time" scenario without non-swelling clays, whereas r denotes repeat experiment. *Italic*: pyrite was not added to the simulated fault gouges, underlined: in case of the open systems simulation, the mineral distribution used for the open system scenarios differed slightly from the closed system scenarios. Modelling outcomes with bold, black names were prepared for friction experiments, and frictional properties obtained for these compositions are listed in Table 5.2.

replaced by analogue minerals, respectively dolomite, Ca-montmorillonite and muscovite, while pyrite was omitted altogether due to its small proportion and the predicted mineral proportions were corrected accordingly.

5.2.4 Experimental apparatus and procedure

Frictional sliding experiments were performed using the hydrothermal rotary shear apparatus at Utrecht University (Figure 5.2 – see also Chapter 4; Niemeijer et al., 2008). Inside the internally heated pressure vessel, a ~1 mm thick ring-shaped gouge layer (radius of 12.5 mm) is sandwiched between two roughened René 41 Super-alloy pistons, and kept in place by two confining and graphite-coated René 41 rings (Figure 5.2c). Distilled water in the pressure vessel acts as the pore fluid phase. Normal stress is applied via the pressure-compensated upper loading piston, in excess of the pore fluid pressure (P_f), such that the effective normal stress (σ_n^{eff}) on the sample is equal to the axially applied stress, assuming the pore fluid saturated the gouge layer. Rotation of the pressure vessel and lower piston, by a servo-controlled motor-gearbox system and with respect to the stationary upper piston, which is held fixed by a torque bar, allow shearing of the gouge layer at constant rate. The generated shear stress (τ) is measured externally using two externally placed load cells (resolution: ± 0.006 MPa), located at the extremities of the torque bar.

The experimental procedure followed has been described in Chapter 4. The experiments were performed at an effective normal stress of 50 MPa, a pore fluid pressure of 25 MPa, temperatures (T) of ~23-100-150°C and at sliding velocities (V) ranging between 0.22 and 100 µm/s. The temperature range of ~23-150°C was selected to investigate (1) the temperature range in which potential CO_2 storage reservoirs are located and (2) the temperature range over which calcite is known to transition from stable to unstable friction behaviour (e.g. Verberne et al., 2010). A total of 11 friction experiments was performed to allow for sufficient cross-comparison of the frictional strength and stability of clay-quartz-calcite fault gouge compositions reacted with CO_2-charged waters with respect to the unreacted clay-quartz-calcite fault gouge material (cf. OPA – Table 5.2).

The experiments are typically subdivided into 4 Stages. In Stages 1 through 3, respectively at ~23, 100 and 150°C, the gouge layers were sheared for a total

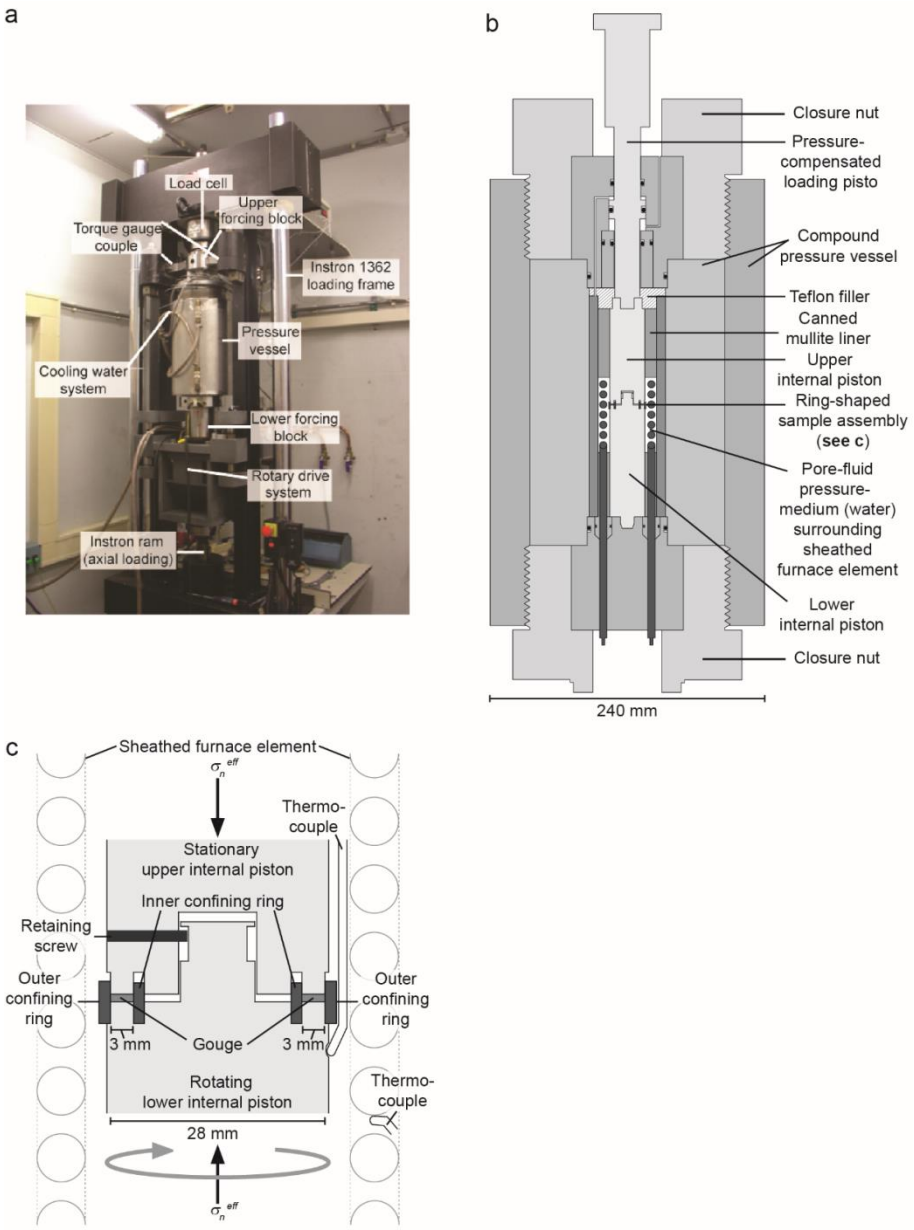

Figure 5.2. Experimental apparatus. a) Photograph of the ring-shear apparatus used in this study (after Niemeijer et al. 2008). The motor plus gearbox system constituting the rotational drive is installed behind the pressure vessel. b) Schematic representations of the pressure vessel. c) Schematic representation of the sample assembly (after Niemeijer et al., 2008, Den Hartog et al, 2012).

displacement of 10.9 mm employing a velocity-stepping sequence. Prior to velocity stepping, shear was initiated at a sliding velocity of 5.43 µm/s for 4.2 mm. The velocity step sequence employed is 0.22-1.086-10.86-1.086-3-10-30-100 µm/s. After completing Stages 1 and 2, the set-up was heated to respectively 100°C (Stage 2) and 150°C (Stage 3), while maintaining a constant effective normal stress and near-constant pore pressure. Upon reaching a new *P-T* equilibrium, the same velocity-stepping sequence as in Stage 1 was imposed during Stages 2 and 3. The velocity-stepping stages were followed by a normal stress-stepping sequence at 150°C (Stage 4). The normal stress-stepping sequence employed is 50, 60, 80 and 100 MPa for 2 mm per step and each at a sliding velocity of 10 µm/s. The CFOPA experiment (Data-set 3, Table 5.2) consisted of the first three stages of velocity-stepping only, Stages 1-3. Shear was stopped at a total (uncorrected) shear displacement of ~40.7 mm, or ~32.7 mm in case of CFOPA (Data-set 3). Each experiment was terminated by removing the torque and axial load, followed by switching off the furnace. To prevent steam formation, the pore pressure was maintained during cooling before venting at ~50°C.

5.2.5 Data acquisition and processing

Shear and axial displacement (resolution ± 1 µm and ± 0.5 µm, respectively), normal force (± 0.05 MPa), torque (better than ± 0.006 MPa), pore fluid pressure (± 0.015 MPa) and sample temperature (± 0.1°C) were acquired at 900 Hz using a 16 bit A/D converter, averaged and logged at frequencies of 10-30-100 Hz (equivalent to logging times of 0.1, 0.3, and 0.01 s, respectively), depending on sliding velocity. Torque and normal force data were corrected for pre-determined seal friction using pre-defined correction factors, to obtain the average shear stress (τ) and effective normal stress (σ_n^{eff}) acting on the gouge layer, whereas the shear displacement was corrected for machine stiffness (distortion), using a linear function. The apparent friction coefficient μ was calculated as the ratio of shear stress to effective normal stress, $\mu = \tau/\sigma_n^{eff}$, ignoring cohesion. Henceforth, the apparent friction coefficient is called friction coefficient.

The velocity-dependence of μ was interpreted in the framework of rate-and-state dependent friction theory (RSF; Dietrich, 1978, 1979; Ruina, 1983), using the parameter:

$$(a\text{-}b) = \frac{\Delta\mu_{ss}}{\Delta lnV} \quad (5.3)$$

(e.g. Marone, 1998). Here *a* reflects the magnitude of the instantaneous change in steady-state friction coefficient μ_{ss} upon a change in sliding velocity from a reference sliding velocity V_0 to a new sliding velocity $V = exp\ V_0$, *b* represents the magnitude of the change in μ during subsequent evolution to a new steady-state value over a characteristic slip distance D_c (Figure 5.3). The stepwise change in sliding velocity yields a change in steady-state friction coefficient of $\Delta\mu_{ss}$. When the friction coefficient increases with increasing sliding velocity, (*a*-*b*) is positive, which is known as "velocity-strengthening" behaviour and implies that the system is inherently stable. Seismogenesis due to accelerating slip is therefore impossible (e.g. Scholz, 1998). Negative (*a*-*b*) values on the other hand, indicate potentially unstable, "velocity-weakening" behaviour, meaning that the friction coefficient decreases with increasing velocity, which is a requirement for seismogenic slip. Values for (*a*-*b*), and *a* and *b* separately are shown in Appendix 5.C. Errors for (*a*-*b*) are generally as high as ±0.001, but may be maximum ±0.0028.

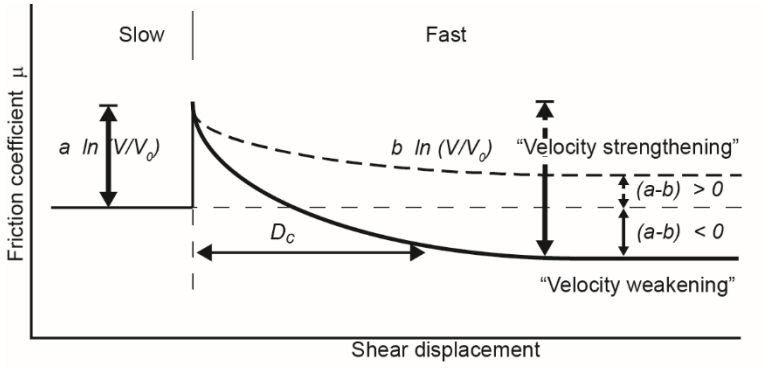

Figure 5.3 Frictional response to an instantaneous imposed velocity increase from V_0 to *V*. Friction typically increases by an amount "*a* ln (V/V_0)", upon a velocity increase, which is known as the direct velocity effect. This initial increase in friction is followed by an evolutionary decrease, of magnitude "*b* ln (V/V_0)".

The observed velocity step-related changes in friction coefficient are often superimposed onto a gradual increase or decrease in frictional strength with increasing slip distance, a so-called strain-hardening or strain-weakening trend, respectively. Strain-hardening is often associated with the on-going grain size reduction of granular material through cataclasis, potentially in combination with

the preferential extrusion of phyllosilicates from a fault gouge (Den Hartog et al., 2012), whereas strain-weakening is associated with ongoing localization of shear deformation along frictionally weak shear bands (Kanagawa et al., 2000; Niemeijer et al., 2008).

5.3 Results: geochemical modelling scenarios and friction experiments

Experimental conditions and key frictional data are provided in Table 5.2 for the different data-sets. First we describe the frictional behaviour of the starting material (OPA), the mineralogical evolution of OPA and its frictional behaviour after long-term exposure to reservoir water ("baseline scenario"). Second, we consider a scenario where carbonate minerals are rapidly removed from the system, prior to longer-term reactions, effectively removing all naturally-occurring calcite from OPA (producing calcite-free OPA – CFOPA). Finally we describe and discuss the chemical changes observed in illite-bearing OPA exposed to CO_2-saturated reservoir water (open and closed system), as well as in muscovite-bearing OPA exposed to CO_2-saturated reservoir water (closed system), and the effect of the observed mineralogy changes on the frictional behaviour of OPA.

For the friction experiments we will only focus on geochemical modelling results showing chemical changes that are expected to show a notable effect on the frictional behaviour. Therefore we have selected mineral compositions with chemical changes that are characterised by the following criterion; (i) >5wt% difference per mineral group (quartz, carbonates, micas, clays), and/or (ii) an increase of >5wt% in strong (quartz + carbonates) vs. weak phase (micas + clays) (Table 5.1; Appendix 5.B). In case multiple scenarios showed roughly similar chemical changes, the scenario characterised by the smallest chemical change, as defined by criterion (i) and (ii), was selected, representative for the minimal impact of chemical changes on frictional behaviour for a given residence/refreshment and reaction time. The baseline scenario served as a point of reference to gauge the long-term chemical impact of CO_2 exposure, as it illustrates the natural long-term evolution of the gouge material exposed to reservoir water.

Table 5.2. Overview of the friction experiments performed in this study, including key data on friction coefficient (μ) and velocity dependence (a-b). Experiments were performed at a constant effective normal stress (σ_n^{eff} = 50 MPa) and pore pressure (P_f = 25 MPa), at temperatures (T) of 23°C (Stage 1), 100°C (stage 2) and 150°C (Stages 3 and 4) using sliding velocities (V) between 0.22 and 100 µm/s. Stage 4 consists of a stress-stepping sequence (50-60-80-100 MPa) for 2 mm of displacement per stress-step, at a constant sliding velocity of 2 µm/s. In the absence of a clear peak, no μ_{peak}-value is listed.

Sample	*Composition (fluid, residence time, reaction time)*	μ_{peak} (V = 5.43 µm/s)			μ_{ss} (at displacement mm)			μ_{final} (at displacement mm)			D_f (mm)	μ_i (-)	C_o (MPa)	(a-b) positive/negative Stage#
		Stage			*Stage*			*Stage*						
		1	2	3	1 (*4.0*)	2 (*14.7*)	3 (*25.4*)	1 (*10.7*)	2 (*21.4*)	3 (*32.1*)				
Data-set 1 – OPA (starting material)														
OPA	OPA	-	0.35	0.36	0.35	0.35	0.36	0.38	0.40	0.42	40.7	0.33	0.77	Positive
Data-set 2 — illite-bearing OPA exposed to reservoir water (OPA)														
RS024*	RW- t_r10-10ka	0.43	0.42	0.47	0.39	0.43	0.47	0.44	0.47	0.49	40.7	0.47	-1.56	Positive
Data-set 3 – Calcite-Free OPA (CFOPA)														
CFOPA	CFOPA	-	0.27	0.30	0.28	0.28	0.30	0.33	0.32	0.31	32.9	-	-	Positive
Data-set 4 – illite-bearing OPA exposed to CO_2-saturated reservoir water														
RS019	IC-t_r10-10ka	0.40	0.49	0.53	0.43	0.47	0.52	0.50	0.54	0.59	40.7	0.44	2.18	Negative; 2,3
RS022	IC-t_r10-10kar	-	0.51	0.57	0.47	0.50	0.54	0.53	0.56	0.56	40.7	0.55	-1.80	Negative; 3
RS020	IC-t_r1000-10ka	0.40	0.40	0.47	0.40	0.43	0.46	0.43	0.47	0.46	40.7	0.47	-1.82	Negative; 3
RS021	IC-t_r10-1Ma	0.36	0.44	0.50	0.42	0.45	0.49	0.46	0.50	0.51	40.7	0.39	4.04	Negative; 2,3
RS023	IC-t_r1000-1Ma	0.41	0.45	0.49	0.44	0.46	0.48	0.47	0.48	0.50	40.7	0.44	2.18	Negative; 2,3
Data-set 5 – muscovite-bearing OPA exposed to CO_2-saturated reservoir water														
RS015	MC-t_r1000-10Ka	-	0.47	0.51	0.42	0.47	0.49	0.48	0.49	0.51	40.7	0.51	-1.77	Negative; 3
RS016	MC-t_r10-10KaS	0.27	0.24	0.28	0.25	0.24	0.27	0.28	0.30	0.33	40.7	0.20	4.43	Positive
RS017	MC-t_r10-10Ka	0.31	0.30	0.33	0.31	0.28	0.29	0.36	0.33	0.33	40.7	0.24	3.11	Positive

Symbols: μ_{peak} = peak frictional strength at V = 5.43 µm/s, μ_{ss} = frictional strength at steady state at V = 5.43 µm/s and μ_{final} = frictional strength at the end of Stage 1, 2, 3 at V = 100 µm/s, D_f = final shear displacement, μ_i = internal friction, C_o = cohesion. Denotation of the 'composition': RW = closed system with reservoir water as the reaction fluid, C = closed system with CO_2-saturated reservoir water, O = open system with CO_2-saturated reservoir water, I = illite-bearing gouge, M = muscovite-bearing gouge, t_r = residence time of CO_2-saturated pore water in the fault (10 vs. 1000 years) for a reaction time of 10 ka or 1 Ma. S denotes smectite referring to the "10 years residence time – 10,000 years reaction time" scenario without non-swelling clays, whereas r denotes repeat experiment. * The pronounced peak during the initial loading phase reflects an experimental artefact caused by over-compaction during the application of the normal stress.

Overall, for the 11 compositions tested, the evolution of the friction coefficient μ with shear displacement x is characterised either by an initial increase in μ to a peak strength (μ_{peak}) and successive drop in μ followed by minor strain-hardening, reaching (near) steady-state at ~4.0 mm displacement or an initial increase in μ followed by yielding, which is taken as the point of maximum curvature, and strain-hardening, reaching (near) steady-state (μ_{ss}) at ~2.0-4.0 mm displacement (Figure 5.4). Similarly, upon re-shear following an increase in temperature, all compositions showed a peak friction immediately followed by a drop in μ before reaching a new steady-state.

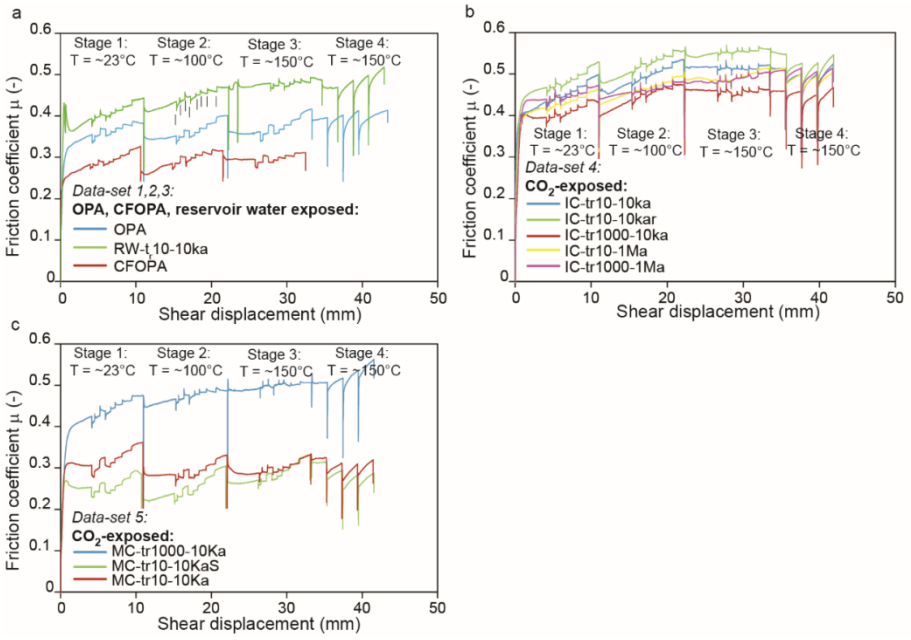

Figure 5.4. Typical evolution of friction coefficient with shear displacement obtained in the present experiments tested at σ_n^{eff} = 50 MPa, P_f =100 MPa and T ≈ 23, 100 and 150 °C (Stages 1-4). Velocity steps employed are 5.43-0.22-1.086-10.86-1.086-3.0-10-30-100 µm/s, with the location of a change in velocity indicated using vertical "ticks". a) Friction curves for OPA (Data-set 1), OPA exposed to reservoir water (Data-set 2) and calcite-free OPA (CFOPA-Data-set 3). b) Friction curves for illite-bearing OPA exposed to CO_2-saturated reservoir water (Data-set 4). c) Friction curves for muscovite-bearing OPA exposed to CO_2-saturated reservoir water (Data-set 5). Note, that peak or yield values, obtained during the normal stress stepping sequence of Stage 4, are plotted as a function of effective normal stress in Figure 5.6.

5.3.1 Frictional behaviour of natural, calcite-bearing OPA (starting material – Data-set 1)

The μ vs. shear displacement curve obtained for the OPA starting material is characterized by slight strain-hardening during the run-in phase (Figure 5.4a) and temperature-insensitive frictional strength, explicitly shown in Figure 5.5a (Table 5.2). Over the temperature range investigated (Stages 1-3), steady-state friction values range between 0.35–0.42 (Figure 5.5a, Table 5.2), showing an increase in μ_{ss} with sliding velocity. The velocity-dependence of the individual velocity-steps, expressed in terms of (*a*-*b*), is plotted for all velocities as a function of temperature in Figure 5.6. OPA displays positive (*a*-*b*) values, reflecting stable, velocity-strengthening behaviour, which increase slightly with temperature (Figure 5.6a). The observed friction coefficients and velocity-strengthening behaviour (T ≈ 23-150°C) agree with those reported in literature for wet, natural calcite-bearing clay gouge materials (e.g. Chapter 3; Boulton et al., 2012; Chen et al., 2015).

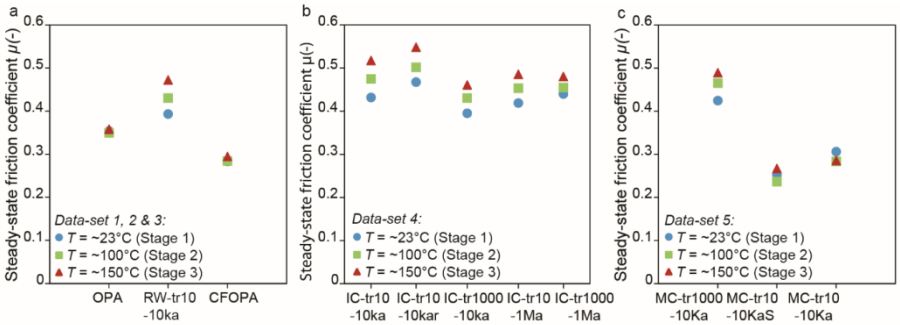

Figure 5.5. Friction coefficient at steady-state (i.e. at 4.0, 14.7 and 25.4 mm after run-in at 5.43 µm/s) as a function of temperature for the different compositions tested at σ_n^{eff} = 50 MPa, P_f = 25 MPa and T ≈ 23, 100 and 150 °C (Stages 1-3). a) OPA (Data-set 1), OPA exposed to reservoir water (closed system - Data-set 2), and calcite-free OPA (CFOPA - Data-set 3). b) Illite-bearing OPA exposed to CO_2-saturated reservoir water (open and closed systems - Data-set 4). c) Muscovite-bearing OPA exposed to CO_2-saturated reservoir water (closed system - Data-set 5).

The sheared OPA gouge was preserved, and prepared for microstructural analysis by impregnation with resin and slicing the gouge sample tangential to the shear direction. Backscatter Electron (BSE) microscopy of the OPA sample showed the development of horizontal and inclined shear bands, comprising mainly boundary and R_1-, and to lesser extent P- and Y-shears (Figure 5.1; terminology following Logan et al. 1979). The shear bands consisting of crushed quartz and calcite

distributed in a fine-grained material divide the gouge layer into distinct zones with a less intensely deformed matrix (Figures 5.1c and d).

5.3.2 Frictional behaviour of OPA (illite-bearing) reacted with reservoir water (baseline – Data-set 2)

In order to be able to evaluate which chemical alterations in OPA gouge, and the effects thereof on the frictional behaviour, would be induced by long-term CO_2-brine-rock interactions, as opposed to reaction with reservoir water (RW) alone, we first investigated the latter to establish a baseline for evaluating the CO_2-saturated fluids scenarios (Table 5.1 and Figure 5.B1). Chemical modelling shows that after 10,000 years, for a t_r of 10 years (RW-t_r10-10ka), the most notable chemical changes in OPA composition is the precipitation of paragonite (muscovite, +11wt%) and nontronite (+6wt%) at the expense of kaolinite (-9wt%) and daphnite (chlorite, -4wt%; Table 5.6). Compared to the starting composition (t = 0), after a time-scale of 1 Ma, the 10 years residence time scenario (RW-t_r10-1Ma) shows a major change in mineral composition, marked by complete dissolution of calcite (-25wt%), dolomite (-1wt%), illite (-25wt%), and daphnite (-4wt%), and to a lesser extent quartz (-5wt%), and the precipitation of saponite (+32wt%), kaolinite (+24wt%) and nontronite (smectite, +7wt%; Table 5.1). Unlike the 10 years residence time scenario (RW-t_r10-10ka), the 1000 years residence time scenario (RW-t_r1000-10ka) shows virtually no chemical changes after 10,000 years (Table 5.1). As time progresses from 10,000 years to 1 Ma (RW-t_r1000-1Ma) shows a composition comparable to that obtained for the "10 year residence time - 10,000 years reaction time" scenario (RW- t_r10-10ka), with a relatively lower illite and higher paragonite content (Table 5.1).

Following criterion (i) and (ii) outlined above, scenarios RW-t_r10-10ka, RW-t_r1000-1ka and RW-t_r1000-1Ma showed comparable compositions. Though scenario RW-t_r10-1Ma showed the largest amount of alteration, the significant amount of smectite precipitation (+32wt%) is generally note observed in nature. Therefore, we selected the RW-t_r10-10ka scenario for further frictional testing.

The μ-curve for the selected baseline scenario (RW- t_r10-10ka) is characterised by strain-hardening and a clear increase in frictional strength with increasing temperature (Figure 5.4a – Table 5.2). The obtained steady-state friction coefficient values range between 0.39 and 0.49 for all three temperatures (Stages 1-3; Figure

5.5a, Table 5.2), up to ~30% stronger than the OPA starting material. Note that the pronounced peak during the initial loading phase is an experimental artefact caused by over-compaction during the application of the normal stress, and does not reflect a true change in frictional properties. Furthermore, the RW-t_r10-10ka sample exhibited velocity-strengthening behaviour, with slightly lower (*a*-*b*) values than seen for the unreacted OPA starting material (Figure 5.6a). Overall, the results obtained for the reservoir-water exposed OPA suggest that with time natural, diagenetic processes will lead to a fault cross-cutting Opalinus Claystone-type caprock becoming slightly more resistant to slip, but will remain velocity-strengthening (Figure 5.6a).

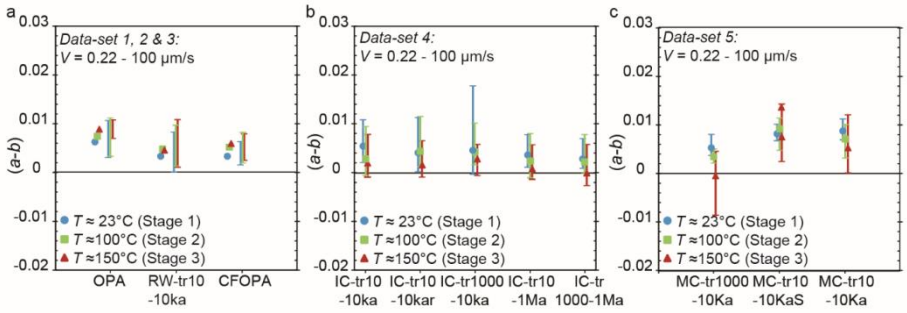

Figure 5.6. Velocity-dependency (*a*-*b*) for velocity up-steps plotted as a as a function of temperature for the different compositions tested at σ_n^{eff} = 50 MPa, P_f = 25 MPa and T ≈ 23, 100 and 150 °C (Stages 1, 2 and 3). Note that the symbols represent the average value of (*a*-*b*), whereas the vertical bars represent the range of the parameters and not the error to the respective average values. Each average and range is based on 6 (*a*-*b*) values determined in 6 velocity up-steps. Data available in supplementary material. a) OPA (Data-set 1), OPA exposed to reservoir water (closed system - Data-set 2) and calcite-free OPA (CFOPA - Data-set 3). b) Friction curves for illite-bearing OPA exposed to CO_2-saturated reservoir water (open and closed system - Data-set 4). c) Friction curves for muscovite-bearing OPA exposed to CO_2-saturated reservoir water (closed system - Data-set 5).

5.3.3 Frictional behaviour of calcite-free OPA (CFOPA) (Data-set 3)

Carbonates are known to dissolve rapidly, in comparison to aluminiumsilicates such are feldspars, clays and micas, which could be important for caprock integrity during and shortly after injection (years-decades timescale) (e.g. Alkattan et al., 1998; Beig and Lüttge, 2006; Cama et al., 2002). Since the OPA contains a significant amount of carbonate minerals (26wt%), we therefore investigated the hypothetical case during which rapid dissolution of carbonates occurs, without

further reaction with the other, slower-reacting minerals, essentially leading to a clay-quartz-dominated fault gouge composition.

The μ-curve obtained for the calcite-free OPA sample (CFOPA) is very similar to the OPA starting material, showing slight strain-hardening in the run-in phase (Figure 5.4a) and a temperature-insensitive frictional strength (Figure 5.5a). Steady-state friction values for the CFOPA sample are ~20% lower than for the OPA, respectively 0.28–0.33 vs. 0.35–0.42 (Stages 1-3; Figure 5.5a, Table 5.2) for a 26wt% decrease in strong mineral content. The observed dependence of friction coefficient on calcite content is in agreement with previous work on clay-calcite mixtures (e.g. Chapter 3 (OPA vs. CFOPA); Chapter 4 (CFOPA-calcite); Giorgetti et al., 2015 (talc-calcite)) showing a similar increase in μ upon a ~20wt% increase in calcite content compared to calcite-free starting material. Like the OPA sample, the CFOPA sample exhibited velocity-strengthening behaviour at all three temperatures (Figure 5.6a). However, while maintaining to exhibit velocity-strengthening behaviour, and showing an increase in value with temperature, the obtained (*a*-*b*) values for the CFOPA sample are somewhat lower than for the OPA sample.

5.3.4 Frictional behaviour of OPA (illite-bearing) reacted with CO_2-saturated reservoir water (closed and open system – Data-set 4)

Careful analysis of the simulations conducted for OPA exposed to CO_2-saturated reservoir water, respectively 4 closed system (C) and 4 open system (O) scenarios (see Appendix 5.B, Figures 5.B2 and 5.B3), revealed that the chemical changes for the scenarios with similar refreshment time and reaction time show virtually no differences in exposed composition (Table 5.1 and Figures 5.B2 and 5.B3).

After 10,000 year, for a t_r of 10 years (IC-t_r10-10ka and IO-t_r10-10ka), chemical changes are characterized by significant calcite (-18wt%) and, to lesser extent, illite (-2wt%), saponite (-5wt%) and daphnite (-4wt%) dissolution, and dolomite (+9wt%), siderite (+4wt%), quartz (+8wt%) and kaolinite (+7wt%) precipitation (Table 5.1). As reaction time progresses from 10,000 years to 1Ma, the 10 years residence time scenarios (IC-t_r10-1Ma and IO-t_r10-1Ma) show significant carbonate (-26wt%), illite (-25wt%), saponite (-5wt%) and daphnite (-4wt%) dissolution, accompanied by the precipitation of large amounts of quartz (+22wt%) and kaolinite (+36wt%) (Table 5.1).

The 1000 years residence time scenarios for a reaction time of 10,000 years (IC-t_r1000-10ka and IO-t_r1000-10ka) are characterised by lesser mineralogical changes, including minor calcite (-5wt%), illite (-4wt%), saponite (-5wt%) and daphnite (-4wt%) dissolution, and dolomite (+8wt%), siderite (+3wt%), quartz (+3wt%) and kaolinite (+3wt%) precipitation, than observed for the 10 years residence time equivalents, but do show an overall increase in total strong phase content (quartz + carbonates) with respect to initial OPA (respectively, 61wt% at t = 10,000 years vs. 52wt% at t = 0 year – Table 5.1). As reaction time progresses to 1 Ma, the mineralogical changes observed for a t_r of 1000 years (IC-t_r1000-1Ma and IO-t_r1000-1Ma) are again more significant than for 10,000 years, including the complete dissolution of illite (-25wt%), saponite (-5wt%) and daphnite (-4wt%), and to lesser extent calcite (-14wt%), and the precipitation of quartz (+11wt%), dolomite (+11wt%) and kaolinite (+24wt%), showing an overall increase in strong phase with respect to the initial OPA composition (62 vs. 52wt% – Table 5.1).

Given the limited differences observed between open and closed systems, for the same refreshment and reaction times, mineralogical changes appear to be rather controlled by the time it takes for the fluid to reach chemical equilibrium with the fault gouge. Our modelling results suggest that in both the open and closed systems, residence times of 10-1000 years are insufficient to approach this equilibrium, leading to similar mineralogical evolutions. Since the observed mineralogical changes between open and closed scenarios, modelled for the same residence and reaction time, are nearly identical only the four closed system scenarios were mechanically tested.

The μ-curves obtained for the four different scenarios of CO_2-exposure are very similar (Figure 5.4b), generally showing an increase in frictional strength with increasing temperature. Overall, steady-state friction coefficient values range between 0.40 and 0.59 for all temperatures (Stages 1-3; Figure 5.5b, Table 5.2), which is ~15-55% stronger than the OPA starting material and 2-20% stronger than the reservoir water-exposed OPA (baseline scenario). Comparing our friction coefficients with those obtained for natural clay-quartz-carbonate mixtures (35:65 weak:strong phase ratio (Chen et al., 2015a)), shows that our mixtures have similar frictional behaviour though they tend to be consistently stronger.

At 23 and 100°C (Stages 1 and 2), predominantly stable, velocity-neutral to velocity-strengthening behaviour is observed for all mixtures at all sliding velocities (i.e. (*a*-*b*)>0 – Figure 5.6b). Although remaining mainly positive, the magnitude of (*a*-*b*) decreases from 23°C to 100°C (Figure 5.6b). The observed decrease in (*a*-*b*) values continues between 100 and 150°C (Stages 2 and 3), transitioning from velocity-strengthening at 100°C to velocity-strengthening and velocity-weakening, i.e. at low sliding velocities only ($V \leq 10$ µm/s – Appendix 5.C), at 150°C for all mixtures. Overall, our results suggest that long-term exposure of OPA fault gouge to CO_2 will lead to a slight increase in frictional strength, i.e. a slightly higher resistance to slip, compared to long-term exposure of reservoir water. They furthermore suggest that, as opposed to the increased velocity-strengthening observed for the reservoir water-exposed OPA, long-term CO_2-exposure has the potential to result in more velocity-neutral to slightly velocity-weakening behaviour, especially at temperatures of 150°C.

5.3.5 Frictional behaviour of OPA (muscovite-bearing) reacted with CO_2-saturated reservoir water (closed system – Data-set 5)

In addition to the illite-bearing fault gouge scenarios, we also modelled 3 additional closed system (C) scenarios employing a muscovite-bearing OPA composition to evaluate the mineralogical changes. After 10,000 years of exposure, for t_r = 10 years, mineralogical changes are dominated by the precipitation of significant amounts of dolomite (+35wt%), saponite (+33wt%) and minor amounts of calcite (+2wt%) at the expense of significant amounts of quartz (-28wt%), muscovite (-20wt%), kaolinite (-18wt%) and minor amounts of illite (-3wt%) and beidellit (-2wt%) (MC-t_r10-10KaS and MC-t_r10-10Ka – Table 5.1). Scenario MC-t_r10-10KaS is based on the modelling result for scenario MC-t_r10-10Ka, showing precipitation of significant amounts of smectite (+44wt%). To maximise the effect of the frictionally very weak mineral saponite (smectite clay) on frictional behaviour, we replaced all non-swelling clay minerals (daphnite, 5wt%) with saponite (MC-t_r10-10KaS – Table 5.1). By comparison, the 1000 years residence time scenario (MC-t_r1000-10Ka) predicted the precipitation of dolomite (+16wt%), quartz (+5wt%) and kaolinite (+5wt%) at the expense calcite (-8wt%), illite (-3wt%), chlorite (-2wt%) and saponite (-11wt%) (Table 5.1).

The friction coefficient curves for scenarios MC-t_r10-10KaS and MC-t_r10-10Ka are very similar, showing strain-neutral behaviour (Figure 5.4c) and no significant temperature-dependence of μ (Figure 5.5c). For all three temperatures (Stages 1-3), the frictional strength of MC-t_r10-10KaS and MC-t_r10-10Ka is ~15-30% lower than obtained for the OPA starting material, with MC-t_r10-10Ka being consistently 10-20% stronger than MC-t_r10-10KaS (μ_{ss} = 0.28-0.36 vs. μ_{ss} = 0.24-0.33 – cf. Figures 5.4a and b). The obtained friction coefficients are in agreement with friction coefficients obtained for smectite-quartz mixtures, confirming the significant weakening effect of smectite when present in a fault gouge (Ikari et al., 2007; Saffer and Marone, 2003; Tembe et al., 2010). The friction curve for MC-t_r1000-10Ka is characterized by strain-hardening (Figure 5.4c), a clear increase in steady-state frictional strength with increasing temperature (Figure 5.5c), and is ~20-40% stronger than OPA (i.e. 0.42-0.51 vs. 0.35-0.42 – Figures 5.4a vs. 5.4c; Table 5.2). Friction coefficients obtained for this low smectite-content (4wt%) composition are comparable to those obtained for smectite-free clay-quartz-feldspar-calcite mixtures (20:80 weak:strong phase ratio) (Boulton et al., 2012).

At 23 and 100°C (Stages 1 and 2), all three mixtures exhibited velocity-strengthening behaviour (i.e. (a-b)> 0). Furthermore, while remaining to be positive, the magnitude of (a-b) shows a decrease from 23°C to 100°C for MC-t_r1000-10Ka and MC-t_r10-10Ka, and an increase for MC-t_r10-10KaS (Figure 5.6c). All three compositions show a decrease in (a-b) between 100 and 150°C (Stages 2 and 3) with MC-t_r1000-10Ka, transitioning from velocity-strengthening at 100°C to potentially velocity-weakening at 150°C (Figure 5.6c; $V \leq 3$ µm/s – Appendix 5.B). The observed velocity-dependence for all three samples with different smectite-content is in agreement with observations for smectite-rich (Ikari et al., 2007; Saffer and Marone, 2003; Tembe et al., 2010 - comparable to MC-t_r10-10KaS and MC-t_r10-10Ka) and smectite mixtures (Boulton et al., 2012 - comparable to MC-t_r1000-10Ka).

5.3.6 Impact of gouge cohesion on frictional strength

Each experiment, except CFOPA (Data-set 3), was concluded by four normal stress steps (Stage 4 – T = 150°C; Figure 5.4) to determine whether the description of our samples in terms of friction coefficient is justified. The obtained shear stress at peak or yield vs. σ_n^{eff} data is plotted in Figure 5.7. All our data show a systematic

increase in τ with increasing normal stress described by a linear, Mohr-Coulomb type of relationship that passes through, or close to, the origin:

$$\tau = \mu_i \cdot \sigma_n^{eff} + C_0 \qquad (5.4)$$

Here μ_i is the internal friction coefficient of the fault gouge (i.e. the slope of the trend) and C_0 represents the cohesion of the simulated gouge (i.e. the intercept of the trend with the vertical axis).

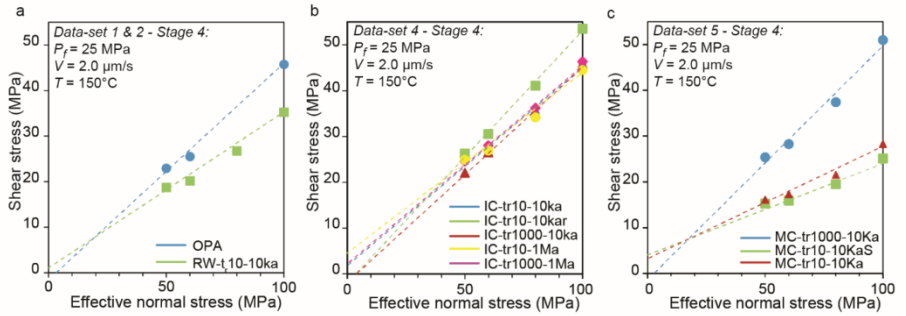

Figure 5.7. Shear strength at peak, or at yield in the absence of a clear peak, versus effective normal stress obtained during Stage 4 at T = 150°C. a) OPA (Data-set 1) and OPA exposed to reservoir water (Data-set 2). b) Effective normal stress versus shear stress for illite-bearing OPA exposed to CO_2-saturated reservoir water (Data-set 4). c) Effective normal stress versus shear stress for muscovite-bearing OPA exposed to CO_2-saturated reservoir water (Data-set 5). Dashed linear trend lines and corresponding data points are colour-coded for the different compositions. Note that for CFOPA the experiment (Data-set 3) was terminated after Stage 3, and therefore no stress-stepping data is shown here.

Note that for granular materials, like fault gouge, cohesion is generally low, but not always equal to zero. In essence, cohesion is a measure for the extent to which grain-to-grain contacts present in the gouge material are actively experiencing frictional sliding or deformation during shear. Though gouge cohesion is generally minor, its relative contribution to the friction coefficient may be significant when the stresses acting on the fault plane are small, i.e. when C_0 is of the same order of magnitude as σ_n^{eff} and τ (cf. Equation (5.4)).

The shear stress obtained at yield or peak, excluding any secondary effects of slip-hardening, was used as a reference strength parameter when interpreting μ_i and C_0. Cohesion values ranged from slightly negative (~-2MPa) to positive (+4.4 MPa –

Table 5.2). Though the negative cohesions are reported in Table 5.2, they most likely reflect errors in the corrections made for the seal friction. The calculated values for μ_i are in good agreement with the friction coefficient values obtained at T = 150°C (Stage 3) for C_0<~2 MPa. A cohesion value of less than ~2 MPa is assumed to be negligibly small compared to the measured shear stress (<10% of the shear stress), justifying the use of $\mu = \tau/\sigma_n^{eff}$ and of the RSF framework to describe our mechanical results. At these low cohesion values, the friction coefficient values derived from the slope of the fit (Figure 5.7) also fit very well with the obtained μ_{ss}-values obtained in the experiments at 150°C (cf. Stage 3 – Table 5.2). However, the friction coefficients obtained for the samples exhibiting ~4.0 MPa (~25-30% of the shear stress) cohesion should be interpreted with a little more caution. Our results show that the calculated μ_i-values for the higher cohesion samples agree less well with the friction coefficient values obtained T = 150°C (Stage 3), hence suggesting a small effect of the cohesion on fault strength, i.e. the fault is less likely to slip upon imposing a shear stress due to gouge cohesion.

5.4 Impact of CO_2-brine-rock interactions on the frictional properties of clay-rich faults

The aim of this study was to evaluate the long-term effects of CO_2-fluid-rock interactions in a gouge-filled fault cutting a clay-quartz-calcite caprock and to subsequently experimentally determine the effect of the observed mineralogical changes on the frictional strength and stability of such fault gouges. We therefore integrated predictive geochemical modelling and laboratory friction experiments. This practice was chosen as it is challenging to reproduce CO_2-induced mineral reactions on laboratory time-scales (week-months vs. mineral reaction time-scales of >thousands of years), as such hindering the study of coupled chemical-mechanical processes. We realise that integrated geochemical modelling and subsequent friction experiments have their own restrictions. First of all, modelling results depend on the kinetic database used, as well as the selected secondary mineral assemblage and the use, or not, of pressure-dependent equilibrium constants (Dethlefsen et al., 2012). However a recent benchmark study using a natural CO_2 analogue field in Utah has shown a good match between modelling efforts and chemical alterations observed in a clay-rich caprock penetrated by CO_2 (Kampman et al., 2016). Therefore, predictive geochemical modelling is currently

the best option to investigate long-term CO_2-fluid-rock interactions. Secondly, another issue that may be raised concerns the preparation of the CO_2-exposed gouge compositions, used in the friction experiments. The natural formation of interlayered illite-smectite clays cannot be reproduced by simple mixing of the powdered clay end-members. Simply mixing illite and smectite might therefore artificially influence the frictional behaviour in manners natural illite-smectite would not do, e.g. by potentially enhancing localization in the frictionally very weak smectite, leading to enhanced slip weakening. We tried to circumvent this by carefully mixing the powdered minerals, to ensure a homogeneous starting microstructure. However, it was not possible to replace the (most likely weak) porous fossil grains in the starting material (Figure 5.1) with porous calcite, so the use of stronger (solid), crushed calcite crystals instead may slightly impact the frictional behaviour. Thirdly, keeping in mind the grain size of the starting material, i.e. a very fine-grained clay-rich matrix with similar-sized hard phases embedded in it, and the fine grain size precipitated phases will have, we prepared our powder composition by sieving all phases to a grain size of less than 35 µm. As such we assume that we have limited the effects introduced by grain size such that the employed method reflects most realistically the frictional behaviour of long-term CO_2-exposed fault rock.

The baseline scenario shows that diagenetic processes, induced by rising reservoir water, will make the OPA fault gouge slightly more resistant to slip, while at the same time remaining velocity-strengthening (Figures 5.4-5.6). Rapid removal of calcite by reaction with CO_2, on the other hand will lead to the OPA fault gouge becoming slightly easier to slip, though it still remains to exhibit velocity-strengthening behaviour (Figures 5.4-5.6). Temperature has a clear, but limited effect on frictional strength and slip stability.

Our various CO_2-exposed OPA gouges (open and closed systems – Figure 5.4b) show that irrespective of the residence time of the CO_2-saturated reservoir water in the OPA gouge, and the total duration of reactions, CO_2-fluid-rock interactions potentially lead to fault-strengthening, compared to the mineralogical evolution in the absence of CO_2 (i.e. reservoir water alone). However, as a result of the changes in mineralogy, there is the potential that upon slip the fault may become prone to unstable behaviour, as (a-b) values tend to become neutral to slightly negative, particularly at 150°C (Figure 5.6a vs. 5.6b). Long-term CO_2-fluid-rock interactions in

a more mature, muscovite-bearing composition appear to result in similar frictional behaviour, unless significant amounts of smectite precipitate, which lower the faults slip resistance (Figure 5.4c). While this reacted gouge will mainly show velocity-neutral to velocity-strengthening behaviour, there is again the possibility for velocity-weakening (unstable slip) behaviour at temperatures of 150°C (Figure 5.6c).

Overall, our results show that mineralogical changes in an OPA fault gouge, whether induced by exposure to reservoir water or CO_2-saturated reservoir water, will affect the frictional behaviour of the OPA. The clear reduction in friction coefficient observed for the two CO_2-exposed, muscovite-bearing OPA gouges (MC-t_r10-10KaS and MC-t_r10-10Ka – Figure 5.4c) with respect to OPA is inferred to be the result of the significant amounts of frictionally weak smectite (respectively 49wt% and 44wt%). The key role of smectite in controlling the observed frictional behaviour of the two prepared gouges is also consistent with the velocity-strengthening nature of smectite reported in literature (Ikari et al., 2007; Saffer and Marone, 2003).

The other seven scenarios all show a roughly similar increase in friction coefficient with respect to the naturally-derived OPA material, temperature-sensitive friction coefficients, slightly varying per composition, and, except for one, a decreasing velocity-dependence with temperature, transitioning to velocity-weakening behaviour at 150°C. The increase in friction coefficient cannot be explained systematically by an overall change in weak:strong phases ratio, or the replacement of frictionally weaker minerals by frictionally stronger ones. As stated above, some influence of the preparation method for the gouges on the frictional behaviour is expected, though we tried to eliminate these effects as much as possible. Furthermore, it should be noted that these preparation effects will be the same for all scenarios, therefore not explaining the slight variations in μ and (a-b) observed between the reservoir water and CO_2-exposed gouges. Detailed analysis correlating the obtained friction coefficients to the respective mineral compositions reveals a correlation between the quartz:calcite ratio and the obtained friction coefficient. Overall, mixtures with higher quartz:calcite ratios exhibited higher frictional strengths.

The observed trend suggests a direct interaction between quartz and calcite during shear, resulting in varying degrees of shear localization due to grain size reduction in preferentially the calcite compared with the more fracture-resistant quartz (Atkinson and Avdis, 1980). This is supported by the higher friction coefficients observed for the samples containing relatively more quartz than calcite. Moreover, the majority of the samples with the higher quartz:calcite ratios are characterised by the lowest (*a*-*b*) values, which might suggest a more strongly reduced grain size of the calcite due to grain neighbour swapping of the more fracture-resistant quartz. This tends to promote thermally-activated compaction via diffusion in the calcite, producing velocity-weakening behaviour. This is in line with the work on 50:50 quartz-calcite mixtures presented in Chapter 4 of this thesis, for which the bulk frictional strength of binary quartz-calcite mixtures is inferred to be a function of the critical stress intensity factor of quartz (0.307-0.593 MPa^{-1} for T = 20-150°C) and calcite (0.187-0.514 MPa^{-1} for T = 20-150°C) (Chapter 4 – see also Atkinson, 1984; Atkinson and Avdis, 1980). This could also explain the observed increase in friction coefficient with temperature as the critical stress intensity factor for both quartz and calcite increases with increasing temperature (Atkinson and Avdis, 1980). The dominant role of quartz and calcite in controlling the bulk frictional behaviour of these polymineralic clay-quartz-calcite mixtures is furthermore consistent with the observed transition from velocity-strengthening behaviour at ~23 and 100°C to velocity-weakening behaviour at 150°C and the reported velocity-weakening nature of calcite at elevated temperature (T >80-100°C) (e.g. Chapter 4; Chen et al., 2015; Verberne et al., 2014). Following the model presented by (Den Hartog and Spiers, 2014) and assuming the velocity-dependency of steady-state friction to reflect competition between compaction and dilatation, the transition from velocity-strengthening to velocity-weakening between 100 and 150°C is inferred to point to thermally-activated compaction via diffusion in the calcite.

From the above, it is clear that even though our mixtures are polymineralic in nature, and mixed with significant amounts of phyllosilicates, the quartz:calcite ratio seems to systematically affect our prepared gouges, with the samples having higher quartz:calcite ratios showing higher friction coefficients and a tendency for velocity-weakening behaviour at high temperature, while a lower quartz:calcite ratio results in slightly lower μ-values and velocity-neutral behaviour. Therefore the direct interaction and proportion between quartz and calcite during shear cannot

be ignored when evaluating the frictional behaviour of a clay-quartz-calcite gouge mixture.

In addition to the quartz:calcite ratio, the presented geochemical modelling efforts for the illite- and muscovite-bearing OPA starting compositions exposed to CO_2-saturated reservoir water have shown the impact of the precipitation of frictionally weak minerals like smectite on the frictional behaviour (Figures 5.4-5.6). In case of significant precipitation of smectite, a fault gouge becomes more prone to slip, though mostly in a stable manner, due to the lower frictional strength of smectite clays (Ikari et al., 2007). This suggests that the composition of a caprock overlying a potential CO_2-storage reservoir has to be carefully determined, before assessing the potential for storage. So, returning to our initial hypothesis that CO_2-induced fluid-rock interactions in clay-rich fault gouges may result in mineralogical changes that might alter the frictional behaviour of the gouge material, our modelling and experimental results show that the frictional behaviour may indeed be affected by the mineralogical changes in a fault gouge, which in turn is controlled by the starting composition of the clay-rich fault gouge. However, unless there are significant quantities of smectite clays (>40-50wt%) or carbonate minerals (>50wt%), no drastic changes in frictional strength and slip stability are to be expected (see also Chapter 4).

5.5 Implications

Our results are directly relevant for evaluating the potential long-term CO_2-fluid-rock interactions in faulted clayey caprocks following CO_2 injection, both in the context of long-term CO_2 storage and enhanced oil and gas recovery, respectively EGR and EOR.

In evaluating the effect of mineral composition on the frictional strength and stability of a clay-quartz-calcite fault gouge, in context of long-term CO_2 storage, EGR or EOR, we consider a depth range of 2-4 km, typical for CO_2-injection, assume a geothermal gradient of 25°C/km and a surface temperature of 20-25°C. The temperature range for potential CO_2 storage complexes is therefore expected to range between 70°C and maximum 125-150°C. We combined relevant friction data (μ and (a-b)) for water-saturated (pure) clay, quartz, and calcite gouges reported in literature, along with other typical caprock minerals such as anhydrite and

dolomite (T = 70-150°C, V = 0.12-100 µm/s) into Figure 5.8. From Figure 5.8, we can evaluate which gouge compositions are likely to have either low frictional strength (i.e. low μ-value) and/or could lead to unstable, velocity-weakening behaviour (i.e. negative (a-b) value).

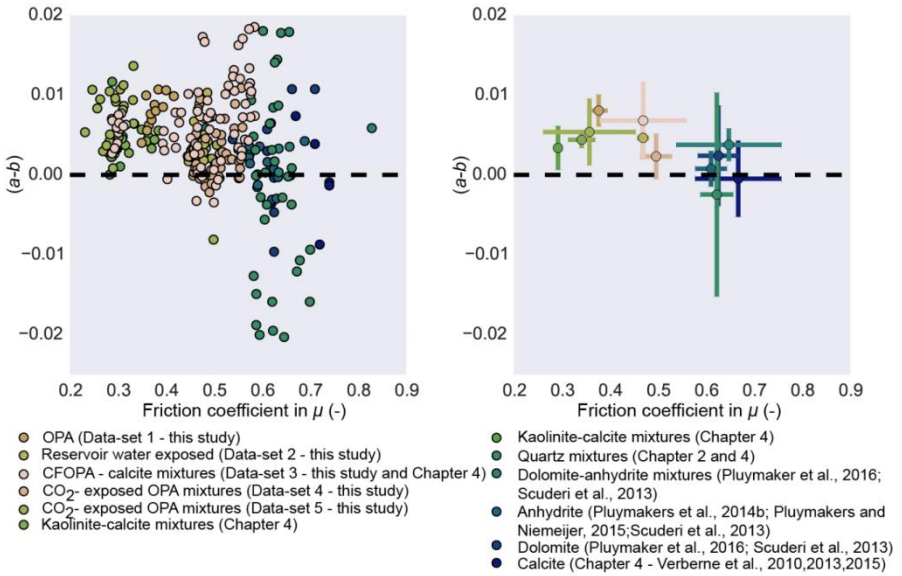

Figure 5.8. Velocity-dependence of steady-state friction, (a-b), as a function of friction coefficient, μ, for wet fault gouges composed of clay, quartz, calcite, dolomite, and anhydrite in the temperature range of 70-150°C (σ_n^{eff} = 10-50 MPa and V = 0.12-300 µm/s). Colour-coding indicates composition or Data-set, for the present samples, of the sheared mixtures. a) (a-b) as a function of μ for present samples along with wet fault gouges reported in literature. b) Similar data as presented in (a), now showing the average and respective range in (a-b) and μ for clarification. The majority of the data falls in the range of 0.2-0.6, having positive (a-b) values. Negative (a-b) values are predominantly seen for the higher μ-values, showing a downward trend in (a-b) with increasing μ.

As can be seen there is a wide spread in friction coefficient (~0.25-0.85) and velocity-dependency (-0.01-0.015) (Figure 5.8) (Chapter 2; Chapter 3; Chapter 4; Pluymakers et al., 2016, 2014a, 2014b; Scuderi et al., 2013; Verberne et al., 2015, 2013, 2010). Furthermore, a clear transition from solely velocity-strengthening behaviour (for $\mu \leq 0.4$) to potentially velocity-weakening behaviour is observed for higher friction coefficient values ($\mu \geq 0.4$) (Figure 5.8). Close examination of the plotted data reveals that the compositions with a frictional behaviour plotting in

the upper left quadrant are dominated by phyllosilicates, either pure or in (natural) mixed compositions, whereas from the upper right to the lower right, compositions become more and more dominated by pure quartz, carbonate (calcite, dolomite) or anhydrite gouges (Figure 5.8). The addition of velocity-strengthening, but frictionally weaker phases like phyllosilicates to a frictionally strong, but velocity-weakening gouge like pure calcite, will on the one hand shift the frictional stability to more stable frictional sliding, while on the other hand reduce the frictional strength of the gouge, i.e. frictional properties roughly corresponding to the data points at the centre of Figure 5.8 (see also Chapter 4).

While a lot of research has been done on polymineralic gouge mixtures at room temperature conditions (e.g. Boulton et al., 2012; Samuelson and Spiers, 2012; Tembe et al., 2010), data is needed to fill this gap at elevated temperature. This chapter, as well as Chapter 4, has made a first step towards filling this knowledge gap. Overall, based on the currently available data shown here (Figure 5.8), faults, both in CCS complexes or in tectonic settings such as orogens, consisting of gouges consisting of either significant quantities of frictionally weak phases (e.g. clays and micas), and/or contain > 40-50 wt% carbonate minerals are particularly important to consider due to their potential of inducing fault slip (low friction coefficient) or (micro-)seismicity upon slip (strongly negative (a-b) values). In context of CO_2 storage, these compositions may pose geotechnical challenges during repressurisation of a field by fluid injection, constraining injection rates and the total amount of injected CO_2.

5.6 Conclusions

We integrated geochemical modelling and frictional testing to assess the chemical effects of long-term CO_2-exposure on the frictional strength and stability of an OPA-like (clay-quartz-calcite) caprock composition (σ_n^{eff} = 50 MPa, P_f = 25 MPa, $T \approx$ 23, 100 and 150°C and V = 0.22-100 µm/s). Our main conclusions are as follows:

1) The frictional behaviour of naturally-derived OPA shows a friction coefficients of 0.35–0.42. Under all conditions, the gouge exhibited velocity-strengthening behaviour, meaning stable, aseismic sliding upon slip acceleration. Long-term exposure (10 ka to 1 Ma) to reservoir water equilibrated with a hypothetical sandstone reservoir showed that

diagenetic processes will lead to slightly higher resistance to slip, while exhibiting stable, aseismic slip.

2) Removal of the naturally-occurring calcite, simulating rapid carbonate dissolution by CO_2-exposure, reduces the frictional strength by ~20%, while maintaining to exhibit velocity-strengthening behaviour at all temperatures.
3) All artificially prepared gouges based on illite-bearing OPA modelling efforts, for both open and closed systems, show an increase in frictional strength with respect to the naturally-derived OPA fault gouge (16-55%) and the reservoir water exposed OPA (2-20%). At temperatures of 100 to 150°C, these gouges show that long-term CO_2-exposure has the potential to result in more velocity-neutral to slightly velocity-weakening behaviour, especially at temperatures of 150°C.
4) Prepared gouges based on muscovite-bearing OPA modelling efforts for a closed system suggest an increase in frictional strength with respect to the naturally-derived OPA fault gouge (20-37%) and a transition to velocity-weakening behaviour between 100 and 150°C. However, in the scenarios where significant quantities of smectite are predicted to precipitate a decrease in frictional strength with respect to the naturally-derived OPA fault gouge (14-32%) and velocity-strengthening behaviour is observed.
5) For the reservoir water and CO_2-exposed gouges, the increase in friction coefficient and velocity-dependence (a-b), superimposed on the effect of mineral composition on the frictional behaviour can be explained qualitatively in terms of the controlling microscales processes. In prepared compositions with near equal amounts of quartz and calcite, but quartz being the dominant phase, deformation in the quartz and calcite, hence granular portion, starts to become more and more accommodated by the preferential cataclastic comminution of the calcite grains over the more fracture-resistant quartz. The transition from velocity-strengthening to velocity-weakening behaviour seen between 100°C and 150°C in those clay-quartz-calcite samples, is therefore inferred to reflect a thermally-activated compaction mechanism, operating in the calcite component, such as thermally-activated diffusion, competing with dilation.
6) Based on the currently available data, presented here and in literature, wet gouges consisting of either significant quantities of frictionally weak phases (e.g. clays and micas), and/or contain >40-50wt% carbonate

minerals are most prone to failure due to the potential of inducing fault slip (low friction coefficient) or (micro-)seismicity upon slip (strongly negative (*a-b*) values), particularly at elevated temperatures (>80-100°C). As such this is important in context of both CO_2-storage, EGR and EOR, posing geotechnical challenges during repressurisation by fluid injection, and faults in tectonic settings.

Acknowledgements

This research has been carried out in the context of the ULTImateCO_2-program. ULTImateCO_2 is a research program on Understanding the Long-Term fate of geologically stored CO_2 and is financially supported by the European Union (FP7). We thank Dr. Christophe Nussbaum (The Mont Terri rock laboratory) for providing the sample material. EB and SdH thank ULTImateCO_2 for providing funding for the research. Eimert de Graaff, Floris van Oort, Gert Kastelein, Peter van Krieken and Thony van der Gon Netscher are thanked for their technical support, and Leonard Bik for making the thick sections. Maartje Houben is thanked for her help with preparing samples for SEM analysis and Bart Verberne is thanked for his help using the SEM.

Supplementary Material

Appendix 5.A: Mineralogy and Geochemical Modelling Parameters

Table 5.A1. Mineralogy of Opalinus Claystone (wt%), as determined in this study. Note that quantitative mineralogy in this study is determined both by conventional X-Ray Diffraction (XRD), and greater precision XRD, including Rietveld refinement. For comparison a range of compositions stated in the literature is given (Pearson et al., 2013).

	This Study "Conventional "			**This Study "Rietveld"**			**Pearson et al. (2003)**
Bulk Rock	***Bulk Rock***	***Clays***	***Mixed Layer Clays***	***Bulk Rock***	***Clays***	***Mixed Layer Clays***	
Quartz	20-40			23			6-24
Calcite	15-40			26			5-28
Dolomite/ankerite	0-1						0.2-2
Siderite							1-4
Pyrite	2			4			0.6-2
Organic carbon							<0.1-1.5
K-feldspar							1-3.1
Albite							0.6-2.2
Total clays	36-66			47			58-76
Sum	100			100			100
Clays							
Muscovite		26-66					
Illite		0-5			5.2		16-40
Illite-smectite mixed layer clay					24.4		5-20
Chlorite		0-20			4.2		4-20
Kaolinite		0-28			13.2		15-33
Illite in illite-smectite			19.6			19.6	
Smectite in illite-smectite			4.9			4.9	

Table 5.A2. Geochemical composition of Opalinus Claystone pore water at 25°C (mmol/kg), as used in the geochemical modelling scenarios, based on existing data (Pearson et al., 2003; Honty et al., 2012).

	Pearson et al. (2003)		**Honty et al. (2012)**		
	low saline	***most saline***	***low saline***	***most saline***	***Geochemical Model (this study)***
	BWS-A3	***BWS-A1***			
Na	125	244.0	134.8	137.2	127
K	1.02	1.5	0.8	1.6	4.98
Ca	6.98	14.8	7.3	25.4	84.8
Mg	5.93	15.9	5.1	16.5	7.07
Fe	4.4×10^{-3}	3.5×10^{-3}	n.d.[1]	n.d.	3.7×10^{-2}
Mn	5.5×10^{-3}	6.3×10^{-3}	---[2]	---	
Al	---	1.5×10^{-3}	n.d.	n.d.	1.8×10^{-4}
SiO_2(aq)	0.10	0.06	0.036	0.036	0.09
HCO_3	4.36	0.67	---	---	3.79
Cl	128	288.0	---	---	316
SO_4	9.45	13.6	11.9	34.4	1.97×10^{-5}
pH	7.3	8.3	7.5	7.5	7.47

Note that: (1) n.d. is not detected. (2) "---" denotes no data reported.

Table 5.A3. Mineralogical composition of the Opalinus Claystone fault gouge, as used in the geochemical modelling scenarios. Note that for each unit of mass of mineral solid one kilogram of water is also present. The initial porosity of the simulated fault gouge is taken to be 21%.

			Illite-bearing fault gouge		**Muscovite-bearing fault gouge**	
			Data-sets 1,2,3		***Data-set 4***	
Mineral	***Chemical formula***	***density (g/cm³)***	***Mass (kg)***	***Wt % of solid***	***Mass (kg)***	***Wt % of solid***
Primary:						
Quartz	SiO_2	2.65	2.59	23.4	3.59	32.0
Daphnite-14A (chlorite)	$Fe_5Al_2Si_3O_{10}(OH)_8$	2.65	0.44	4.0	0.70	6.2
Kaolinite	$Al_2Si_2O_5(OH)_4$	2.59	1.50	13.5	2.0	17.8
Ca-saponite (smectite)	$Ca_{0.165}Mg_3Al_{0.33}Si_{3.67}O_{10}(OH)_2$	2.84	0.60	5.5	1.05	9.3
Ca-nontronite (smectite)	$Ca_{0.165}Fe_2Al_{0.33}Si_{3.67}O_{10}(OH)_2$	2.50	0.01	0.1	0.01	0.0
Illite	$K_{0.6}Mg_{0.25}Al_{2.3}\ Si_{3.5}O_{10}(OH)_2$	2.76	2.74	24.7	0	0
Muscovite	$KAl_3Si_3O_{10}(OH)_2$	2.83	0	0	2.18	19.5
Calcite	$CaCO_3$	2.71	2.73	24.7	1.59	14.2
Dolomite	$CaMg(CO3)_2$	2.86	0.06	0.6	0.10	0.9
Pyrite	FeS_2	5.01	0.40	3.6	0.001	0.0
Secondary:						
Siderite	$FeCO_3$	4.05	---	---	---	---
Na-nontronite (smectite)	$Na.33Fe2Al.33Si3.67O_{10}(OH)_2$	2.50	---	---	---	---
Mg-nontronite (smectite)	$Mg_{0.165}Fe_2Al_{0.33}Si_{3.67}O_{10}(OH)_2$	2.48	---	---	---	---
Paragonite	$NaAl_3Si_3O_{10}(OH)_2$	2.88	---	---	---	---
Mg-saponite (smectite)	$Mg_{3.165}Al_{0.33}Si_{3.67}O_{10}(OH)_2$	2.86	---	---	---	---

Table 5.A4. Geochemical composition of the reservoir water (mmol/kg) in equilibrium with a hypothetical, idealised sandstone reservoir underlying the caprock in our scenarios (T = 100 °C), both in the presence and absence of CO_2. Note that CO_2-saturation in reservoir water was determined using the equation of state of Duan et al. (2006).

	Reservoir water	**CO_2-saturated reservoir water**
Na	127	144
K	0.7	0.8
Ca	1.2	1.4
Mg	0.4	0.6
Fe	0.001	0.07
SiO_2(aq)	0.8	0.8
HCO_3	2	3180
Cl	113	89.7
SO_4	8.3	9.4
pH	7.0	4.38
Ionic strength	0.135	0.15

Table 5.A5. Kinetic parameters used in the geomechanical modelling of Opalinus Claystone fault gouge. Note that all rate constants are listed for dissolution, where k is the kinetic rate constant and n is the power term (Equation (5.2)). All kinetic parameters are from Palandri and Kharaka (2004) except parameters for illite, which are from Köhler et al. (2003). Furthermore, calcite, dolomite, siderite, and pyrite (see Table 5.A3) were treated as equilibrium phases.

			Kinetic parameters at 100°C		
Mineral	***Grain Size (μm)***	***Surface area (cm^2/g)***	***Neutral mechanism***	***Acid mechanism***	
			Log k ($mol/m^2/s$)	***Log k ($mol/m^2/s$)***	***n (H^+)***
Quartz	35	647	-10.20	-10.20	none
Chlorite	4	5660	-9.42	-8.01	0.50
Kaolinite	4	5783	-12.40	-8.99	0.78
Smectite	4	6010	-11.55	-10.15	0.34
Muscovite	4	5298	-12.78	-11.08	0.37
Illite	4	5429	-14.56	-10.10	0.60

Appendix 5.B: Geochemical modelling results

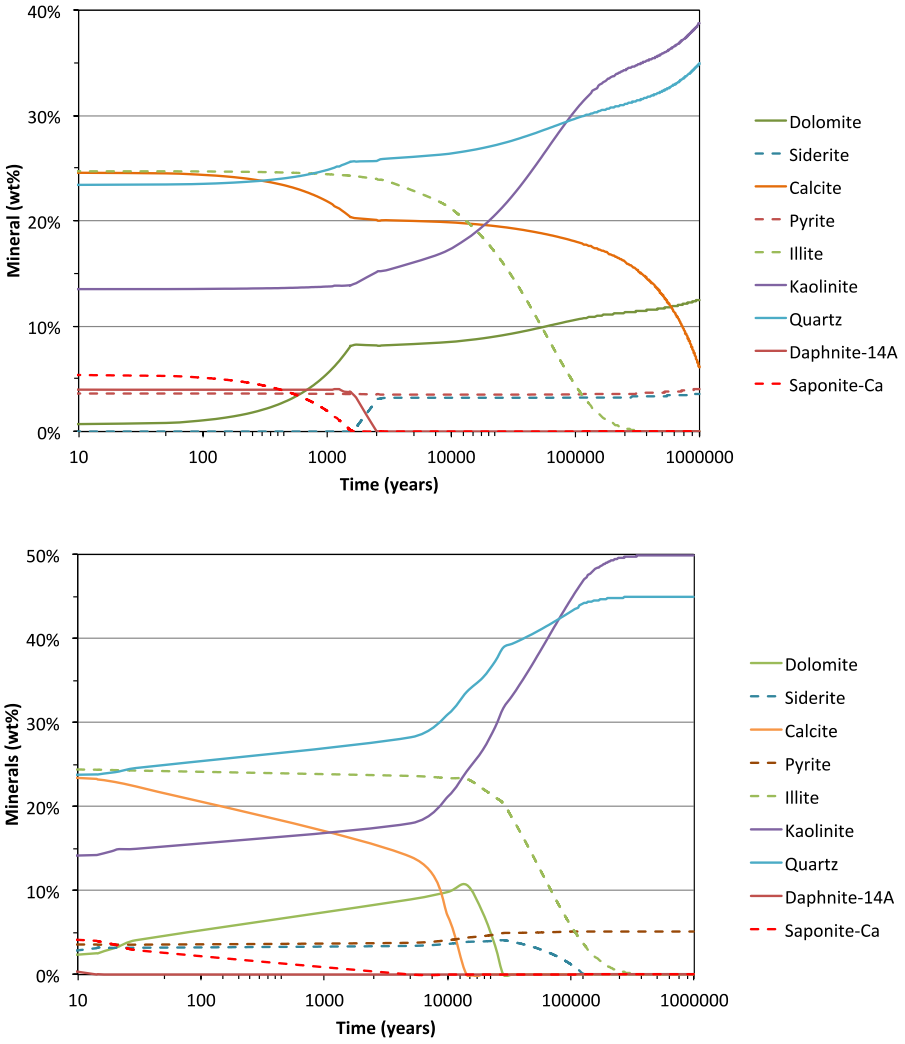

Figure 5.B1. Mineralogical-evolution of the illite-bearing OPA gouge composition exposed to reservoir water at 100°C. a) Diagram plotting the mineral evolution (wt%) versus log time (years) for the 10 years residence time scenarios (RW-t_r10-10ka and RW-t_r10-1Ma). Mineralogical changes are observed after ~2,000 years of exposure, characterized by the rapid precipitation of paragonite and smectite and the dissolution of illite and calcite. b) Diagram plotting the mineral evolution (wt%) versus log time (years) for the 1000 years residence time scenarios (RW-t_r1000-10ka and RW-t_r1000-1Ma), showing less rapid mineralogical changes initiating after ~10,000 years of exposure.

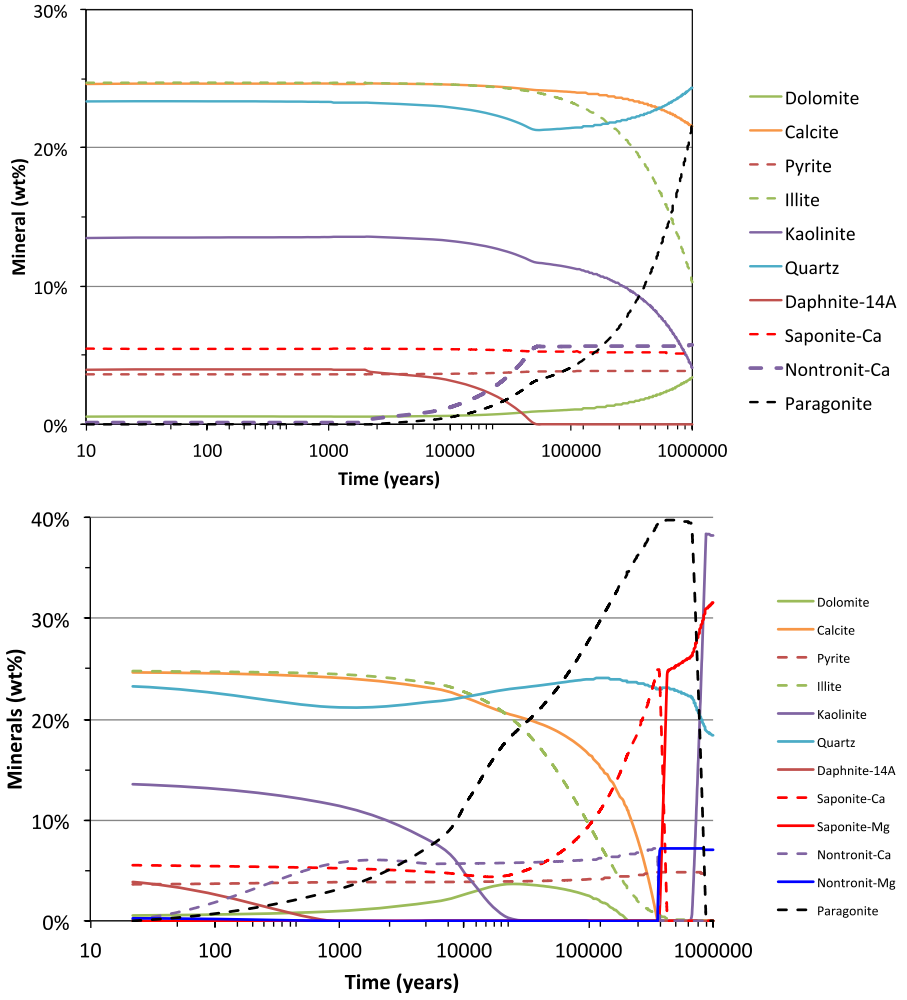

Figure 5.B2. Mineralogical-evolution of the illite-bearing OPA gouge composition exposed to CO_2-saturated reservoir water at 100°C. The fault forms a closed system with respect to the CO_2. a) Diagram plotting the mineral evolution (wt%) versus log time (years) for the 10 years residence time scenarios (IC-t_r10-10ka and IC-t_r10-1Ma). Notable mineralogical changes are observed after ~8,000 years of exposure, characterized by the rapid precipitation of kaolinite and quartz at the expense of illite. b) Diagram plotting the mineral evolution (wt%) versus log time (years) for the 1000 years residence time scenarios (IC-t_r1000-10ka and IC-t_r1000-1Ma), showing similar mineralogical changes as for the 10 years residence time, starting at ~ 1,000 years of exposure.

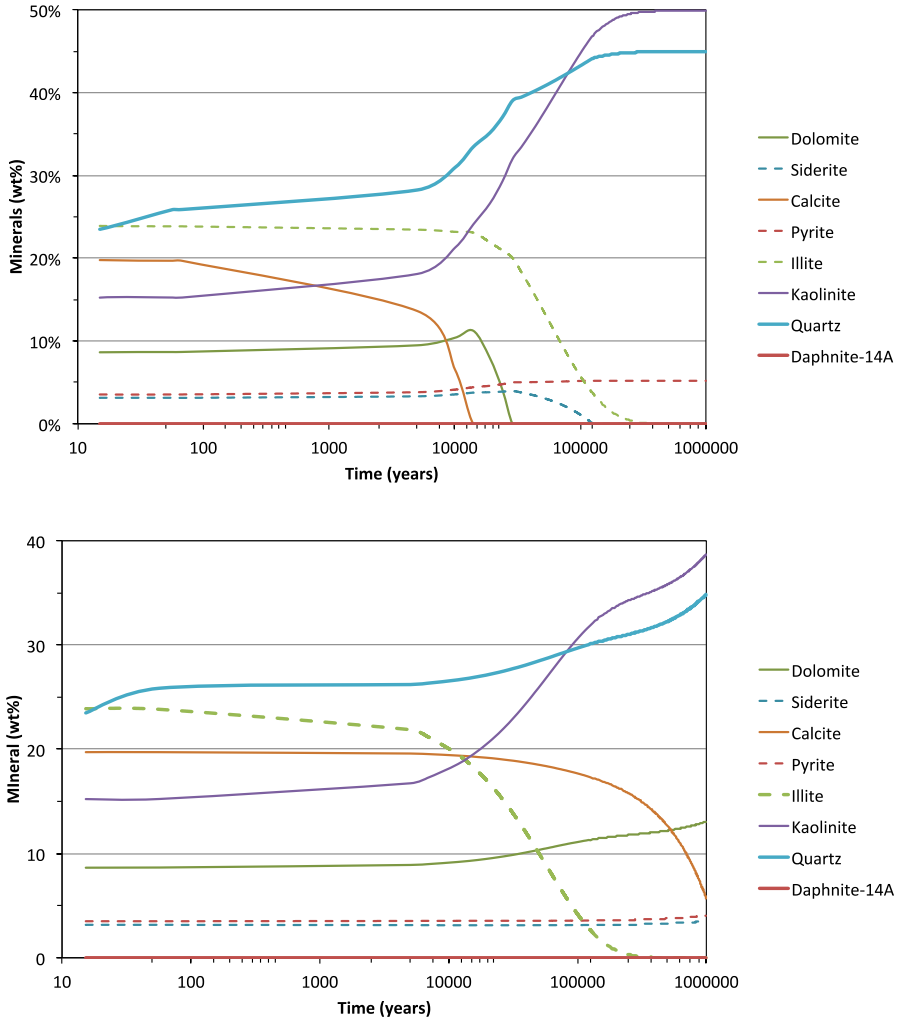

Figure 5.B3. Mineralogical-evolution of the illite-bearing OPA gouge composition exposed to CO_2-saturated reservoir water at 100°C. The fault forms an open system with respect to the CO_2, but not to the residing reservoir water. a) Diagram plotting the mineral evolution (wt%) versus log time (years) for the 10 years residence time scenarios (IO-t_r10-10ka and IO-t_r10-1Ma). Similar as for the closed system, observed notable mineralogical changes (~8,000 years of exposure) are characterized by the rapid precipitation of kaolinite and quartz at the expense of illite. b) Diagram plotting the mineral evolution (wt%) versus log time (years) for the 1000 years residence time scenarios (IO-t_r1000-10ka and IO-t_r1000-1Ma), again showing similar mineralogical changes as for the 10 years residence time, though starting at ~ 10,000 years of exposure.

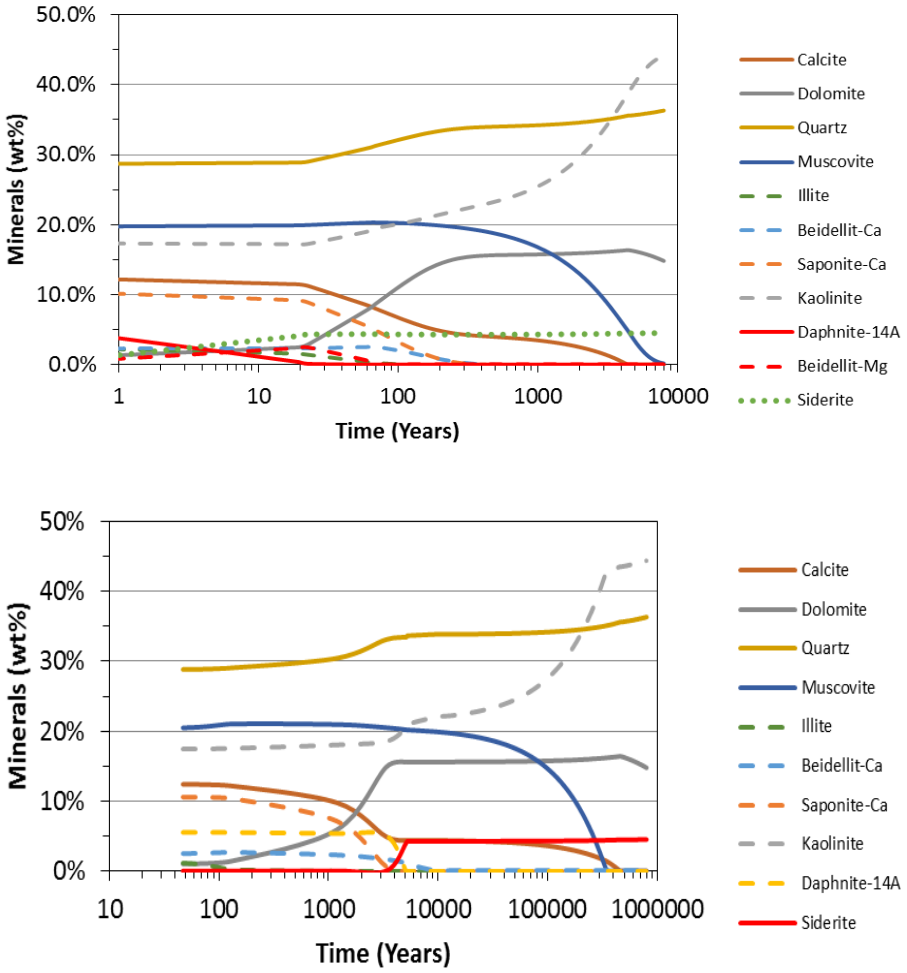

Figure 5.B4. Mineralogical-evolution of the muscovite-bearing OPA gouge composition exposed to CO_2-saturated reservoir water at 100°C for 10,000 years. The fault forms a closed system with respect to the CO_2 and the residing reservoir water. a) Diagram plotting the mineral evolution (wt%) versus log time (years) for the 10 years residence time scenarios (MC-t_r10-10Ka). Notable mineralogical changes (~800 years of exposure) are characterized by the rapid precipitation of kaolinite and the dissolution of muscovite and calcite. b) Diagram plotting the mineral evolution (wt%) versus log time (years) for the 1000 years residence time scenarios (MC-t_r1000-10Ka), again showing similar mineralogical changes as for the 10 years residence time, though starting at ~ 2,000 years of exposure.

Appendix 5.C: Rate-and-State Friction

To obtain individual values for a, b and D_c for individual velocity-steps we used the rate-and-state friction tool within XLook, which was kindly made available by C. Marone (PSU) (Blanpied et al., 1998; Marone, 1998). In the case that our data showed minor slip-strengthening or weakening we applied the detrending procedure for μ versus shear displacement curves as described by Blanpied et al. (1998).

Whether a fault gouge slips in stable or unstable way is not only determined by the gouge itself, but also by the material surrounding the slipping portion of the fault, depending on the elastic stiffness of the surrounding material compared to the critical stiffness of the system, given as (Ruina, 1983):

$$\frac{d\mu}{dt} = S\left(V_{lp} - V\right) \qquad (5.C1)$$

Here S is the shear stiffness of the fault zone plus surroundings (or in the experiments, the gouge layer plus the shear apparatus corrected for normal stress effects), V_{lp} is the load point velocity and V is the fault/sample shear velocity. With Equation 5.3 as a constraint, Xlook combines and solves Equation 5.C1, using a fifth-order Runge-Kutta method. The constitutive parameters are then obtained as solutions to the nonlinear inverse problem using an iterative least squares method (Blanpied et al., 1998; Reinen and Weeks, 1993; Saffer and Marone, 2003).

Table 5.C1. Overview of constitutive parameters *a*, *b* and (*a*-*b*) for least squares fit of the Dieterich Law listed per temperature for individual velocity-steps. Experiments were performed at a constant effective normal stress (σ_n^{eff} = 50 MPa) and pore pressure (P_f = 25 MPa), at temperatures (*T*) of 23°C (Stage 1), 100°C (Stage 2) and 150°C (Stage 3), using sliding velocities (*V*) between 0.22 and 100 µm/s. Symbols: (*a*-*b*) = velocity-dependence of steady state friction, *a* = the "direct effect" in friction coefficient upon an instantaneous change in sliding velocity, *b* = the "evolution effect" in friction coefficient evolving, with shear, to a new steady state friction. Denotation of the 'composition': RW = closed system with reservoir water as the reaction fluid, C = closed system with CO_2-saturated reservoir water, O = open system with CO_2-saturated reservoir water, I = illite-bearing gouge, M = muscovite-bearing gouge, t_r = residence time of CO_2-saturated pore water in the fault (10 vs. 1000 years) for a reaction time of 10 ka or 1 Ma. S denotes smectite referring to the "10 years residence time – 10,000 years reaction time" scenario without non-swelling clays, whereas r denotes repeat experiment.

Composition (fluid, residence time, reaction time)	*Velocity-step (µm/s)*	*Stage 1*			*Stage2*			*Stage3*		
		(a-b)	*a*	*b*	*(a-b)*	*a*	*b*	*(a-b)*	*a*	*b*
Data-set 1 – OPA (starting material)										
OPA	0.22-1.086	0.005488	0.0072	0.001712	0.004044	0.016477	0.012432	0.009982	0.008078	-0.0019
	1.086-10.86	0.006195	0.007461	0.001266	0.006264	0.007516	0.001252	0.008816	0.006893	-0.00192
	1.086-3.0	0.003768	0.007515	0.003746	0.005584	0.008985	0.003401	0.007661	0.006655	-0.00101
	3.0-10.0	0.007867	0.00785	-1.7E-05	0.006924	0.008017	0.001093	0.008035	0.00688	-0.00116
	10.0-30.0	0.01021	0.007168	-0.00304	0.010731	0.009601	-0.00113	0.008538	0.007266	-0.00127
	30.0-100.0	0.004862	0.001064	-0.0038	0.010627	0.010304	-0.00032	0.009891	0.006425	-0.00347
Data-set 2 — illite-bearing OPA exposed to reservoir water (OPA)										
RW- t_r10-10ka	0.22-1.086	0.002456	0.019659	0.017203	-	-	-	0.003548	0.012088	0.00854
	1.086-10.86	0.000798	0.007594	0.006796	0.001719	0.008527	0.006808	0.002841	0.008064	0.005224
	10.86-1.086	0.002081	0.007336	0.005255	0.003351	0.008989	0.005638	0.003163	0.00891	0.005748
	1.086-3.0	0.002354	0.007635	0.005281	0.00309	0.009059	0.00597	0.001843	0.008475	0.006632
	3.0-10.0	0.001884	0.008051	0.006168	0.003363	0.008986	0.005623	0.003875	0.008875	0.005
	10.0-30.0	0.005402	0.009267	0.003865	0.006733	0.009633	0.0029	0.005065	0.00992	0.004855
	30.0-100.0	0.007868	0.010844	0.002976	0.008912	0.018545	0.009633	0.010326	0.012067	0.00174
Data-set 3 – Calcite-Free OPA (CFOPA)										
CFOPA	0.22-1.086	0.003328	0.004555	0.000564	0.002716	0.004775	0.002059	0.006809	0.002839	-0.00397
	1.086-10.86	0.003191	0.004945	0.001754	0.005314	0.006281	0.000967	0.007557	0.000231	-0.00733
	10.86-1.086	0.001723	0.004188	0.002465	0.006135	0.003934	-0.0022	0.005621	0.002729	-0.00289
	1.086-3.0	0.002297	0.004423	0.001531	0.003998	0.005013	0.001014	0.003357	0.003585	0.000228
	3.0-10.0	0.002617	0.004941	0.002324	0.005786	0.006332	0.000546	0.005953	0.001436	-0.00452
	10.0-30.0	0.003312	0.005164	0.001852	0.007729	0.008091	0.000363	0.006534	0.002032	-0.0045
	30.0-100.0	0.005571	0.003865	-0.00171	0.006317	0.00001	-0.00631	0.006098	0.002057	-0.00404
Data-set 4 – illite-bearing OPA exposed to CO_2-saturated reservoir water										

IC-t_r10-10ka	0.22-1.086	0.002658	0.008781	0.006123	-2.5E-05	0.008018	0.000041	0.001813	0.007938	0.000057
	1.086-10.86	0.003952	0.008494	0.004542	0.000639	0.008716	0.000047	0.00091	0.008885	0.000039
	10.86-1.086	0.003215	0.010167	0.006952	0.001554	0.009869	0.000196	0.000272	0.010002	0.000117
	1.086-3.0	0.004533	0.014816	0.010282	0.001337	0.018972	0.000027	-0.00038	0.009034	0.00005
	3.0-10.0	0.003724	0.00926	0.005537	0.001319	0.010731	0.000216	-0.00018	0.008699	0.000071
	10.0-30.0	0.007422	0.021439	0.014017	0.004198	0.012534	0.00028	0.002675	0.011518	0.000211
	30.0-100.0	0.01023	0.013034	0.002804	0.008924	0.017335	0.000136	0.007064	0.014853	0.000335
IC-t_r10-10kar	0.22-1.086	0.001981	0.008166	0.006185	0.002906	0.008973	0.006067	0.001701	0.008373	0.006672
	1.086-10.86	0.00349	0.009549	0.006059	0.002668	0.010203	0.007536	-0.0004	0.008652	0.00905
	10.86-1.086	0.002521	0.008984	0.006463	0.003497	0.012989	0.009492	0.000338	0.010071	0.009732
	1.086-3.0	0.000699	0.009121	0.008421	0.001908	0.012247	0.010339	0.000825	0.009498	0.008673
	3.0-10.0	0.002154	0.009516	0.007362	0.001976	0.01057	0.008594	-0.00028	0.009756	0.010036
	10.0-30.0	0.005729	0.01056	0.004831	0.005856	0.012737	0.006881	0.001985	0.010632	0.008647
	30.0-100.0	0.010459	0.012653	0.002194	0.010915	0.021217	0.010302	0.005982	0.01237	0.006388
IC-t_r1000-10ka	0.22-1.086	0.002689	0.008187	0.005498	0.002363	0.007627	0.005264	0.004455	0.010977	0.006522
	1.086-10.86	0.000384	0.009418	0.009035	0.00226	0.010012	0.007751	0.002339	0.010755	0.008416
	10.86-1.086	0.003332	0.009874	0.006543	0.001947	0.013252	0.011305	0.002847	0.012954	0.010107
	1.086-3.0	0.001992	0.010579	0.008587	0.003285	0.012005	0.008721	0.002319	0.020569	0.018249
	3.0-10.0	0.002458	0.011021	0.008563	0.00300	0.011892	0.008891	-	-	-
	10.0-30.0	0.002882	0.011763	0.008881	0.004945	0.012458	0.007514	-8.2E-05	0.011569	0.011651
	30.0-100.0	0.017167	0.012999	-0.00417	0.009521	0.020713	0.011193	0.005153	0.013017	0.007864
IC-t_r10-1Ma	0.22-1.086	0.003607	0.004992	0.001385	0.002446	0.009117	0.006671	-0.00015	0.0071	0.007245
	1.086-10.86	0.001571	0.007205	0.005634	0.000041	0.007836	0.007795	-0.00069	0.008086	0.008773
	10.86-1.086	0.002459	0.008005	0.005546	0.001574	0.012236	0.010662	0.000321	0.008679	0.008357
	1.086-3.0	0.002323	0.007101	0.004778	0.000369	0.009565	0.009196	-0.00052	0.008637	0.009157
	3.0-10.0	0.002435	0.011049	0.008614	-0.00044	0.008741	0.009185	-0.00021	0.009211	0.009424
	10.0-30.0	0.004557	0.009381	0.004824	0.004594	0.009778	0.005183	0.001526	0.010364	0.008838
	30.0-100.0	0.007121	0.010035	0.002914	0.007322	0.011874	0.004552	0.005038	0.013087	0.008049
IC-t_r1000-1Ma	0.22-1.086	0.001704	0.008235	0.006531	0.000328	0.009395	0.009067	-0.00101	0.010687	0.011701
	1.086-10.86	0.001904	0.010293	0.00839	0.0009	0.010872	0.009972	-0.00144	0.010643	0.012083
	10.86-1.086	0.002505	0.009613	0.007108	0.001496	0.012351	0.010855	-0.00063	0.011256	0.011884
	1.086-3.0	0.002088	0.010427	0.008339	0.001386	0.011323	0.009936	-0.00216	0.011598	0.01376
	3.0-10.0	0.001455	0.011292	0.009837	0.000668	0.011855	0.011187	-0.00107	0.01203	0.013095
	10.0-30.0	0.003622	0.012721	0.009099	0.002717	0.013033	0.010316	-	-	-
	30.0-100.0	0.006394	0.013342	0.006948	0.007104	0.017053	0.009949	0.005242	0.015908	0.010666
Data-set 5 – muscovite-bearing OPA exposed to CO_2-saturated reservoir water										

MC-t_t1000-10Ka	0.22-1.086	0.004472	0.012165	0.007693	0.002933	0.012011	0.009078	0.002067	0.010514	0.008446
	1.086-10.86	0.005075	0.010711	0.005636	0.003465	0.011201	0.007736	-0.00085	0.009096	0.009941
	1.086-3.0	0.005178	0.013021	0.007843	0.002728	0.02438	0.021652	-0.00027	0.025803	0.026074
	3.0-10.0	0.004632	0.011717	0.007085	0.003373	0.012267	0.008893	-0.00809	0.010804	0.01889
	10.0-30.0	0.005209	0.013536	0.008327	0.004212	0.019056	0.014844	0.00079	0.012159	0.011369
	30.0-100.0	0.007538	0.017472	0.009934	0.004243	0.022255	0.018012	0.003782	0.007579	0.003797
MC-t_t10-10KaS	0.22-1.086	0.007475	0.009357	0.001883	0.005368	0.009521	0.004153	0.002993	0.007598	0.004605
	1.086-10.86	0.009487	0.008764	-0.00072	0.008363	0.007926	-0.00044	0.007043	0.008129	0.001086
	1.086-3.0	0.007479	0.007883	0.000404	0.010693	0.012786	0.002093	0.004228	0.008679	0.004451
	3.0-10.0	0.008546	0.013217	0.004671	0.009507	0.00822	-0.00129	0.009192	0.009091	-0.0001
	10.0-30.0	-	-	-	0.010485	0.007919	-0.00257	0.008669	0.008204	-0.00047
	30.0-100.0	0.007864	0.007177	-0.00069	0.010737	0.008909	-0.00183	0.01368	0.008956	-0.00472
MC-t_t10-10Ka	0.22-1.086	0.008164	0.007684	-0.00048	0.003713	0.008592	0.004879	0.000864	0.007255	0.006391
	1.086-10.86	0.007826	0.007722	-0.0001	0.007033	0.00827	0.001237	0.004747	0.00783	0.003083
	1.086-3.0	0.008775	0.009933	0.001158	0.005088	0.008646	0.003557	0.003256	0.008994	0.005738
	3.0-10.0	0.007911	0.008292	0.000381	0.00962	0.008578	-0.00104	0.005304	0.008051	0.002748
	10.0-30.0	0.009085	0.007207	-0.00188	0.008178	0.008021	-0.00016	0.011271	0.007364	-0.00391
	30.0-100.0	0.010643	0.007196	-0.00345	0.009398	0.00856	-0.00084	0.006471	0.007563	0.001092

Chapter 6

General conclusions and suggestions for further research

6.1 Main findings and conclusions

In this thesis, I have reported on an experimental study aimed at investigating the effect of long-term CO_2-fluid-rock interactions on the frictional behaviour and transport properties of simulated faults in sandstone reservoir rocks and clay-rich caprocks under pressure-temperature (*P*-*T*) conditions relevant for Carbon Capture and Storage (CCS) in the subsurface. The study focused primarily on the effect of CO_2-induced mineralogical changes, such as changes in carbonate content, on the frictional behaviour and, to a limited extent, on the transport properties of simulated fault gouges. The gouges investigated were derived from lithologies chosen to represent a sandstone reservoir rock and a clay-rich caprock. The objectives included 1) determining the effect of long-term CO_2-exposure on the frictional and transport properties of simulated fault gouges derived from a natural CO_2-charged sandstone reservoir, 2) evaluating the effect of shear displacement and effective normal stress on the permeability of simulated, caprock-derived clay-quartz-calcite fault gouges, 3) investigating the effect of systematically varying the calcite content on the frictional properties of a simulated clay-quartz-calcite fault gouge, and 4) integrating geochemical modelling and friction experiments to investigate coupled chemical-mechanical effects of long-term CO_2-exposure on clay-quartz-calcite fault gouges. In the following, the main findings and conclusions are reviewed and integrated. The implications for long-term storage of CO_2 in systems comprising sandstone reservoir rock and/or clay-quartz-calcite caprocks are then discussed, along with the implications for faults in similar rock types in active tectonic terrains. The chapter is concluded by identifying remaining and newly-surfaced questions and knowledge gaps, suggesting possible directions for future research.

6.1.1 Effects of CO_2 on the frictional and transport properties of simulated fault gouges derived from a natural CO_2 reservoir

Direct shear experiments have been performed, with and without permeability measurements, on simulated fault gouges prepared from unexposed and CO_2-exposed Entrada Sandstones (60-90% quartz, 0-11% carbonates (calcite and dolomite), 3-30% feldspar, 2-10% phyllosilicates, and 0.5% hematite), and carbonate-rich fault rock (40% aragonite) taken from a CO_2-leaking fault cutting the Entrada Sandstone. The experiments were performed in a triaxial deformation

apparatus with the aim of evaluating the effect of natural, long-term CO_2-exposure on the frictional and transport properties of simulated quart-rich and carbonate-rich fault gouges. Four sets of direct shear experiments were conducted. The first set of experiments was aimed at investigating the effect of mineralogy, effective normal stress and shear displacement on the frictional behaviour of a simulated reservoir rock-derived fault gouge (σ_n^{eff} = 5-50 MPa, T ≈ 23°C, room humidity). The second and third sets of experiments investigated the effect of temperature and pore fluid on the frictional behaviour of the same fault gouges (σ_n^{eff} = 50 MPa, P_f = 0 or 25 MPa, T ≈ 100°C), whereas in the fourth set of experiments, the effect of mineralogy and shear displacement on the transport properties of the same fault gouges was investigated (σ_n^{eff} = 5-50 MPa, P_f ≈ 2 MPa, T ≈ 23°C).

The results showed that long-term CO_2-exposure in nature does not affect the frictional behaviour of fault gouge significantly, as CO_2-induced mineralogical changes in sandstones are limited due to the limited amounts of reactive minerals (Gunter et al., 1997). Unexposed and CO_2-exposed Entrada Sandstone fault gouges, tested both dry and wet showed friction coefficients ranging between 0.50 and 0.70 and exhibited stable (velocity-strengthening, non-seismogenic) slip behaviour at 23 and 100°C. Simulated sandstone fault gouges rich in precipitated aragonite (~40%) showed friction coefficient values ranging between 0.56 and 0.90, depending on the effective normal stress (respectively 90 to 5 MPa), plus a transition from stable sliding behaviour (velocity-strengthening; room temperature, dry) to velocity-weakening (unstable, seismogenic) slip behaviour at in-situ CCS temperatures of 100°C (dry and wet). This transition mirrors that reported in literature for other simulated carbonate gouges (e.g. Chen et al., 2015a; Verberne et al., 2014; Verberne et al., 2010). In addition, high aragonite concentrations increased cohesion as well as friction coefficient. Pre-shear argon-permeability measurements on dry, unexposed and CO_2-exposed Entrada sandstone gouge ranged between $\sim 10^{-15}$–$10^{-16} m^2$, decreasing to $\sim 10^{-17} m^2$ (decrease by a factor of 10) after 7 mm of displacement. Pre-shear argon-permeability on dry, aragonite-rich Entrada is $\sim 7*10^{-17}$, decreasing to slightly lower values in the same order of $10^{-17} m^2$ (decrease by a factor of 2-3) for 7 mm of displacement. These argon gas permeability values for the simulated fault gouges can be assumed equally valid for CO_2-charged pore water, liquid CO_2 and super-critical CO_2, provided no chemical reactions occur during the time-scale of flow, i.e. over typical laboratory time-

scales. The results presented showed that cohesion played a significant role in controlling the shear strength of all of the gouges at low normal stresses, and hence that fault friction coefficient alone is insufficient to model static fault strength in context of geological storage of CO_2. A further important implication is that significantly carbonate-cemented faults in potential CCS reservoir have the potential to exhibit (seismogenic) slip behaviour, but they are also characterized by lower permeability values than the non-seismogenic quartz-rich fault gouges.

6.1.2 Effect of shear and normal stress on the permeability evolution of a simulated clay-quartz-calcite fault gouge

Direct shear experiments, comprising permeability measurements, reported in Chapter 3, were aimed at investigating the effect of shear displacement, dynamic shear, static holding, and effective normal stress on along- and across-fault permeability evolution in a simulated clay-quartz-calcite fault gouge. This was prepared by crushing Opalinus Claystone material (OPA) and sieving it to a grain size <35 µm. The direct shear experiments were conducted at room temperature conditions at effective normal stresses ranging between 5 and 50 MPa and a pore pressure of ~2 MPa in the triaxial deformation apparatus (connected to an argon permeametry set-up) referred to above.

Klinkenberg uncorrected, initial permeability values for unleached Opalinus Claystone gouges fell in the range of 10^{-15} (5 MPa) to 10^{-17} m^2 (50 MPa) along the fault, versus 10^{-16} (5 MPa) to 10^{-18} m^2 (50 MPa) across the fault. The decrease in permeability with shear displacement, both along- and across-fault, was largest in the first millimetres of shear displacement. Steady-state shearing was characterized by a well-developed internal foliation with permeability decreasing to near constant values during shear displacement and holding. The maximum observed permeability decrease for 4-6 mm of shear displacement was up to an order of magnitude. Pre-shear, along-fault permeability was up to an order of magnitude higher than across-fault. By 4-6 mm shear displacement, this anisotropy had decreased to <0.5.

The frictional strength of argon-saturated simulated OPA gouges decreased with increasing effective normal stress, demonstrating minor effects of cohesion at low effective normal stresses (<25 MPa). Taken into account literature and present data on the permeability of intact Opalinus Claystone, the present data on gouges imply

that pre-existing faults with a clay-quartz-calcite gouge are likely to act as a leakage pathway for fluids, as across-fault permeabilities are expected to be at least 1-2 orders of magnitude higher than the intact rock (ranging for gouges between 10^{-16} (σ_n^{eff} = 5 MPa) and 10^{-19} m^2 (σ_n^{eff} 50 MPa) at a depth range of respectively 1-4 km vs. an intact rock permeability of $7.7 \cdot 10^{-20}$ m^2 (15 MPa) at ~0.7 km depth, respectively). An increase in the fault zone pore fluid pressure, due to the migration of supercritical CO_2 at superhydrostatic pressures, has the potential to decrease the effective normal stress and to further reduce the sealing capacity of a fault, irrespectively of fluid flow orientation, with a preference for leakage along-fault into over- or possibly even underlying-formations.

6.1.3 Effect of calcite content on the frictional properties of simulated clay-quartz-calcite fault gouges

Direct and ring-shear experiments (Chapters 2 and 4, respectively) have been performed on simulated clay-quartz-calcite fault gouge mixtures, under dry and wet conditions, to evaluate how the frictional strength and its velocity-dependence (*a*-*b*) change with calcite and water content under in-situ CCS conditions (Figure 6.1). These experiments were motivated by the potential for changes in the calcite content of gouge-bearing faults in clastic caprocks due to long-term reaction with CO_2-charged formation water in geological storage system. Simulated fault gouge was prepared by crushing fragments of Opalinus Claystone material (OPA) and sieving the product to a grain size <35 µm. A second batch was prepared by taking half of the simulated fault gouge and removing, via leaching, the naturally present calcite, producing calcite-free OPA (CFOPA). In addition to the OPA and CFOPA compositions, other compositions were prepared by mixing CFOPA with systematically varied amounts of added calcite. Supplementary binary-mixture experiments were performed on kaolinite-calcite and quartz-calcite mixtures, including the 100% pure endmembers and 50:50 combinations. Direct and ring-shear experiments were performed under upper crustal reservoir conditions (σ_n^{eff} = 50 MPa, P_f = 25 MPa and $T \approx$ 23, 60, 100, 120 and 150°C), and at sliding velocities of 0.22 to 11 or 100 µm/s, in the direct and ring-shear experiments respectively. Microstructural analysis was performed on selected cross-sections of the preserved samples.

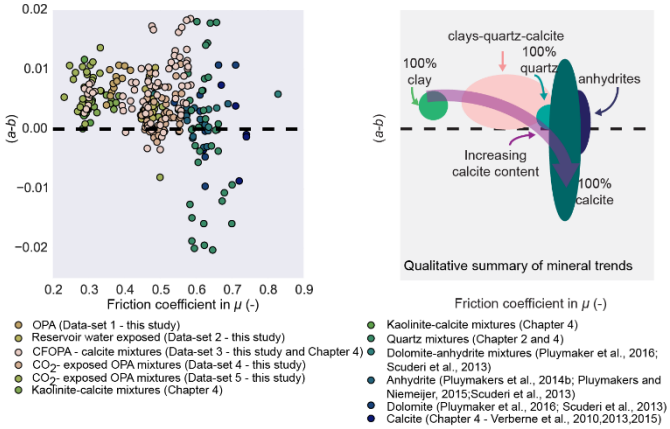

Figure 6.1. Velocity-dependence of steady-state friction, (a-b), as a function of friction coefficient, μ, for wet fault gouges composed of clay, quartz, calcite, dolomite, and anhydrite in the temperature range of 70-150°C (σ_n^{eff} = 10-50 MPa and V = 0.12-300 µm/s). Colour-coding indicates composition or Data-set, for the present samples, of the sheared mixtures. a) (a-b) as a function of μ for present samples along with wet fault gouges reported in literature. b) Qualitative summary of frictional strength and slip stability as a function of calcite content.

At 23 and 100°C, both the steady-state friction coefficient (μ_{ss}) and (a-b) values obtained for the wet CFOPA-calcite mixtures increased with increasing calcite content, with the steepest increase between 70-100% calcite (Figure 6.1). Corresponding values of the steady-state friction coefficient, determined at 5.43 µm/s, ranged from 0.28 (0% calcite) to 0.71 (100% calcite). At these temperatures, all mixtures exhibited velocity-strengthening behaviour. A transition from velocity-strengthening to velocity-weakening behaviour was observed between 100 and 150°C for a calcite content >90%. Dry samples of simulated OPA fault gouge exhibited double the frictional strength of the fault gouge, plus stable, velocity-strengthening slip behaviour.

A similar asymmetric trend in μ_{ss} and (a-b) versus calcite content was obtained for the kaolinite-calcite samples as for the CFOPA samples with added calcite, with μ_{ss} ranging from 0.26 (0% calcite) to 0.71 (100% calcite), and showing no systematic dependence on temperature. A transition from velocity-strengthening, at 100°C, to velocity-weakening behaviour, at 150°C, was observed only in the 100% calcite experiment (Figure 6.1). In the case of the quartz-calcite mixtures tested, the steady-state friction coefficient for 50:50 quartz-calcite mixtures at 23 and

especially 100°C (0.58 to 0.73), were both higher and lower than both end-member compositions. At these temperatures, the 50:50 quartz-calcite samples exhibited velocity-strengthening behaviour. However, highly unstable (stick-slipping) velocity-weakening behaviour, with (*a*-*b*) being significantly lower than in either end-member, was observed for the 50:50 calcite-quartz samples at 150°C.

The dependencies of μ_{ss} and (*a*-*b*) on calcite content observed for the CFOPA-calcite samples at 23, 100 and 150°C are asymmetric in the sense that for an increase in calcite content up to ~70% no significant increase in μ_{ss} or (*a*-*b*) is observed, followed by a steepening in both parameters between 70 and 100% calcite. This asymmetry can be reasonably described by a Reuss mixing model including a power law dependence of μ_{ss} and (*a*-*b*) on a) the proportions of the CFOPA vs. calcite and b) on the composition of the individual phyllosilicate phases vs. quartz and calcite content. Based on microstructural evidence, the observed trends in μ_{ss} and (*a*-*b*) with calcite content can be explained in terms of a change in controlling microscales processes, with shear being concentrated in the phyllosilicate-rich shear bands at low calcite concentrations, shifting to more homogenously distributed, cataclastic comminution of the calcite grains in the calcite-rich samples.

By comparison with previous work on calcites (e.g. Chen et al., 2015a; Verberne et al., 2010) and with recent microphysical models (e.g. Den Hartog and Spiers, 2014), the velocity-weakening behaviour observed at 150°C in the calcite-rich (>90%) clay-quartz-calcite samples, and in the 50:50 quartz-calcite mixtures is inferred to reflect a thermally-activated compaction creep mechanism, operating in the calcite component, such as thermally-activated diffusion, competing with dilation. The very intense calcite crushing in quartz-calcite mixtures, probably points to grain neighbour swapping of the more fracture-resistant quartz, promoting enhanced thermally-activated compaction via diffusion.

Overall, the results imply that a transition from stable to potentially unstable, seismic fault slip is to be expected for calcite contents of >90% at *T* >100°C (cf. depth range of >3 km) in clay-quartz-calcite gouges, and for calcite contents of >~50% at *T* >100°C (cf. depth of > 3 km) in quartz-calcite gouges (Figure 6.1). Additionally, drying of a clay-quartz-calcite fault gouge, via desiccation induced by dry CO_2-flow, has the potential to roughly double the frictional strength of a fault

gouge, while potentially having the unwanted effect of inducing (clay) shrinkage (Busch et al., 2016), thus enhancing fault gouge permeability.

6.1.4 Effects of CO_2 on the frictional properties of a simulated clay-quartz-calcite fault gouge

Aside from long-term dissolution and precipitation of carbonates, the slow reaction rates of particularly of clays and micas (Cama et al., 2002, 2000; Kalinowski and Schweda, 1996; Knauss and Thomas J, 1989; Zysset and Schindler, 1996), means that it is challenging to reproduce mineral transformations due to CO_2-fluid-rock interactions, in clay-quartz-calcite gouge compositions, on laboratory time-scales (week-months). This virtually rules out direct experimental studies of the effect of coupled long-term chemical reactions on the evolution of fault mechanical and transport properties in such materials. Therefore, predictive geochemical modelling and laboratory friction experiments have been integrated in Chapter 5, to assess the effect of mineralogical changes, induced by long-term CO_2-exposure, on the frictional strength and stability of a simulated clay-quartz-calcite fault gouge (OPA). For CCS to be considered safe, caprock sealing integrity needs to be maintained for at least 10,000 years (Haszeldine et al., 2005). In addition to exploring 10,000 year scenarios, the present geochemical models were extended to time-scales of 1 Ma to evaluate mineralogical changes beyond the minimal required time-span. To distinguish mineralogical changes induced by reactions involving CO_2, from fluid-rock interaction induced by pore water only, a baseline was established for 10 and 1000 years of CO_2-free pore water refreshment times in a closed fault system. These refreshment times were chosen to simulate the effects of pulsed through-flow of pore fluid. The baseline models were complemented by CO_2-fluid-rock interaction models, for both 10 and 1000 years of refreshment time, assuming a closed fault system, i.e. isolating the pore water during these 10 and 1000 year refreshment periods from the underlying reservoir. However, with respect to the rising CO_2, models were run assuming the fault forming a closed or open fault system. In the closed system, the CO_2 was also isolated from the underlying reservoir, whereas in the open system, continuous CO_2-flow from the reservoir was allowed. The combined geochemical modelling and friction experiments focused on illite-bearing clay-quartz-calcite mixtures, roughly simulating Opalinuc Claystone compositions in the starting condition. However, to evaluate the effect of the starting composition, and to extend the applicability of the study to a broader

range of caprock compositions, additional scenarios were modelled. These focused on muscovite-quartz-calcite compositions in a closed fault system, employing refreshment times of 10 and 1000 years and 10,000 years of total reaction time. Selected compositions were manually prepared and tested in ring-shear experiments (σ_n^{eff} = 50 MPa, P_f = 25 MPa and $T \approx$ 23, 100 and 150°C), similar to those described above, and their frictional behaviour was compared to that of natural OPA and calcite-free OPA (CFOPA) samples.

The present geochemical modelling has shown that long-term CO_2-fluid-rock interactions in clay-quartz-calcite fault gouges (illite- or muscovite-bearing) are expected to result in reacted compositions characterized by a near equal distribution of clays vs. quartz and calcite, irrespectively of the residence time of the reservoir pore water in the fault (cf. 10 vs. 1000 years) or the total exposure time of the gouge (10,000 vs. ~1 Ma years). For the illite-bearing clay-quartz-calcite compositions, reactions are expected to be predominantly characterised by quartz precipitation, carbonate dissolution and reprecipitation, illite and smectite dissolution and kaolinite precipitation (Table 6.1). On the contrary, reactions in the muscovite-bearing compositions are expected to be characterised by the dissolution of quartz, the dissolution and reprecipitation of carbonates, the dissolution of muscovite and kaolinite and the precipitation of saponite and kaolinite (Table 6.1). Friction experiments on gouges prepared directly from OPA and CFOPA showed that the dissolution of naturally-occurring calcite (CFOPA) reduced the frictional strength of a simulated OPA fault gouge by 10-20% (from 0.35-0.42 to 0.27-0.33; Chapters 3 and 4), while exhibiting stable sliding at all temperatures (Figure 6.1).

All manually prepared gouges, based on the geochemical modelling results obtained for the CO_2-exposed illite-bearing OPA starting composition, showed an increase in wet frictional strength with respect to the naturally-derived OPA fault gouge (by 16-55%) and the reservoir water exposed OPA (by 2-20%). Unlike the OPA, CFOPA and reservoir water-exposed OPA, these illite-bearing gouges showed a transition from stable velocity-strengthening to potentially unstable velocity-weakening slip behaviour between 100 and 150°C. At all temperatures tested, manually prepared gouges based on muscovite-bearing OPA starting compositions showed either a) an increase in frictional strength with respect to the naturally-derived OPA fault gouge (by 20-37%) and a transition to velocity-weakening

behaviour between 100 and 150°C, or b) a decrease in frictional strength with respect to the naturally-derived OPA fault gouge (by 14-32%) and velocity-strengthening behaviour.

Comparing the predicted mineral compositions for the illite-bearing OPA starting compositions shows remarkably different compositions after exposure than observed for the muscovite-bearing OPA starting compositions (Table 6.1). The gouges assembled for the exposed illite-bearing compositions all showed an increase in frictional strength, and a transition between 100 and 150°C from stable velocity-strengthening to slightly velocity-weakening behaviour for the compositions with higher quartz:calcite ratios. The exposed muscovite-bearing gouges consisting of significant amounts of smectite showed a decrease in frictional strength, whereas the muscovite-rich sample showed an increase in frictional strength. Aside from the effect of altered mineral composition on the frictional behaviour, part of the observed increase in friction coefficient and the transition in the velocity-dependence (*a*-*b*), most clearly seen in the experiments on manually assembled gouges of exposed illite-bearing OPA compared with the gouges derived directly from natural OPA, can be explained qualitatively in terms of the controlling microscale processes. In the manually prepared compositions consisting of near equal amounts of quartz and calcite, the higher friction coefficients are generally observed for the higher quartz:calcite ratios, suggesting a correlation between the quartz:calcite ratio and the frictional behaviour, similar as observed for the 50:50 quartz-calcite mixtures in Chapter 4. This is supported by the observed transition from velocity-strengthening to velocity-weakening behaviour seen between 100°C and 150°C in those clay-quartz-calcite samples, pointing to thermally-activated compaction via diffusion in the calcite. These results imply that clay-quartz-calcite compositions are not only controlled by the type of clay, but also by the interaction between quartz and calcite.

Table 6.1. Geochemical modelling outcome. Listed is the illite-bearing OPA starting composition used for the geochemical modelling, followed by the outcomes for the reservoir water exposed, closed system CO_2-exposed and open system CO_2-exposed scenarios. The muscovite-bearing OPA starting composition used for modelling is listed next to the modelling outcomes for the closed system, CO_2-exposed scenarios.

	Illite-bearing starting composition												Muscovite-bearing starting composition			
	Reservoir water					*CO_2-saturated reservoir water*								*CO_2-saturated reservoir water*			
	Model composition	**RW-t:10-10ka**	RW-t:10-1Ma	RW-t:1000-10ka	RW-t:1000-1Ma	**IC-t:10-10ka**	**IC-t:10-1Ma**	**IC-t:1000-10ka**	**IC-t:1000-1Ma**	IO-t:10-10ka	IO-t:10-1Ma	IO-t:1000-10ka and	IO-t:1000-1Ma	***Model composition***	**MC-t:10-10KaS**	**MC-t:10-10Ka**	**MC-t:1000-10Ka**
Residence time t_r (yr)	0	10	10	1000	1000	10	10	1000	1000	10	10	1000	1000	0	10	10	1000
Reaction time t (yr)	0	10ka	10Ma	10ka	1Ma	10ka	10Ma	10ka	1Ma	10ka	10Ma	10ka	1Ma	0	10ka	10Ma	10ka
Pyrite	*4*	*4*	*4*	*5*	*4*	*4*	*4*	*5*	*4*	*4*	*4*	*5*	*4*	*0.04*	*0.04*	*0.04*	*5*
(Total) Quartz	**23/26**	**22**	**23**	**18**	**24**	**31**	**26**	**45**	**34**	**31**	**27**	**45**	**35**	**29**	**0.2**	**0.2**	**34**
Calcite	25	22	25	0	22	7	20	0	9	7	19	0	6	13	15	15	4
Dolomite	1	3	1	0	3	10	9	0	12	10	9	0	13	1	36	36	16
Siderite	0	0	0	0	0	4	3	0	4	4	3	0	4	0	0	0	0
Total carbonate	**26**	**25**	**26**	**0**	**25**	**21**	**32**	**0**	**25**	**21**	**31**	**0**	**23**	**14**	**51**	**51**	**20**
Paragonite (Total mica)	**0**	**11**	**1**	**0**	**18**	**0**	**0**	**0**	**0**	**0**	**0**	**0**	**0**	**20**	**0**	**0**	**20**
Illite	25/24	23	25	0	13	23	21	0	0	23	19	0	0	2	0	0	0
Kaolinite	14/13	5	13	38	6	21	17	50	38	21	19	50	39	17	0	0	22
Daphnite (chlorite)	4	0	3	0	0	0	0	0	0	0	0	0	0	6	5	0	0
Saponite (smectite)	5/0	5	5	32	0	0	0	0	0	0	0	0	0	11	44	49	0
Nontronite (smectite)	0	6	1	7	6	0	0	0	0	0	0	0	0	0	0	0	4
Pyrophyllite	0/1	0	0	0	0	0	0	0	0	0	0	0	0	0	0	0	0
Total clay	**48/42**	**39**	**47**	**77**	**25**	**44**	**38**	**50**	**38**	**44**	**38**	**50**	**39**	**36**	**49**	**49**	**26**
Weak:strong (excluding pyrite)	49:48 52:42	50:47	48:49	77:18	43:49	44:52	38:58	50:45	38:59	44:52	38:58	50:45	39:58	56:43	49:51	49:51	46:54

RW = reservoir water exposure, I = illite-bearing OPA starting composition, M = muscovite-bearing OPA starting composition. S denotes smectite referring to the "10 years residence time – 10,000 years reaction time" scenario without non-swelling clays, whereas r denotes repeat experiment. *Italic*: pyrite was not added to the simulated fault gouges, underlined: in case of the open systems simulation, the mineral distribution used for the open system scenarios differed slightly from the closed system scenarios. Modelling outcomes with bold, black names were prepared for friction experiment.

6.2 Implications for CO_2 storage

In the context of CO_2 storage, but also in the context of Enhanced Gas Recovery (EGR) and Enhanced Oil Recovery (OER), the injection phase of CO_2 into (near) depleted gas and oil reservoirs, is assumed to pose the highest risk in terms of fault slip reactivation. Reactivation may accompany or follow injection due to processes such as the poro-elastic response (i.e. heave or compaction) of the storage complex, thermal expansion or shrinkage near the injection well, or a (locally) increased pore pressure (e.g. Wang, 2000; Hawkes et al., 2005; Vilarrasa et al., 2014). If the induced changes in pore fluid pressure, reservoir temperature, and any overall stress changes in the storage complex, comprising the reservoir and top seal, can be limited by limiting reservoir pressure or injection rate, and if the frictional strength of any present gouge-filled faults is not exceeded, the potential to fault slip reactivation can be reduced. As a consequence, the overall integrity of a storage complex is best maintained when injection rates are controlled and the total amounts of injected CO_2 are limited, constrained by the frictional strength and stability of faults in both reservoir rock and caprock.

When assessing the integrity of any potential storage complex, it can be assumed that subsurface faults are wet and located at a reasonable distance from detectable faults. Then, based on the experimental results presented in this thesis, several important implications regarding the frictional and transport properties of (pre)existing gouge-filled faults in both sandstone reservoirs and clay-rich caprocks of potential CCS storage complexes, depth range of ~1-4 km, temperatures of ~50 to 150°C and pressures of 0 to 100 MPa, can be drawn.

The friction experiments on simulated quartz-rich fault gouges reported in this thesis have demonstrated that the steady-state frictional strength of gouge-filled faults in sandstone reservoirs (58-90% quartz) can be expected to range between 0.5 and 0.7 (Chapters 2 and 4), while exhibiting stable slip behaviour (Figure 6.1). After long-term CO_2-exposure of these fault gouges, minimal mineralogical changes are expected due to limited availability of reactive minerals (Gunter et al., 1997), and such faults will continue to exhibit stable slip behaviour at similar frictional strengths. By contrast, the present experiments on aragonite and calcite-rich fault gouges suggest that the precipitation of significant concentrations of Ca-carbonates in CO_2-leaking faults may potentially strengthen a fault gouge (Chapters 2 and 4).

However, the increase in strength is accompanied by an increased potential for (highly) unstable, velocity-weakening slip behaviour upon re-shear at temperatures of >100-150 °C (Figure 6.1). Associated microstructures showed evidence that the transition to velocity-weakening behaviour at $T \geq 100$°C is likely to be related to the more significant comminution of the calcite clasts with respect to the quartz. This difference in grain size reduction can be explained by the difference in fracture toughness between quartz and calcite, related to the perfect rhombohedral cleavage of calcite, which as such lowers its fracture toughness with respect to the quartz (Schultz et al., 1994). Due to the significantly lower grain size of calcite, time-dependent thermally-activated diffusion enhances compaction competing with dilation and as such causing enhanced velocity-weakening.

Besides affecting the frictional behaviour of quartz-rich fault gouges, significant Ca-carbonate precipitation may lead to a reduction in fault gouge permeability, reducing the leakage potential of faults. The present results show that, overall, limited CO_2-induced precipitation of Ca-carbonate has the potential to strengthen a gouge-filled quartz fault, while reducing its permeability. Concentrations of Ca-carbonate >40% on the other hand could lead to unstable slip behaviour upon slip reactions. However, such concentrations are unlikely to precipitate as very large volumes of Ca-rich fluids would be required to pass along a permeable fault, which would already imply failure of a CO_2 storage system making further risk factors irrelevant.

In the situation of a clay-rich caprock, early dissolution of the naturally-occurring calcite (~20%) may reduce the frictional strength of clay-rich fault gouges by as much as 20%, while maintaining to exhibit stable slip behaviour (Chapter 3, 4 and 5). This would reduce the storage potential of a CO_2 storage complex. However, significant calcite precipitation (of ~50-70%) in clay-rich fault gouges, to locally maximum amounts of 70%, has the capacity to strength a clay-rich fault gouge by ~10-15% with respect to the strength of a natural calcite-bearing clay-rich fault gouge (~20% calcite; friction coefficient ~0.3), and as much as ~35-60% for a calcite-free clay-rich fault gouge. For these concentrations, clay-quartz-calcite compositions have proven to exhibit stable slip behaviour at temperatures relevant for CCS, as such improving the overall storage potential of the CO_2-storage complex. Attention must be paid to local calcite concentrations >90%, as for these concentrations faults may exhibit unstable and dilatant slip behaviour, thereby

unintentionally reducing the fault integrity and increasing induced seismogenic potential. However, the precipitation of such amounts of calcite, or any other carbonate, requires a significant down-fault Ca-source (or a source of magnesium or iron), which as shown by previous studies will generally not be provided by sandstone reservoirs considered for CO_2 storage (Bickle and Kampman, 2013; Busch et al., 2014; Hangx et al., 2015). In any case, if carbonate-saturated fluids infiltrate faults in clay-rich caprocks from the reservoir, fault invasion is likely to be very limited due to low fault core permeability ($<10^{-19}m^2$ – depth ≥2km), especially when showing a substantial off-set (Chapter 3). Little data is available about the transport properties of the damage zone surrounding the fault core in faulted clay-rich caprocks, but considering the plastic behaviour of clays, these zones are unlikely to form important leakage pathways.

6.3 Suggestions for future research

The work presented in this thesis has addressed how CO_2-induced mineralogical changes may impact the frictional strength and transport properties of gouge-filled faults in CO_2-storage systems comprising of sandstone reservoirs and clay-rich caprocks under in-situ conditions. Although this work has answered many of the questions initially posed, others have remained unanswered and new ones were brought up and need to be addressed in the future. These new issues point the way for new research to obtain a better understanding of the long-term effect of CO_2-fluid-rock interactions in natural storage reservoirs and in particular on the effect of CO_2-induced mineralogical changes on the frictional and transport properties of (pre-)existing gouge-filled faults in these complexes. In the following, a number of unsolved questions and suggestions for further research are identified and described.

6.3.1 Unsolved problems and remaining data needs

The effect of calcite-content on quartz

In Chapter 2 of this thesis, the frictional data showed a transition from velocity-strengthening (stable) at room temperature to velocity-weakening (unstable) at 100°C for gouges with near equal amounts of quartz and calcite, cf. heavily-cemented faults. Though the current work was adequate for identifying that

velocity-weakening in these compositions depends on temperature, as also observed for pure calcite by Verberne et al. (2010, 2014), more data are needed to systematically describe the effect of calcite content on the frictional behaviour of quartz-calcite mixtures. A first attempt was made in Chapter 5 where 50:50 quartz-calcite mixtures were tested. However, a more extended data-set is required to determine the compositional range and associated *P-T* conditions from which stable velocity-strengthening slip transitions to velocity-weakening slip behaviour.

The effect of temperature on the frictional strength of (pure) clay fault gouges

It was shown in Chapter 4 that the frictional strength and stability of a clay-quartz-calcite fault gouge depends on the relative porportions of each of the mineral components. Based on frictional data for and the relative amount of the individual mineral components, the frictional behaviour of a mixture can roughly be calculated, or predicted. This can be done at room temperature conditions, using widely available data (Crawford et al., 2008; Moore and Lockner, 2004; Morrow et al., 2000; Takahashi et al., 2007; Tembe et al., 2010). However to adequately describe the frictional behaviour of natural caprock-derived fault gouges representing various geological settings in the subsurface, more frictional data for pure clay minerals are needed at upper crustal *P-T* conditions, such as for pure kaolinite obtained in this study.

Systematic comparison of man-made mixtures vs. natural compositions

The manually assembled, phyllosilicate-rich gouge mixtures prepared in this study, on the basis of geochemical modelling results for long-term CO_2-fluid-rock interactions (Chapter 5), showed significant differences in frictional strength with respect to mixtures of the same composition prepared by crushing and sieving samples of Opalinus starting material studied in Chapter 4. Although a systematic relationship was observed between the quartz:calcite ratio and frictional strength, and between the presence of large amounts of weak phyllosilicates and frictional strength, it cannot be excluded that preparation of the manually-assembled mixtures may have played a role also. To unravel this, a systematic comparison between the frictional behaviour of man-made and naturally-derived gouge mixtures is needed in future.

Damage zone vs. fault core

The attempts in this thesis, to assess the effect of shear displacement and effective normal stress on the transport properties of clay-rich faults, focused on experiments relevant to the fault core. However, it is well-known that a fault zone consists of both a fault core and a damage zone (e.g. Caine et al., 1996). For brittle faults in nature, the fault permeability is known to be enhanced by the fracture network in the damage zone (Chen et al., 2013; Evans et al., 1997; Mitchell and Faulkner, 2012). Though full understanding of the permeability structure of a fault zone is key for predicting fluid flow in and leakage potential of rocks such as clay-rich caprocks (Ingram and Urai, 1999; Knipe et al., 1998), the present research has focused solely on the fault core. Experiments that couple both fluid flow in the damage zone and fault core (e.g. Chen et al., 2013) would therefore allow a more detailed determination of the fault permeability, hence leakage potential of a caprock.

The effect of calcite-content on fault gouge permeability

Most of the work reported in this thesis ultimately focused on the effect of calcite content on the frictional strength and stability of both simulated sandstone-derived and caprock-derived fault gouges. Comparatively little attention has been paid to the effect of CO_2-induced calcite dissolution/precipitation on the fault permeability of both quartz-rich and clay-rich fault gouges, hence leakage potential. Though many previous experimental studies have shown that both the frictional strength and permeability of clay-quartz mixtures depend on the relative composition (Behnsen and Faulkner, 2012; Crawford et al., 2008; Takahashi et al., 2007; Zhang et al., 2001), little data is available on the permeability of clay-calcite and quartz-calcite mixtures. Therefore such data would be a valuable addition.

Effect of Klinkenberg on the permeability

In Chapter 3 we showed that for clay-quart-calcite mixtures at effective normal stresses >17.5 MPa the Klinkenberg effect could no longer be ignored and permeability should be corrected for that accordingly. Due to the applied experimental procedure in this work, no systematic correction could have been made as during shear the maturity of the fault, and therefore the experimental situation, continuously changed. However, in future research using gas to measure permeability it might be an option to determine the pre-shear and post-shear

Klinkenberg effect, giving some measure for Klinkenberg corrected permeability values.

Permeability to aqueous pore fluids and effect of temperature

The argon gas permeability data presented in this thesis has been obtained at dry, room temperature conditions. In order for future data to be more representative of natural conditions, permeability measurements should be conducted using water or brine as the pore fluid, at in-situ temperature and pore pressure conditions. The effect of temperature on the permeability would be particularly interesting for mixtures with >50% calcite for quartz-calcite mixtures and >90% calcite for clay-quartz-calcite mixtures to investigate the effect of stick-slip behaviour on the transport properties of a fault gouge. Suitable methods for measuring the permeability to water at in-situ conditions include, for example transient pulse or sinusoidal, pore pressure oscillation methods (Bernabe et al., 2003; Faulkner and Rutter, 1998; Liang et al., 2001).

Discrete permeability measurements vs. continuous permeability measurements

The permeability measurements conducted in Chapter 3 are discrete measurements describing the measurement at specific displacement-intervals. However, to obtain a better insight in the permeability evolution during shear and hold, continuous measuring the permeability would allow to measure the slightest effect of dilation during re-shear upon permeability, which due to the current experimental procedure might have been missed. A suitable method for continuous measuring the permeability would be sinusoidal, pore pressure oscillation (Bernabe et al., 2003).

References

Alemu, B.L., Aagaard, P., Munz, I.A., Skurtveit, E., 2011. Caprock interaction with CO_2: A laboratory study of reactivity of shale with supercritical CO_2 and brine. Appl. Geochemistry 26, 1975–1989. doi:10.1016/j.apgeochem.2011.06.028

Alkattan, M., Oelker, E.H., Dandurand, J.-L., 1998. An experimental study of calcite and limestone dissolution rates as a function of pH from −1 to 3 and temperature from 25 to 80°C. Chem. Geol. 151, 199–214. doi:10.1016/S0009-2541(98)00080-1

Allen, P.A., Allen, J.R., 2005. Basin Analysis - Principles and applications, 2nd editio. ed. Blackwell Science Ltd.

André, L., Audigane, P., Azaroual, M., Menjoz, A., 2007. Numerical modeling of fluid-rock chemical interactions at the supercritical CO_2-liquid interface during CO_2 injection into a carbonate reservoir, the Dogger aquifer (Paris Basin, France). Energy Convers. Manag. 48, 1782–1797. doi:10.1016/j.enconman.2007.01.006

Andreani, M., Gouze, P., Luquot, L., Jouanna, P., 2008. Changes in seal capacity of fractured claystone caprocks induced by dissolved and gaseous CO_2 seepage. Geophys. Res. Lett. 35, 1–6. doi:10.1029/2008GL034467

Armitage, P.J., Faulkner, D.R., Worden, R.H., Aplin, A.C., Butcher, A.R., Iliffe, J., 2011. Experimental measurement of, and controls on, permeability and permeability anisotropy of caprocks from the CO_2 storage project at the Krechba Field, Algeria. J. Geophys. Res. Solid Earth. doi:10.1029/2011JB008385

Atkinson, B.K., 1984. Subcritical Crack Growth in Geological Materials. J. Geophys. Res. 89, 4077–4114. doi:10.1029/JB089iB06p04077

Atkinson, B.K., Avdis, V., 1980. Fracture mechanics parameters of some rock-forming minerals determined using an indentation technique. Int. J. Rock Mech. Min. Sci. 17, 383–386. doi:10.1016/0148-9062(80)90523-9

Aydin, A., 2000. Fractures, faults, and hydrocarbon entrapment, migration and flow. Mar. Pet. Geol. doi:10.1016/S0264-8172(00)00020-9

Baars, D.L., Stevenson, G.M., 1981. Tectonic evolution of the Paradox Basin, Utah and Colorado, Rocky Mountains Association of Geologists Guidebook, in: Wiegand, W.L. (Ed.), Geology of the Paradox Basin, pp. 23-31.

Bachu, S., Gunter, W.D., Perkins, E.H., 1994. Aquifer disposal of CO_2: hydrodynamic and mineral trapping. Energy Conversion and Management 35, 269-279.

Baines, S.J., Worden, R.H., 2004. The long-term fate of CO_2 in the subsurface: natural analogues for CO_2 storage, in: Baines, S.J., Worden, R.H. (Eds.), Geological storage of carbon dioxide. Geological Society of London, London, pp. 59-85.

Behnsen, J., Faulkner, D.R., 2012. The effect of mineralogy and effective normal

stress on frictional strength of sheet silicates. J. Struct. Geol. doi:10.1016/j.jsg.2012.06.015

Benson, S., Cook, P., Anderson, J., Bachu, S., Nimir, H., Basu, B., Bradshaw, J., Deguchi, G., Gale, J., von Goerne, G., 2005. Underground geological storage. IPCC special report on carbon dioxide capture and storage, 195-276.

Beig, M.S., Lüttge, A., 2006. Albite dissolution kinetics as a function of distance from equilibrium: Implications for natural feldspar weathering. Geochim. Cosmochim. Acta 70, 1402–1420. doi:10.1016/j.gca.2005.10.035

Bense, V.F., Person, M.A., 2006. Faults as conduit-barrier systems to fluid flow in siliciclastic sedimentary aquifers. Water Resour. Res. doi:10.1029/2005WR004480

Bernabe, Y., Mok, U., Evans, B., 2003. Permeability-porosity Relationships in Rocks Subjected to Various Evolution Processes 160, 937–960.

Bethke, C.M., Yeakel, S., 2014. The Geochemist's Workbench Release 10.0.

Bickle, M., Kampman, N., 2013. Lessons in carbon storage from geological analogues. Geology 41, 525–526. doi:10.1130/focus0420132.1

Blanpied, M.L., Marone, C.J., Lockner, D. a., Byerlee, J.D., King, D.P., 1998. Quantitative measure of the variation in fault rheology due to fluid-rock interactions. J. Geophys. Res. 103, 9691. doi:10.1029/98JB00162

Boulton, C., Carpenter, B.M., Toy, V., Marone, C., 2012. Physical properties of surface outcrop cataclastic fault rocks, Alpine Fault, New Zealand. Geochemistry, Geophys. Geosystems 13, 1–13. doi:10.1029/2011GC003872

Brace, W.F., 1978. Volume changes during fracture and frictional sliding: A review. Pure Appl. Geophys. PAGEOPH 116, 603–614. doi:10.1007/BF00876527

Burnside, N.M., Shipton, Z.K., Dockrill, B., Ellam, R.M., 2013. Man-made versus natural CO_2 leakage: A 400 k.y. history of an analogue for engineered geological storage of CO_2. Geology 41, 471-474.

Burton, E.A., Walter, L.M., 1987. Relative precipitation rates of aragonite and Mg calcite from sea water: temperature or carbonate ion control? Geology 15, 111-114.

Busch, A., Bertier, P., Gensterblum, Y., Rother, G., Spiers, C.J., Zhang, M., Wentinck, H.M., 2016. On sorption and swelling of CO_2 in clays. Geomech. Geophys. Geo-Energy Geo-Resources 2, 111–130. doi:10.1007/s40948-016-0024-4

Busch, A., Kampman, N., Hangx, S.J., Snippe, J., Bickle, M., Bertier, P., Chapman, H., Spiers, C.J., Pijnenburg, R., Samuelson, J., Evans, J.P., Maskell, A., Nicholl, J., Pipich, V., Di, Z., Rother, G., Schaller, M., 2014. The green river natural analogue as a field laboratory to study the long-term fate of CO_2 in the subsurface, in: Energy Procedia. pp. 2821–2830. doi:10.1016/j.egypro.2014.11.304

Byerlee, J., 1978. Friction of Rocks. Pageoph. 116.

Byerlee, J.D., Summers, R., 1976. A note on the effect of fault gouge thickness on fault stability. Int. J. Rock Mech. Min. Sci. Geomech. Abstr 13, 35–36.

Caine, J.S., Evans, J.P., Forster, C.B., 1996. Fault zone architecture and permeability structure. Geology 24, 1025–1028.

Cama, J., Ganor, J., Ayora, C., Lasaga, C.A., 2000. Smectite dissolution kinetics at 80°C and pH 8.8. Geochim. Cosmochim. Acta 64, 2701–2717.

Cama, J., Metz, V., Ganor, J., 2002. The effect of pH and temperature on kaolinite dissolution rate under acidic conditions. Geochim. Cosmochim. Acta 66, 3913–3926. doi:10.1016/S0016-7037(02)00966-3

Cappa, F., Rutqvist, J., 2011. Modeling of coupled deformation and permeability evolution during fault reactivation induced by deep underground injection of CO_2. Int. J. Greenh. Gas Control. doi:10.1016/j.ijggc.2010.08.005

Carpenter, B.M., Collettini, C., Viti, C., Cavallo, A., 2016. The influence of normal stress and sliding velocity on the frictional behaviour of calcite at room temperature: insights from laboratory experiments and microstructural observations. Geophys. J. Int. 205, 548–561. doi:10.1093/gji/ggw038

Carpenter, B.M., Saffer, D.M., Marone, C., 2012. Frictional properties and sliding stability of the San Andreas fault from deep drill core. Geology. doi:10.1130/G33007.1

Carpenter, B.M., Scuderi, M.M., Collettini, C., Marone, C., 2015. Frictional heterogeneities on carbonate-bearing normal faults: Insights from the Monte Maggio Fault, Italy. J. Geophys. Res. B Solid Earth. doi:10.1002/2014JB011337

Chadwick, R.A., Zweigel, P., Gregersen, U., Kirby, G.A., Holloway, S., Johannessen, P.N., 2004. Geological reservoir characterization of a CO_2 storage site: The Utsira Sand, Sleipner, northern North Sea. Energy 29, 1371–1381. doi:10.1016/j.energy.2004.03.071

Chen, J., Verberne, B.A., Spiers, C.J., 2015a. Effects of healing on the seismogenic potential of carbonate fault rocks: Experiments on samples from the Longmenshan Fault, Sichuan, China. J. Geophys. Res. B Solid Earth 120, 5479–5506. doi:10.1002/2015JB012051

Chen, J., Verberne, B.A., Spiers, C.J., 2015b. Interseismic re-strengthening and stabilization of carbonate faults by “non-Dieterich” healing under hydrothermal conditions. Earth Planet. Sci. Lett. 423, 1–12. doi:10.1016/j.epsl.2015.03.044

Chen, J., Yang, X., Duan, Q., Shimamoto, T., Spiers, C.J., 2013. Importance of thermochemical pressurization in the dynamic weakening of the Longmenshan Fault during the 2008 Wenchuan earthquake : Inferences from experiments and modeling. J. Geophys. Res. SOLID EARTH 118, 4145–4169. doi:10.1002/jgrb.50260

Cheng, A.H.-D., 2016. Poroelasticity, first edit. ed. Springer International Publishing. doi:10.1007/978-3-319-25202-5

Chester, F.M., 1994. Effects of temperature on friction: Constitutive equations and experiments with quartz gouge. Journal of Geophysical Research: Solid Earth 99, 7247-7261.

Collettini, C., Niemeijer, A., Viti, C., Smith, S.A.F., Marone, C., 2011. Fault structure, frictional properties and mixed-mode fault slip behavior. Earth Planet. Sci. Lett. doi:10.1016/j.epsl.2011.09.020

Condon, S.M., 1997. Geology of the Pennsylvanian and Permian Cutler Group and

Permian Kaibab Limestone in the Paradox Basin, southeastern Utah and southwestern Colorado, in: Huffman, A.C. (Ed.), U.S. Geological Survey bulletin ; 2000 Evolution of sedimentary basins--Paradox Basin, Washington, DC, p. 59.

Crawford, B.R., Faulkner, D.R., Rutter, E.H., 2008. Strength, porosity, and permeability development during hydrostatic and shear loading of synthetic quartz-clay fault gouge. J. Geophys. Res. Solid Earth 113, 1–14. doi:10.1029/2006JB004634

Credoz, A., Bildstein, O., Jullien, M., Raynal, J., Pétronin, J.C., Lillo, M., Pozo, C., Geniaut, G., 2009. Experimental and modeling study of geochemical reactivity between clayey caprocks and CO_2 in geological storage conditions. Energy Procedia 1, 3445–3452. doi:10.1016/j.egypro.2009.02.135

Delle Piane, C., Giwelli, A., Clennell, M.B., Esteban, L., Nogueira Kiewiet, M.C.D., Kiewiet, L., Kager, S., Raimon, J., in press. Frictional and hydraulic behaviour of carbonate fault gouge during fault reactivation — An experimental study. Tectonophysics.

Den Hartog, S.A.M., Niemeijer, A.R., Spiers, C.J., 2013. Friction on subduction megathrust faults: Beyond the illite–muscovite transition. Earth and Planetary Science Letters 373, 8-19.

Den Hartog, S.A.M., Peach, C.J., de Winter, D.A.M., Spiers, C.J., Shimamoto, T., 2012. Frictional properties of megathrust fault gouges at low sliding velocities: New data on effects of normal stress and temperature. J. Struct. Geol. 156–171. doi:10.1016/j.jsg.2011.12.001

Den Hartog, S.A.M., Spiers, C.J., 2014. A microphysical model for fault gouge friction applied to subduction megathrusts. J. Geophys. Res. Solid Earth 119, 1510–1529. doi:10.1002/2013JB010580

Den Hartog, S.A.M., Spiers, C.J., 2013. Influence of subduction zone conditions and gouge composition on frictional slip stability of megathrust faults. Tectonophysics. doi:10.1016/j.tecto.2012.11.006

Den Hartog, S., Saffer, D.M., Spiers, C.J., 2014. The roles of quartz and water in controlling unstable slip in phyllosilicate-rich megathrust fault gouges. Earth, Planets Sp. 66, 1–9. doi:10.1186/1880-5981-66-78

Dethlefsen, F., Haase, C., Ebert, M., Dahmke, A., 2012. Uncertainties of geochemical modeling during CO 2 sequestration applying batch equilibrium calculations. Environ. Earth Sci. 65, 1105–1117. doi:10.1007/s12665-011-1360-x

Dewhurst, D.N., Brown, K.M., Clennell, M.B., Westbrook, G.K., 1996. A comparison of the fabric and permeability anisotropy of consolidated and sheared silty clay. Eng. Geol. 42, 253–267. doi:10.1016/0013-7952(95)00089-5

Dieterich, J.H., 1979. Modeling of rock friction: 1. Experimental results and constituve equations. J. Geophys. Res. 84, 2161–2168. doi:10.1007/BF00876539

Dieterich, J.H., 1978. Time-dependent friction and the mechanics of stick-slip. Pageoph. 116, 790–806. doi:10.1029/JB084iB05p02161

Duan, Z., Sun, R., 2003. An improved model calculating CO_2 solubility in pure water and aqueous NaCl solutions from 273 to 533 K and from 0 to 2000 bar. Chem. Geol. 193, 257–271. doi:10.1016/S0009-2541(02)00263-2

Duan, Z.H., Sun, R., Zhu, C. and Chou, I.M. (2006) An improved model for the calculation of CO_2 solubility in aqueous solutions containing Na^+, K^+, Ca^{2+}, Mg^{2+}, Cl^-, and SO_4^{2-}. *Mar. Chem.* **98**, 131-139.

Edlmann, K., Haszeldine, S., McDermott, C.I., 2013. Experimental investigation into the sealing capability of naturally fractured shale caprocks to supercritical carbon dioxide flow. Environ. Earth Sci. 70, 3393–3409. doi:10.1007/s12665-013-2407-y

Elzinga, D., International, R. and analists of the, Technology, E.P. and S.A., 2014. Energy Technology Perspectives 2014 - Harnessing Electricity's Potential 382.

Evans, J.P., Forster, C.B., Goddard, J. V, 1997. Permeability of fault-related rocks, and implications for hydraulic structure of fault zones. J. Struct. Geol. 19, 1393–1404.

Farrell, N.J.C., Healy, D., Taylor, C.W., 2014. Anisotropy of permeability in faulted porous sandstones. J. Struct. Geol. doi:10.1016/j.jsg.2014.02.008

Faulkner, D.R., Jackson, C.A.L., Lunn, R.J., Schlische, R.W., Shipton, Z.K., Wibberley, C.A.J., Withjack, M.O., 2010. A review of recent developments concerning the structure, mechanics and fluid flow properties of fault zones. J. Struct. Geol. doi:10.1016/j.jsg.2010.06.009

Faulkner, D.R., Mitchell, T.M., Behnsen, J., Hirose, T., Shimamoto, T., 2011. Stuck in the mud? Earthquake nucleation and propagation through accretionary forearcs. Geophys. Res. Lett. 38, 1–5. doi:10.1029/2011GL048552

Faulkner, D.R., Rutter, E.H., 2000. Comparisons of water and argon permeability in natural clay-bearing fault gouge under high pressure at 20°C. J. Geophys. Res. 105, 16415. doi:10.1029/2000JB900134

Faulkner, D.R., Rutter, E.H., 1998. The gas permeability of clay-bearing fault gouge at 20°C. Geol. Soc. London, Spec. Publ. doi:10.1144/gsl.sp.1998.147.01.10

Gaus, I., Azaroual, M., Czernichowski-Lauriol, I., 2005. Reactive transport modelling of the impact of CO_2 injection on the clayey cap rock at Sleipner (North Sea). Chem. Geol. doi:10.1016/j.chemgeo.2004.12.016

Giorgetti, C., Carpenter, B.M., Collettini, C., 2015. Frictional behavior of talc-calcite mixtures. J. Geophys. Res. B Solid Earth 120, 6614–6644. doi:10.1002/2015JB011970

Gozalpour, F., Ren, S., R., Tohidi, B., 2005. CO_2 EOR and Storage in Oil Reservoirs. Oil & Gas Science and Technology - Rev. IFP 60, 537-546.

Guéllar-Franca, R.M., Azapagic, A., 2015. Carbon capture , storage and utilisation technologies : A critical analysis and comparison of their life cycle environmental impacts. J. Util. 9, 82–102. doi:10.1016/j.jcou.2014.12.001

Gunter, W.D., Perkins, E.H., McCann, T.J., 1993. Aquifer disposal of CO_2-rich gases: Reaction design for added capacity. Energy Convers. Manag. 34, 941–948. doi:10.1016/0196-8904(93)90040-H

Gunter, W.D., Wiwchar, B., Perkins, E.H., 1997. Aquifer disposal of CO_2-rich

Greenhouse Gases: Extension of the time scale of experiment for CO_2-sequestering reactions by geochemical modelling. Mineral. Petrol. 59, 121–140. doi:10.1007/BF01163065

Haines, S.H., Van Der Pluijm, B.A., Ikari, M.J., Saffer, D.M., Marone, C., 2009. Clay fabric intensity in natural and artificial fault gouges: Implications for brittle fault zone processes and sedimentary basin clay fabric evolution. J. Geophys. Res. Solid Earth. doi:10.1029/2008JB005866

Handy, M.R., 1990. The Solid-State Flow of Polymineralic Rocks. Journal of Geophysical Research 95, 8647-8661.

Hangx, S., Bakker, E., Bertier, P., Nover, G., Busch, A., 2015. Chemical–mechanical coupling observed for depleted oil reservoirs subjected to long-term CO_2-exposure – A case study of the Werkendam natural CO_2 analogue field. Earth Planet. Sci. Lett. 428, 230–242. doi:10.1016/j.epsl.2015.07.044

Hangx, S., van der Linden, A., Marcelis, F., Bauer, A., 2013. The effect of CO_2 on the mechanical properties of the Captain Sandstone: Geological storage of CO_2 at the Goldeneye field (UK). Int. J. Greenh. Gas Control 19, 609–619. doi:10.1016/j.ijggc.2012.12.016

Hangx, S.J.T., Spiers, C.J., Peach, C.J., 2010a. Creep of simulated reservoir sands and coupled chemical-mechanical effects of CO_2 injection. J. Geophys. Res. Solid Earth 115. doi:10.1029/2009JB006939

Hangx, S.J.T., Spiers, C.J., Peach, C.J., 2010b. The effect of deformation on permeability development in anhydrite and implications for caprock integrity during geological storage of CO_2. Geofluids 10, 369–387. doi:10.1111/j.1468-8123.2010.00299.x

Haszeldine, R.S., Quinn, O., England, G., Wilkinson, M., Shipton, Z.K., Evans, J.P., Heath, J., Crossey, L., Ballentine, C.J., Graham, C.M., 2005. Natural geochemical analogues for carbon dioxide storage in deep geological porous reservoirs, a United Kingdom perspective. Oil Gas Sci. Technol. 60, 33–49. doi:10.2516/ogst:2005004

Haszeldine, R.S., 2009. Carbon Capture and Storage: How Green Can Black Be? Science 325, 1647-1652.

Haszeldine, S., Lu, J., Wilkinson, M., Macleod, G., 2006. Long-timescale interaction of CO_2 storage with reservoir and seal : Miller and Brae natural analogue fields North Sea. Greenh. gas Control Technol. 8, 1–6.

Hawkes, C., Mclellan, P., Bachu, S., 2005. Geomechanical factors affecting geological storage of CO_2 in depleted oil and gas reservoirs. J. Can. Pet. Technol. 44.

Herzog, R.E., Shi, Q., Patil, J.N., Katz, J.L., 1989. Magnetic water treatment: the effect of iron on calcium carbonate nucleation and growth. Langmuir 5, 861-867.

Hintze, L.F., Willis, G.C., Laes, D.Y.M., Sprinkel, D.A., Brown, K.D., 2000. Digital Geologic Map of Utah: Utah Geological Survey Map 179DM, scale 1:500,000. Utah Geological Survey.

Hirth, G., Teyssier, C., Dunlap, J.W., 2001. An evaluation of quartzite flow laws

based on comparisons between experimentally and naturally deformed rocks. International Journal of Earth Sciences 90, 77-87.

Hitchon, B., 1996. Aquifer disposal of carbon dioxide: hydrodynamic and mineral trapping - proof of concept. Geoscience Publishing Ltd., Sherwood Park, Alberta, Canada.

Holloway, S., 2001. Storage of fossil fuel-derived carbon dioxide beneath the surface of the earth. Annu. Rev. Energ. Environ. 26, 145-166.

Hoagland, R.G., Hahn, G.T., Rosenfield, A.R., 1973. Influence of microstructure on fracture propagation in rock. Rock Mech. 5, 77–106. doi:10.1007/BF01240160

Honty, M., Wang, L., Osacky, M., Uhlik, P., Czimerova, A. and Madejoya, J. (2012) Experimental interactions of the Opalinus Clay and Boom Clay with various repository relevant solutions at 90 °C under closed conditions. *Appl. Clay Sci.* **59-60**, 50-63.

Hooper, E.C.D., 1991. Fluid migration along growth faults in compacting sediments. J. Pet. Geol. 14, 161–180. doi:10.1111/j.1747-5457.1991.tb00360.x

Huq, F., Haderlein, S.B., Cirpka, O.A., Nowak, M., Blum, P., Grathwohl, P., 2015. Flow-through experiments on water-rock interactions in a sandstone caused by CO_2 injection at pressures and temperatures mimicking reservoir conditions. Appl. Geochemistry 58, 136–146. doi:10.1016/j.apgeochem.2015.04.006

Ide, S., Takeo, M., 1997. Determination of constitutive relations of fault slip based on seismic wave analysis. J. Geophys. Res. 102, 27379–27391.

Ikari, M.J., Niemeijer, A.R., Spiers, C.J., Kopf, A.J., Saffer, D.M., 2013. Experimental evidence linking slip instability with seafloor lithology and topography at the Costa Rica convergent margin. Geology 41, 891–894. doi:10.1130/G33956.1

Ikari, M.J., Saffer, D.M., Marone, C., 2009. Frictional and hydrologic properties of clay-rich fault gouge. J. Geophys. Res. Solid Earth 114, 1–18. doi:10.1029/2008JB006089

Ikari, M.J., Saffer, D.M., Marone, C., 2007. Effect of hydration state on the frictional properties of montmorillonite-based fault gouge. J. Geophys. Res. Solid Earth 112, 1–12. doi:10.1029/2006JB004748

Ingram, G.M., Urai, J.L., 1999. Top-seal leakage through faults and fractures; the role of mudrock properties.pdf, in: Muds and Mudstones. pp. 125–135.

IPCC, 2014. Climate Change 2014: Synthesis Report . Contribution of Working Groups I, II and III to the Fifth Assessment Report of the Intergovernmental Panel on Climate Change, IPCC.

IPCC, 2007. Climate change 2007: Synthesis report. Contribution of Working Groups I, II and III to the fourth assessment report of the Intergovernmental Panel on Climate Change 104. doi:10.1038/446727a

Jaeger, J.C., Cook, N.G.W., Zimmerman, R.W., 2007. Fundamental of rock mechanics, 4th editio. ed. Blackwell Publishing, Singapore.

Johnson, J.W., Nitao, J.J., Morris, J.P., 2004. Reactive Transport Modeling of Cap Rock Integrity During Natural and Engineered CO2 Storage Carbon Dioxide

Capture for Storage in Deep Geologic Formations (two-volume set published by Elsevier: ISBN 0080445705).

Kalinowski, B.E., Schweda, P., 1996. Kinetics of muscovite, phlogopite, and biotite dissolution and alteration at pH 1-4, room temperature. Geochim. Cosmochim. Acta 60, 367–385.

Kampman, N., Bickle, M., Maskell, A., Chapman, H., Evans, J., Purser, G., Zhou, Z., Schaller, M., Gattacceca, J.C., Bertier, P., 2014. Drilling and sampling a natural CO_2 reservoir: Implications for fluid flow and CO_2-fluid–rock reactions during CO_2 migration through the overburden. Chemical Geology 369, 51-82.

Kampman, N., Busch, A., Bertier, P., Snippe, J., Hangx, S., Pipich, V., Di, Z., Rother, G., Harrington, J.F., Evans, J.P., Maskell, A., Chapman, H.J., Bickle, M.J., 2016. Observational evidence confirms modelling of the long-term integrity of CO2-reservoir caprocks. Nat. Commun. 7, 12268. doi:10.1038/ncomms12268

Kanagawa, K., Cox, S.F., Zhang, S., 2000. Effects of dissolution-precipitation processes on the strength and mechanical behavior of quartz gouge at high-temperature hydrothermal conditions. Journal of Geophysical Research: Solid Earth 105, 11115-11126.

Kaszuba, J., Yardley, B., Andreani, M., 2013. Experimental Perspectives of Mineral Dissolution and Precipitation due to Carbon Dioxide-Water-Rock Interactions. Rev. Mineral. Geochemistry 77, 153–188. doi:10.2138/rmg.2013.77.5

Kaszuba, J.P., Janecky, D.R., Snow, M.G., 2005. Experimental evaluation of mixed fluid reactions between supercritical carbon dioxide and NaCl brine: Relevance to the integrity of a geologic carbon repository. Chem. Geol. doi:10.1016/j.chemgeo.2004.12.014

Kearney, C., Zhao, Z., Bruet, B.J.F., Radovitzky, R., Boyce, M.C., Ortiz, C., 2006. Nanoscale Anisotropic Plastic Deformation in Single Crystal Aragonite. Physical Review Letters 96, 255505.

Kestin, J., Sokolov, M., Wakeham, W.A., 1978. Viscosity of liquid water in the range of -8 to 150C. J. Phys. Chem. Ref. Data 7, 941–948.

Kestin, Wakeham, 1972. Viscosity of the noble gases in the temperature range 25-700C. J. Chem. Phys. 56, 41194124.

Keulen, N., Heilbronner, R., Stünitz, H., Boullier, A.M., Ito, H., 2007. Grain size distributions of fault rocks: A comparison between experimentally and naturally deformed granitoids. J. Struct. Geol. 29, 1282–1300. doi:10.1016/j.jsg.2007.04.003

Klinkenberg, L.J., 1941. The permeability of porous media to liquids and gases, Drilling and Production Practice. American Petroleum Institute, New York, pp. 200-213.

Knauss, K.G., Thomas J, W., 1989. Muscovite dissolution kinetics as a function of pH and time at 70C. Geochim. Cosmochim. Acta 53, 1493–1501. doi:10.1016/0016-7037(89)90232-9

Knipe, R.J., Jones, G., Fischer, Q.J., 1998. Faulting , fault sealing and fluid flow in hydrocarbon reservoirs : an introduction. Geol. Soc. London Spec. Publ. 147, vii–xxi.

Knipe, R.J., Jones, G., Fisher, Q.J., 1998. Faulting, fault sealing and fluid-flow in hydrocarbon reservoirs: an introduction.

Köhler, S.J., Dufaud, F. and Oelkers, E.H. (2003) An experimental study of illite dissolution kinetics as a function of pH from 1.4 to 12.4 and temperature from 5 to 50ºC. *Geochim. Cosmochim. Acta* **67**, 3583-3594.

Lamy-Chappuis, B., Angus, D., Fisher, Q., Grattoni, C., Yardley, B.W.D., 2014. Rapid porosity and permeability changes of calcareous sandstone due to CO_2-enriched brine injection. Geophys. Res. Lett. 41, 399–406. doi:10.1002/2013GL058534.Received

Lamy-chappuis, B., Angus, D., Fisher, Q.J., Yardley, B.W.D., 2016. The effect of CO 2 -enriched brine injection on the mechanical properties of calcite-bearing sandstone. Int. J. Greenh. Gas Control 52, 84–95. doi:10.1016/j.ijggc.2016.06.018

Langerak, E.P.A.v., Beekmans, M.M.H., Beun, J.J., Hamelers, H.V.M., Lettinga, G., 1999. Influence of phosphate and iron on the extent of calcium carbonate precipitation during anaerobic digestion. Journal of Chemical Technology & Biotechnology 74, 1030-1036.

Le Guen, Y., Renard, F., Hellmann, R., Brosse, E., Collombet, M., Tisserand, D., Gratier, J.P., 2007. Enhanced deformation of limestone and sandstone in the presence of high P CO_2 fluids. J. Geophys. Res. Solid Earth 112, 1–21. doi:10.1029/2006JB004637

Liang, Y., Price, J.D., Wark, D.A., Watson, E.B., 2001. Nonlinear pressure diffusion in a porous medium: Approximate solutions with applications to permeability measurements using transient pulse decay method. J. Geophys. Res. 106, 529–535.

Liteanu, E., Spiers, C.J., 2009. Influence of pore fluid salt content on compaction creep of calcite aggregates in the presence of supercritical CO_2. Chemical Geology 265, 134-147.

Liteanu, E., Spiers, C.J., De Bresser, J.H.P., 2013. The influence of water and supercritical CO_2 on the failure behavior of chalk. Tectonophysics 599, 157–169. doi:10.1016/j.tecto.2013.04.013

Lockner, D.A., Beeler, N.M., 2002. Rock failure and earthquakes 81, 505–537. doi:10.1016/S0074-6142(02)80235-2

Logan, J.M., Rauenzahn, K.A., 1987. Frictional dependence of gouge mixtures of quartz and montmorillonite on velocity, composition and fabric. Tectonophysics 144, 87–108.

Lupini, J.F., Skinner, A.E., Vaughan, P.R., 1981. The drained residual strength of cohesive soils. Géotechnique 31, 181–213. doi:10.1680/geot.1981.31.2.181

Luquot, L., Gouze, P., 2009. Experimental determination of porosity and permeability changes induced by injection of CO_2 into carbonate rocks. Chem. Geol. 265, 148–159. doi:10.1016/j.chemgeo.2009.03.028

Mair, K., Marone, C., 1999. Friction of simulated fault gouge for a wide range of velocities and normal stresses. J. Geophys. Res. 104, 28,899-28,914.

Mair, K., Marone, C., 2001. Shear Heating in Granular Layers, in: Mora, P.,

Matsu'ura, M., Madariaga, R., Minster, J.-B. (Eds.), Microscopic and Macroscopic Simulation: Towards Predictive Modelling of the Earthquake Process. Birkhäuser Basel, Basel, pp. 1847-1866.

Major, J.R., Eichhubl, P., Dewers, T.A., Urquhart, A.S., Olson, J.E., Holder, J., 2014. The Effect of CO_2-Related Diagenesis on Geomechanical Failure Parameters: Fracture Testing of CO_2-Altered Reservoir and Seal Rocks From a Natural Analog at Crystal Geyser, Utah. American Rock Mechanics Association.

Mandl, G., Jong, L.N.J., Maltha, A., 1977. Shear zones in granular material. Rock mechanics 9, 95-144.

Marcon, V., Kaszuba, J.P., 2015. Carbon dioxide-brine-rock interactions in a carbonate reservoir capped by shale: Experimental insights regarding the evolution of trace metals. Geochim. Cosmochim. Acta. doi:10.1016/j.gca.2015.06.037

Marone, C., 1998. Laboratory-Derived Friction Laws and Their Application To Seismic Faulting. Annu. Rev. Earth Planet. Sci. 26, 643–696. doi:10.1146/annurev.earth.26.1.643

Marone, C., Scholz, C.H., 1989. Particle-size distribution and microstructures within simulated fault gouge. J. Struct. Geol. 11, 799–814. doi:10.1016/0191-8141(89)90099-0

Marston, P., 2013. Pressure profiles for CO_2-EOR and CCS: Implications for regulatory frameworks. Greenh. Gases Sci. Technol. 3, 165–168. doi:10.1002/ghg

McGarr, A., 2014. Maximum magnitude earthquakes induced by fluid injection. J. Geophys. Res. Solid Earth 119, 1008–1019. doi:10.1002/2013JB010597.Received

Mikhaltsevitch, V., Lebedev, M., Gurevich, B., 2014. Measurements of the elastic and anelastic properties of sandstone flooded with supercritical CO_2. Geophysical Prospecting 62, 1266-1277.

Mitchell, T.M., Faulkner, D.R., 2012. Towards quantifying the matrix permeability of fault damage zones in low porosity rocks. Earth Planet. Sci. Lett. 24–31. doi:10.1016/j.epsl.2012.05.014

Moore, D.E., Lockner, D.A., 2011. Frictional strengths of talc-serpentine and talc-quartz mixtures. J. Geophys. Res. Solid Earth. doi:10.1029/2010JB007881

Moore, D.E., Lockner, D.A., 2004. Crystallographic controls on the frictional behavior of dry and water‐saturated sheet structure minerals. J. Geophys. Res 109, 1–16. doi:10.1029/2003JB002582

Morrow, C.A., Moore, D.E., Lockner, D.A., 2000. The effect of mineral bond strength and adsorbed water on fault gouge frictional strength. Geophys. Res. Lett. 27, 815–818. doi:10.1029/1999GL008401

Morrow, C.A., Shi, L.Q., Yerlee, J.D.B., 1984. Permeability of Fault Gouge Under Confining Pressure and Shear Stress State Seismological Bureau, People's Republic of China. J. Geophys. Res. 89, 3193–3200. doi:10.1029/JB089iB05p03193

Morrow, C., Shi, L.Q., Byerlee, J., 1981. Permeability and strength of San Andreas

Fault gouge under high pressure. Geophys. Res. Lett. 8, 325–328. doi:10.1029/GL008i004p00325

Morse, J.W., Mucci, A., Millero, F.J., 1980. The solubility of calcite and aragonite in seawater of 35%. salinity at 25°C and atmospheric pressure. Geochimica et Cosmochimica Acta 44, 85-94.

Neuzil, C.E., 1994. How permeable are clays and shales? Water Resour. Res. doi:10.1029/93WR02930

Niemeijer, A.R., Spiers, C.J., 2007. A microphysical model for strong velocity weakening in phyllosilicate-bearing fault gouges. J. Geophys. Res. Solid Earth 112, 1–12. doi:10.1029/2007JB005008

Niemeijer, A.R., Spiers, C.J., Peach, C.J., 2008. Frictional behaviour of simulated quartz fault gouges under hydrothermal conditions: Results from ultra-high strain rotary shear experiments. Tectonophysics. doi:10.1016/j.tecto.2008.09.003

Niemeijer, A.R., Vissers, R.L.M., 2014. Earthquake rupture propagation inferred from the spatial distribution of fault rock frictional properties. Earth and Planetary Science Letters 396, 154-164.

Nuccio, V.F., Condon, S.M., 1996. Burial and Thermal History of the Paradox Basin, Utah and Colorado, and Petroleum Potential of the Middle Pennsylvanian Paradox Formation, in: Huffman, A.C., Lund, W.R., Godwin, L.H. (Eds.), Geology and Resources of the Paradox Basin: Utah Geological Association Guidebook pp. 57-76.

Ogata, K., Senger, K., Braathen, A., Tveranger, J., 2014. Fracture corridors as seal-bypass systems in siliciclastic reservoir-cap rock successions: Field-based insights from the Jurassic Entrada Formation (SE Utah, USA). Journal of Structural Geology 66, 162-187.

Orlic, B., 2013. Site-specific geomechanical modeling for predicting stress changes around depleted gas reservoirs considered for CO_2 storage in the Netherlands. Proc. 47th US Rock Mech. Geomech. Symp. ARMA 13-44.

Palandri, J.L., Kharaka, Y.K., 2004. A compilation of rater paramters of water-mineral interaction kinetics for application to geochemical modeling. US Geol. Surv. Menlo Park. Calif. 64.

Palandri, J.L., Kharaka, Y.K., 2005. Ferric iron-bearing sediments as a mineral trap for CO_2 sequestration: iron reduction using sulfur-bearing waste gas. Chemical Geology 217, 351-364.

Pauwels, H., Gaus, I., Le Nindre, Y.M., Pearce, J., Czernichowski-Lauriol, I., 2007. Chemistry of fluids from a natural analogue for a geological CO_2 storage site (Montmiral, France): lessons for CO_2-water-rock interaction assessment and monitoring. Applied Geochemistry 22, 2817-2833.

Peach, C.J., 1991. Influence of deformation on the fluid transport properties of salt rocks, Faculty of Geosciences. Utrecht University, Utrecht, p. 238.

Peach, C.J., Spiers, C.J., 1996. Influence of crystal plastic deformation on dilatancy and permeability development in synthetic salt rock. Tectonophysics 256, 101–128.

Pearce, J., Czernichowski-Lauriol, I., Lombard, S., Brune, S., Nador, A., Baker, J., Pauwels, H., Hatziyannis, G., Beaubien, S., Faber, E., 2004. A review of natural CO_2 accummulations in Europe as analogues for geological sequestration, in: Baines, S.J., Worden, R.H. (Eds.), Geological Storage of Carbon Dioxide. Geological Society, London, Special Publications, pp. 29–41. doi:doi:10.1144/GSl.SP.2004.233.01.04

Pearson, F.J., Arcos, D., Bath, A., Boisson, J.-Y., Fernández, A.M., Gäbler, H.-E., Gaucher, E., Gautschi, A., Griffault, L., Hernán, P., Waber, H.N., 2003. Mont Terri Project – Geochemistry of Water in the Opalinus Clay Formation at the Mont Terri Rock Laboratory. Geol. Ser. 10, 5–1.

Pluymakers, A.M.H., Niemeijer, A.R., Peach, C.J., 2014a. Frictional and sealing behavior of simulated anhydrite fault gouge: Effects of CO 2 and implications for fault stability and caprock integrity. Thesis.

Pluymakers, A.M.H., Niemeijer, A.R., Spiers, C.J., 2016. Frictional properties of simulated anhydrite-dolomite fault gouge and implications for seismogenic potential. J. Struct. Geol. 84, 31–46. doi:10.1016/j.jsg.2015.11.008

Pluymakers, A.M.H., Samuelson, J.E., Niemeijer, A.R., Spiers, C.J., 2014b. Effects of temperature and CO_2 on the frictional behavior of simulated anhydrite fault rock. J. Geophys. Res. B Solid Earth. doi:10.1002/2014JB011575

Preisig, M., Prévost, J.H., 2011. Coupled multi-phase thermo-poromechanical effects. Case study: CO_2 injection at In Salah, Algeria. Int. J. Greenh. Gas Control 5, 1055–1064. doi:10.1016/j.ijggc.2010.12.006

Reinen, L.A., Weeks, J.D., 1993. Determination of rock friction constitutive parameters using an iterative least squares inversion method. J. Geophys. Res. 98, 15,937-15,950. doi:10.1029/93JB00780

Rinaldi, A.P., Rutqvist, J., Cappa, F., 2014. Geomechanical effects on CO_2 leakage through fault zones during large-scale underground injection. Int. J. Greenh. Gas Control 20, 117–131. doi:10.1016/j.ijggc.2013.11.001

Rohmer, J., Pluymakers, A., Renard, F., 2016. Mechano-chemical interactions in sedimentary rocks in the context of CO_2 storage: Weak acid, weak effects? Earth Sci. Rev. 157, 86–110. doi:10.1016/j.earscirev.2016.03.009

Ruina, A., 1983. Slip Instability and State Variable Friction Laws. J. Geophys. Res. 88370, 359–10. doi:10.1029/JB088iB12p10359

Rutqvist, J., Cappa, F., Mazzoldi, A., Rinaldi, A., 2013. Geomechanical modeling of fault responses and the potential for notable seismic events during underground CO_2 injection. Energy Procedia 37, 4774–4784. doi:10.1016/j.egypro.2013.06.387

Rutter, E.H., Maddock, R.H., Hall, S.H., White, S.H., 1986. Comparative microstructures of natural and experimentally produced clay-bearing fault gouges. Pure Appl. Geophys. 124, 3-30.

Saffer, D.M., Marone, C., 2003. Comparison of smectite- and illite-rich gouge frictional properties: Application to the updip limit of the seismogenic zone along subduction megathrusts. Earth Planet. Sci. Lett. doi:10.1016/S0012-821X(03)00424-2

Samuelson, J., Elsworth, D., Marone, C., 2009. Shear-induced dilatancy of fluid-saturated faults: Experiment and theory. J. Geophys. Res. Solid Earth 114, 1–15. doi:10.1029/2008JB006273

Samuelson, J., Spiers, C.J., 2012. Fault friction and slip stability not affected by CO_2 storage: Evidence from short-term laboratory experiments on North Sea reservoir sandstones and caprocks. Int. J. Greenh. Gas Control 11S, S78–S90. doi:10.1016/j.ijggc.2012.09.018

Scholz, C.H., 1998. Earthquakes and Friction laws 391, 37–42.

Scholz, C.H., 2002. The Mechanics of Earthquakes and Faulting, 2nd ed. Cambridge University Press.

Schultz, R.A., Jensen, M.C., Bradt, R.C., 1994. Single crystal cleavage of brittle materials. Int. J. Fract. 65, 291–312. doi:10.1007/BF00012370

Scruggs, V.J., Tullis, T.E., 1998. Correlation between velocity dependence of friction and strain localization in large displacement experiments on feldspar, muscovite and biotite gouge. Tectonophysics 295, 15-40.

Scuderi, M.M., Niemeijer, A.R., Collettini, C., Marone, C., 2013. Frictional properties and slip stability of active faults within carbonate-evaporite sequences: The role of dolomite and anhydrite. Earth Planet. Sci. Lett. doi:10.1016/j.epsl.2013.03.024

Shimamoto, T., Logan, J.M., 1981. Effects of simulated clay gouges on the sliding behavior of Tennessee sandston. Tectonophysics 75, 243–255. doi:10.1016/0040-1951(81)90276-6

Shipton, Z.K., Evans, J.P., Kirschner, D., Kolesar, P.T., Williams, A.P., Heath, J., 2004. Analysis of CO_2 leakage through 'low-permeability' faults from natural reservoirs in the Colorado Plateau, east-central Utah. Geological Society, London, Special Publications 233, 43-58.

Shukla, R., Ranjith, P.G., Choi, S.K., Haque, A., 2011. Study of Caprock Integrity in Geosequestration of Carbon Dioxide. Int. J. Geomech. 11, 294–301. doi:10.1061/(ASCE)GM.1943-5622.0000015

Sibson, R.H., 1992. Fault-valve behavior and the hydrostatic-lithostatic fluid pressure interface. Earth Sci. Rev. 32, 141–144. doi:10.1016/0012-8252(92)90019-P

Sibson, R.H., 1990. Conditions for fault-valve behaviour, in: Knipe, R.J., Rutter, E.H. (Eds.), Deformation Mechanism, Rheology and Tectonics. Geological Society, London, Special Publications, pp. 15–28.

Smith, M.M., Sholokhova, Y., Hao, Y., Carroll, S.A., 2013. Evaporite Caprock Integrity: An Experimental Study of Reactive Mineralogy and Pore-Scale Heterogeneity during Brine-CO_2 Exposure. Environmental Science & Technology 47, 262-268.

Smith-rouch, B.L.S., Norton, G.A., Survey, U.S.G., 2006. Oligocene – Miocene Maykop / Diatom Total Petroleum System of the South Caspian Basin Province , Azerbaijan , Iran , and Turkmenistan. U.S. Geol. Surv. Bull. 2201-I 27.

Soltanzadeh, H., Hawkes, C.D., 2008. Semi-analytical models for stress change and

fault reactivation induced by reservoir production and injection. J. Pet. Sci. Eng. doi:10.1016/j.petrol.2007.05.006

Solum, J.G., Hickman, S.H., Lockner, D.A., Moore, D.E., Van Der Pluijm, B.A., Schleicher, A.M., Evans, J.P., 2006. Mineralogical characterization of protolith and fault rocks from the SAFOD Main Hole. Geophys. Res. Lett. doi:10.1029/2006GL027285

Sone, H., Shimamoto, T., Moore, D.E., 2012. Frictional properties of saponite-rich gouge from a serpentinite-bearing fault zone along the Gokasho-Arashima Tectonic Line, central Japan. J. Struct. Geol. 38, 172–182. doi:10.1016/j.jsg.2011.09.007

Song, J., Zhang, D., 2013. Comprehensive review of caprock-sealing mechanisms for geologic carbon sequestration. Environ. Sci. Technol. 47, 9–22. doi:10.1021/es301610p

Stumm, W., Morgan, J.J., 1981. Aquatic chemistry. J. Wiley and sons Inc.

Suckale, J., 2010. Moderate-to-large seismicity induced by hydrocarbon production. Lead. edge 310–319.

Sutherland, H.J., Cave, S.P., 1980. Argon gas permeability of New Mexico rock salt under hydrostatic compression. International Journal of Rock Mechanics and Mining Science & Geomechanics Abstracts 17, 281-288.

Takahashi, M., 2003. Permeability change during experimental fault smearing. J. Geophys. Res. 108, 2234. doi:10.1029/2002JB001984

Takahashi, M., Mizoguchi, K., Kitamura, K., Masuda, K., 2007. Effects of clay content on the frictional strength and fluid transport property of faults. J. Geophys. Res. Solid Earth 112. doi:10.1029/2006JB004678

Tanikawa, W., Shimamoto, T., 2009. Comparison of Klinkenberg-corrected gas permeability and water permeability in sedimentary rocks. International Journal of Rock Mechanics and Mining Sciences 46, 229-238.

Tembe, S., Lockner, D.A., Solum, J.G., Morrow, C.A., Wong, T.F., Moore, D.E., 2006. Frictional strength of cuttings and core from SAFOD drillhole phases 1 and 2. Geophys. Res. Lett. doi:10.1029/2006GL027626

Tembe, S., Lockner, D.A., Wong, T.F., 2010. Effect of clay content and mineralogy on frictional sliding behavior of simulated gouges: Binary and ternary mixtures of quartz, illite, and montmorillonite. J. Geophys. Res. Solid Earth 115, 1–22. doi:10.1029/2009JB006383

Tesei, T., Collettini, C., Barchi, M.R., Carpenter, B.M., Di Stefano, G., 2014. Heterogeneous strength and fault zone complexity of carbonate-bearing thrusts with possible implications for seismicity. Earth Planet. Sci. Lett. doi:10.1016/j.epsl.2014.10.021

Tesei, T., Collettini, C., Carpenter, B.M., Viti, C., Marone, C., 2012. Frictional strength and healing behavior of phyllosilicate-rich faults. J. Geophys. Res. Solid Earth. doi:10.1029/2012JB009204

Tenthorey, E., Cox, S.F., 2006. Cohesive strengthening of fault zones during the interseismic period: An experimental study. Journal of Geophysical Research: Solid Earth 111, n/a-n/a.

Trippetta, F., Collettini, C., Barchi, M.R., Lupattelli, A., Mirabella, F., 2013. A multidisciplinary study of a natural example of a CO_2 geological reservoir in central Italy. Int. J. Greenh. Gas Control 12, 72–83. doi:10.1016/j.ijggc.2012.11.010

Twiss, R.J., Moore, E.M., 2000. Structural Geology, Second. ed.

Uehara, S. ichi, Shimamoto, T., 2004. Gas permeability evolution of cataclasite and fault gouge in triaxial compression and implications for changes in fault-zone permeability structure through the earthquake cycle. Tectonophysics. doi:10.1016/j.tecto.2003.09.007

Van der Meer, L.G.H., Kreft, E., Geel, C.R., D'Hoore, D., Hartman, J., 2006. CO_2 storage and testing enhanced gas recovery in the K12-B reservoir, 23rd World Gas Conference Amsterdam, the Netherlands, p. 11.

Verberne, B.A., de Bresser, J.H.P., Niemeijer, A.R., Spiers, C.J., de Winter, D.A.M., Plümper, O., 2013. Nanocrystalline slip zones in calcite fault gouge show intense crystallographic preferred orientation: Crystal plasticity at subseismic slip rates at 18-150 °C. Geology 41, 863–866. doi:10.1130/G34279.1

Verberne, B.A., He, C., Spiers, C.J., 2010. Frictional properties of sedimentary rocks and natural fault gouge from the Longmen Shan fault zone, Sichuan, China. Bull. Seismol. Soc. Am. 100, 2767–2790. doi:10.1785/0120090287

Verberne, B.A., Niemeijer, A.R., De Bresser, J.H.P., Spiers, C.J., 2015. Mechanical behavior and microstructure of simulated calcite fault gouge sheared at 20–600°C: Implications for natural faults in limestones. J. Geophys. Res. Solid Earth 120, 8169–8196. doi:10.1002/2015JB012292

Verberne, B.A., Plümper, O., Matthijs De Winter, D.A., Spiers, C.J., 2014. Superplastic nanofibrous slip zones control seismogenic fault friction. Science (80-.). 346, 1342–44. doi:10.1126/science.1259003

Verberne, B.A., Spiers, C.J., Niemeijer, A.R., De Bresser, J.H.P., De Winter, D.A.M., Mper, O.P., 2014. Frictional Properties and Microstructure of Calcite-Rich Fault Gouges Sheared at Sub-Seismic Sliding Velocities. Pure Appl. Geophys. 171, 2617–2640. doi:10.1007/s00024-13-0760-0

Verdon, J.P., 2014. Significance for secure CO_2 storage of earthquakes induced by fl uid injection. Environ. Res. Lett. 9, 1–11. doi:10.1088/1748-9326/9/6/064022

Verdon, J.P., Kendall, J.-M., Stork, A.L., Chadwick, R.A., White, D.J., Bissell, R.C., 2013. Comparison of geomechanical deformation induced by megatonne-scale CO_2 storage at Sleipner, Weyburn, and In Salah. Proc. Nat. Acad. Sci. 110, E2762-E2771.

Vialle, S., Contraires, S., Zinzsner, B., Clavaud, J.-B., Mahiouz, K., Zuddas, P., Zamora, M., 2014. Percolation of CO_2-rich fluids in a limestone sample: Evolution of hydraulic, electrical, chemical, and structural properties. J. Geophys. Res. Solid Earth 119, 2828–2847. doi:10.1002/2014JB011198.Received

Vialle, S., Vanorio, T., 2011. Laboratory measurements of elastic properties of carbonate rocks during injection of reactive CO_2-saturated water. Geophys. Res. Lett. 38, 1–5. doi:10.1029/2010GL045606

Vilarrasa, V., Olivella, S., Carrera, J., Rutqvist, J., 2014. Long term impacts of cold

CO_2 injection on the caprock integrity. Int. J. Greenh. Gas Control 24, 1–13. doi:10.1016/j.ijggc.2014.02.016

Vrolijk, P., Van Der Pluijm, B.A., 1999. Clay gouge. J. Struct. Geol. 21, 1039–1048. doi:10.1016/S0191-8141(99)00103-0

Wang, H.F., 2000. Theory of linear poroelasticity with applications to geomechanics and hydrology. Princeton University Press.

Watson, M.N., Zwingmann, N., Lemon, N.M., 2004. The Ladbroke Grove-Katnook carbon dioxide natural laboratory: A recent CO_2 accumulation in a lithic sandstone reservoir. Energy 29, 1457–1466. doi:10.1016/j.energy.2004.03.079

Watson, M.N., Zwingmann, N., Lemon, N.M., Tingate, P.R., 2003. Onshore Otway Basin carbon dioxide accumulations: CO_2-induced diagenesis in natural analogues for underground storage of greenhouse gas. APPEA Journal 2003, 637-653.

White, J.A., Chiaramonte, L., Ezzedine, S., Foxall, W., Hao, Y., Ramirez, A., Mcnab, W., 2014. Geomechanical behavior of the reservoir and caprock system at the In Salah CO 2 storage project. PNAS 111, 8747–8752. doi:10.1073/pnas.1316465111

White, J.A., Foxall, W., 2016. Assessing induced seismicity risk at CO_2 storage projects: Recent progress and remaining challenges. International Journal of Greenhouse Gas Control 49, 413-424.

Wiprut, D., Zoback, M.D., 2000. Article Wiprut and Zoback - Fault reactivation and fluid flow along previously dormant normal fault in the northen North Sea. Geology 28, 595–598.

Wigley, M., Dubacq, B., Kampman, N., Bickle, M., 2013. Controls of sluggish, CO_2-promoted, hematite and K-feldspar dissolution kinetics in sandstones. Earth and Planetary Science Letters 362, 76-87.

Wigley, M., Kampman, N., Dubacq, B., Bickle, M., 2012. Fluid-mineral reactions and trace metal mobilization in an exhumed natural CO_2 reservoir, Green River, Utah. Geology 40, 555-558.

Wilkinson, M., Gilfillan, S.M.V., Haszeldine, R.S., Ballentine, C.J., 2008. Plumbing the depths – testing natural tracers of subsurface CO_2 origin and migration, Utah, USA. , in: Grobe, M., Pashin, J.C., Dodge, R.L. (Eds.), Carbon Dioxide Sequestration in Geological Media - State of the Science, pp. 1-16.

Zhang, S., Cox, S.F., 2000. Enhancement of fluid permeability during shear deformation of a synthetic mud. J. Struct. Geol. doi:10.1016/S0191-8141(00)00065-1

Zhang, S., Tullis, T.E., 1998. The effect of fault slip on permeability and permeability anisotropy in quartz gouge. Tectonophysics 295, 41–52. doi:10.1016/S0040-1951(98)00114-0

Zhang, S., Tullis, T.E., Scruggs, V.J., 2001. Implications of permeability and its anisotropy in a mica gouge for pore pressures in fault zones. Tectonophysics. doi:10.1016/S0040-1951(01)00044-0

Zhang, S., Tullis, T.E., Scruggs, V.J., 1999. Permeability anisotropy and pressure

dependency of permeability in experimentally sheared gouge materials. J. Struct. Geol. 21, 795–806. doi:10.1016/S0191-8141(99)00080-2

Zhang, Y., Schaubs, P.M., Zhao, C., Ord, A., Hobbs, B.E., Barnicoat, A.C., 2007. Fault-related dilation , permeability enhancement , fluid flow and mineral precipitation patterns : numerical models, in: The Internal Structure of Fault Zones: Implications for Mechanical and Fluid-Flow Properties. pp. 239–255. doi:10.1144/SP299.15

Zoback, M.D., Byerlee, J.D., 1975. The Effect of Microcrack Dilatancy on the Permeability of Westerly Granite. J. Geophys. Res. 80, 752–755. doi:10.1029/JB080i005p00752

Zoback, M.D., Gorelick, S.M., 2012. Earthquake triggering and large-scale geologic storage of carbon dioxide. PNAS 109, 10164–10168. doi:10.1073/pnas.1202473109

Zysset, M., Schindler, P.W., 1996. The proton promoted dissolution kinetics of K-montmorillonite. Geochim. Cosmochim. Acta 60, 921–931.

Acknowledgements

At one point I did not expect to write this section anymore, but here we are, at the end of my PhD. And as with all major achievement, this study could not have been realised without the help and support of many people, therefore I would like to take some time to thank the people I have worked with during my PhD, inspired me, relaxed with or anyone who helped me through this intense period of time. And if I, by mistake, forgot any of you, I'm truly sorry, but I have appreciated your time or help contributing to my PhD research.

First and foremost, I would like to thank **Chris Spiers**. In the last 5-6 years you have been my promotor, teacher and mentor. With you positive approach, enthusiasm, knowledge and also critical and perfectionistic way of working, you have taught and challenged me to become the kind of researcher I want to be. But besides a dedicated professor and researcher, you have always been a kind and thoughtful man, who never forgot to ask how the person behind the researcher was doing. This journey has been inspiring and so much fun, and yes at times it also was very intense and frustrating, but I am and always will be grateful that you offered me a position in your lab and under your wings, giving me the opportunity to learn how to do proper research.

Suzanne, my first co-promotor, without you I would not have finished this work. Besides an inspiring researcher, you have been my daily-supervisor and friend (in- and outside the lab) ever since you came back from Shell. Thank you for your valuable and enthusiastic help whether it concerned sparring about CCS and CO_2-induced reactions, new experiments, writing up my work, or keeping me positive about finalising my PhD, you were always there for me. I'm truly grateful for your help, but also enjoyed all of our trips either around town or to Vienna(chocolate?)/ Zurich/San Francisco etc. **André**, my second co-promotor, thank you for helping me with the more technical parts of doing a PhD, as well as sparring about what the frictional strength and stability of gouges mean. You were not one of my (co-) promotors, but **Hans** thank you for helping me with the most complex chapter I have reported in this thesis, without your clear directions, and no-nonsense approach, I finally wrote it down. From my "profiel-werkstuk" until my PhD thesis,

you have helped me become a geological researcher. **Colin**, we did not interact on a daily basis, but thank you for all your help, either in the Tuesday meetings or during our technical talks about doing experiments, your knowledge is enormous.

Besides all the help I have gotten from the academic staff, I could not have done any of the research without the practical, technical and/or mental help from our supporting staff, and I'm happy and grateful to have worked with you all. **Magda**, onze secretaresse, bedankt voor alle hulp die u geboden heeft tijdens mijn PhD, van alle bureacratische rompslomp tot het aansporen van het invullen en inleveren van mijn "urenstaten". Mijn tijd als PhD-er (en ons lab) had niet hetzelfde en zo georganiseerd geweest zonder uw aanwezigheid en doortastendheid. Maar bovenal bedankt voor alle gesprekken die we hebben gehad en de peptalks die u mij de laatste jaren gegeven hebt, ik ga ze missen. **Gert**, bedankt voor al je technische en mentale ondersteuning de afgelopen jaren. Ik vind het machtig interessant wat je in de werkplaats doet en maakt, en heb regelmatig gedacht dat ik voor het verkeerde vak heb gestudeerd (ik overweeg nog steeds om een cursus werkbank draaien te gaan volgen). **Eimert** bedankt dat u me altijd Elisenda hebt genoemd, ik heb dat erg gewaardeerd. Ondanks dat we qua werk weinig met elkaar te maken hadden, heb ik altijd genoten van onze praatjes in het lab of tijdens de koffie. Geniet van uw pensioen. **Peter**, ik denk dat ik je soms helemaal gek maakte met mijn zandstenen en kleien, maar bedankt voor alle XRD en TGA analyses, klusjes en bestellingen die u over de jaren voor mij gedaan heeft. **Thony**, bedankt voor alle technische hulp met de ring-shear of daar waar nodig (het reficeren van de Heard etc.), en de gesprekken al dan niet onder het genot van een kop koffie. **Floris**, jij kwam pas toen ik aan mijn laatste jaar begon, maar jouw vrolijke en opgewekte humeur zorgde voor leuke gesprekken. Ik hoop dat jij net zo'n leuke tijd in het HPT gaat hebben als ik altijd heb gehad.

Otto, Leonard en Ingrid, officieel gezien horen jullie niet tot onze groep, maar we deelden wel een gang. Otto en Leonard, bedankt voor het maken van mijn thin en thick-sections, het was niet altijd makkelijk, maar het resultaat is heel mooi geworden. Ingrid, als student was ik altijd een beetje bang om bij u naar binnen te moeten, maar dat veranderde toen we collegas werden. Het was altijd gezellig om even een praatje met u te hebben bij de printer of met de hond. En als laatste **Reinoud**. Bedankt dat ik bij u voor raad en daad terecht kon toen het voor mij uitzichtloos leek, ik heb mijn PhD gelukkig met plezier (!) af kunnen ronden.

My time in the HPT-lab would have been boring without all its former and current family-members (PhD-students, Post-docs, long/short-term visitors and any other associates). First, a special thanks goes to my roommate **Jinfeng** "Ross", from the beginning to the end, we have made it both and I hope you will find a job that will make you happy, good luck with your future! Next I want to specifically thank three of my fellow HPT-family members; **Sabine, Tim and Nino**. Sabine, wederzijdse paranimf, ik wil je bedanken voor al je hulp in de afgelopen jaren, ik heb enorm veel van jou gedetailleerde en precieze manier van schrijven en werken geleerd! Maar daarnaast was het gewoon ook erg gezellig, zowel binnen als buiten het lab. Tim, de laatste van de "oude generatie", bedankt voor alle steun en hulp die je me zeker in het laatste jaar hebt geboden, het was soms wel erg fijn dat jij net voor mij zat en alles uitgevogeld hebt (zonder jou had dit boekje er niet gelegen..). And Nino, thank you for allowing me to show you I'm not a Figa… well you know what I mean, wherever I was (Utrecht or SF) I could always count on good company and delicious food. And of course thanks to all other HPT'ers (in any form) for sharing a cup of coffee, a chat, a complaining session, a nice meal or anything else you have made my PhD-life enjoyable and memorable, so thank you; **Sabrina, Esther, Sander, Jon, Amir, Maartje, Anne, Sander, Ken, Chen, Michiyo, Ayumi, Joost, Eva, Maartje, Luca, Bart** (bedankt voor de leerzame SEM-sessies!), **Nawaz, Miao, Martijn** (bedankt voor de mooie figuren!), **Ronald, Evangelos, Mariska** (nog eens dansen?), **Luuk** (stoelendans?), **George, Amin, Zahra, Loes, Yu, Peter, Piercarlo, Bill, Derek** and **Paul, Gill, Martyn, Oliver** and **Helen**. Finally, I would like to thank **John Kaszuba** for our collaboration, I learned a lot about CO_2 and geochemical modelling and enjoyed our weekly Skype-meetings after you left (I might take you up on your offer).

Hoewel ik het soms heel moelijk vond om mijn "normale" leven buiten de het lab te combineren met het doen van een PhD, zijn jullie mijn lieve vrienden er altijd geweest en gebleven. Zelfs wanneer ik weer eens af zei omdat ik tot laat moest werken of ik, wanneer ik niet af zei, jullie uren heb zitten vervelen met mijn "problemen" in mijn onderzoek, hebben jullie geluisterd en geprobeerd mij op te vrolijken. Zo was jij **Marielle**, als de stress me weer eens te veel werd en ik even uit mijn hoofd moest komen, altijd in om even op donderdag, zaterdag of zondag te gaan dansen. Bedankt dat ik je al ruim 25 jaar mijn vriendin mag en kan noemen! Of kon ik altijd rekenen op jullie, **His en Eef**, voor een gezellige (vriendinnen-

)avond/weekend in Rotterdam of Amsterdam ;-). En niet te vergeten mijn “kook”-vrienden (**Arne, Lisette en Julian, Bennard** en **Oliva, Dennis, Janine** en **Luuk, Luuk** en **His** en **Jean-Marc** en **Sabina**), die altijd de leukste, lekkerste en soms bijzondere gerechten op tafel zetten om vervolgens mede te delen dat ik “tante” wordt. Onze etentjes zijn en waren altijd hoogtepunten om naar uit te kijken en ik hoop er nog vele mee te mogen maken (en vaker “tante” te worden).

Het doen van een PhD is niet alleen een intellecuele uitdaging, maar ook een mentale, daarom wil ik jullie graag bedanken **Jolanda** en **Marga**. Jolanda, bedankt dat ik afgelopen anderhalf jaar regelmatig, en soms last-minute, bij je langs kon komen om met je te praten. Die momenten hebben niet alleen inzicht gegeven qua werk, maar ook qua persoonlijke keuzes. Zij hebben mij enorm gestimuleerd om door te gaan. Marga, bedankt voor je luistered oor, praktische tips en heerlijke maaltijden.

Last but not least, my family. Een PhD doe je nooit alleen, of in ieder geval niet in mijn geval. Ik ben intens dankbaar en blij dat jullie mij de afgelopen jaren altijd met veel interesse, liefde, geduld en bemoedigende woorden hebben gesteund. Bedankt dat jullie luisterden naar de frustraties die gepaard gingen met mijn leven als PhD-student, zo kon ik met hernieuwde energie weer aan de slag. Mijn enorme dank gaat dan ook uit naar jullie; **Oma, Jordi, Teuny** en **Fol, Adrie** en **Margreth, Sjoerd** en **Eva, Irmgard** en **Rob, Brian** en **Priscilla**. En in blijvende herinnering **Opa**, **Oma**, **en Opa**, jullie zijn (net) te vroeg gegaan, maar ieder van jullie heeft mij levenslessen meegegeven die in mijn PhD van onschatbare waarde zijn gebleken. **Mama en Papa**, bedankt voor jullie tomeloze support aan en het vertrouwen in mij. Zonder jullie had ik mij nooit zo ver kunnen ontplooien en had ik niet het doorzettingsvermogen aan de dag kunnen leggen dat dit werk met zich mee bracht. En als allerlaatste dank ik mijn zus **Amarantha**, van allemaal heb jij wel het meeste te “verduren” gehad van mijn PhD. Het heeft geregeld tot verhitte disuccsies en ruzies geleid, maar je was er wel altijd wanneer ik je nodig had! Bedankt dat je me altijd gesteund hebt, en ik ben heel erg blij dat jij mijn paranimf wil zijn!

“Enlightenment says the world is nothing
nothing but a dream, everything's an illusion
and nothing is real”

Van Morrison, Enlightenment

Curriculum vitae

29 September 1987	Born in Zwijndrecht, the Netherlands
2000-2006	Pre-university education (VWO) Develstein College, Zwijndrecht
2006-2009	B.Sc. Earth Sciences Utrecht University, Utrecht
2009-2011	M.Sc. Geology Utrecht University, Utrecht
2011-2017	Ph.D. Experimental Rock Deformation Utrecht University, Utrecht